RESEARCH

2007-47

Shear Capacity of Prestressed Concrete Beams

Technical Report Documentation Page

1. Report No.	2.	3. Recipients Accession No.
MN/RC 2007-47		

4. Title and Subtitle	5. Report Date
Shear Capacity of Prestressed Concrete Beams	November 2007
	6.

7. Author(s)	8. Performing Organization Report No.
Brian Runzell, Carol Shield, Catherine French	

9. Performing Organization Name and Address	10. Project/Task/Work Unit No.
Department of Civil Engineering University of Minnesota 500 Pillsbury Dr. S.E. Minneapolis, Minnesota 55455	11. Contract (C) or Grant (G) No. (c) 81655 (wo) 145

12. Sponsoring Organization Name and Address	13. Type of Report and Period Covered
Minnesota Department of Transportation 395 John Ireland Boulevard Mail Stop 330 St. Paul, Minnesota 55155	Final Report 14. Sponsoring Agency Code

15. Supplementary Notes
http://www.lrrb.org/PDF/200747.pdf

16. Abstract (Limit: 200 words)

The shear provisions of the American Association of State Highway and Transportation Officials bridge design code have changed significantly in recent years. The 2004 Load and Resistance Factor Design (LRFD) and 2002 Standard shear provisions for the design of prestressed concrete bridge girders typically require more shear reinforcement than the 1979 Interim shear provisions. The purpose of this research was to determine whether or not bridge girders designed according to the 1979 interim shear provisions were underdesigned for shear and develop a method to identify potentially underdesigned girders. Two shear capacity tests were performed on opposite ends of a bridge girder removed from Mn/DOT Bridge No. 73023. The stirrup spacing in the girder suggested it was designed according to the 1979 Interim shear provisions. The results from the shear tests indicated the girder was capable of holding the required shear demand because the applied shear at failure for both tests was larger than the factored shear strength required by the 2004 LRFD HL-93 and 2002 Standard HS20-44 loading. The results of a parametric study showed that girders designed using the 1979 Interim were most likely to be underdesigned for shear near the support and that the girders most likely to be underdesigned in this region had smaller length to girder spacing ratios.

17. Document Analysis/Descriptors	18. Availability Statement
Shear Prestressed concrete girders	No restrictions. Document available from: National Technical Information Services, Springfield, Virginia 22161

19. Security Class (this report)	20. Security Class (this page)	21. No. of Pages	22. Price
Unclassified	Unclassified	237	

Shear Capacity of Prestressed Concrete Beams

Final Report

Prepared by:

Brian Runzel
Carol K. Shield
Catherine W. French

Department of Civil Engineering
University of Minnesota

November 2007

Published by:

Minnesota Department of Transportation
Research Services Section
395 John Ireland Boulevard, MS 330
St. Paul, Minnesota 55155-1899

Acknowledgements

The authors would like to thank the Minnesota Department of Transportation (Mn/DOT) for its contributions to this research project. The funding was provided entirely by Mn/DOT. In addition, the authors would like to thank the Advance Shoring Company for the technical support and shoring equipment used during the laboratory portion of this research.

Table of Contents

List of Tables

List of Figures

Executive Summary

The shear provisions of the American Association of State Highway and Transportation Officials (AASHTO) bridge design code have changed significantly in recent years. The 2004 Load and Resistance Factor Design (LRFD) and 2002 Standard shear provisions for the design of prestressed concrete bridge girders, current at the time of this research, typically required more shear reinforcement than the 1979 Interim shear provisions. As of 2007, the Minnesota Department of Transportation (Mn/DOT) bridge inventory contained many bridge girders designed according to the 1979 Interim shear provisions. The purpose of this research was to determine whether or not bridge girders designed according to the 1979 Interim shear provisions were understrength for shear and develop a method to identify potentially understrength girders.

Two shear capacity tests were performed on opposite ends of a bridge girder removed from Mn/DOT Bridge No. 73023. The stirrup spacing in the girder suggested it was designed according to the 1979 Interim shear provisions. The results from the shear tests indicated the girder was not understrength for shear, because the applied shear at failure for both tests was larger than the factored shear strength required by the 2004 LRFD HL-93 and 2002 Standard HS20-44 loading.

The tested bridge girder was 54 in. deep, 88 ft. long, had a nominal concrete compressive strength of 6 ksi, and came from a bridge with 10 ft. girder spacing. Because the tested girder was not undercapacity, it is likely that 1979 Interim era bridge girders with similar characteristics also have adequate shear strength. To expand on the experimental results, a parametric study of typical 1979 Interim era Mn/DOT bridge girders was performed to identify which, if any, girders in the Mn/DOT bridge inventory were likely understrength for shear.

Twelve prestressed concrete bridge girders believed to represent the range of girders in the Mn/DOT bridge inventory were selected from existing Mn/DOT bridges. The bridge girders in the parametric study ranged from 36 in. to 54 in. deep, 40 ft. to 100 ft. long, had a nominal concrete compressive strength between 5 ksi and 6 ksi, and were from bridges with girder spacing between 7 ft. and 14 ft. Because there was no way to verify that the selected girders had been designed according to the 1979 Interim provisions, the stirrup spacing for these girders was recalculated using the 1979 Interim shear provisions. The 2002 Standard shear provisions were then used to calculate the nominal shear resistance of the bridge girders in the parametric study, because based upon test results available in the literature, the shear provisions of the 2002 Standard were reliable for predicting the shear capacity of prestressed concrete members.

The results of the parametric study showed that the girders were most likely to be underdesigned for shear between 0.1L (L is the girder span length) and the support. In this region, the factored nominal shear resistance to factored ultimate shear ratio, $\frac{\phi V_{n,2002Std}}{V_u}$, for the girders varied between 0.73 and 1.09, and was proportional to $\frac{L}{S_g}$, where S_g is the girder spacing. Girders with a $\frac{L}{S_g}$ of 10 or greater were not underdesigned for shear, while girders with an $\frac{L}{S_g}$ of 8.5 or less had a $\frac{\phi V_{n,2002Std}}{V_u}$ of approximately 0.9 or less and are at risk of being understrength for shear.

Mn/DOT has sponsored a companion research project titled: *Discrepancies in Shear Strength of Prestresssed Beam with Different Specifications* that includes a study of the effect of concrete arching action near the support and concrete strength gain with time on the shear capacity of existing bridge girders. The results of this companion study can be used to determine, with reasonable confidence, the reserve shear capacity of existing bridge girders. For girders with a $\frac{L}{S_g}$ of 8.5 or less, the expected reserve shear capacity can then be added to the 2002 Standard predicted shear capacity ($\phi V_{n,2002Std}$) to determine if any bridge girders in the Mn/DOT inventory require retrofit for shear.

.

Chapter 1
Introduction

1.1 AASHTO Shear Design Provisions for Prestressed Concrete Beams

The 12th edition of the American Association of State Highway and Transportation Officials, AASHTO, Standard Specifications for Highway Bridges published in 1983 contained a major revision to the shear provisions for prestressed concrete beams. These revisions were a significant departure from the shear provisions for prestressed concrete beams given in the 1979 Interim revisions to the Standard specifications. The shear provisions in the 1983 Standard specifications were identical to those in the 2002 Standard specifications (AASHTO, 2002), which were current as of 2007.

Another major revision of the shear provisions was introduced in the 1st edition of the AASHTO Load and Resistance Factor Design, LRFD, Bridge Design Specifications published in 1994. The shear provisions in the 1994 LRFD were largely the same as those in the 4th edition published in 2004 (AASHTO, 2004), which were also current as of 2007.

The 1983 and 1994 revisions to the shear provisions were the result of extensive research on the shear behavior of prestressed concrete beams and were believed to be more reliable than the shear provisions of the 1979 Interim specifications. The revised provisions have largely resulted in an increase in the shear reinforcement required in prestressed concrete beams, which implies that bridge girders designed according to the 1979 Interim specifications do not meet the shear capacity requirements of the subsequent bridge design codes. As of 2007, there were many prestressed concrete bridge girders in service throughout Minnesota that were designed using the 1979 Interim shear provisions. The goal of this research project was to determine whether or not these bridge girders were at risk of being undercapacity, and if they posed a potential safety hazard.

1.2 Research Methodology

Two ends of an 88 ft. bridge girder likely designed according to the 1979 Interim shear provisions were removed from service and tested to measure shear capacity. The measured capacities were compared to the shear demand of the 2004 LRFD, 2002 Standard, and 1979 Interim specifications to determine if the bridge girders were undercapacity relative to any of the specifications. The shear test results were also used, in conjunction with data available in the literature, to determine which of the shear provisions were the most reliable for predicting the shear capacity of prestressed concrete beams. These provisions were then used to conduct a parametric study of typical Minnesota Department of Transportation, Mn/DOT, bridge girders to determine if other girders in the Mn/DOT bridge inventory were at risk of being undercapacity.

1.3 Organization

The results from the research are organized into chapters as follows:

Chapter 2 is a general introduction to the shear provisions, including equations and definition of the variables, from the AASHTO 2004 LRFD, 2002 Standard, and the 1979 Interim Specifications. In Chapter 3 a detailed description of the test specimens, along with capacity calculations based on the 2004 LRFD, 2002 Standard, and the 1979 Interim specifications, are presented. Trends in the shear provisions are also investigated in this chapter. Chapter 4 provides a description of the laboratory test setup, instrumentation, and the shear provision parameters measured with the instrumentation. Chapter 5 is a presentation of the results from material testing of the concrete, transverse reinforcing steel, and the prestressing steel. In this chapter, revised shear capacity calculations based on the measured material properties are presented. In Chapter 6 the results and analysis from the shear capacity tests are discussed. The parametric study used to determine girders most at risk of being undercapacity is presented in Chapter 7. Supplemental data is provided in the appendices.

Chapter 2
Shear Capacity Models

2.1 Introduction

Many models are available to predict the shear strength of prestressed concrete girders, however, there is little consensus among researchers as to which is the most accurate and suited for use in design. As a result, there are several design specifications based on several different models. At the time of this research, there were three AASHTO bridge design codes for the design of prestressed concrete bridge girders, including: the AASHTO 2004 LRFD (AASHTO, 2004), 2002 Standard (AASHTO, 2002), and the 1979 Interim (AASHTO, 1979). A total of four shear design methods were contained in these three codes: three sectional methods and the 2004 LRFD version of the Strut-and-Tie model. This chapter is intended to provide background on the models behind the AASHTO shear provisions and to explain the provisions in detail.

2.2 Shear Resistance in Prestressed Concrete Beams

Cracked, prestressed concrete beams resist shear through a variety of mechanisms. According to ASCE-ACI Committee 426 (ASCE, 1973), the predecessor to ASCE-ACI Committee 445, the generally accepted mechanisms are: interface shear transfer, shear transfer in the compression zone, dowel action of the reinforcement, shear transfer from the transverse steel, and the vertical component of the force in the draped prestressing strands. All of these mechanisms are illustrated in Figure 2.1. Beams with a small shear span to depth ratio also transfer shear through arching action, which is not discussed in this chapter, as the sectional methods in the codes are not based on arching action.

When a normal strength concrete beam initially cracks, the two surfaces on either side of the crack are rough, with aggregate protruding across the plane of the crack. Shear is transferred across this interface because these rough surfaces prevent slip. This resistance mechanism is also known as aggregate interlock. The magnitude of the shear resistance provided by aggregate interlock is dependent upon the size of the aggregate and width of the crack. Larger aggregate and narrower cracks increase the shear transferred through aggregate interlock.

The uncracked portion of a cracked concrete beam is subjected to both compressive and shearing stresses. Thus, this portion of the concrete beam contributes to shear resistance. The magnitude of the resistance is dependent upon the depth of the uncracked concrete.

Dowel action of the reinforcement occurs when a shear crack intersects longitudinal reinforcing steel. The dowel action of the reinforcement introduces tension into the surrounding concrete, which can cause the concrete to split along the axis of the bar. The contribution of dowel action to shear resistance is dependent upon the amount of longitudinal reinforcement in a beam, and for beams with shear reinforcement: the ability of transverse reinforcement to restrain the splitting cracks.

Transverse reinforcement resists shear once the concrete cracks by developing tension in the transverse steel. It also helps increase shear resistance by keeping inclined crack widths small, which improves aggregate interlock. The magnitude of the shear resistance provided by

transverse reinforcement is dependent upon the yield strength, cross-sectional area, and distribution of the steel.

Most of the AASHTO design methods, with the exception of the Strut-and-Tie model, superimpose the shear resistance of the concrete, V_c, due to aggregate interlock, shear transfer in the compression zone, and dowel action with the shear resistance provided by the stirrups, V_s, and the shear resistance provided by the vertical component of the force in the draped prestressing strand, V_p, to determine the shear capacity of the section:

$$V_n = \left(V_c + V_s + V_p\right) \tag{2.1}$$

The main difference among the various AASHTO methods is the procedure for determining the different contributions.

2.3 Truss Model

The truss model is the basis for the stirrup contribution to shear capacity for many of the shear methods (MacGregor, 1997). This model represents the load paths in cracked concrete as a truss with the stirrups acting as the vertical tension members, the concrete acting as the compression chord and the compression diagonals, and the flexural reinforcement acting as the tension chord. An example of a truss model for a reinforced concrete beam is shown in Figure 2.2. Knowing the stirrup forces, $A_v f_{sy}$, the truss in this figure becomes statically determinate. In this model, the beam is proportioned so that the stirrups yield before the concrete crushes, and sufficient longitudinal steel is provided for horizontal equilibrium.

The shear resistance of the model is entirely dependent upon the amount and distribution of transverse reinforcement. The stirrup contribution to shear capacity is illustrated in Figure 2.3, and given by the following equation:

$$V_s = \frac{A_v f_{sy}(\, jd \cot\theta)}{s} \tag{2.2}$$

The shear provisions that include a form of Eqn. (2.2) either implicitly define, or provide a method for calculating, the angle of the inclined struts, θ. This model does not explicitly address the vertical component of the effective prestressing force and the concrete contribution to shear capacity, and, therefore, does not provide a means for estimating V_c and V_p.

2.4 AASHTO 2002 Standard Section 9.20

The shear provisions in the 2002 Standard are based on a 45° truss model with an additional term to account for the concrete contribution to shear resistance. The concrete contribution is a function of the type of shear cracking that controls (flexure-shear or web-shear) at a given cross-section. Flexure-shear cracking controls where moment is large and shear exists, and web-shear cracking typically controls in thin web members near the supports where moment is small and shear is large. The contribution of prestressing to shear resistance is included in the equations for the concrete contribution.

A flexure-shear crack originates as a vertical flexural crack in a member. As the crack penetrates deeper into the cross-section it becomes inclined as a result of the shear stresses

within the section. Shear capacity controlled by flexure-shear cracking is the sum of the shear required to initiate flexural cracking plus an increment necessary to extend the crack to a flexure-shear crack. The flexure-shear cracking capacity is given in the 2002 Standard as:

$$V_{ci} = \left\{ 1.7\sqrt{f_c'}bd \le 0.6\sqrt{f_c'}bd + V_d + \frac{V_i M_{cr}}{M_{max}} \right\} \tag{2.3}$$

where b is the width of the web, d is the distance from the extreme compression fiber to the centroid of the tension reinforcement, and f_c' is the 28-day concrete compressive strength. For composite members V_d is the shear force at the cross-section of interest due to unfactored self weight and unfactored superimposed dead loads; M_{max} is the maximum factored moment at the cross-section of interest due to externally applied loads; and V_i is the factored shear force at the cross-section of interest due to externally applied loads occurring simultaneously with M_{max}. The term M_{cr} is the moment causing flexural cracking at the cross-section due to externally applied loads, and is given in the code as:

$$M_{cr} = \frac{I_{gc}}{y_{tc}} \left(6\sqrt{f_c'} + f_{pe} - f_d \right) \tag{2.4}$$

In this equation I_{gc} is the gross moment of inertia of the composite cross-section; y_{tc} is the distance from centroidal axis of the gross composite section to the extreme tension fiber; f_{pe} is the compressive stress in the concrete due to the effective prestressing force at the extreme tension fiber of the cross-section; and f_d is the tensile stress due to the unfactored dead load (self weight and superimposed) at the extreme tension fiber of the cross-section.

The other type of shear failure considered in the design of prestressed concrete members is the result of web-shear cracking. Web-shear cracks form when the principal tensile stresses from shear exceed the tensile strength of the concrete. The resistance to web-shear cracking is due to the tensile strength of the concrete and the compressive forces in the section due to the prestressing force and the applied loads. In addition, the vertical component of the prestressing force due to draped strands provides resistance to the shear. The expression for web-shear strength usually governs for heavily prestressed beams with thin webs, especially when the beam is subject to large concentrated loads near the supports.

The web-shear equation predicts the shear strength at the onset of web-shear cracking and is given in the 2002 Standard code as:

$$V_{cw} = \left(3.5\sqrt{f_c'} + 0.3 f_{pc} \right) bd + V_p \tag{2.5}$$

In this equation, f_{pc} is the compressive stress in the concrete at the centroid of the cross-section resisting externally applied loads or at the junction of the web and top flange when the centroid lies within the flange of a composite section, and V_p is the vertical component of the effective prestressing force at the cross-section of interest.

In the 2002 Standard, the stirrup contribution to shear capacity is based on a truss model assuming a 45° crack pattern. This assumption is conservative for prestressed members, because the effect of prestressing causes diagonal cracking to form at a shallower angle, thus intercepting more stirrups than predicted by the 45° truss model. With the angle of inclination conservatively set to 45°, the horizontal projection of the crack is taken as d, which is the distance from the

extreme compression fiber to the centroid of the tension steel. With these assumptions, Eqn. (2.2) becomes:

$$V_s = \frac{A_v f_{sy} d}{s} \tag{2.6}$$

where A_v is the cross-sectional area of the vertical legs of the transverse reinforcement; f_{sy} is the yield strength of the transverse reinforcement; and s is the center-to-center spacing of the transverse reinforcement.

The code requires a minimum amount of web reinforcement to ensure ductility at failure. The minimum amount of transverse reinforcement is specified in the code by the following equation:

$$A_{v_{\min}} = 50\frac{bs}{f_{sy}} \tag{2.7}$$

where b and s are in inches, and f_{sy} is in psi. The maximum stirrup spacing allowed by the code is the smaller of $0.75h$ or 24 inches, to ensure that each crack is crossed by at least one stirrup. The maximum spacing is reduced in half when V_s exceeds $4\sqrt{f_c'}bd$.

A limitation on the maximum amount of transverse reinforcement is given in the code as:

$$V_{s\max} = 8\sqrt{f_c'}bd \tag{2.8}$$

The steel contribution is limited to avoid crushing of the diagonal concrete struts.

The location of the critical section for a prestressed member is $h/2$ away from the face of the support. If the cross-section of interest in the shear analysis is within the transfer length of the prestressing strands, the effective prestressing force must be reduced. According to the code, the effective prestressing force after losses is transferred linearly to the concrete over a transfer length of 50 strand diameters.

2.5 AASHTO 1979 Interim Specifications

A footnote in Section 9.20 of the 2002 Standard code permits the use of the 1979 Interim code for shear design. Like the 2002 Standard, this code is also based on the truss model, with an additional term to account for the concrete contribution to shear resistance. The 1979 Interim has one equation for the concrete contribution:

$$V_c = 0.06 f_c' bjd \le 180bjd \tag{2.9}$$

where j is calculated as the ratio of the distance between the centroid of compression and centroid of tension, to d at ultimate flexural capacity. In Eqn. (2.9), the limit of 180 psi controls for all concrete strengths of 3000 psi or greater. Thus the concrete contribution from Eqn. (2.9) is independent of concrete strength for high strength concrete.

The stirrup contribution in the 1979 Interim is derived from the truss model, but the angle is assumed to be shallower than 45°. The V_s equation in the 1979 Interim is double the V_s term from the 2002 Standard code, and is given in the code as:

$$A_v = \frac{(V_u - V_c)s}{2 f_{sy} jd} \tag{2.10}$$

which can be rewritten as:

$$V_s = \frac{2 A_v f_{sy} jd}{s} \tag{2.11}$$

There is no explanation for the factor of two in the code, but according to the Precast/Prestressed Concrete Institute (PCI) Bridge Design Manual it accounts for the beneficial effect of prestressing (PCI, 2003). Essentially the factor of two reduces the angle of the diagonal compression in the truss model from 45° to 29.1°, which means more stirrups cross a given crack in the truss model for the 1979 Interim code compared to the model for the 2002 Standard.

The minimum shear reinforcement required in the 1979 Interim is twice that required by the 2002 Standard, and is given by:

$$A_v = \frac{100 bs}{f_{sy}} \tag{2.12}$$

It is important to note that there is no maximum limit on V_s, thus a designer using the 1979 Interim code could prescribe an unlimited amount of transverse reinforcement in a prestressed beam to carry the required shear and still be within code requirements. This is potentially unconservative, because there is nothing in the code to ensure that the compression diagonals do not fail by crushing, which is a brittle failure.

The 1979 Interim does not require shear design at a specified critical section. Instead the code says that the critical section of a beam is not likely to be in a region where shear is a maximum, but rather at a location with a large moment. It further recommends that shear be investigated between the midspan and quarter points of the span length. According to the code, the design at the quarter points should be used in the outer quarters of the beam. For long span members, this suggestion in the code could be particularly unconservative.

2.6 Modified Compression Field Theory

The Modified Compression Field Theory, MCFT, is a shear model developed by Vecchio and Collins (1986), which is based on a variable angle truss model. The formulation of MCFT includes equilibrium, strain compatibility, and a constitutive relationship for diagonally cracked concrete. Using these principles, the MCFT model accounts not only for V_s, but also the combined effect of the complex shear resistance mechanisms that contribute to V_c without having to consider each mechanism individually. The intent of this section is to introduce the MCFT equations for V_c and V_s, and also to describe the constitutive relationship for diagonally cracked concrete, which is a fundamental component of the model.

2.6.1 Formulation of V_c and V_s

Unlike the truss model presented in Section 2.3, MCFT includes the concrete contribution to the vertical tension ties. Figure 2.4 shows the principal tensile and compressive stresses, f_1

and f_2 respectively on a cracked cross-section with zero moment. The principal tensile stresses are assumed to vary in between cracks as shown in the figure, therefore, f_1 is the average value over a gage length long enough to include several cracks. In this figure, the vertical components of both f_1 and f_2 contribute to the shear resistance.

Using Mohr's circle for stresses, the average principal stresses are related through the following equation (Collins and Mitchell, 1991):

$$f_2 = (\tan\theta + \cot\theta)v - f_1 \tag{2.13}$$

where v is the average uniform shear stress in the cross-section:

$$v = \frac{V}{bjd} \tag{2.14}$$

Prior to cracking, θ in Figure 2.4 is 45°, and the principal stresses are equal in magnitude. When the specimen cracks, θ is no longer 45°, and the stirrups must resist the difference between the principal stresses as shown in Figure 2.5 and given by (Collins and Mitchell, 1991):

$$A_v f_{sy} = (f_2 \sin^2\theta - f_1 \cos^2\theta)bs \tag{2.15}$$

Substituting Eqns. (2.13) and (2.14) into Eqn. (2.15), and rearranging the terms produces (Collins and Mitchell, 1991):

$$V = f_1 bjd \cot\theta + \frac{A_v f_{sy}}{s} jd \cot\theta \tag{2.16}$$

The first and second terms in this equation are V_c and V_s respectively. Thus, the shear resistance of a member is dependent upon the quantity of transverse steel, and the magnitude and direction of the principal tensile stress in the cracked concrete.

2.6.2 Constitutive Relationship for Cracked Concrete

A constitutive relationship for cracked concrete is a key component required to make Eqn. (2.16) useful for design. The tensile stress distribution in cracked concrete shown in Figure 2.4 is complicated, and according to MCFT there are two states of tensile stress that govern the constitutive relationship; the average state, and the local state at the surface of a crack, both of which are shown in Figure 2.6 (Collins et al., 1996). The vertical component of the average principal tensile stress in the concrete must be statically equivalent to the vertical components of the stresses at the surface of a crack. Because the local tensile stress in the concrete at a crack face is zero, according to MCFT, the vertical component of the average tensile stress is carried by tensile stress in the shear reinforcement until the stirrups yield. After the stirrups yield, any increase in the vertical component of the average tensile stresses must be carried by the vertical component of the shear stresses on the crack interface, otherwise known as aggregate interlock. Therefore, the magnitude of f_1 in Eqn. (2.16) is dependent upon the widths of the concrete cracks.

According to MCFT, the width along a crack is related to the magnitude of the principal tensile strain, ε_1; a larger ε_1 results in a wider crack. Vecchio and Collins (1986) performed tests on reinforced concrete panels in pure shear, which relate the average ε_1 to the average f_1. Their

tests defined this relationship, as shown in Figure 2.7, from initial cracking until the stirrups begin to yield, and the cracks start to open. The equation that describes the relationship between the average f_1 and ε_1 is:

$$f_1 = \frac{f_{cr}}{1+\sqrt{500\varepsilon_1}} \tag{2.17}$$

where f_{cr} is the tensile strength of the concrete. Once the stirrups begin to yield and the cracks begin to open, local equilibrium at the crack interface (i.e., the ability of the crack surface to transfer tensile stresses through aggregate interlock) limits the magnitude of the average f_1 given by Eqn. (2.17) as shown in Figure 2.7.

To define the constitutive relationship after the stirrups yield, and local equilibrium at the crack interface limits f_1, Vecchio and Collins (1986) developed a set of empirical equations based entirely on research conducted by Walraven (1981) on aggregate interlock. The empirical equations are:

$$f_1 = v_{ci}\tan\theta \tag{2.18}$$

$$v_{ci} = \frac{2.16\sqrt{f_c'}}{0.3+\frac{24w}{a+0.63}} \tag{2.19}$$

$$w = \varepsilon_1 s_c \tag{2.20}$$

In these equations, v_{ci} is the shear stress on the crack surface, which is a function of the crack width, w, and the size of the aggregate, a. The crack width in turn is a function of the average ε_1 and the crack spacing, s_c. These equations for local equilibrium limit the magnitude of the average f_1 as indicated in Figure 2.7.

2.6.3 MCFT Summary

Although the MCFT is based more on the fundamentals of mechanics than other shear models, empiricism is still involved. The accuracy of the model relies heavily on the constitutive relationship developed by Vecchio and Collins, and the assumption that tension is "transmitted" across cracks in an average sense. Furthermore, to use the constitutive model to solve Eqn. (2.16), the magnitude of ε_1 at ultimate must be known. The authors of the model (Collins et al., 1996) suggest performing an analysis at ultimate, assuming plane sections remain plane, to determine the axial strain, ε_x, in a cross-section at the level of the tension reinforcement. The axial strain can then be related to ε_1 using Mohr's circle. However, now the principal tensile stress and the truss angle in Eqn. (2.16) are no longer independent and the solution requires iteration.

The elements of MCFT presented in this section provide a brief overview of the method, and an introduction to the key component of the model: the constitutive relationship of cracked concrete. In addition, MCFT includes the effect of prestressing on the average ε_1, and a method to check the tensile stresses in the longitudinal steel and stresses in the compression diagonals. The 2004 AASHTO LRFD shear provisions are based on the MCFT, and are presented in the subsequent section.

2.7 AASHTO 2004 LRFD Section 5.8

The 2004 LRFD assumes that the total shear resistance is the sum of the concrete contribution, steel contribution, and the vertical component of the draped prestressing strand:

$$V_n = \left[\left(V_c + V_s + V_p\right) \le \left(0.25 f_c' b d_v + V_p\right)\right] \tag{2.21}$$

where b is the effective web width taken as the minimum web width within the depth d_v, and d_v is the flexural lever arm which is the distance from the resultant tension force to the resultant compressive force which need not be taken less than the greater of $0.9d$ or $0.72h$. The term $0.25f_c'bd_v$ is intended to ensure that the concrete will not crush prior to yield of the transverse reinforcement.

The concrete shear resistance is expressed in the code as:

$$V_c = 0.0316\beta\sqrt{f_c'}bd_v \tag{2.22}$$

where β is a factor that indicates the ability of diagonally cracked concrete to transmit tension in an average sense. To simplify the code, there are two tables that provide β depending on whether or not a given section has transverse steel. The constitutive relationships defined by Eqns. (2.17) through (2.20) were used to determine the values of β in the tables.

The steel contribution to shear is given in the code as:

$$V_s = \frac{A_v f_{sy} d_v}{s}\cot(\theta) \tag{2.23}$$

where θ is the angle of the diagonal compressive stresses and is also tabulated in the code along with the β factor .

As described in Section 2.6, the concrete capacity to resist shear is dependent upon the average principal tensile strain, ε_1, at the cross-section of interest. The value of the average ε_1 is difficult to calculate, so the code provides an equation for longitudinal strain, ε_x, which is related to the average ε_1 through Mohr's circle. Increasing axial tension increases longitudinal strains in the section, which reduces the ability of the concrete to resist shear cracking and decreases V_c.

As described in the code, the transverse reinforcement helps a member evenly distribute the shear stresses in cracked concrete; therefore, calculating ε_x at the level of the longitudinal reinforcement is too conservative. For members with transverse reinforcement, the code suggests using the longitudinal strain at middepth for shear design:

$$\varepsilon_x = \frac{\frac{M_u}{d_v} + 0.5N_u + 0.5V_u\cot(\theta) - A_{ps}f_{po}}{2(E_s A_s + E_p A_{ps})} \tag{2.24}$$

where N_u is the applied factored axial force; f_{po} can be taken as the jacking stress and is not reduced for transfer length; E_p and E_s are the moduli of elasticity of the prestressed and nonprestressed reinforcing steel respectively; and A_{ps} and A_s are the areas of prestressed and nonprestressed reinforcement, respectively, on the flexural tension side of the member. If the value of ε_x is negative, then the concrete section is in compression and the denominator of the

above expression for ε_x is modified to include the stiffness of the concrete, $E_c A_{gc}$, where E_c is the modulus of elasticity of the concrete and A_{gc} is the gross area of the composite section. The longitudinal strain parameter given by Eqn. (2.24) accounts for the influence of moment, shear, and axial load on shear strength.

Both θ and β depend on ε_x and average shear stress at the cross-section of interest. The shear stress is given in the code as:

$$v = \frac{(V_u - V_p)}{bd_v} \tag{2.25}$$

Using the resulting values of longitudinal strain and shear stress from Eqns. (2.24) and (2.25), the values of θ and β are obtained from the respective table in the 2004 AASHTO code.

In addition to the shear design equations, the following equation is a check of the longitudinal reinforcement to ensure it is proportioned to carry the tensile stresses from moment, shear and axial load:

$$A_y f_{sy} + A_{ps} f_{ps} \geq \frac{M_u}{d_v} + 0.5N_u + \left(V_u + 0.5V_s - V_p\right)\cot(\theta) \tag{2.26}$$

The minimum shear reinforcement is given in the code as:

$$A_{v,\min} = 0.0316\sqrt{f_c'}\,\frac{b_v s}{f_{sy}} \tag{2.27}$$

This minimum is required to ensure adequate ductility in the section, and to limit the amount of diagonal cracking. The code directly accounts for a required increase in the minimum amount of transverse reinforcement as the concrete compressive strength increases. The maximum amount of transverse reinforcement allowed in the section is indirectly specified by the limit set on V_n in Eqn. (2.21).

The 2004 LRFD specifies that the critical section be taken as the distance d_v from the support. To use Eqns. (2.21) through (2.26) for shear design, an initial guess of θ is made, ε_x is calculated, a new value of θ (which is a function of ε_x) is read from the appropriate table in the 2004 LRFD, and the new θ is used as the next "guess" to recalculate ε_x. This process is repeated until the value of θ converges, at which point β is also read from the appropriate table, and the shear strength is subsequently calculated. This method requires multiple iterations for shear design.

2.8 Strut and Tie Model

The Strut-and-Tie Model, covered in the 2004 AASHTO LRFD Section 5.6.3, is suited for "disturbed" regions where plane sections no longer remain plane. This type of behavior is found near supports and concentrated loads. The Strut-and-Tie Model provides insight into the flow of forces in disturbed regions. All stresses are condensed into compression and tension members, and nodes are used to join the members. The model uses "struts" to represent the concrete in compression, "ties" to model the tension reinforcement, and nodal zones to represent regions of the concrete subjected to multidirectional stresses where the struts and ties meet.

The strength of an unreinforced strut is given by the 2004 LRFD as:

$$P_n = f_{cu} A_{cs} \tag{2.28}$$

where f_{cu} is the limiting concrete compressive stress and A_{cs} is the effective cross-sectional area of the strut. The limiting compressive stress is given in the code as:

$$f_{cu} = \frac{f_c'}{0.8 + 170\varepsilon_1} \leq 0.85 f_c' \tag{2.29}$$

in which:

$$\varepsilon_1 = \varepsilon_s + (\varepsilon_s + 0.002)\cot^2 \alpha_s \tag{2.30}$$

where α_s is the smallest angle between the compressive strut and an adjoining tension tie, ε_1 is the principal tensile strain in the cracked concrete, and ε_s is the tensile strain in the concrete in the direction of the tension tie. For prestressed concrete members, ε_s is zero until the precompression is overcome. If the strut is reinforced, the yield strength of the reinforcement, multiplied by the area of steel in the strut, is added to Eqn. (2.28). In Eqn (2.29), ε_1 essentially acts to limit f_{cu}: the larger the principal tensile strain in the concrete, the less effective it is in carrying compression in the strut.

The strength of the tension ties are given in the code as:

$$P_n = f_y A_s + A_{ps}\left(f_{pe} + f_y\right) \tag{2.31}$$

where f_y and A_s are the yield strength and area of the nonprestressed reinforcement respectively, f_{pe} is the stress in the prestressing steel after losses, and A_{ps} is the area of the prestressing steel. According to the 2004 LRFD, the second term in Eqn. (2.31) is intended to ensure that the prestressing steel does not reach yield. The limit on the stress in the prestressing strand to the sum of f_{pe} and f_y is an arbitrary limit. In addition to Eqn. (2.31), the tension ties must be anchored in the nodal zone so that the reinforcement is developed before it extends beyond the boundary of the node.

The dimensions of the nodal region are defined by the size of the strut and tie "members" connected by the node, and the strength of a nodal region is dependent on the state of stress in the node. For a nodal region connecting only compression "members", the allowable stress on the node face is $0.85f_c'$. For a node containing one tension tie the limit is $0.75f_c'$, and for more than one tension tie it is $0.65f_c'$.

The Strut-and-Tie Model does not produce unique solutions. Any model is allowed that satisfies geometry and strength requirements. When the Strut-and-Tie Model is used for design, the components of the model are proportioned so that the tension ties fail prior to the compression struts to provide ductility at failure.

2.9 Evaluation of the Shear Design Provisions

Rationality, ease of use, and reliability are important considerations in evaluating the effectiveness of shear design provisions. A rational method is defined as having a firm physical basis. The code should give designers an indication of the mechanisms and paths used to

transfer loads to the supports. For ease of use, the code must give the designer a clear understanding of the required procedure, and the parameters used should be simple and well defined. A reliable code should provide reasonable estimates of shear capacity, and be applicable for many different cross-sections, load types, and amounts of prestressing. One way to evaluate the reliability of the shear design methods is to compare predicted shear strength to experimental data available in the literature. In this section, the ability of the AASHTO shear provisions to predict the response of prestressed concrete members is discussed.

2.9.1 NCHRP Project 12-61

The Transportation Research Board, TRB, administered the National Cooperative Highway Research Program, NCHRP, Project 12-61 *Simplified Shear Design of Structural Concrete Members*. The goal of this project was to evaluate the various shear design methods in existence and propose a simplified approach to shear design that could ultimately replace the current AASHTO LRFD shear provisions. Part of the research conducted under Project 12-61 included compiling a comprehensive database of shear tests on both regular reinforced and prestressed concrete beams. This database, along with analysis, was published in the appendices of NCHRP Report 549 (Hawkins et al., 2005).

The entire database for prestressed concrete members contained the results from 743 shear tests. To evaluate the shear design provisions from various codes, a smaller subset of the database consisting of 85 prestressed members was used. This was a subset of members all containing shear reinforcement and considered to have properties similar to members used in real world applications. The subset of data was also published in the appendices of Report 549, with the distribution of member properties shown in Figure 2.8. This select database was compiled specifically to avoid having a database skewed by short span, shallow depth, and heavily reinforced members. Any members that possibly failed in flexure were also excluded from this database.

2.9.2 Evaluation of the AASHTO Shear Design Provisions

In the appendices of Report 549, the results compiled in the select database were compared to the predictions of several design codes, and shear design methods available in the literature. The comparisons to the 2002 AASHTO Standard, 2004 AASHTO LRFD, and 1979 AASHTO Interim codes are summarized in this section. The Strut-and-Tie Model was not discussed in the appendices of Report 549, so there is no discussion of the Strut-and-Tie Model in this section.

The test-to-predicted shear strength ratios for the three AASHTO codes are compared in Table 2.1. The 2004 LRFD was the most reliable of the three codes with the lowest mean, standard deviation, and coefficient of variation. The mean, standard deviation, and coefficient of variation were higher for the 2002 Standard, which meant that there was more scatter in the data for this method, but it was also more conservative on average. The results from both the 2004 LRFD and 2002 Standard were similar and suggested that these methods were conservative, but not overly so.

The 1979 Interim code had the lowest mean, but also the highest standard deviation and coefficient of variation. Because the mean was 1.09 with a standard deviation of 0.417 and coefficient of variation of 0.383, a significant number of members had a $\frac{V_{test}}{V_{pred}}$ ratio below 1.0 (i.e., the 1979 Interim over-predicted the strength of these test specimens, and was thus unconservative). These results in the NCHRP report indicated that the 1979 Interim code provided a lower reliability for shear design.

Figure 2.9 and Figure 2.10 are both from the parametric study published in the appendices of Report 549 and help explain the unconservatism of the 1979 Interim. These figures show there was a clear trend in the data when the test to predicted shear strength ratios were plotted relative to f_c' and the stirrup reinforcement ratio, $\rho_v f_{sy}$.

The 1979 Interim code was clearly unconservative for concrete strengths below 8ksi, and for members with large amounts of shear reinforcement. The latter resulted because the 1979 Interim code did not place a limit on the maximum amount of shear reinforcement. According to the 1979 Interim, the shear capacity of a member will continue to increase indefinitely in proportion to the amount of transverse reinforcement. In reality, there must be a physical limit on the amount of transverse reinforcement in a member, because the concrete diagonals in a beam that is heavily reinforced in shear will crush before the stirrups reach yield. This is a brittle failure, which must be avoided in design. Members with a low concrete compressive strength were particularly susceptible to this type of failure.

All of the members with a $\frac{V_{test}}{V_{pred}}$ below 0.5 in Figure 2.9 and Figure 2.10 were those with an f_c' below 7 ksi and a $\rho_v f_{sy}$ greater than 1,800 psi. Unlike the 1979 Interim, the 2004 LRFD and 2002 Standard both had limits intended to address this issue.

From the results in the NCHRP report, it was apparent that the 1979 Interim code was unreliable for predicting shear capacity. Conversely, both the 2004 LRFD and the 2002 Standard provided reliable predictions of shear capacity, and thus were found to be useful tools for predicting the shear capacity of prestressed concrete members.

Chapter 3
Investigation of the AASHTO Shear Provisions

3.1 Introduction

The AASHTO 2004 LRFD, 2002 Standard, and 1979 Interim specifications contain different provisions to calculate the shear capacity of prestressed concrete bridge girders. The shear provisions in these codes are presented in detail in Chapter 2, and were all permitted for use in design in 2007. The underlying theory behind each of these shear provisions is different, and result in different stirrup spacing for the design of the same bridge girder. To investigate how the codes differ, each of the shear provisions was used to predict the shear capacity of the two specimens described in the subsequent section that were tested as part of this investigation. The results presented in this chapter do not include strength capacity reduction factors, ϕ.

3.2 Specimen Description

The two specimens tested for this project were obtained from a girder in Mn/DOT Bridge No. 73023, which was removed from service. Two 30.5 ft. long ends were cut from the same 88 ft. bridge girder to make the specimens. According to information from the bridge construction plans, the original bridge girder was likely more than 20 years old when it was removed from service. This meant the girder was designed according to either the 1983 Standard or 1979 Interim specifications. The 1983 Standard specifications contained the same shear design provisions as the 2002 Standard.

The specimens were Mn/DOT Type 54 girders which had the dimensions and gross section properties shown in Figure 3.1. They had 10 draped and 33 straight ½ in., 270 ksi, stress relieved strands spaced 2 in. on center. The strand patterns at the end and harp point are shown in Figure 3.2 and Figure 3.3, respectively. The harp points for the draped strands were 38 ft. from each end of the original 88 ft. girder, which were outside of the 30.5 ft. long test specimens.

The stirrup spacing in the specimens is shown in Figure 3.4, and was essentially 21 in. over the entire length of the beam, except at the original ends of the 88 ft. girder, which had closer spacing over the support in the prestressing strand anchorage zone. The stirrups were specified as double leg, Grade 60, #4 reinforcing bars. In addition to the full depth stirrups, shown in Figure 3.4, there were stirrups spaced at 21 in. for horizontal shear. These were non-continuous stirrups that terminated at the top web/flange intersection, and were designed to ensure composite action between the girder and bridge deck.

The specimens were identical; therefore the predicted shear capacities presented in this chapter apply to both. To investigate the influence of the deck on shear capacity, calculations were performed with and without a bridge deck. Figure 3.5 shows the cross-section of the specimen with the bridge deck. The width of the deck was 48 in. for the capacity calculations, because this was width used in the shear test described in a subsequent section. The reinforcement layout shown in Figure 3.5 was identical to the layout in the deck of Mn/DOT Bridge No. 73023.

3.3 Investigation of the AASHTO Shear Provisions

To investigate trends in the AASHTO shear provisions, each were used to calculate the shear capacity of the specimens. For this exercise, the load was applied at midspan as shown in Figure 3.4. This loading configuration was different than that used during the specimen tests described in Chapter 4. In addition to the nominal material and section properties described in Section 3.2, the capacities reported below used assumed concrete compressive strengths, f_c', of 6 ksi for the prestressed beam, and 4 ksi for the bridge deck. A sample of the capacity calculations for each of the AASHTO shear provisions is provided in Appendix A.

3.3.1 AASHTO 2004 LRFD

According to the 2004 LRFD code, the shear strength of prestressed concrete members is composed of a concrete contribution, V_c, transverse steel component, V_s, and vertical component of the prestressing force, V_p. The concrete contribution, V_c, for a given cross-section is related to the magnitude of the moment-to-shear ratio from applied loads; a larger ratio reduces shear capacity. The stirrup contribution, V_s, is dependent on the angle of the principal compressive stress at the cross-section of interest. Shear-moment interaction diagrams were constructed to determine V_c and V_s, because they could not be calculated directly.

The 2004 LRFD code was cumbersome to use for predicting the shear capacity of the specimen, because the ultimate shear force and moment were unknowns in the equations. To calculate capacity, a shear-moment interaction diagram was constructed at each cross-section of interest along the beam. The shear capacity was then determined based on the moment-to-shear ratio at the section of interest. A non-iterative spreadsheet, developed with the same equations found in the 2004 LRFD, was used to assist in creating the shear-moment interaction diagrams (Bentz and Collins, 2000a). A sample of the calculations performed by the spreadsheet is given in Section A.1.1.

The results of this analysis for the specimen with and without a bridge deck are shown in Figure 3.6 and Table 3.1. The axis labeled "position" in the plot refers to the location of the cross-section under consideration in Figure 3.4, with origin of the axis coinciding with the roller support. The plot in the figure terminates prior to the roller support to avoid including the stirrups from the prestressing strand anchorage zone in the shear capacity calculations, which would greatly distort the scale of the "Shear Capacity" axis. The general shape of both plots was controlled by the moment-to-shear ratio, and value of the effective shear depth, d_v, at each cross-section because these were the only parameters that changed along the length of the specimen.

The moment-to-shear ratio at each cross-section was unaffected by the bridge deck (neglecting the negligible additional dead load), therefore, the effect of this parameter on the calculations with and without a bridge deck was identical. The moment-to-shear ratio increased from both the roller and pinned supports to the applied load, which reduced the shear capacity. If this were the only parameter affecting shear capacity, the plots in Figure 3.6 would be symmetric about the applied load at the midpoint of the figure.

The effective shear depth, d_v, was responsible for the lack of symmetry about the applied load in Figure 3.6. Due to the draped strands shown in Figure 3.4, d_v changed along the length and affected shear capacity; a larger d_v increased shear capacity. The draping was not symmetric about the midpoint of the specimen (because both specimens were cut from the beam ends of a

single girder), as a result, the effective shear depth increased from the roller to the pinned support. The 2004 LRFD included a minimum d_v of 0.72h that controlled when the calculated effective shear depth was unrealistically small. If the moment-to-shear ratio had been constant, the change in d_v along the length would have linearly increased shear capacity from the point where the minimum d_v stopped controlling to the pinned support.

To explain the behavior of the shear capacity plots in Figure 3.6, the combined effects of the moment-to-shear ratio and d_v must be considered. When the deck was included in the calculations, the change in these parameters from the roller support to the applied load combined to make the shear capacity essentially constant. When the deck was not included, 0.72h controlled d_v from the roller support to near the applied load, which allowed the change in the moment-to-shear ratio to cause a decrease in the shear capacity. From the applied load to the pinned support, the change in moment-to-shear ratio and d_v combined to increase the shear capacity for the calculations with and without a bridge deck.

Including the bridge deck in the calculations increased the shear capacity of every cross-section along the entire length of the specimen compared to the case with no deck. This increase was due to the increase in d_v of the specimen with a bridge deck. Without the bridge deck, there was a distinct minimum shear capacity directly under the applied load as evident in Figure 3.6. Adding the bridge deck eliminated the distinct minimum, and made it difficult to predict where failure would occur.

3.3.2 AASHTO 2002 Standard

Unlike the 2004 LRFD, the 2002 Standard code provided a straightforward means to predict capacity. At each cross-section, V_c was determined by calculating whether flexure-shear, V_{ci}, or web shear, V_{cw}, controlled. The effect of the prestressing force was included in the V_{ci} and V_{cw} calculations through the M_{cr} and V_p terms, respectively.

The results of the shear capacity calculations for the specimen with and without a bridge deck are shown in Figure 3.7 and given in Table 3.1. As with the shear capacity plot in the previous section, the axis labeled "position" refers to the location of the cross-section under consideration in Figure 3.4, with the origin of the axis coinciding with the roller support. Adding the bridge deck to the specimen slightly decreased the shear capacity along the entire length except for the region between 11 ft. and 17 ft. This was counterintuitive, because the distance from the extreme compression fiber to the centroid of the prestressing force, d, was larger in the specimen with a bridge deck. If considered independently, a larger d would raise both the concrete and steel contributions to shear capacity. Thus, the explanation for why the shear capacity plots behaved as shown in the figure lies in how the bridge deck affected other parameters in the equations for V_{ci} and V_{cw}. Equations (3.1) and (3.2) are the equations for flexure-shear and web shear, respectively.

$$V_{ci} = 0.6\sqrt{f_c'}bd + V_d + \frac{V_i M_{cr}}{M_{max}} \tag{3.1}$$

$$V_{cw} = \left(3.5\sqrt{f_c'} + 0.3 f_{pc}\right)bd + V_p \tag{3.2}$$

Web shear cracking, V_{cw}, controlled V_c from the roller support to 11 ft. and from 17 ft. to the pinned support for the specimen without a bridge deck, and over the entire length of the specimen with a bridge deck, as shown in Figure 3.8 and Figure 3.9. A major parameter in Eqn. (3.2) for V_{cw} was the magnitude of the compressive stress at the neutral axis, f_{pc}. For a noncomposite specimen, only axial compression from the prestressing force contributed to f_{pc}:

$$f_{pc} = \frac{P}{A_g} \tag{3.3}$$

where P is the force in the prestressing strand, and A_g is the gross area of the noncomposite specimen. When the deck was included, f_{pc} was the compressive stress at the neutral axis of the composite specimen due to the prestressing force and self weight moments (of the girder, M_g, and deck, M_d) assuming the girder acted alone:

$$f_{pc} = \frac{P}{A} - \frac{Pe(y_{tc} - y_t)}{I_g} + \frac{(M_g + M_d)(y_{tc} - y_t)}{I_g} \tag{3.4}$$

where y_t, and y_{tc} are the distances from the extreme tension fiber to the centroid of the noncomposite and composite specimens, respectively (note that if y_{tc} is in the flange, it is limited to the distance from the extreme tension fiber to the web/flange intersection); and I_g is the moment of inertia of the noncomposite specimen. The stress from the self-weight moments in Eqn. (3.4) was negligible compared to the stress from the prestressing force. The tensile stress due to the eccentricity of the prestressing force at the location where f_{pc} was calculated for the composite section reduced the value of f_{pc}, and therefore V_{cw}, at every cross-section when compared to the noncomposite specimen. When the bridge deck was included in the shear capacity calculations, the beneficial effect from an increased d was more than offset by the reduction in f_{pc}. In the regions where both specimens were controlled by web shear cracking, the reduction in f_{pc} caused the shear capacity of the composite section to fall below that of the noncomposite section.

Between the roller support and 11 ft., the difference in shear capacity between the two specimens was not as significant compared to the region between 17 ft. and the pinned support, because the minimum d, $0.8h$, in the code controlled for the calculations without a bridge deck, while d_p, controlled d for the calculations with a deck. This meant that the value of d was growing larger for the composite section while d for the noncomposite section remained constant between the roller support and 11 ft. In the region between 17 ft. and the pinned support, d_p controlled d in both cases, which caused a more significant difference in shear capacity between the two.

Adding the bridge deck significantly increased the predicted shear capacity between 11ft and 17ft as shown in Figure 3.7. The increase in shear capacity was due to the influence of the deck on the cracking moment, M_{cr}, of the section. Without the deck, V_{ci} controlled the shear capacity in this region, however, when the deck was added it increased M_{cr} and caused V_{cw} to control over the entire length of the specimen. This is illustrated in Figure 3.8 and Figure 3.9.

If the assumed loading in Figure 3.4 were applied to the specimen without a bridge deck, the behavior shown in the plots of Figure 3.7 suggest this specimen would fail directly under the applied load. Because V_{ci} controlled in this region, the expected failure would be a flexure-shear type failure. By including the bridge deck in the calculations, the dip in capacity under the applied load was eliminated, and failure would likely be through web-shear.

3.3.3 AASHTO 1979 Interim

A footnote in Section 9.20 of the 2002 Standard code permitted the use of the 1979 Interim code for shear design. The 1979 Interim had one equation for V_c, but limited the allowed shear stress in the concrete to no more than 180 psi regardless of f_c'. The upper limit controlled V_c for all concrete strengths of 3,000 psi or greater, which applied to the 6,000 psi design strength of the specimen. There was no equation for V_p in the code; instead the prestressing was accounted for by doubling the V_s contribution to shear capacity. The stirrup contribution to shear capacity, according to the 1979 Interim, was twice that of the 2002 Standard code.

A plot of shear capacity versus position using the 1979 Interim is provided in Figure 3.10. The linear increase in shear strength shown in the figure resulted from the draped strands in the specimen. The distance from the center of gravity of the prestressing strands to the bottom of the girder decreased linearly from the roller to the pinned support as shown in Figure 3.4, which increased *d*. The 1979 Interim code had no minimum *d*, so the impact on shear strength was a linear increase in shear capacity from the roller support to the pinned support. Including the bridge deck in the shear capacity calculations increased *d* along the entire specimen length and uniformly amplified the shear capacity plot shown in the figure.

If the assumed loading in Figure 3.4 were applied to the specimen, regardless of whether it had a bridge deck or not, the shear capacity shown in Figure 3.10 indicated failure would occur close to the support. In this situation the applied shear due to the concentrated load, assuming self-weight was negligible, would be constant and the lowest capacity for both cases would be near the support.

3.4 Comparison among the AASHTO 2004 LRFD, 2002 Standard, and 1979 Interim Specifications

Figure 3.11 and Figure 3.12 show plots of the predicted shear capacity according to the three codes without and with a deck, respectively. There was quite a range in the results. The 1979 Interim code was the most conservative, followed by the 2004 LRFD and finally the 2002 Standard code. Including the bridge deck in the shear capacity calculations eliminated the dip in capacity at midspan predicted by both the 2002 Standard and 2004 LRFD. If considered independently, the data in Figure 3.11and Figure 3.12 suggests that the 1979 Interim shear provisions were the most conservative. However, these figures must be considered in the context of shear design.

For simply supported members, the 1979 Interim code recommended shear design between the midspan and quarter points of the span length. The stirrup spacing required at the quarter points could be used from the quarter points to the supports. This design method was less conservative than the 2004 LRFD and 2002 Standard methods, which required sectional design much closer to the support where the shear demand was typically greater. Therefore, while the 1979 Interim equation and limit for V_c given in Eqn. (2.9) was the most conservative, the implementation of the 1979 Interim shear provisions in design was not conservative.

3.5 Design Using the AASHTO 2004 LRFD, 2002 Standard, and 1979 Interim Specifications

To illustrate that implementation of the 1979 Interim shear provisions was the least conservative, the original 88 ft. girder was designed for vertical and horizontal shear using the three different shear provisions. The girder was designed assuming: simple supports, AASHTO HL-93 loading for the 2004 LRFD live load and HS20-44 loading for the 2002 Standard and 1979 Interim live load, 10 ft. girder spacing, 9 in. bridge deck, and dead load from the girder, deck, diaphragms, barriers and wearing course. The load and strength capacity reduction factors are given in Table 3.2. Sample calculations at the critical section from each of the shear provisions are given in Section A.2. Results for half of the girder are summarized in Table 3.3 and are symmetric for the remainder of the girder.

The stirrup requirements from the 2004 LRFD shear provisions were the most conservative along much of the beam, particularly near the supports. From the support to 9 ft., the 1979 Interim required significantly fewer stirrups than the other shear provisions. However, at the critical section defined by the 1979 Interim, which was 22 ft. from the support, the stirrup spacing required by the 1979 Interim was the most conservative (of the requirements for vertical shear). These results support the notion that the 1979 Interim equation and limit for V_c was the most conservative, but implementation of the provisions was not.

Note the stirrup spacing in the column labeled "provided spacing" in Table 3.3 varies slightly from the 1979 Interim required stirrup spacing. The exact 1979 Interim required stirrup spacing was 21.8 in. and it is likely the designer rounded the required spacing to 22 in., which is slightly unconservative.

3.6 Strut and Tie Model

The 2004 LRFD code required that deep beams and beams with discontinuities be designed according to the strut and tie model. Although the specimens did not fall into either of these two categories, the strut and tie model in the 2004 LRFD was used to predict the shear capacity of the specimens. The strut and tie model for half of the specimen without a bridge deck is shown in Figure 3.13. This half represents the portion of the specimen from the roller support to the applied load shown in Figure 3.4. The discussion in this section is focused on this portion of the strut and tie model, because it contained the segment of the original 88 ft. bridge girder from the support to 9 ft. which was the segment most likely to be under-designed for shear.

The strut and tie model was not based on a sectional analysis, so it did not result in a shear capacity vs. position plot like the methods presented previously in this chapter. Rather, the shear capacity of the strut and tie model was dependent upon the limit state of one of the elements in the model. The model in Figure 3.13 consisted of compression struts in the concrete, tension ties (i.e., the vertical stirrups and horizontal prestressing strand), and nodes to connect these elements. The stirrups are all shown in their proper locations in the specimen. This particular strut and tie model was the result of a few iterations, and is presented here because it produced the highest predicted shear capacity of the strut and tie model iterations.

The results from analysis of the model are given in Table 3.1, and sample calculations are provided in Section A.1.4. The shear capacity listed in the table is dependent upon the contribution from: all seven stirrups, a direct compression strut from the applied load to the support, and the vertical component of the draped strands (which is not pictured in Figure 3.13).

The strength of the nodal regions did not control the strength of the compression struts. The specimen was I-shaped, and as a result, the nodal regions were in the top and bottom flanges, which were significantly wider than the web. Therefore, it was the strength of the compression struts in the web region that controlled their contribution to shear capacity. The nodal dimensions were used to determine the area of the struts, but the thickness of the web and allowable compressive stress determined the strength of the struts.

According to the 2004 LRFD, the strength of a compression strut is controlled by an allowable stress that is dependent on the angle of the strut:

$$f_{cu} = \frac{f_c'}{0.8 + 170\varepsilon_1} \leq 0.85 f_c' \tag{3.5}$$

in which:

$$\varepsilon_1 = \varepsilon_s + (\varepsilon_s + 0.002)\cot^2 \alpha_s \tag{3.6}$$

These equations were presented in Chapter 2. According to Eqn. (3.6), a shallower angle results in a larger principal tensile strain in the concrete, ε_1, which reduces the allowable compressive stress in a strut, f_{cu}. In Figure 3.13, the strut connecting to each stirrup was capable of resisting the magnitude of the compressive stress resulting from yield of the stirrup. Thus, the compressive forces in all of these struts were limited by yielding of the stirrups. The strength of the direct compression strut between the applied load and the roller support was controlled by α_s in Eqn. (3.6). Therefore, yielding of the stirrups and strength of the direct compression strut limited the shear capacity in Table 3.1.

Including the bridge deck in the strut and tie model increased the shear capacity of the specimen by increasing α_s of the direct compression strut between the applied load and the roller support. The angle was increased because the depth of the top node in Figure 3.14 was much shallower when the bridge deck was included in the model. As a result, f_{cu} for the direct compression strut was larger, and the contribution of the direct compression strut to shear resistance was increased. The compressive force in the struts connected to each stirrup was controlled by yield of the stirrups, as was the case for the specimen with no bridge deck.

Chapter 4
Experimental Setup and Instrumentation

4.1 Introduction

A detailed description of the test specimens and preliminary capacity calculations were presented in Chapter 3. This chapter describes the experimental setup and instrumentation for the shear capacity tests of both specimens. This chapter also describes how the test results were used to evaluate the accuracy of the AASHTO shear capacity specifications presented in Chapter 2.

4.2 Experimental Setup

The test specimens were brought to the University of Minnesota Structures Laboratory and tested with a MTS 600 kip Universal Testing Machine. The specimens were moved into the testing apparatus using the Structures Laboratory crane, which had a maximum capacity of 15 tons. To avoid exceeding this capacity, the specimen length delivered to the laboratory was limited to 30.5 ft. with the bridge deck removed.

To investigate the effect of the deck on shear capacity, the specimens were tested with and without a deck, referred to subsequently as Specimens I and II, respectively. Since the deck had been removed prior to transport, a new deck was added to the specimen after it was situated in the testing apparatus. The maximum deck width the 600 kip Universal Testing Machine could accommodate was 48 in. The bridge deck was designed to be the same thickness and have the same longitudinal steel layout as the deck from the in-service bridge. The cross-section of the bridge deck is shown in Figure 3.5. The transverse steel is not shown in the figure, but was the minimum required for shrinkage and temperature; two layers of Grade 60, #4 reinforcing bars spaced at 18 in. horizontally. The concrete mix used in the deck was the Mn/DOT 3Y33 design, which had a nominal 28-day compressive strength of 4 ksi. Shored construction was used for the deck because it was simpler to construct in the laboratory.

The testing machine was designed to apply a single concentrated load to the specimens. To avoid transferring shear to the support via a direct compressive strut, it was decided to maintain a shear span-to-depth ratio of at least 2.7. The depth of Specimen I was 63 in, which made it necessary to apply the load at least 14 ft. away from either support to achieve the proper shear span. With the test setup shown in Figure 3.4, the predicted shear capacity from Table 3.1 for Specimen I was 276 kips according to the 2002 Standard code, which was close to the maximum capacity that could be attained with the 600 kip testing machine for the desired shear span-to-depth ratio. Thus, it was decided to modify the test specimens to maintain the shear span-to-depth ratio of 2.7 and provide ample buffer between the predicted shear capacity and maximum capacity of the MTS machine.

The specimen modification involved lengthening the beams from 30.5 ft. to approximately 40 ft. by splicing a cast-in-place beam extension onto the original prestressed girder section. The cast-in-place extension was designed to resist the moment and shear from the maximum possible load applied by the 600 kip machine. The plan for extension of Specimen I is shown in Figure 4.1. The extension was identical for Specimen II. The cross-section marked A-

A in Figure 4.1 is shown in Figure 4.2. Photos from construction of the extensions are shown in Figure 4.3 and Figure 4.4.

The moment and shear diagrams in Figure 4.5 apply to both specimens, neglecting dead loads. The portion of the test specimen from the load to the roller support is pictured in Figure 4.6. Instrumentation was installed in this region on each beam to monitor the behavior of the specimens during the shear tests.

4.3 Measured AASHTO Shear Provision Parameters

This section provides a brief description of the parameters measured by the instrumentation described in subsequent sections. These parameters contribute to the shear capacity predicted by one of the versions of the AASHTO shear provisions. Because the specimens were constructed approximately 20 years prior to this project, it was only possible to use external instrumentation. This limited the parameters that could be measured to those described in this section.

4.3.1 Average Longitudinal Strain, ε_x

A major parameter in the 2004 AASHTO LRFD shear provisions is the predicted, ultimate longitudinal strain, ε_x, at middepth of the cross-section. The magnitude of ε_x at the cross-section is correlated to the principal tensile strain in the concrete and the ability of the concrete to transmit tension across cracks. It essentially serves as a gage of the damage in the cross-section. The longitudinal strain is used along with $\frac{v_u}{f_c'}$ to determine the angle of crack inclination, θ, and the concrete strength parameter, β, from the tables in the 2004 LRFD code. The code equation for calculating the longitudinal strain at middepth is:

$$\varepsilon_x = \frac{\frac{M_u}{d_v} + 0.5N_u + 0.5(V_u - V_p)\cot\theta - A_{ps}f_{po}}{2(E_sA_s + E_pA_{ps})} \tag{4.1}$$

This equation was derived from the equilibrium of external forces diagram given in the 2004 LRFD, which is recreated in Figure 4.7. The $A_{ps}f_{po}$ term, which was not shown in the diagram given in the 2004 LRFD, accounts for the internal prestressing force. The code equation was derived assuming the linear strain profile pictured, and is essentially half the longitudinal strain at the depth of the tension reinforcement.

Equation (4.1) was developed with the implicit assumption that up to failure, plane sections remain plane in cracked concrete in an average sense. Therefore, Eqn. (4.1) is an equation for average longitudinal strain at ultimate. Average strain in cracked concrete is strain measured over a distance long enough to include several cracks. Figure 4.8 illustrates the concept of average longitudinal strain. The gage length in the figure is long enough to cover at least one crack, so both cracked and uncracked concrete contribute to the magnitude of ε_x. Instrumentation was used to measure the vertical distribution of average longitudinal strains at several cross-sections on both specimens.

4.3.2 Shear Stress at Ultimate, ν_u

The shear stress at ultimate divided by the concrete compressive strength, $\frac{\nu_u}{f_c'}$, is a parameter in the 2004 LRFD shear provisions. This parameter is necessary to obtain θ and β from the tables in the 2004 LRFD code. The shear stress distribution over the cross-section of an I-shaped bridge girder is shown in Figure 4.9. This shear stress distribution is complex and difficult to model precisely. The 2004 LRFD code simplifies the shear stress calculation by assuming the rectangular distribution also shown in Figure 4.9. The rectangular distribution in this figure is essentially a graphical representation of the 2004 LRFD shear stress equation:

$$\nu_u = \frac{V_u - V_p}{bd_v} \tag{4.2}$$

The measured ν_u at a cross-section was calculated using the measured values of V_u and V_p.

4.3.3 Angle of Principal Compression, θ

The angle of principal compression, θ, is a parameter in the 2004 LRFD code, which is dependent upon the value of ε_x at middepth and $\frac{\nu_u}{f_c'}$. The value of θ for a given cross-section represents the angle of the principal compressive stress and is used to predict the angle at which shear cracks form. The crack angle is important, because it determines how many stirrups cross the crack and directly influences the shear capacity through V_s:

$$V_s = \frac{A_v f_{sy} d_v}{s} \cot(\theta) \tag{4.3}$$

A smaller θ in Eqn. (4.3) results in a greater stirrup contribution to shear capacity. Instruments and visual observation were used to measure θ.

4.3.4 Cracking Moment, M_{cr}

As described in Chapter 2, the AASHTO 2002 Standard equations for the concrete contribution to shear capacity are empirical. The V_{ci} and V_{cw} terms are dependent on when the beam cracks in flexure and web shear, respectively. There is no method to directly measure any of the parameters in the V_{cw} equation, and the only verifiable parameter in the V_{ci} equation is the moment at first flexural cracking, M_{cr}. Instruments and visual observation were used to measure M_{cr}.

4.3.5 Compression Struts

The strut and tie model was essentially the same for both test specimens and is presented in greater detail in Chapter 3. The strut and tie model for the test end of the modified specimen

is shown in Figure 4.10. Two critical components of this Strut and tie model were the location and angle of the compressive struts. If this information were known, particularly whether or not there was a direct compression strut between the nodes, it would help verify the accuracy of the model depicted in Figure 4.10. Instruments and visual observation were used to verify the location and angles of the compressive struts.

4.4 Instrumentation

This section describes the instrumentation used in the experiments. The types of instrumentation and their locations are given in Table 4.1 and Figure 4.11, respectively. The instruments were used primarily to collect data to verify the parameters in the AASHTO shear provisions as described in Section 4.3. The means by which the instruments were used to measure the parameters in Section 4.3 is discussed in Section 4.5.

4.4.1 Linear Variable Differential Transformers

The linear variable differential transformers, LVDTs, were used to measure the displacements at the locations shown in Figure 4.11. The data from these LVDTs were used to correlate the visual cracking loads to the start of nonlinear load versus displacement behavior of the specimen. The displacements from the LVDTs directly under the extension helped monitor the behavior of the extension. A larger increase in the displacement at the extension compared to the displacement under the applied load would indicate premature failure of the extension.

4.4.2 Surface Mounted Rosette and Horizontal Strain Gages

There were two types of Texas Measurements surface mounted strain gages. The strain gages labeled "rosette strain gages" in Figure 4.11 and Figure 4.12 were Texas Measurements, FRA-6-11-5LT gages with a gage length of 6mm. The rosette gages each had three arms, which measured strains at 45°, 0°, and -45° to the horizontal axis of the test specimen. The main purpose of the rosette strain gages was to measure the shear strains and angle of principal compression in the test specimen. The data from these gages was transformed using Mohr's circle to produce these quantities. The labels and coordinates of the rosette gages are given in Figure 4.13 and Table 4.2, respectively.

The strain gages labeled "horizontal strain gages" in Figure 4.11 were Texas Measurements, PL-60-11-5LT gages with a gage length of 60 mm. They were applied 3.5 ft. from the load point at six locations through the depth (Specimen II only had five through the depth because this specimen did not have a bridge deck), and on the bottom surface over a 5.8 ft. span at 2 in. spacing. The horizontal gages installed in a single vertical column to measure the distribution of strains over the depth of the cross-section were used to verify the predicted moment at the cross-section, and were only useful until the specimen cracked. The gages on the bottom flange, shown in Figure 4.14, were used to detect initial cracking. The labels and coordinates of the horizontal gages are given in Figure 4.15 and Table 4.2, respectively.

Both the rosettes and the horizontal strain gages measured strain only from the applied load, and did not include strains from the prestressing force or self-weight moment. The

calculated strains from the prestressing force and self-weight moment were added to the results presented in Chapter 6.

4.4.3 Dynamic Coordinate Measurement Machine

The K600 was a dynamic coordinate measurement machine manufactured by Krypton, a division of Metris. The system was used to track the displacements of light emitting diode (LED) surface targets mounted on the specimens. The K600 is referenced in the rest of this document as the "Krypton." The Krypton consisted of three charged coupled device (CCD) cameras, a control unit, and LEDs. To measure displacements, the LEDs were attached to the specimen at the locations shown in Figure 4.11 using hot glue, and the camera was set up so its viewing area captured the light from the LEDs. Both the LEDs and the camera were connected to the controller, which operated the entire system.

The LEDs were mounted on the web of Specimen I on a 10 in by 10 in grid between the applied load and support. The labels and coordinates of the LEDs are given in Figure 4.16 and Table 4.3, respectively. Figure 4.17 shows the Krypton setup for Specimen I. The CCD cameras were positioned at the end of the specimen to view the LEDs down the longitudinal axis of the specimen. This configuration, however, resulted in large levels of noise in the data, because the reliability of the data collected by the CCD cameras was affected by the position of the LEDs relative to the camera. As a result, the test configuration was altered for Specimen II by reducing the number of LEDs included in the viewing area and orienting the CCD cameras to view the LEDs from the side of the specimen as shown in Figure 4.18.

The displacement data from the tests were used to calculate horizontal, vertical, and shear strains as well as direction and magnitude of the principal strains. These strains were calculated using the displacement field analysis described in Appendix B. The results from the displacement field analysis were then transformed to provide the magnitude and direction of the principal strains using Mohr's circle. As with the strain gages, the Krypton only measured deformations due to the applied load. The calculated strains from the prestressing force and self-weight moment were added to the Krypton results presented in Chapter 6.

4.4.4 DEMEC Points

Krypton LEDs were not installed on the bottom flange because the CCD camera viewing area was limited. To obtain strain data over the bottom flange, DEMEC points were installed at the locations shown in Figure 4.11. The DEMEC point measurement system consisted of a brass insert, steel contact seat, and digital Whittemore gage. To install the DEMEC points, a hole was drilled into the specimen at the desired location, and a brass insert was glued into the hole with Hilti non-expanding epoxy. Once the epoxy had set, the contact seats were screwed into the brass inserts. The labels and coordinates of the DEMEC points are given in Figure 4.19 and Table 4.4, respectively.

Figure 4.12 shows a portion of the DEMEC points installed on Specimen I. During both tests, the loading was paused at discrete load increments, and the displacements were read manually between each DEMEC point pair using a digital Whittemore gage as illustrated in Figure 4.20. The same person took all of the DEMEC point readings and each measurement,

starting at the 1 and 2 DEMEC point pair and finishing at the 22 and 23 pair, was repeated three times to keep the error in the readings to a minimum.

The displacements between each adjacent DEMEC point were used to calculate horizontal strains. As with the previous strain measuring devices, the measured strain between DEMEC points was due to the applied load. The calculated strains from the prestressing force and self-weight moment were added to the DEMEC point results presented in Chapter 6

4.4.5 Data Acquisition Systems

The data from all of the horizontal strain gages were collected on an Optim MEGADAC 3008AC system. The data from all the rosette strain gages and LVDTs were collected on a National Instruments SCXI 1000 system. The controller that was part of the K600 system recorded the Krypton displacements. All data were recorded at a rate of 1Hz.

4.5 Measurement of the AASHTO Design Equation Parameters

The AASHTO parameters measured in the laboratory were described in Section 4.3. This section describes how the instrumentation introduced in Section 4.4 was used to measure the AASHTO parameters.

4.5.1 Average Longitudinal Strain, ε_x

To verify the assumption that, on average, plane sections remain plane in cracked concrete and to compare $\varepsilon_{x,pred}$ from Eqn. (4.1) with $\varepsilon_{x,meas}$, instrumentation was located through the depth of the cross-section to provide average strain profiles up to failure. The Krypton LEDs in the web of the specimen, shown in Figure 4.11, provided displacement data from which longitudinal strains were calculated (see Appendix B). It was possible to obtain strain data over a distance spanning several cracks, because relative displacements between any two LEDs were known. Strains calculated over a gage length that included at least one crack provided the average strains in the cracked concrete up to failure.

To supplement the Krypton data, DEMEC points shown in Figure 4.11 were located along the bottom flange of the beam, which provided data to create longitudinal strain profiles. The DEMEC points were located 8 in. on center, and typically spanned at least one crack. Thus, the strain between DEMEC pairs also represented average longitudinal strain.

Traditional resistance type strain gages mounted on the bottom flange of the specimen could be used to determine the longitudinal strain profiles until the concrete cracked. Once the concrete cracked, the traditional strain gages provided local strain data that was highly dependent on the proximity of the gage to a crack. Concrete relieves strain through cracking, therefore, the closer a gage was to a crack the lower the strain reading would be relative to a gage centered between two cracks. Beyond cracking these gages could not be used to help construct the average longitudinal strain profiles.

None of the longitudinal strain measurements from any of the gages provided direct measurement of the longitudinal strain predicted by Eqn. (4.1). Because Eqn. (4.1) is essentially

half the strain in the longitudinal reinforcement, the most direct way to measure ε_x would have been to put strain gages at the centroid of the prestressing strand, and divide the results by two. This was not possible because the test specimens were manufactured 20 years ago, and were not designed specifically for this experiment. The only alternative was to use the data from all three gage types to prepare longitudinal strain profiles prior to concrete cracking. Once the concrete cracked, only the DEMEC and Krypton gages were used to determine average longitudinal strain profiles. The average longitudinal strain profile at ultimate provided the measured strain at mid-height to compare to the strain predicted by Eqn. (4.1).

Response 2000 (R2k) was used as a tool to verify the accuracy of the of the average longitudinal strain profiles. Response 2000 is a sectional analysis program (Bentz and Collins, 2000b) that uses the MCFT to predict the behavior of a given cross-section subjected to moment and shear. The program provided the average strain distribution assuming that, on average, plane sections remain plane in cracked concrete. According to the appendices of NCHRP Report 549, R2k accurately predicted the shear strength of prestressed concrete beams from many experimental tests (Hawkins et al., 2005). For the select database of prestressed beam shear tests described earlier in Section 2.9.1 the mean and coefficient of variation for $\frac{V_u}{V_{test}}$ were 1.107 and 0.170, respectively.

Both R2k and the 2004 LRFD are based on the MCFT. They differ in that the 2004 LRFD equations are a simplification of the MCFT and provide member response only at ultimate, while R2k performs a much more detailed analysis and provides a full load-deformation response for a given member. Therefore any prediction from R2k provides a reasonable means to compare the measured strain distributions with respect to MCFT. The accuracy of the measured longitudinal strain profiles, and comparison to R2k are presented in Section 6.3.2.2.

4.5.2 Shear Stress, ν_u

The Krypton LEDs and rosette strain gages shown in Figure 4.11 provided data to calculate measured shear strains at discrete locations along the length of the test specimens. The measured shear strains from these instruments, however, could not be used to compare $\nu_{u,pred}$ to $\nu_{u,meas}$, because there was no reliable constitutive model that related nonlinear shear strains to stresses. Therefore, the only data available to compare $\nu_{u,pred}$ to $\nu_{u,meas}$, assuming a rectangular stress distribution, was the shear force applied at ultimate. The value of V_u was plugged directly into Eqn. (4.2) to provide $\nu_{u,meas}$. The Optim Megadac 3008AC data collection system recorded the loading history through the entire test, and provided V_u.

4.5.3 Angle of Principal Compression, θ

The most straightforward method to verify θ_{pred} was to visually measure the angle of the diagonal shear cracks directly from the beam. The visual θ_{meas} provided the angle of the principal compressive stress when the shear cracks formed, which was directly compared to θ_{pred}

from the 2004 LRFD. In addition to visual measurement, the Krypton LEDs and rosette strain gages also provided information on the angle of the principal compressive stress.

The rosette gages were small and measured local data, which was useful to verify θ_{pred} if the gage happened to be located in between cracks where the stress distribution was a maximum. The Krypton LEDs had a large gage length, which allowed measurement of the average angle of principal compression after cracking.

4.5.4 Cracking Moment, M_{cr}

Visual inspection was one method used to verify M_{cr}. Prior to the test, the specimen was whitewashed so cracks were easy to identify. During the test, the load was paused at 25 kip increments, and an observer with a hand-held light carefully inspected the specimen surface for signs of the first flexural cracking. This method was highly dependent upon the frequency of loading pauses and care of the observer. Furthermore, the M_{cr} measured by visual inspection only captured the applied moment when flexural cracks were first visible to the human eye. The horizontal strain gages shown on the bottom flange of the specimen in Figure 4.11 were installed to measure the earliest flexural cracks that were too small to be visually observed.

The moment distribution between the applied load and support was linear as shown in Figure 4.5. While the test specimen remained uncracked, the longitudinal strains at a given depth were governed by the following equation:

$$\varepsilon_x = \frac{My_{tr}}{I_{tr}E_c} \tag{4.4}$$

Prior to cracking, all of the variables in this equation changed linearly along the length, except E_c, which was constant. The longitudinal strain at any given depth should change linearly with these variables until the concrete cracks, which is when Eqn. (4.4) is no longer valid. Once the concrete cracks, the strain at any given depth is nonlinear along the length.

According to the numerator of Eqn. (4.4), the largest tensile strain occurs at the extreme tension fiber of the specimen at the location of the greatest moment. The horizontal strain gages shown on the bottom flange in Figure 4.11 were used to capture strains in the region most likely to crack first. According to Eqn. (4.4), a plot of these strains for every value of the applied moment should be linear until the section cracked. The value of the applied moment when the plot became nonlinear was the initial value of M_{cr} measured by the strain gages. The accuracy of M_{cr} measured in this manner was dependent upon the proximity of the initial flexural crack to a strain gage. This method was intended to detect the first flexural crack before it was visible.

4.5.5 Compression Struts

The simplest way to verify the location and angle of the struts was through visual observation. The struts were bottle shaped and likely to split along their axis due to transverse tension. Thus the cracks observed during the shear tests provided a good indication of the inclination and possible location of the struts. In addition, the rosette strain gages were positioned as shown in Figure 4.21 to try and capture the behavior of the compression struts. Although not shown in the figure, the Krypton LEDs were also located through the web of the

specimen and provided data on the inclination of the struts. See Section 4.5.3 for more information on how the compression strut angles were measured.

Chapter 5

Shear Capacity Based on Measured Material Properties

5.1 Introduction

An investigation of trends in the AASTHO 2004 LRFD, 2002 Standard, and 1979 Interim shear provisions using nominal material properties was presented in Chapter 3. The results from material testing and an explanation of how the measured material properties affected the predicted shear capacities are presented in this chapter. First the individual influence of each measured material parameter on the predicted shear capacity is investigated at the cross-section under the applied load. The individual analysis is followed by analysis of the combined effect of all the measure material properties. Both the nominal and measured shear capacities presented in this chapter were based on the modified specimen shown in Figure 4.1.

The material properties measured in the laboratory were concrete compressive strength, concrete modulus of elasticity, stirrup yield strength, and effective prestressing. The procedures used to measure these properties are described in Appendix C. Both the nominal and measured material properties are summarized in Table 5.1.

5.2 The Effect of f_c' on Predicted Shear Capacity

The effect of compressive strength on the predicted shear capacity of the cross-section under the applied load is summarized in Table 5.2. The third column in this table shows the predicted shear capacities for both specimens using the 2004 LRFD, 2002 Standard, 1979 Interim and the strut and tie model assuming nominal values for all material properties. The fourth column provides the revised shear capacities when the measured value of f_c' was used in the calculations with all other properties remaining nominal. According to the 2004 LRFD, 2002 Standard, and the strut and tie model, using the measured f_c' increased the predicted capacity of both specimens. Only the 1979 Interim predicted capacities were unaffected by the increase in f_c' because $0.06f_c'$ was limited to 180 psi, which controlled for f_c' greater than 3,000 psi (see Section 2.5).

5.2.1 The Effect of f_c' on the 2004 LRFD Predicted Shear Capacity

The magnitude of the increase in shear capacity for both specimens was similar for the 2004 LRFD code, but not identical because the concrete compressive strength affected the shear capacity in a complex manner. Both the concrete and stirrup contribution to shear capacity were affected by the magnitude of f_c':

$$V_c = 0.316\beta\sqrt{f_c'}bd_v \tag{5.1}$$

$$V_s = \frac{A_v f_{sy} d_v \cot\theta}{s} \tag{5.2}$$

The concrete compressive strength is directly included in Eqn. (5.1), and is also indirectly in the equation through the term β. In Eqn. (5.2), the concrete compressive strength is required to calculate d_v, which is the distance between the resultants of the tensile and compressive forces due to flexure. In addition, the concrete compressive strength is required to obtain θ.

At the cross-section under the applied load, d_v for the specimen without the bridge deck (Specimen II) was controlled by $0.9d_p$ (the minimum given in the 2004 LRFD) for both nominal and measured concrete compressive strength. Therefore, d_v for Specimen II was not affected by an increase in f_c'. However, d_v for the specimen with the deck (Specimen I) was not controlled by the minimum and the increase in f_c' increased d_v, as shown in Table 5.3. The change in d_v produced a slight increase in the shear capacity of Specimen I.

The θ and β parameters in the 2004 LRFD could not be calculated directly, so a non-iterative spreadsheet was used to determine how the measured f_c' affected θ and β (Bentz and Collins, 2000a). The values in Table 5.3 show how θ and β changed when nominal material properties were used for everything except the measured f_c'. Table 5.3 shows that an increase in f_c' increased θ, and decreased β. This change in θ and β had a negative effect on shear capacity, and was the reason why the measured f_c' increased the shear capacity by only a maximum of 7.6% for either specimen, as shown in Table 5.2. The impact of the measured f_c' on shear capacity would have been greater if it had not affected θ and β.

5.2.2 The Effect of f_c' on the 2002 Standard Predicted Shear Capacity

The measured f_c' resulted in an increase in the shear capacity predicted by the 2002 Standard code for both specimens, with a more significant increase in the capacity of Specimen I. The results in Table 5.2 show that the increase for this specimen at the cross-section under the applied load was approximately 12.8% versus 5.6% for Specimen II. The reason for this difference lies in the relative importance of f_c' and the level of prestressing in the equations for web shear cracking, V_{cw}, and flexure-shear cracking, V_{ci}.

The concrete contribution to the predicted shear capacity of Specimen I was controlled by the web shear term:

$$V_{cw} = (3.5\sqrt{f_c'} + 0.3 f_{pc})bd + V_p \tag{5.3}$$

For this specimen, f_{pc} was the compressive stress in the concrete at the centroid of the composite section due to the prestressing force and self-weight moment. When multiplied by 0.3, f_{pc} became essentially the same magnitude as $3.5\sqrt{f_c'}$, which was the stress assumed to be required to crack the web. As a result, any increase in f_c' had a significant impact on the predicted shear capacity, because the level of prestressing and resistance to web cracking were equally important in the calculation. The magnitudes of these stresses are shown in Table 5.4.

In contrast, the concrete contribution to shear capacity for Specimen II was controlled by V_{ci}:

$$V_{ci} = 0.6\sqrt{f_c'}bd + V_d + \frac{V_i M_{cr}}{M_{\max}} \tag{5.4}$$

which was not as affected by the measured f_c'. In this equation, the level of prestressing played a larger role than f_c' through the term for the cracking moment:

$$M_{cr} = \frac{I}{y_t}(6\sqrt{f_c'} + f_{pe} - f_d) \tag{5.5}$$

For Specimen II, the compressive stress at the extreme tension fiber due to the prestressing force, f_{pe}, was approximately four times larger than $6\sqrt{f_c'}$, which was the tensile stress required to crack the section. This disparity significantly limited the influence of f_c' on V_{ci}, because any increase in $6\sqrt{f_c'}$ was dwarfed by the magnitude of f_{pe}, as shown in Table 5.4.

The other term in Eqn. (5.4) affected by f_c' was $0.6\sqrt{f_c'}$, which accounted for the shear required to develop a flexure crack into a shear crack. This term also had little effect on predicted shear capacity. Therefore, the reason why Specimen I had a 12.8% increase in predicted shear capacity versus a 5.6% increase for Specimen II was the relative importance of f_c' and the effective prestressing in V_{cw} and V_{ci}.

5.2.3 The Effect of f_c' on the 1979 Interim Predicted Shear Capacity

As shown in Table 5.2, the measured f_c' had no effect on the shear capacity predicted by the 1979 code for either test specimen. The equation for the concrete contribution to shear capacity was:

$$V_c = 0.06\, f_c'\, jd \tag{5.6}$$

The $0.06f_c'$ term was limited to 180 psi, which effectively limited f_c' to 3,000 psi. Therefore, the increase in concrete compressive strength of the girder from the design value of 6,000 psi to the measured value of 10,130 psi had no impact on the predicted shear strength of either specimen.

5.2.4 The Effect of f_c' on the Strut and Tie Model Predicted Shear Capacity

The shear capacities of the strut and tie models shown in Figure 3.13 and Figure 3.14 were dependent upon the limit states of individual elements in the models. The strength of the stirrups and of the direct compression strut between the applied load and support were the elements that controlled the shear capacities reported in Table 5.2. The allowable stress, f_{cu}, in the direct compression strut was increased when the measured f_c' was included in the strut and tie model:

$$f_{cu} = \frac{f_c'}{0.8 + 170\varepsilon_1} \le 0.85\, f_c' \tag{5.7}$$

in which:

$$\varepsilon_1 = \varepsilon_s + (\varepsilon_s + 0.002)\cot^2 \alpha_s \tag{5.8}$$

In addition to the effect on Eqn. (5.7), the measured f_c' also affected Eqn. (5.8) through the term for the angle of the direct compression strut, α_s. The measured f_c' reduced the depth of the compression block at the applied load shown in Figure 3.13 and Figure 3.14, which increased α_s.

5.3 The Effect of E_c on the Predicted Shear Capacity

The results in Table 5.5 show that E_c had no effect on the shear capacity of Specimen II, and according to the 2002 Standard code only a minimal effect on Specimen I. For this specimen, Eqn. (5.3), V_{cw}, controlled V_c. A component of this equation was f_{pc}, which was the compressive stress at the neutral axis of the composite specimen due to the prestressing force and self weight moments (of the girder, M_g, and deck, M_d) assuming the girder acted alone:

$$f_{pc} = \frac{P}{A} - \frac{Pe(y_{tc} - y_t)}{I_g} + \frac{(M_g + M_d)(y_{tc} - y_t)}{I_g} \tag{5.9}$$

where y_t, and y_{tc} are the distances from the extreme tension fiber to the centroid of the noncomposite and composite specimens, respectively; and I_g is the moment of inertia of the noncomposite specimen.

The stress from the eccentricity of the prestressing strand was larger than the stress due to the self-weight moments. Therefore, the value of f_{pc} was increased by a smaller difference between y_{tc} and y_t. The measured E_c of the girder reduced the effective width of the bridge deck, which reduced the value of y_{tc} and the difference between y_{tc} and y_t. This resulted in an increase in the value of f_{pc}, and was the reason for the slight increase in shear capacity for Specimen I shown in Table 5.5.

5.4 The Effect of f_{sy} on the Predicted Shear Capacity

The equations for V_s in the 2004 LRFD, 2002 Standard, and the 1979 Interim are based on the assumption that the stirrups yield at ultimate. The stirrups also yield at ultimate according to the strut and tie models for both specimens. The measured f_{sy}, therefore, increased the shear capacity predictions of all the shear provisions, as shown in Table 5.6.

Exactly how the measured f_{sy} affected the shear capacity predicted by the 2004 LRFD code was difficult to discern. The stirrup yield strength directly contributed to V_s, however, it also affected the θ and β terms in the equations for V_s and V_c. The values in Table 5.7 are from the non-iterative spreadsheet (Bentz and Collins, 2000a) and show how θ and β changed when nominal material properties were used for everything except the measured f_{sy} of 67.3 ksi. This table shows that an increase in f_{sy} increased θ, and decreased β. This change in θ and β had a negative effect on shear capacity, and was the reason why the measured f_{sy} did not have a larger impact on the 2004 LRFD predictions.

The impact of f_{sy} on the shear capacities predicted by the 2002 Standard and 1979 Interim shear provisions was more straightforward. According to both of these provisions, the measured stirrup strength only affected the f_{sy} term. The 1979 Interim was noticeably more affected by the increase in f_{sy}, as shown in Table 5.6, because the equation for V_s includes a factor of two that is not in the 2002 Standard equation for V_s.

Use of the measured f_{sy} in the strut and tie models shown in Figure 3.13 and Figure 3.14, increased the shear capacity by increasing the strength of the vertical ties. Because the vertical ties were one of the elements that controlled the strength of the models, an increase in f_{sy} increased shear capacity.

5.5 The Effect of f_{pe} on the Predicted Shear Capacity

The measured effective prestressing, f_{pe}, was the only material property that had a negative effect on predicted shear capacity. Using the predicted effective prestressing in the initial capacity calculations was unconservative for both test specimens. The lower measured effective prestressing relative to the nominal value given in Table 5.1 resulted in a reduced V_p in the 2004 LRFD equation for total shear capacity:

$$V_n = V_c + V_s + V_p \tag{5.10}$$

The effect on V_p was small; the measured effective prestressing reduced V_p by 2 kips or approximately 1% of the total shear resistance for both specimens.

The measured losses had only a minor effect on the 2004 LRFD V_c (through V_p in Eqn. (5.11)), which was counterintuitive given that the longitudinal strain at middepth, ε_x, is a parameter in the shear provisions. The equation for ε_x:

$$\varepsilon_x = \frac{\frac{M_u}{d_v} + 0.5N_u + 0.5(V_u - V_p)\cot\theta - A_{ps}f_{po}}{2(E_sA_s + E_pA_{ps})} \tag{5.11}$$

contains the term f_{po}, which accounts for the prestressing at given cross-section. The 2004 LRFD suggests taking f_{po} as the jacking stress and does not mention that losses should be considered. According to Eqn. (5.11), a larger f_{po} reduces the predicted longitudinal strain at a cross-section at ultimate, thereby increasing the ability of the cracked concrete to resist applied shear. Intuitively, larger losses should reduce the beneficial effect of f_{po} in Eqn. (5.11) and decrease the concrete shear resistance. The 2004 LRFD, however, does not address this issue.

Only the 2002 Standard shear provisions include f_{pe} in the V_c contribution to predicted shear capacity. According to these provisions, V_{cw} and V_{ci} provide a prediction of the shear required to crack the web and form flexure-shear cracks, respectively, and a reduction in f_{pe} reduces the magnitude of both. Because the measured f_{pe} was less than predicted, V_c and thus the shear strength predicted by the 2002 Standard code shown in Table 5.8 were reduced. Specimen II had the greatest decrease in capacity because V_{ci} controlled V_c for this specimen, and, as discussed in Section 5.2.2, the effective prestressing had a significant effect on V_{ci} through M_{cr}.

The measured f_{pe} had no effect on the shear capacity predicted by the 1979 Interim shear provisions, and only a small negative effect on the predictions from the strut and tie model (through the vertical component of the prestressing force).

5.6 Combined Effect of the Measured Properties on the Predicted Shear Capacity

The combined effect of the measured material properties on shear capacity at the cross-section under the applied load is shown in Table 5.9. The shear provisions from all of the codes predicted an increase in shear capacity for both test specimens when the measured material properties were used in the capacity calculations. The magnitude of the increase in shear capacity predicted by the 1979 Interim shear provisions was identical at every cross-section. However, according to the 2004 LRFD and the 2002 Standard shear provisions, the cross-section under the applied load had the smallest increase in shear capacity.

5.6.1 Combined Effect of the Measured Properties on the 2004 LRFD Predicted Shear Capacity

Figure 5.1 and Figure 5.2 show the 2004 LRFD predicted shear capacity with nominal and measured material properties for Specimens I and II, respectively. These figures are for the specimen shown in Figure 4.1, and are only plotted from the prestressing strand anchorage zone near the roller support to the applied load at 14.5 ft. The behavior of the predicted shear capacity in these figures was directly related to the behavior of θ and β which is shown in Figure 5.3 and Figure 5.4 for Specimen I, and Figure 5.5 and Figure 5.6 for Specimen II.

The behavior of θ and β was nearly identical for both specimens. When nominal material properties were used, θ increased at an approximately constant rate from the support to the applied load, and β was relatively constant with just a slight downward trend. When measured material properties were used, θ increased at a relatively constant rate from the support to approximately 8 ft., but it increased at a larger rate from 8 ft. to the applied load. Compared to β from nominal material properties, the measured material properties resulted in a larger rate of decrease in β over the length of both specimens. The change in behavior of θ and β over the length of the specimen when measured material properties were used resulted in the downward trend in shear capacity, which is shown in Figure 5.1 and Figure 5.2.

5.6.2 Combined Effect of the Measured Properties on the 2002 Standard Predicted Shear Capacity

Figure 5.7 and Figure 5.8 show the 2002 Standard predicted shear capacity with nominal and measured material properties for Specimens I and II, respectively. The values of V_{cw} and V_{ci} for Specimen I are shown in Figure 5.9 and Figure 5.10 with all nominal and all measured material properties, respectively. As discussed in Sections 5.2.2 and 5.5, the measured f_c' had a large beneficial effect on V_{cw}, and the measured f_{pe} had a significant negative effect on V_{ci}. When considered concurrently, these effects caused V_{ci} to control V_c of Specimen I at the cross-section directly under the applied load, as shown in the figures. Without the bridge deck, V_{ci} controlled V_c of Specimen II from 11 ft. to the applied load. In this region, measured material properties only modestly increased the shear capacity of Specimen II because the negative effect of f_{pe} countered the beneficial effect f_c' on V_{ci}.

Chapter 6
Experimental Results

6.1 Introduction

The test setup was described in Chapter 4. In this chapter, the data from both experiments are presented, along with analyses of the results. Specimen I and Specimen II refer to the specimens with and without a bridge deck, respectively. In the following sections, the results from each experiment are compared individually to quantities predicted by the 2004 AASHTO LRFD shear provisions, 2002 AASHTO Standard shear provisions, 1979 Interim shear provisions, and the Strut and Tie design method. Subsequent to the individual analyses, the behaviors of Specimen I and II are compared. The results from the shear tests presented in this chapter were instrumental in determining whether or not the original 88 ft. bridge girder was safe while in service as part of Mn/DOT Bridge No. 73023, which is discussed in Chapter 7.

6.2 Specimen I

Testing of the specimen with a bridge deck began on February 2, 2006. The loading was paused every 25 kips while cracks were marked and DEMEC readings were taken. The first visible evidence of cracking was at a load of 350 kips. The crack was a flexural crack on the bottom flange approximately 4 in. from the cross-section at the applied load. A few minor flexural cracks formed beyond 350 kips with no major cracks forming until 468 kips. At 468 kips, an audible popping sound was heard and several large diagonal web cracks formed simultaneously, which are shown in Figure 6.1 and Figure 6.2. (The photograph of Specimen I shown in Figure 6.1 was taken from the opposite side of the beam as that depicted in Figure 6.2. No photograph was taken from the side of the specimen shown in Figure 6.2. For consistency, the crack drawings for Specimens I and II are shown from the prospective depicted in Figure 6.2.)

The specimen was next loaded to 486 kips, at which point the load suddenly dropped as shown in Figure 6.3. At 486 kips, large cracks formed on the specimen extension as shown in Figure 6.4, suggesting that the prestressed girder was rotating within the extension. Once these cracks formed, further displacement of the actuator only resulted in displacement of the specimen with no increase in load. This indicated the extension had failed, so the test was halted to make the repairs shown in Figure 6.5. The repairs were essentially two clamps installed over the damaged area, with the threaded rods tensioned to approximately 80% of yield. After repairs were complete, testing resumed on February 14, 2006.

For the second test of Specimen I the loading was paused in 100 kip increments up to 400 kips to take DEMEC point readings. Beyond 400 kips, the loading was paused at 450 and 500 kips followed by pauses at every 0.25 in. of displacement until the load peaked at 622 kips. Beyond the peak load, the specimen was displaced until the applied load dropped to approximately 40% of the peak value.

From the beginning of the test until the load reached 500 kips, the web cracks that initially formed during the first test slowly began to open but did not grow. From 500 kips to 622 kips

the existing web shear cracks grew longer, and a few news one formed. The crack pattern at the peak load of 622 kips is shown in Figure 6.6 and Figure 6.7.

The large crack labeled "failure crack" in Figure 6.8 and Figure 6.9 extended from the load to the support and traveled through the deck beyond the peak load of 622 kips. Once this crack extended through the deck, the test was terminated, because the load carrying capacity rapidly dropped below 40% of the peak, as indicated in Figure 6.3. Besides the large crack at failure, there was crushing at the web/flange interface as the compression struts in the beam began to fail. This crushing is shown in Figure 6.10, and is described in more detail in subsequent sections.

6.2.1 Load-Displacement

Figure 6.3 is a plot from the linear variable differential transformer (LVDT) directly under the load from both tests of Specimen I. The load-displacement relationship was nonlinear with respect to load beyond an applied load of 500 kips. The nonlinear behavior between 500 kips and the peak load of 622 kips was attributed to development of most of the flexural cracking shown in Figure 6.7.

Beyond 622 kips, the capacity of the girder began to drop as additional displacement from the actuator resulted in crushing at the web/flange interface, and further development of the crack labeled "failure crack" in Figure 6.9. At 495 kips, post peak, the "failure crack" extended through the deck, and the load instantly dropped to 367 kips. After this drop in capacity the test was terminated and the specimen was unloaded.

6.2.2 AASHTO 2004 LRFD; Predicted vs. Measured Parameters

Many factors affect the shear capacity predicted by the AASHTO 2004 LRFD code. To evaluate the accuracy of this code, it is important to compare not only the predicted and measured shear capacity, but also the major parameters that influence the predicted capacity. For the 2004 LRFD these parameters include the longitudinal strain at middepth of the cross-section, shear stress, and angle of the principal strains at ultimate. Chapter 4 outlines the methodology and instrumentation used to measure these parameters during the ultimate test of Specimen I. Unfortunately due to the test setup, there was significant error in the data from the Krypton system recorded during the test of Specimen I. As a result, the data from the Krypton had large levels of noise and were unusable. The data from the rosette and horizontal strain gages, DEMEC points, and LVDTs were used to evaluate the accuracy of the codes in the following sections.

6.2.2.1 Predicted vs. Measured Shear Capacity

Figure 6.11 shows the 2004 AASHTO LRFD predicted shear capacity for Specimen I, and the maximum applied shear including dead load. The capacity in this figure was calculated using measured material properties as described in Chapter 5, with the load applied 14.5 ft. from the end as shown in the drawing above the plot. In Figure 6.11 there is a distinct minimum directly under the applied load, which was not present when the shear capacity was calculated

with nominal material properties as shown in Figure 3.6. The reason for this change in predicted behavior was because of the effect of the measured material properties on β and θ as described in Chapter 5. According to Figure 6.11, failure should have occurred near the applied load. This was the location along the specimen with the greatest disparity between applied shear and predicted capacity.

The test result and predicted shear capacity are compared in Table 6.1. Using measured material properties, the 2004 LRFD predicted shear capacity directly under the applied load was 259 kips. Specimen I failed at a shear of 392 kips under the applied load, including dead load. The ratio of $\frac{V_{test}}{V_{pred}}$ for the 2004 LRFD was 1.51, which was more conservative than the 2002 Standard, but not the most conservative of all the shear provisions.

As mentioned previously, it appeared as though Specimen I should have failed near the applied load. If a shear failure were to occur there, it would likely be a flexure/shear type of failure because of the combination of high moment and shear. These failures are characterized by vertical flexural cracks in the bottom flange that turn towards the load once they reach the web due to the high shear stresses in the web. If the LRFD predictions in Figure 6.11 were correct, the test specimen should have had significant flexure/shear cracking in the region near the applied load, which was not the case.

The web shear cracks pictured in Figure 6.6 were significantly wider than the flexure/shear cracks shown in Figure 6.7 (there is no photograph available of the flexure/shear cracks). For safety reasons, the last measurement of the crack widths was at a shear under the applied load, including dead load, of 357 kips. At 357 kips, the widest web crack at middepth of the cross-section was $^1/_8$ in., and all of the flexure shear cracks were hairline cracks. Beyond 357 kips the web cracks continued to widen, and the crack labeled "failure crack" in Figure 6.8 clearly dominated the behavior of Specimen I beyond the peak applied shear. The flexure/shear cracks never widened significantly.

6.2.2.2 Predicted vs. Measured Longitudinal Strain

The predicted longitudinal strain at failure, $\varepsilon_{x,pred}$, was provided by the non-iterative spreadsheet used to predict shear capacity as described in Section 3.3.1. Using the measured material properties from Chapter 5, $\varepsilon_{x,pred}$ for Specimen I was 228 με. This prediction could not be verified, however, because the data from the Krypton was essential in obtaining $\varepsilon_{x,meas}$.

6.2.2.3 Predicted vs. Measured Shear Stress

The 2004 LRFD predicted shear stress, $v_{u,pred}$, was calculated by substituting V_{pred} for V_u in the equation for v_u:

$$v_{u,\,pred} = \frac{V_{pred} - V_p}{bd_v} \tag{6.1}$$

with the measured material properties from Chapter 5 included in the calculated V_{pred} and V_p.

The V_{pred} for Specimen I, for the cross-section under the applied load, is given in Table 6.1 as 259 kips. Using this V_{pred} and the V_p calculated with measured losses, the 2004 LRFD $\nu_{u,pred}$ for Specimen I was 629 psi. When $\nu_{u,pred}$ was combined with the measured f_c' of 10,130 psi given in Chapter 5, the $\frac{\nu_{u,\,pred}}{f_c'}$ ratio was 0.062, which was required to look up values of θ and β in the 2004 LRFD tables. The measured ultimate shear, V_{test}, under the applied load for Specimen I was 392 kips, including dead load. This V_{test}, when used with V_p calculated assuming measured losses, resulted in a $\nu_{u,meas}$ of 981 psi. For an f'_c of 10,130 psi, the corresponding $\frac{\nu_{u,\,meas}}{f_c'}$ ratio was 0.094.

Table 6.2 is the 2004 LRFD θ and β table for sections with at least the minimum shear reinforcement. The first column is the $\frac{\nu_u}{f_c'}$ ratio, which was used in conjunction with ε_x to determine θ and β for a given section. The minimum $\frac{\nu_u}{f_c'}$ given in Table 6.2 is 0.075. If a section has a value below 0.075, as was predicted for Specimen I, the values from the table are conservative. The θ and β that resulted from $\frac{\nu_{u,\,pred}}{f_c'}$ and the $\varepsilon_{x,pred}$ from Section 6.2.2.2 of 228 με were 26.2° and 2.99, respectively. There was no data available for $\varepsilon_{x,meas}$, so it was impossible to investigate how these values change using only measured properties. The best alternative was to use $\frac{\nu_{u,\,meas}}{f_c'}$ and $\varepsilon_{x,pred}$ to investigate how θ and β change with $\nu_{u,meas}$. According to Table 6.2, an increase in $\frac{\nu_u}{f_c'}$ from the predicted 0.062 to the measured 0.094, with ε_x held constant, increased θ to 26.6 ° and decreased β to 2.83. These changes in θ and β, if used to calculate shear capacity, would lower V_{pred} and make the 2004 LRFD more conservative. Both 26.2° and 26.6° were close to the visual crack angle measurements of the two web shear cracks nearest the applied load as shown in Figure 6.12. The predicted angle of principal compression is discussed in the subsequent section.

6.2.2.4 Predicted vs. Measured Angle of Principal Compression

The 2004 LRFD predicted angle of principal compression at ultimate, θ_{pred}, for Specimen I varied along the length as shown in Figure 6.12. In the figure, the values of θ_{pred} listed above the beam were interpolated from Table 6.2 using $\frac{\nu_{u,\,pred}}{f_c'}$ and $\varepsilon_{x,pred}$ at each cross-section marked by the vertical line. The terms $\frac{\nu_{u,\,pred}}{f_c'}$ and $\varepsilon_{x,pred}$ were calculated with measured material properties from Chapter 5. In the 2004 LRFD, the value of θ_{pred} was critical in determining the stirrup contribution to shear capacity, V_s.

The angles of the major web shear cracks that formed when the beam first cracked in shear, described in the beginning of Section 6.2, are recorded on the respective cracks in Figure 6.12. The visual θ_{meas} of each crack was calculated from the dimensions labeled in the figure as "H" and "L," which were formed by the intersection of the crack with the top and bottom flanges. The crack angles at the peak applied load are shown in Figure 6.13, which illustrates that the angle of the web cracks at initial cracking remained unchanged at ultimate.

The visual crack angles were all in reasonable agreement with the predicted angles, particularly the crack with an angle of 20.8°. The remaining web crack angles were all slightly larger than the 2004 LRFD predictions at the sections where they occurred. Therefore the predicted angles were slightly unconservative compared to the visual crack angles.

The angles of principal compression at first shear cracking were calculated from the rosette strain gage data, including the calculated strains from the prestressing force and self-weight moment. The results shown in Figure 6.14 were the θ_{meas} values when the web of Specimen I cracked during the first shear test on the specimen. The shear vs. angle of principal compression for the first test from the four rosette strain gages closest to the applied load, labeled R1-R4 in Figure 6.14, are plotted in Figure 6.15. The behavior of these four rosettes was typical of all the rosettes. The angle of principal compression was essentially zero at the beginning of the shear test because of the compression from the prestressing (which was calculated and added to the results from the rosette gages). As the specimen was loaded, the angle began to increase due to increasing shear strains. The dashed line in the figure denotes the applied shear that cracked the web of Specimen I. Beyond this applied shear θ_{meas} no longer changed in a predictable manner, and the angle at some of the rosette gages decreased, while the angle at others increased depending on the proximity of the gage to a shear crack.

Figure 6.16 shows the results from R1-R4 from the second test of Specimen I. The specimen was already cracked at the start of this test; therefore, at the visual shear-cracking load there was no abrupt change in the results. Instead θ_{meas} from R2 and R4 were similar to those from the first test, because the rosettes were located between cracks. R2 and R4 recorded more erratic measurements above the visual cracking load as new shear cracks began to form in the specimen. The results from R1 and R3 were unreliable because they were located close to a crack surface that formed during the first test of Specimen I.

The angle at R1 from Figure 6.14 was 21.2°, which was smaller than the visual crack angle of 26.4° at the nearest crack. The angles at R2-R4 were in good agreement with the visual crack angle of 20.8° at the nearest crack. The magnitudes of θ_{meas} from both visual measurement and the rosette gages were reasonably close to θ_{pred} along the length, indicating that the shear model used to develop the 2004 LRFD accurately predicted the number of stirrups engaged by each shear crack. The 2004 LRFD V_s contribution to shear capacity was 126 kips using the most conservative θ_{pred} of 26.2°, and was likely more accurate than the V_s of 60 kips predicted by the 2002 Standard code which assumed a crack angle of 45°. This result provides an indication of the reliability of the stirrup contribution to shear capacity, however, the overall reliability of the codes is dependent on the sum of $V_c + V_s + V_p$.

6.2.3 AASHTO 2002 Standard; Predicted vs. Measured Parameters

The shear provisions in the 2002 Standard code were based primarily on empirical data. As a result, the most important comparison for this version of the code was between the predicted and measured shear capacity. The only parameter from the code that was experimentally verified was the moment at first flexural cracking. The results from the experiment on Specimen I and comparison to the 2002 Standard code are presented in the following sections.

6.2.3.1 Predicted vs. Measured Shear Capacity

Figure 6.17 is a plot of the 2002 AASHTO Standard predicted shear capacity for Specimen I, and the maximum applied shear including dead load. This plot shows the capacity of the test specimen assuming measured material properties as described in Chapter 5, with the load applied 14.5 ft. from the end as shown in the drawing above the plot. According to this figure, there was no well-defined minimum shear capacity. This meant that the data in Figure 6.17 did not provide a definitive indication as to where failure might occur.

Using measured material properties, the 2002 Standard predicted shear capacity directly under the applied load was 316 kips, as given in Table 6.1. Specimen I failed at a shear of 392 kips under the applied load, including dead load. The ratio of $\frac{V_{test}}{V_{pred}}$ for the 2002 Standard was 1.24, which implied the code was conservative. When compared to the other shear provisions, the 2002 Standard predicted shear capacity was the closest to the experimental capacity.

The 2002 Standard equation for web shear, V_{cw}, controlled the concrete contribution to shear capacity, V_c, for Specimen I from the support to 14ft, which was close to the applied load. There was very little change in the value of V_{cw} over this region, which is why the predicted shear capacity has only a slight slope in Figure 6.17. Therefore, based on the prediction of the 2002 Standard, it appeared as if Specimen I would fail somewhere between the load and the support through web shear.

Figure 6.6 is evidence that Specimen I failed as predicted, because it shows the worst damage to the specimen, which was largely in the web. There were minor flexure/shear cracks in the specimen as shown in Figure 6.9, however, they were not the cause of failure. The web shear cracks were clearly dominant, because they were much wider than the flexural cracks which were never wider than a hairline crack.

6.2.3.2 Predicted vs. Measured Cracking Moment

The shear that causes flexure cracks to turn into flexure/shear cracks, V_{ci}, is one of two equations for the concrete contribution to shear capacity in the 2002 Standard shear provisions. The cracking moment, M_{cr}, was an important parameter in V_{ci}. The $M_{cr,pred}$ for Specimen I was 3,110 kip-ft. at the cross-section directly under the applied load, when calculated using the measured material properties from Chapter 5.

The first flexural crack to form is labeled in Figure 6.2 and was first visible on the underside of the specimen at a shear of 224 kips under the applied load, including dead load,

which corresponded to a moment of 3,390 kip-ft. This resulted in a $\frac{M_{cr,\,meas}}{M_{cr,\,pred}}$ ratio of 1.09, which meant that according to visual observation, the 2002 Standard slightly under-predicted the cracking moment.

The horizontal strain gages shown in Figure 4.11 and Figure 4.14 were located on the bottom flange of the test specimen to determine when the beam first cracked in flexure. Figure 6.18 is a plot of the longitudinal strains along the bottom flange of the specimen for various levels of applied shear, not including dead load. Every data point in the figure represented strain, including the calculated strain from the prestressing force and dead load, from one of the horizontal gages shown in the drawing of the beam above the plot. The longitudinal strain along the bottom flange should have changed linearly along the length as long as the specimen was uncracked. Therefore, lines in Figure 6.18 were essentially straight until the specimen cracked.

The lines in Figure 6.18 were relatively straight, and the beam was clearly uncracked, up to 100 kips of applied shear. A few minor kinks in the lines were observed at an applied shear of 150 kips as indicated in the figure. These kinks, however, were slightly noticeable from the beginning of the shear test and became more pronounced throughout the test. Rather than resulting from cracking, it is likely these kinks were the result of misaligned horizontal strain gages. Regardless of gage alignment, however, it was clear that by 225 kips the beam had cracked, and the strain distribution became nonlinear. To determine more precisely when the beam cracked, further refinement of Figure 6.18 was needed between 150 kips and 225 kips.

The results from the horizontal strain gages in 5 kip increments between 150 kips and 215 kips are displayed in Figure 6.19. To determine when the beam cracked, it was important to consider not only whether or not the lines in the figure were straight, but also if the rate of change in strain at each gage was approximately constant as the shear was increased in constant increments. The rate of change in strain at each of the kinks was uniform up to an applied shear of 215 kips, which suggested that the beam was uncracked. At 215 kips the gages labeled L21 and L22 clearly began to unload, which indicated they were in close proximity to a crack.

The individual plots of L21 and L22 are shown in Figure 6.20 and Figure 6.21, respectively. Both of these figures, which do not include dead load, were linear until an applied shear of 215 kips, and thus confirm the result from Figure 6.19. None of the individual plots from the other horizontal gages indicated cracking prior to 215 kips, which confirmed that the kinks in lines in Figure 6.19 were likely the result of slight gage misalignments when they were installed.

With the dead load at the cross-section under the applied load added to the result from Figure 6.19, the corresponding moment, $M_{cr,meas}$ was 3,380 kip-ft. , which was essentially the same value obtained from visual measurement. This resulted in a $\frac{M_{cr,\,meas}}{M_{cr,\,pred}}$ ratio of 1.09, which meant the 2002 Standard code prediction of the cracking moment was almost identical to the measured value.

6.2.4 AASHTO 1979 Interim Predicted vs. Measured Shear Capacity

The predicted shear capacity was the only element of the 1979 Interim shear provisions that could be compared to a measured value. Figure 6.22 is a plot of the 1979 Interim predicted shear capacity for Specimen I (with measured material properties) and the maximum applied shear including dead load. The 1979 Interim shear provisions were the only provisions unaffected by the location of the applied load, which resulted in linear predicted shear capacity from 2 ft. to 25 ft. It is evident from the figure that the 1979 Interim provisions significantly under-predicted the capacity of Specimen I. Furthermore, the $\frac{V_{test}}{V_{pred}}$ ratio of 2.07 given in Table 6.1 was the largest of all the AASTHO shear provisions making the 1979 Interim shear provisions the most conservative and unreliable for predicting the capacity of Specimen I.

6.2.5 Strut and Tie; Predicted vs. Measured Parameters

The 2004 AASHTO LRFD code allows designers to use the strut and tie model to design for shear. This model is not a sectional design method like the three previously described methods, so no shear capacity vs. position plot could be developed. The shear strength predicted by this model was controlled by the limit state of an element in the model. The shear strength predicted by the strut and tie model, as well as a discussion regarding the element that limited the strength, are presented in the following sections.

6.2.5.1 Predicted vs. Measured Shear Capacity

Figure 6.23 shows the strut and tie model for the test end of Specimen I. In order for the strut and tie model to produce a reasonable predicted shear capacity, the struts from all of the stirrups, along with a direct compressive strut, had to go directly to the support. If the direct compressive strut was not included in the model, the predicted shear capacity was significantly below the capacity predicted by the 2004 LRFD and 2002 Standard, and was very conservative. As a result, the two factors that controlled the strut and tie model were the number of stirrups in the shear span, and the strength of the direct compressive strut.

The predicted shear capacity of the model shown in Figure 6.23 was 281 kips, assuming the measured material properties from Chapter 5. This was the shear capacity also assuming that there was a direct compressive strut from the load to the support. Specimen I failed at a shear of 392 kips under the applied load, including dead load, which produced a $\frac{V_{test}}{V_{pred}}$ ratio of 1.40. This value was conservative, and very similar to the value from the 2004 LRFD code. If the direct compressive strut was left out of the model, and only the struts from all of the stirrups in Figure 6.23 were considered, the predicted shear resistance was reduced to 204 kips. This would have resulted in a $\frac{V_{test}}{V_{pred}}$ ratio of 1.92, which was more conservative than either the 2002 Standard or the 2004 LRFD methods (but still less conservative than the 1979 Interim shear provisions).

The elements likely to fail in the strut and tie model were the stirrups through yielding far enough to fracture, and the compression struts through crushing. The center of the web is

marked in Figure 6.23 and was the area where compression from all of the struts fanned out. A compression failure was most likely in this region, because of the narrow web and lack of confinement. There was no evidence that the stirrups fractured at any time during the test, but there was evidence of a compressive failure at the top web/flange interface as indicated in Figure 6.23. Figure 6.10 is a photograph of the area marked in Figure 6.23. Failure of the compressive struts occurred beyond the peak applied load.

6.2.5.2 Predicted vs. Measured Strut Angle

The strut and tie model for Specimen I is superimposed over the cracking pattern at 40% beyond the peak applied load in Figure 6.24. The shear cracks closest to the support, as well as the flexure-shear crack indicated in the figure, were in good agreement with the predicted strut angles. The figure also shows that a direct compressive strut might have formed in the specimen, because some of the cracking was steep enough to be from a direct strut, and the crack labeled "failure crack" extended from the load to the support. There was no direct evidence of the struts from the three stirrups closest to the support.

The angles of the predicted struts are shown along the top chord in Figure 6.25. Also shown in the figure are the measured angles of principal compression from the rosette strain gages at initial cracking. The only gages in good agreement with the predicted strut angles are the three marked in the figure. All of the gages to the left of these three, recorded angles smaller than predicted. The measured angles from the rosettes closest to the three struts near the support were significantly less than the angles predicted by the strut and tie model, which may have been due to their location in a disturbed region.

As discussed in the previous section, in order for the strut and tie model to produce a reasonable prediction of the shear capacity, the struts from all of the stirrups had to go directly to the support, and there had to be a direct compressive strut from the load to the support. If any of these struts were left out of the model, the results would be unrealistically conservative. The evidence from the shear test, particularly the post-peak "failure crack," suggested that a direct compressive strut had formed, and thus out of all possible strut and tie models, the assumed model in Figure 6.23 was the closest match to the observed behavior.

6.3 Specimen II

Specimen II was the specimen without a bridge deck, which was tested on May 16, 2006. A few changes were made to the test setup and procedure based on lessons learned from the test on Specimen I. Prior to the start of this test, the modifications shown in Figure 6.5 were added to the specimen to ensure the extension would not fail as it had during initial testing of Specimen I. The instrumentation layout was also slightly altered to address the inaccuracies in the Krypton data collected during the first test. The LEDs labeled 1-9 and 34-54 in Figure 4.16 were removed, resulting in the revised instrumentation layout shown in Figure 6.26. The camera was also repositioned, as shown in Figure 4.18, to obtain more accurate measurements.

The ultimate test on Specimen II began with initial readings of all the instrumentation to obtain offset data with no applied load. The loading was applied with pauses at increments of 50 kips from 0 to 200 kips and with pauses at increments of 25 kips beyond 200 kips to take

DEMEC readings and mark cracks. The test was uneventful until the first visible evidence of cracking occurred at a load of 275 kips. The crack was a flexural crack on the bottom flange directly below the applied load. A few minor flexural cracks formed beyond 275 kips with no major cracks forming until 394 kips. At 394 kips, an audible popping sound was heard and several large diagonal web cracks formed simultaneously, which are shown in Figure 6.27. A photograph of the specimen at 394 kips was unavailable.

After the initial web cracks formed, the specimen was displaced in 0.25 in. increments until the applied load peaked at 520 kips, as shown in Figure 6.28. From 394 kips to 520 kips the initial web cracks continued to grow and widen, and many flexural cracks formed. The cracking pattern at the peak load is shown in Figure 6.29 and Figure 6.30. The test was terminated when the applied load fell to 292 kips, or 44% of the peak. At this stage the specimen was damaged as shown in Figure 6.31 and Figure 6.32 with significant crushing at the web/flange interface that resulted in spalling of the web concrete shown in Figure 6.33. This spalling indicated that the specimen failed through crushing at the web/flange interface.

6.3.1 Load-Displacement

Due to a loss of power to the transducers, the LVDTs for this specimen were not operating during the test. The only load-displacement data available were from the displacement of the actuator, which also captured displacement of the neoprene pad at the pinned support. As a result, these displacement data were slightly different than the actual displacement of the member.

The plot in Figure 6.28, however, is intended to illustrate the general load-displacement behavior of the member. Immediately after the web initially cracked at a load of 394 kips, the beam began to exhibit nonlinear load-displacement behavior with respect to load. The nonlinearity was due to the formation of extensive web and flexural cracking between 394 kips and 520 kips, the extent of which is illustrated by the contrast between Figure 6.27 and Figure 6.30. The displacement at 520 kips was 2.3 in., and any displacement beyond this value resulted in crushing of the web concrete shown in Figure 6.33. Figure 6.34 shows the extent of the crushing, which caused the specimen to slowly lose its ability to maintain the applied load.

6.3.2 AASHTO 2004 LRFD; Predicted vs. Measured Parameters

In this section, the 2004 LRFD predicted shear capacity, longitudinal strain at middepth of the cross-section, shear stress, and angle of the principal strains at ultimate are compared to measured results. The details regarding the methodology and instrumentation used to measure these parameters during the shear test of Specimen II are outlined in Chapter 4.

6.3.2.1 Predicted vs. Measured Shear Capacity

Figure 6.35 is a plot of the 2004 LRFD predicted shear capacity for test Specimen II, and the maximum shear, including dead load. This plot shows the capacity of the test specimen assuming measured material properties as described in Chapter 5, with the load applied 14.5 ft.

from the end as shown in the drawing above the plot. According to this figure, the greatest disparity between applied shear and predicted capacity was directly under the applied load.

Using measured material properties, the 2004 LRFD predicted shear capacity directly under the applied load, given in Table 6.1, was 204 kips. Specimen II failed at a shear of 329 kips under the applied load, including dead load. The ratio of $\frac{V_{test}}{V_{pred}}$ for the 2004 LRFD was 1.61, which meant the code provided a conservative prediction of the shear capacity. Compared to the other shear provisions, the 2004 LRFD was not the most conservative, but it was more conservative than the 2002 Standard.

From the prediction in Figure 6.35, it appeared as though Specimen II would fail under the applied load. A failure in this region would likely be a flexure/shear type of failure. If the 2004 LRFD prediction in Figure 6.35 were correct, the test specimen should have had significant flexure/shear cracks that dominated behavior at failure, which was not the case.

The majority of the damage was in the web of the specimen as shown in Figure 6.29. Although there is significant flexural cracking shown in Figure 6.30, these cracks were not dominant. The last measurement of the crack widths, due to safety concerns, was at a shear under the applied load, including dead load of 315 kips. At this level of shear, the crack labeled "widest web crack" was $^{7}/_{16}$ in. at the bottom of the web, and the flexure/shear cracks were all less than $^{1}/_{32}$ in. From 315 kips to 329 kips, the web cracks continued to widen, with no perceptible change in the width of the flexure/shear cracks.

6.3.2.2 Predicted vs. Measured Longitudinal Strain

In this section, the data from the Krypton LEDs and DEMEC points shown in Figure 6.26 are used to validate the plane sections remain plane assumption implicit in the 2004 LRFD equation for ε_x, Eqn (4.1). The $\varepsilon_{x,meas}$ from the Krypton measurement sub grids were calculated using the displacement field analysis described in Appendix B. Longitudinal strain profiles at peak load, which include the calculated strain from the prestressing force and dead load, are presented in this section to determine if the average distribution was approximately linear through the cross-section. If plane sections remained plane at peak load, the longitudinal strain profiles also provide $\varepsilon_{x,meas}$ to compare with the $\varepsilon_{x,pred}$ from Eqn. (4.1). The predicted longitudinal strain at failure was provided by the non-iterative spreadsheet used to predict shear capacity as described in Section 3.3.1. Using the measured material properties from Chapter 5, $\varepsilon_{x,pred}$ for Specimen II was 295 με.

The longitudinal strain profiles shown in Figure 6.36 were from the cross-section shown above the plot, at various levels of applied shear, including dead load. The cross-section shown was outside of the disturbed region, and was therefore assumed to be unaffected by any disturbance in the strain distribution caused by the applied load. The strain at the cross-section was relatively linear and behaved as expected prior to cracking: as the shear increased, compression above and tension below the neutral axis increased. However, when the web of Specimen II cracked at an applied shear of 254 kips, including dead load, the profile became nonlinear.

Figure 6.37 through Figure 6.44 contain the longitudinal strain profiles of every cross-section with Krypton LEDs. The points marked “measured” in the figures show the longitudinal strain profile at the peak applied shear for the cross-section marked with the dashed line in the figure. Because the beam was severely cracked and data from the horizontal strain gages was highly dependent on the proximity of a gage to a crack, only the strains from the Krypton LEDs and DEMEC points were used to construct the strain profiles. The data from the Krypton LEDs and DEMEC points were not as dependent on the location of the cracks, due to the large gage lengths shown in the figures. These measuring devices spanned at least one crack and provided average results because both cracked and uncracked concrete contributed to the measurements. The lines labeled “Response 2000” in each figure are the predicted average strain distribution.

Response 2000, R2k, and its ability to predict longitudinal strains is described in more detail in Section 4.5.1. R2k was used to predict the strain distribution at each cross-section when subjected to the maximum applied shear, including dead load. The predictions were linear because R2k was based on the assumption that on average, plane sections remain plane in cracked concrete. If this assumption was correct the measured strain profiles at the peak applied shear should be approximately linear like the pre-cracking strain profiles shown in Figure 6.36, and reasonably similar to the R2k predictions. The results in Figure 6.37 through Figure 6.44, however, show that the strain distribution at the peak applied shear was nonlinear at every cross-section. The only distribution close to the R2k prediction is shown in Figure 6.40. The "best fit" line in the figure was relatively close to the R2k prediction, and would have been even closer if the strain at the middle LED was in better agreement with the prediction.

One possible reason that the results in Figure 6.37 through Figure 6.44 were nonlinear was that the gage lengths shown in the figures were not long enough to capture average behavior. Most of the gage lengths were long enough to include at least one crack, however, it is important to investigate whether increasing the gage length would improve the results by further eliminating the effects of local strain variations. Figure 6.45 is a plot of the strain distribution for the same cross-section shown in Figure 6.40 with the gage length increased from 20 in. to 40 in. as shown in the figure. Unfortunately, the strain distribution in Figure 6.45 is more nonlinear than the distribution from the 20 in. gage length.

Table 6.3 lists the Krypton strains for both the 20 in. and 40 in. gage lengths for the cross-section 60 in. from the applied load. For the top krypton LED, one additional crack was included in the gage length when it was changed from 20 in. to 40 in. This changed the strain at the top Krypton LED from compression to tension with a difference in magnitude of nearly 750 με. The 40 in. gage lengths for the middle and bottom LEDs were not intersected by any additional cracks. As a result, more concrete in compression contributed to the strain at these LEDs and the tensile strains at both LEDs were reduced. The increase in gage length had little effect on the DEMEC strain.

To average strain over an even larger distance, the gage length was further increased to 60 in. Figure 6.46 shows that the strain profile is still clearly nonlinear, despite the fact that at least three cracks crossed the 60 in. gage length of each Krypton measurement sub grid. The strains at the top and middle Krypton LEDs listed in Table 6.3 were nearly identical, with the largest change occurring at the bottom LED. All three Krypton strains fell in a relatively straight line; however, the DEMEC strain was the closest to the R2k prediction. If the DEMEC strain was ignored, the resulting strain profile was approximately linear as shown in Figure 6.47, but

the "best fit" line in the figure also shows that the Krypton LEDs form a distribution of only tensile strains through the depth of the cross-section, which was not physically possible.

The longitudinal strain profiles shown in Figure 6.37 through Figure 6.44 were nonlinear, and further averaging of the strains at the cross-section 60 in. from the applied load failed to produce results any closer to linear. This was consistent with the results at other cross-sections. Therefore, the linear nature of the data in Figure 6.36 prior to cracking is evidence that plane sections remain plane until the concrete cracks, but there was no evidence to suggest that after cracking plane sections still remained plane, even in an average sense.

As described previously, the concrete behavior model used to develop the AASHTO 2004 LRFD code was based on the assumption that on average, plane sections remain plane in cracked concrete. Equation 4.1 for ε_x represents essentially half the strain in the longitudinal reinforcement, and because strain gages were not located at the centroid of the prestressing strand, the longitudinal strain profiles were necessary to verify $\varepsilon_{x,pred}$. Because the average strain profiles beyond cracking were nonlinear, it was not possible to accurately obtain $\varepsilon_{x,meas}$ at middepth to compare to $\varepsilon_{x,pred}$.

6.3.2.3 Predicted vs. Measured Shear Stress

The predicted shear stress, $\nu_{u,pred}$ was calculated as described in Section 6.2.2.3 using the measured material properties from Chapter 5, and the V_{pred} given in Table 6.1 as 204 kips. This resulted in a $\nu_{u,pred}$ for Specimen II of 600 psi. The measured ultimate shear, V_{test}, under the applied load, including dead load, for Specimen II was 329 kips. This V_{test}, when used with V_p calculated assuming measured losses, resulted in a $\nu_{u,meas}$ of 998 psi.

Table 6.2 requires $\frac{\nu_u}{f_c'}$ to look up values of θ and β. When $\nu_{u,pred}$ and $\nu_{u,meas}$ were combined with the measured f_c' of 10,130 psi, given in Chapter 5, the $\frac{\nu_{u,\,pred}}{f_c'}$ and $\frac{\nu_{u,\,meas}}{f_c'}$ ratios were 0.059 and 0.098, respectively. The θ and β that resulted from $\frac{\nu_{u,\,pred}}{f_c'}$ and the $\varepsilon_{x,pred}$ from Section 6.3.2.2 of 295 με were 27.3° and 2.88, respectively. These values were conservative predictions, because they were from the top row of the table where the minimum $\frac{\nu_u}{f_c'}$ of 0.075 controlled. There was no way to investigate how these values changed using only measured properties, because the results from Section 6.3.2.2 did not provide reliable data for $\varepsilon_{x,meas}$. The only other option available was to use $\frac{\nu_{u,\,meas}}{f_c'}$ and $\varepsilon_{x,pred}$ to investigate how θ and β change with $\nu_{u,meas}$. An increase in $\frac{\nu_u}{f_c'}$ from the predicted 0.059 to the measured 0.098, with ε_x held constant, changed θ and β to 27.7° and 2.73, respectively. If the revised θ and β were used to calculate shear capacity, they would make the 2004 LRFD V_{pred} more conservative.

6.3.2.4 Predicted vs. Measured Angle of Principal Compression

The 2004 LRFD predicted angle of principal compression at ultimate, θ_{pred}, is shown in Figure 6.48 at several locations along the length of Specimen II. The values of θ_{pred} were interpolated from Table 6.2 using $\frac{v_{u,\,pred}}{f_c'}$ and $\varepsilon_{x,pred}$ at each cross-section marked by the vertical line above the beam. The terms $\frac{v_{u,\,pred}}{f_c'}$ and $\varepsilon_{x,pred}$ were calculated at each cross-section with measured material properties from Chapter 5. The shear cracks shown in Figure 6.48 were the cracks that formed when the beam first cracked in shear, as described in Section 6.3. The visual θ_{meas} of each crack marked in the figure was calculated from the dimensions of the crack within the web. The cracks were steeper closer to the applied load, as predicted by the 2004 LRFD, due to increased moment.

Figure 6.49 contains the applied shear vs. angle of principal compression plots for the four rosette strain gages closest to the applied load, labeled R1-R4 in Figure 6.50. The calculated angle of principal compression from the rosette data included the calculated strains from the prestressing force and dead load. The dashed line in Figure 6.49 was the applied shear that cracked the web of Specimen II, and was the point beyond which θ_{meas} no longer changed in a predictable manner. After web cracking, the angle at the rosette gages was dependent upon the proximity of the gage to a shear crack. The behavior of these four strain gages was typical of all the rosettes.

The angle of principal compression at every rosette when the web of the specimen cracked is shown in Figure 6.50. The gages between the critical section and the applied load had crack angles in reasonable agreement with the 2004 LRFD θ_{pred} values and the visual measurements from Figure 6.48. Between the critical section and the support, the angles generally became steeper, particularly at the lower strain gage closest to the support, which had an angle of 35.8°. This was a disturbed region, so θ_{meas} likely did not compare well to θ_{pred} from the 2004 LRFD code because of the complicated strain distribution in this region.

The θ_{meas} from the 10 in. by 10 in. Krypton measurement sub grids were calculated using the displacement field analysis described in Appendix B, including calculated strains from the prestressing force and dead load. The results were highly variable prior to cracking, because the displacements between LEDs were relatively small compared to the displacements after cracking. This magnified the error in the Krypton data prior to cracking, and made θ_{meas} unresolvable. Figure 6.51 is a plot of θ_{meas} from the three LEDs labeled on the beam also shown in the figure. These LEDs were located outside the disturbed region and are representative of the graphs from the other LEDs. The dashed line in Figure 6.51 denotes when the beam cracked in shear, and defined the point at which the Krypton θ_{meas} became resolvable.

Figure 6.52 shows the values of θ_{meas} for the Krypton LEDs, and visual measurements at peak load. The visual θ_{meas} in the figure shows that a few more web shear cracks developed beyond initial cracking, and some of the flexure cracks grew into flexure shear cracks. At ultimate, the diagonal cracks that initiated near the support when the specimen first cracked extended through the entire web. The web shear cracks marked 24.7° and 26.2° were slightly steeper than adjacent cracks, but were still reasonably close to the angles predicted by the 2004

LRFD code. The flexural shear cracks in the figure were steeper than the LRFD predicted values, however, they were not the dominant cracks as described in Section 6.3.2.1. The values of θ_{meas} from the Krypton were uncorrelated to the visual cracks and the 2004 LRFD θ_{pred} values.

The magnitude of θ_{meas} from visual measurement at initial cracking and ultimate, and θ_{meas} from the rosette gages at initial cracking, closely matched θ_{pred}. Thus the number of stirrups engaged by each shear crack was close to that predicted by the 2004 LRFD. According to the 2004 LRFD, the stirrup contribution to shear capacity was 98 kips using the most conservative θ_{pred} of 27.7°. From the evidence presented in this section, the 2004 LRFD estimate of V_s was better than the 2002 Standard estimate that assumed a crack angle of 45° and produced a V_s of 56 kips.

6.3.3 AASHTO 2002; Standard Predicted vs. Measured Parameters

In this section the 2002 Standard predicted shear capacity and predicted cracking moment are compared to the measured values obtained from the shear capacity test of Specimen II.

6.3.3.1 Predicted vs. Measured Shear Capacity

The 2002 Standard predicted shear capacity and maximum shear, including dead load, for the test of Specimen II are shown in Figure 6.53. The predicted capacity in this figure was calculated assuming measured material properties as described in Chapter 5, with the load applied as shown. According to the 2002 Standard, Specimen II should have failed near the applied load, because this was the location with the greatest disparity between applied shear and predicted capacity.

The 2002 Standard predicted shear capacity at the cross-section directly under the applied load is listed in Table 6.1 as 238 kips. For the maximum shear of 329 kips, including dead load, the ratio of $\frac{V_{test}}{V_{pred}}$ for the 2002 Standard was 1.38. The only shear provision with a closer prediction to the measured shear capacity was strut and tie method.

The 2002 Standard equation for web shear, V_{cw}, controlled the concrete contribution to shear capacity, V_c, from the support to 10 ft. Between 10 ft. and the applied load at 14.5 ft., the equation for flexure shear, V_{ci}, controlled V_c, which was responsible for the dip in capacity under the applied load shown in Figure 6.53. Because V_{ci} controlled in this region, the implied failure mode for Specimen II was flexure/shear. If the predicted shear capacity in Figure 6.53 was correct, the test specimen should have had significant flexure/shear cracking near the applied load. Figure 6.30 shows that there was flexure/shear cracking at failure, however, these cracks were not dominant at failure as described in Section 6.3.2.1.

If the 2002 Standard had predicted the web shear failure of Specimen II, V_{cw} would have controlled V_c from the support to the applied load. This would have eliminated the dip in capacity in Figure 6.53, and V_c would have been relatively constant in this region at 246 kips. When combined with the V_s under the applied load of 56 kips, a V_c of 246 kips would have

resulted in a V_{pred} of 302 kips and a $\frac{V_{test}}{V_{pred}}$ ratio of 1.09. This would have made the 2002 Standard predicted shear capacity the closest to the measured capacity.

6.3.3.2 Predicted vs. Measured Cracking Moment

The cracking pattern when the web first cracked is shown in Figure 6.27. Besides the web cracks shown in this figure there were four flexural cracks that formed prior to the web cracks. The largest of the four cracks, located almost directly under the applied load, was the first visible flexural crack. This crack was first observed at a shear of 177 kips under the applied load, including dead load, and was only visible on the underside of Specimen II. This shear corresponded to a moment of 2,660 kip-ft. directly under the applied load, including dead load.

Horizontal strain gages located on the bottom flange of the test specimen, as shown in Figure 6.26 and Figure 4.14, were used to determine when the beam first cracked in flexure. Figure 6.54 is a plot of the longitudinal strains along the bottom flange of the specimen at various levels of applied shear, not including dead load. The strains in the figure include the calculated strain from the prestressing force and dead load. As long as the specimen was uncracked, the strain distribution along the bottom flange should have increased linearly in proportion with the applied load.

The strain distribution in Figure 6.54 was relatively straight, and the beam was clearly uncracked, up to 100 kips of applied shear. A few slight kinks in the distribution were evident at an applied shear of 100 kips. However, as was the case with Specimen I, these kinks were the likely the result slightly misaligned horizontal gages that became more pronounced with increasing applied load. By 170 kips of applied shear the distortion in the strain distribution indicated the beam had cracked.

Figure 6.55 is a refined plot of the longitudinal strains between 140 kips and 170 kips of applied shear. At 155 kips, the strain gages begin to show evidence of strain redistribution from cracking. It is important to note that the locations of the horizontal gages in relation to the flexural cracks in the figure are only approximate. The gages were applied on the underside of the beam as shown in Figure 4.14, but Figure 6.55 shows the location of the cracks on the profile of the specimen. Information on how the cracks extended under the specimen was not recorded. What is clear from Figure 6.55, is that flexural cracking first occurred in the region close to the applied load at an applied shear of 155 kips.

Figure 6.56 through Figure 6.63 are plots from horizontal gages L16 through L23, not including dead load. A change in slope in the figures indicates strain redistribution from cracking. The lowest applied shear that caused a change in slope in any of the figures was 155 kips, which confirms the conclusion drawn from Figure 6.55 that the beam first cracked at a cross-section near the applied load at 155 kips.

Specimen II cracked at a shear of 162 kips, including the dead load of 7 kips from the cross-section under the applied load, which corresponded to a $M_{cr,meas}$ of 2,440 kip-ft. The $M_{cr,pred}$ from the 2002 Standard code was 2,235 kip-ft. directly under the applied load, when calculated using the measured material properties from Chapter 5. This resulted in a $\frac{M_{cr,\,meas}}{M_{cr,\,pred}}$

ratio of 1.09 and 1.19 for the horizontal strain gage and visual methods of measuring the cracking moment, respectively. The $M_{cr,meas}$ from the horizontal strain gages was very close to the 2002 Standard $M_{cr,pred}$.

6.3.4 AASHTO 1979 Interim Predicted vs. Measured Shear Capacity

The 1979 Interim predicted shear capacity (with measured material properties) and the maximum applied shear including dead load are shown in Figure 6.64. The 1979 Interim shear provisions were unaffected by the location of the applied load, which resulted in linear predicted shear capacity from 2 ft. to 25 ft. These provisions significantly under-predicted the capacity of Specimen II with a $\frac{V_{test}}{V_{pred}}$ ratio of 2.09. As shown in Table 6.1, the 1979 Interim shear provisions provided the most conservative predicted shear capacity of all the AASHTO shear provisions.

6.3.5 Strut and Tie; Predicted vs. Measured Parameters

Figure 6.65 shows the strut and tie model for the test end of Specimen II. The strut and tie model is not a sectional model, so the shear capacity of this model was controlled by the limit state of an element in the model. The two elements that controlled the shear strength predicted by this model were the number of stirrups in the shear span, and the strength of the direct compressive strut from the applied load to the roller support. The following sections provide analyses of the strut and tie model for Specimen II.

6.3.5.1 Predicted vs. Measured Shear Capacity

The shear capacity of the model in Figure 6.65 was 246 kips, assuming the measured material properties from Chapter 5. Specimen II failed at a shear of 329 kips under the applied load, including dead load, which resulted in a $\frac{V_{test}}{V_{pred}}$ ratio of 1.34. The strut and tie model for Specimen II predicted the shear capacity closest to the measured capacity, and was very similar to the predicted capacity from the 2002 Standard code. However, if only the struts from the stirrups were used to create the strut and tie model, the predicted shear resistance was reduced to 204 kips, which was identical to the 2004 LRFD prediction given in Table 6.1.

The two critical components of the strut and tie model were the stirrups and the compression struts, which could fail through yielding far enough to fracture and crushing, respectively. The middle of the web, marked in Figure 6.65, was the area most susceptible to crushing failure. This region was the most vulnerable because it was narrow and did not have much steel to provide confinement.

There was no evidence at either the peak load or beyond that the stirrups fractured, but there was evidence of compressive failure. Figure 6.33 and Figure 6.34 show the extent of the web crushing that occurred beyond the peak load. In these figures, there was crushing through the depth of the web in the area marked by the vertical arrows in Figure 6.65, and along the top web flange intersection. The concrete crushing caused the drop in load from the peak shown in Figure 6.28.

6.3.5.2 Predicted vs. Measured Strut Angle

The strut and tie model for Specimen II is superimposed over the final cracking pattern in Figure 6.66. The predicted strut angles are shown along the top chord in the figure. There were two locations where the cracks lined up reasonably well with the strut locations, particularly close to the applied load. However, there was no visual evidence of a strut shallow enough (i.e. oriented at 14°) to be a direct compression strut from the load to the support.

Figure 6.67 shows the calculated angle of principal compression from the rosette data, including the calculated strains from the prestressing force and dead load. The only rosettes in good agreement with the predicted strut angles were the five marked in the figure. All of the gages closer to the roller support recorded angles smaller than predicted. The predicted angles of the two struts closest to the support were nearly double those from the measured rosette data. The rosettes near the support were located in a disturbed region, which may account for the discrepancy between the measured and predicted angles. At initial cracking, none of the rosette data produced an angle shallow enough to be from a direct compressive strut between the load and the support.

The angles measured by the Krypton at peak load were discussed in Section 6.3.2.4, and are shown in Figure 6.52. Although the data from the Krypton was resolvable after cracking, the resulting distribution of angles shown in Figure 6.52 did not correlate to the predicted strut angles. Thus only the visual evidence was available to determine if a direct compressive strut existed at the peak load or beyond. None of the visual crack angles were shallow enough to indicate the existence of a direct strut oriented at 14°.

6.4 Comparison between the two Specimens

According to the predictions in Chapter 3, adding the bridge deck to the test specimen should have increased the shear capacity, and changed the predicted behavior of the specimen at ultimate. The results from both shear tests are compared to the predicted capacities from the ASSHTO shear provisions in Table 6.1. All of the codes conservatively predicted the shear capacity of both specimens, but on average, the predictions from the 2002 Standard were the closest to the measured capacity. One possible reason the predictions were conservative was the lift hooks present in the specimens from the manufacturing process. Typically the lift hooks were three prestressing strands embedded in the beam as shown in Figure 6.68. The lift hooks were not accounted for in the shear capacity calculations because their exact location was unknown.

The behavior of both specimens throughout the shear tests was similar. At peak load both specimens had significant web shear cracks that were clearly dominant over the flexure/shear cracks. From the peak load to 40% beyond peak, Specimen I crushed along the top web/flange interface over the 5 ft. region shown in Figure 6.23, and developed the dominant crack labeled in Figure 6.8. Specimen II also crushed along the top web/flange interface, but over a larger region, including through the depth of the web, as shown in Figure 6.34 and Figure 6.65. The test on Specimen I was terminated when the dominant shear crack formed, while the test on Specimen II was terminated because of the significant concrete crushing. The 2004 LRFD predictions indicated that both specimens would fail through flexure/shear, but the 2002 Standard predicted

that Specimen I would fail through web shear and Specimen II would fail through flexure shear. Both specimens appeared to fail through web shear.

The comparison between the predicted and measured parameters from the 2004 LRFD, 2002 Standard, and the strut and tie model discussed in the previous sections was essentially the same for both specimens. The only parameter that was predicted well by the 2004 LRFD code was the angle of principal compression, which is the key variable in the V_s contribution to shear capacity. Therefore, it was likely that the predicted V_s from the 2004 LRFD was close to the test V_s, and the reason why the code was overly conservative was related to the V_c term.

The 2002 Standard predicted cracking moment was nearly identical to the measured cracking moment for Specimen I, and close to the measured cracking moment for Specimen II. This was the only parameter from the code that could be measured, so it was difficult to draw any conclusions regarding the V_c and V_s terms. However, if the term for V_s was calculated with the measured angle of principal compression instead of the implicitly assumed 45°, the predicted shear capacity from the 2002 Standard would have been nearly identical to the V_{test} of both specimens. The results from the two shear tests in this experiment, therefore, suggest that the 2002 Standard code would be the most reliable method for predicting shear capacity if the V_s term was calculated with a variable angle. This is illustrated in Table 6.4, which shows the $\frac{V_{test}}{V_{pred}}$ ratio with V_{pred} calculated from the combination of the 2004 LRFD term for V_s and the 2002 Standard term for V_c.

When the bridge deck was added to the specimen the effective shear area was increased by approximately 17%. The specimen with a bridge deck failed at an applied shear approximately 19% greater than the specimen without a deck. This simple observation, when combined with the fact that both specimens behaved in a similar manner at ultimate, indicates that adding the bridge deck simply increased the shear capacity in proportion to the increased shear area.

Chapter 7
Parametric Study

7.1 Evaluation of the Bridge Girder from Mn/DOT Bridge No. 73023

The primary purpose of the laboratory tests was to determine whether or not the girder from Mn/DOT Bridge No. 73023 was undercapacity and if it was safe in service. The region of the original 88 ft. girder with the greatest difference between required and provided stirrup spacing was the region most likely to be undercapacity. Table 3.3 gives the stirrup spacing required by the 2004 LRFD, 2002 Standard, and 1979 Interim shear provisions for the 88 ft. girder. According to the 2002 Standard stirrup spacing given in the table, the section of the girder from the support to 9 ft. had the greatest difference between required and provided stirrup spacing with a required spacing of 13 in. compared to the provided spacing of 21 in. The two specimens tested in the laboratory were the 30.5 ft. long ends from the original 88 ft. girder, which included the 9 ft. portion of the original beam most likely to be undercapacity, as shown in Figure 7.1.

Figure 7.2 is a plot of the 1979 Interim predicted shear capacity of the original 88 ft. bridge girder and the shear demand due to dead load and live load. This figure is plotted for the portion of the beam from the support to just beyond the quarter point of the original 88 ft. girder. At the quarter point, the shear capacity was slightly below the shear demand of the dead load and HS20-44 live load due to the difference between the 1979 Interim required stirrup spacing and the provided stirrup spacing (both given in Table 3.3).

Figure 7.3 shows that V_{test} along the "test span" from both shear tests was larger than the factored V_u required by the 2004 LRFD HL-93 and 2002 Standard HS20-44 loading. The factored values of V_u plotted in the figure were the same values used to calculate the required stirrup spacing of the original 88 ft. girder given in Table 3.3. The moment at shear failure, M_{test}, shown in Figure 7.4, was also larger than the factored M_u required by the 2004 LRFD HL-93 and 2002 Standard HS20-44 loading. The combination of shear and moment at shear failure were larger than the factored shear and moment resistance required by the 2004 LRFD and 2002 Standard, which meant the "test span" section of the original 88 ft. girder exceeded capacity requirements. These results suggest the entire 88 ft. girder was safe in Bridge No. 73023, because the "test span" included the region of the girder most likely to be undercapacity.

7.2 Parametric Study

Because the stirrup spacing in the test specimens, shown in the "provided spacing" column in Table 3.3, most closely matched the requirements of the 1979 Interim shear provisions, the girders in Mn/DOT Bridge No. 73023 were likely designed using the 1979 Interim shear provisions. The conclusion, however, in Section 7.1 that the girders were safe does not necessarily apply to all bridge girders designed with these provisions. Therefore, a parametric study was performed to investigate whether or not bridge girders with different characteristics were likely to be undercapacity, and to determine which girders might be the most susceptible to shear failure.

Parameters that affect the shear design of prestressed concrete bridge girders include girder depth, span length, concrete compressive strength, amount of prestress, stirrup spacing, and girder spacing. Many of these parameters are interrelated. Because of the interdependence of these parameters, a subset of parameters, namely, girder depth, span length, concrete compressive strength, and girder spacing where chosen as the main variables of the study. The ranges for these parameters given in Table 7.1 were believed to be representative of bridges in the Mn/DOT inventory that were designed according to the 1979 Interim shear provisions. For the parametric study, girders with the parameters given in Table 7.2 were selected from existing Mn/DOT bridges. Table 7.3 shows the distribution of the key shear design parameters from the selected girders. Because there was no way to verify that the selected girders had been designed according to the 1979 Interim provisions, the stirrup spacing for these girders was recalculated using the 1979 Interim shear provisions, nominal material properties, and HS20-44 live load. The spacing for #4, double leg, grade 60 stirrups required by the 1979 Interim shear provisions is given in Table 7.4.

The shear capacity of the bridge girders with the 1979 Interim required stirrup spacing was then calculated using the 2002 Standard shear provisions, because as discussed in Section 2.9, the 2002 Standard shear provisions were reliable for predicting shear capacity, V_n. Based on these results the $\frac{\phi V_{n,2002Std}}{V_u}$ ratio, with V_u equal to the dead load plus HS20-44 live load, was calculated at the critical section and every tenth point along the span length.

Note that the numbers in parenthesis in Table 7.4 were the stirrup spacing of the Mn/DOT girders given on the bridge construction plans. The existing stirrup spacing was relatively close to the 1979 Interim required spacing, however, several girders had less shear reinforcement than that required by the 1979 Interim. It is unknown which edition of the AASHTO shear provisions was used to design the stirrup spacing of the existing girders; use of an edition that differed from the 1979 Interim shear provisions might explain the discrepancy. It is also possible that a ϕ of 1.0 was used in the original design rather than 0.9, which was used in this study. In the prestressed concrete design section of the 1977 edition of the AASHTO Standard code, Section 1.6.5 contains the following:

For factory produced precast, prestressed concrete members $\phi = 1.0$

For post-tensioned cast in place concrete members $\phi = 0.95$

For shear $\phi = 0.9$

This may have been misinterpreted to mean that ϕ should be 1.0 for the design of precast, prestressed concrete girders in flexure and shear, and that the ϕ of 0.9 only applied to nonprestressed members. A ϕ of 1.0 versus 0.9 results in a 2-3 in. larger stirrup spacing for most girders in this study. Another possible explanation is the bridge girders were designed using a shear demand reduced by the vertical component of the prestressing strand (i.e. V_u-V_p). AASHTO shear provisions between 1961 and 1973 defined V_u as "the shear due to ultimate load and effect of prestressing." This definition changed in the 1977 shear provisions to "the total design shear force at [the] section," and bridge designers may have continued to use the previous definition. Furthermore, it is also possible that the computer program used to design these bridge girders contained an error.

7.2.1 Results of the Parametric Study

The mean of the test-to-predicted shear strength ratios, $\left(\frac{V_{test}}{V_{pred}}\right)$, from the database of shear tests compiled as part of NCHRP Project 12-61, was 1.32 with a standard deviation of 0.21 (discussed in Section 2.9.2). These values quantify the conservatism of the 2002 Standard shear provisions. Girders from the parametric study with a $\frac{\phi V_{n,2002Std}}{V_u}$ ratio of at least 0.90 were within one standard deviation of the mean and were not likely to fail in shear because of other sources of shear strenght in the end regions.

The results of the parametric study are given in Table 7.5, and show that between 0.1*L* and 0.5*L* only the girder from Bridge No. 48010 had a $\frac{\phi V_{n,2002Std}}{V_u}$ ratio below 0.90. The critical section of all the girders was clearly the cross section with the lowest $\frac{\phi V_{n,2002Std}}{V_u}$ ratio and seven of the twelve girders were below 0.90. In Table 7.6 the girder parameters are compared to $\frac{\phi V_{n,2002Std}}{V_u}$ at the critical section. The data in Table 7.6 show that within each depth-based subset of girders, the girders with the shortest span length and widest girder spacing performed the worst. The goal of the remainder of this section is to identify why the short girders with a wide spacing were the most susceptible to being undercapacity at the critical section and develop a method to identify these girders.

7.2.1.1 Girders Most Susceptible to Being Undercapacity

The last column in Table 7.7 shows that the contribution of V_s to predicted shear capacity at the critical section was approximately 30% for most of the girders. Therefore, it was primarily a variation in the values of V_c and V_u among the girders that caused the short girders with a wide spacing to have the lowest $\frac{\phi V_{n,2002Std}}{V_u}$ ratio. Table 7.8 shows which 2002 Standard equation for V_c controlled at each section of interest. None of the sections controlled by V_{ci} had a $\frac{\phi V_{n,2002Std}}{V_u}$ ratio below 0.96, and at the critical section V_{cw} controlled V_c for all the girders. The $\frac{\phi V_{n,2002Std}}{V_u}$ ratio was the lowest at the critical section for all of the girders in part because V_u was the highest at this location; however, the short girders with a wide spacing performed the worst because short span length was correlated with low V_{cw}, and wide girder spacing was correlated with high V_u.

In the equation for V_{cw}:

$$V_{cw} = (3.5\sqrt{f_c'} + 0.3 f_{pc})bd + V_p \qquad (7.1)$$

the value of f_{pc} is the compressive stress at the neutral axis of the composite girder due to the prestressing force and self weight moments (M_{sw}) assuming the girder acted alone (unless the

composite neutral axis was in the flange, then it was the compressive stress at the web/flange intersection):

$$f_{pc} = \frac{P}{A} - \frac{Pe(y_{tc} - y_t)}{I_g} + \frac{(M_{sw})(y_{tc} - y_t)}{I_g} \tag{7.2}$$

At the critical section, the two terms for the prestressing contributed significantly to f_{pc}, and thus V_{cw}, because the self weight moment was small. However, because the prestressing force (P) is in both the first and second terms of Eqn (7.2), it was important to determine which term controlled the prestressing contribution to f_{pc} for each girder depth.

Near the critical section, by ignoring self-weight, Eqn (7.2) can be rewritten as:

$$f_{pc} \approx \frac{P}{A}\left(1 - \frac{e(y_{tc} - y_t)}{r^2}\right) \tag{7.3}$$

where r is the radius of gyration, and the value of y_{tc}-y_t is taken as either the distance between the centroids of the composite and noncomposite section if the centroid of the composite section lies in the web, or the distance between the flange/web intersection and the centroid of the noncomposite section if the centroid of the composite section lies above the web. The values of $\frac{e(y_{tc} - y_t)}{r^2}$ for each girder are given in Table 7.9. The results in the last column of the table varied little within each depth-based subset of girders, with the exception of the girder from Bridge No. 27068b, which had a large eccentricity relative to the other girders of the same depth. The affect of eccentricity on the rest of the girders was similar amongst girders of the same depth, which meant any relative increase in P among the girders with the same depth would result in an increase in f_{pc} (and thus V_{cw}).

For flexural design of a girder with a given depth, length corresponds to quantity of prestressing reinforcement; relatively longer beams for the same depth require relatively more prestressing reinforcement, given that they typically experience greater flexural demands. Thus girder length (L) was related to the number of prestressing strands in the girders, as shown in Figure 7.5, and because the quantity of prestressing strands in the girders was directly related to P, girder length, L, must have also corresponded to P. Based on these relationships, and the relationship between P and V_{cw} discussed earlier; L is correlated to V_c at the critical section as shown in Figure 7.6.

Figure 7.6 clearly shows that the number of strands (and hence the span length) was directly proportional to V_c at the critical section. However, as shown in Figure 7.7, the shear demand, V_u, at the critical section was not correlated to L. Instead V_u was directly proportional to girder spacing (S_g), which is shown in Figure 7.8. This indicates that the live load shear demand is significantly higher than the dead load shear demand. One would expect the dead load demand to be linearly proportional to both L and S_g, however, the live load demand due to a truck at the critical section will be linearly related to S_g, but have only a small dependence on L. The live load shear demand due to a point load at the critical section is proportional to $(1-\alpha)$ as illustrated in Figure 7.9, where α is the ratio of the distance from the support to the critical section relative to the span length. Typically, α is small because the distance to the critical section is much smaller than the span length, so there is little L dependence in this term.

Based on the correlation of L to V_c and S_g to V_u, the performance of each girder at the critical section can be measured with the quantity $\frac{L}{S_g}$. Figure 7.10 shows the relationship between $\frac{\phi V_{n,2002Std}}{V_u}$ at the critical section and $\frac{L}{S_g}$. The trend in this figure is nearly linear for both the 45 in. and 54 in. deep girders, with R^2 values of 0.98 and 0.99, respectively. The results in the figure suggest that girders with a $\frac{L}{S_g}$ of 10 or greater were not underdesigned for shear.

Although the results from the 36 in. deep girders in Figure 7.10 were not linear (due to the girder from Bridge No. 27068b, which had a large $\frac{e(y_{tc} - y_t)}{r^2}$ relative to the other 36 in. girders), they still followed the same basic trend.

7.3 Recommendations

The girders tested in the laboratory from Mn/DOT Bridge No. 73023 were not undercapacity, and were safe in service. The results from the parametric study were intended to supplement the laboratory results and help identify which, if any, girders are likely to be understrength for shear. According to the parametric study, the bridge girders studied were most likely to be undercapacity at the critical section, and the girders most at risk tended to have a small $\frac{L}{S_g}$ ratio. The results from NCHRP Report 12-61 regarding the conservatism of the 2002 Standard shear provisions suggest that girders with a $\frac{\phi V_{n,2002Std}}{V_u}$ of at least 0.90 were likely not understrengh for shear. Girders in the parametric study with a $\frac{L}{S_g}$ ratio below approximately 8.5 (rounded up from 8.3) had a $\frac{\phi V_{n,2002Std}}{V_u}$ ratio below 0.90 and were potentially understrength for shear.

The calculations in the parametric study were based on nominal material properties, and ignored any inherent conservatism in the predicted capacity. Therefore, the results from the parametric study should be further evaluated to determine if any of these factors would be likely to improve the results, or increase confidence that girders with a $\frac{\phi V_{n,2002Std}}{V_u}$ value below 1.0 are safe.

Chapter 8
Summary and Conclusions

The results from NCHRP, Project 12-61 *Simplified Shear Design of Structural Concrete Members* show (see Table 2.1) that both the 2002 Standard and 2004 LRFD shear provisions provide reliable and conservative shear capacity predictions for prestressed concrete members. The 2002 Standard shear provisions, however, are recommended for predicting the capacity of existing members because they are significantly less cumbersome to use than the 2004 LRFD provisions. The 1979 Interim shear provisions are unreliable and, in the case of members with heavy shear reinforcement, unconservative because no limit is put on the maximum amount of shear reinforcement and there is no check for crushing of the concrete diagonals in the 1979 Interim.

The critical section for shear is defined in the 1979 Interim provisions as a quarter of the span length away from the support. The transverse steel requirements at this location apply from the quarter point to the support. The prescribed critical section in both the 2004 LRFD and 2002 Standard shear provisions is significantly closer to the support where the shear demand is greater, and as a result, these provisions require more stirrups near the support than the 1979 Interim provisions.

Two shear capacity tests were performed using the two ends from a bridge girder from Mn/DOT Bridge No. 73023 to investigate whether or not bridge girders designed using the 1979 Interim provisions meet capacity requirements. The stirrup layout in the girder removed from Mn/DOT Bridge No. 73023 suggested they were designed according to the 1979 Interim shear provisions, because the provided stirrups in the end region were significantly less than required by the 2004 LRFD and 2002 Standard provisions. Despite the apparent stirrup deficiency (relative to the 2004 LRFD and 2002 Standard provisions), the peak shear applied to both specimens was greater than the factored shear demand of the 2004 LRFD and 2002 Standard bridge design codes. Thus, the results from the capacity tests suggested the girder would have been capable of supporting the code required shear demand.

To expand on the experimental results, a parametric study of typical 1979 Interim era Mn/DOT bridge girders was performed to identify which, if any, girders in the Mn/DOT bridge inventory were likely understrength for shear. Several bridge girders from the inventory were selected and designed for shear using the 1979 Interim shear provisions. The capacity of these members, with the 1979 Interim required stirrup spacing, was then calculated using the 2002 Standard provisions and compared to the 2002 Standard shear demand.

The results of the parametric study showed that the girders in the study were most likely to be underdesigned for shear between $0.1L$ (L is the girder span length) and the support. In this region, the $\frac{\phi V_{n,2002Std}}{V_u}$ ratio for the girders varied between 0.73 and 1.09, and was proportional to $\frac{L}{S_g}$, where S_g is girder spacing. Girders with a $\frac{L}{S_g}$ of 10 or greater were not underdesigned for

shear, while girders with an $\frac{L}{S_g}$ of 8.5 or less had a $\frac{\phi V_{n,2002Std}}{V_u}$ of approximately 0.9 or less and were at risk of being understrength for shear.

These results assume that girders designed using the 1979 Interim shear provisions meet the stirrup requirements of the provisions. However, one unexpected result of the parametric study was that the provided stirrup spacing in seven of the twelve girders selected for the study did not meet the requirements of the 1979 Interim shear provisions at 0.25*L* (see Table 7.4). Likely explanations for this discrepancy in stirrup design include use of an incorrect strength capacity reduction factor (ϕ), a design shear demand reduced by the vertical component of the prestressing force (V_p), or an error in the computer code used to design the bridge girders. Regardless of the reason for the discrepancy, the implication is the results of the parametric study do not represent the lower bound of girders underdesigned for shear.

The results of the parametric study are applicable to bridge girders designed using the 1979 Interim shear provisions. To determine if bridge girders designed during the 1979 Interim era are underdesigned for shear, Mn/DOT should first evaluate the bridge girders to ensure they meet the stirrup requirements of the provisions. Bridge girders that do not meet the stirrup requirements are outside the scope of this research. However, bridge girders that meet the stirrup requirements of the 1979 Interim provisions and have a $\frac{L}{S_g}$ of 8.5 or less require further investigation to determine if the girders have additional shear strength not considered in the 2002 Standard shear provisions.

Mn/DOT has sponsored a companion research project titled: *Discrepancies in Shear Strength of Prestresssed Beam with Different Specifications* that includes a study of the effect of concrete arching action near the support and concrete strength gain with time on the shear capacity of existing bridge girders. The results of this companion study can be used to determine, with reasonable confidence, the reserve shear capacity of existing bridge girders. For girders with a $\frac{L}{S_g}$ of 8.5 or less, the expected reserve shear capacity can be accounted for when evaluating the shear strength to determine if any bridge girders in the Mn/DOT inventory require retrofit for shear.

References

ASCE-ACI Committee 426, "The Shear Strength of Reinforced Concrete Members." *Journal of the Structural Division*, ASCE, vol. 99, no. ST6, (June 1973): 1091-1187.

AASHTO, *Standard Specifications for Highway Bridges*, 17th edition, Washington, D.C., 2002.

AASHTO, *AASHTO LRFD Bridge Design Specifications*, 3rd edition, Washington, D.C., 2004.

AASHTO, *Interim Specifications: Standard Specifications for Highway Bridges*, Washington, D.C., 1979.

ASTM, "Standard Test Method for Compressive Strength of Cylindrical Concrete Specimens." *Annual Book of Standards*, vol. 04.02, no. C39/C39M-01, West Conshohocken, PA, 2001.

ASTM, "Standard Test Method for Obtaining and Testing Drilled Cores and Sawed Beams of Concrete." *Annual Book of Standards*, vol. 04.02, no. C42/C42M-99, West Conshohocken, PA, 1999.

ASTM, "Standard Test Method for Static Modulus of Elasticity and Poisson's Ratio of Concrete in Compression." *Annual Book of Standards*, vol. 04.02, no. C469-94, West Conshohocken, PA, 1994.

Bentz, E.C., and Collins, M.P. (Internet), "AASHTO Non-Iterative Spreadsheet." 2000a (cited April 2006), http://www.ecf.utoronto.ca/~bentz.

Bentz, E.C., and Collins, M.P. (Internet), "Response 2000." 2000b (cited April 2006), http://www.ecf.utoronto.ca/~bentz/r2k.htm.

Collins, M.P., Mitchell, D., Adebar, P., and Vecchio, F.J., "A General Shear Design Method." *ACI Structural Journal*, vol. 93, no. 1, (January-February 1996): 36-45.

Collins, M.P., and Mitchell, D., *Prestressed Concrete Structures*, Prentice-Hall Inc., Englewood Cliffs, New Jersey, 1991.

Hawkins, N.M., Kuchma, D.A., Mast, R. F., Marsh, M.L., and Reineck, K.H., "NCHRP Report 549; Simplified Shear Design of Structural Concrete Members." *Transportation Research Board*, 2005.

MacGregor, J.G., *Reinforced Concrete Mechanics and Design*, Prentice-Hall Inc., Englewood Cliffs, New Jersey, 1997.

PCI, *Precast Prestressed Concrete Bridge Design Manual*, 2nd edition, Chicago, IL, 2003.

Vecchio, F.J., and Collins, M.P., "The Modified Compression-Field Theory for Reinforced Concrete Elements Subjected to Shear." *ACI Structural Journal*, vol. 83, no. 22, (March-April 1986): 213-231.

Walraven, J.C., "Fundamental Analysis of Aggregate Interlock." *Proceedings*, ASCE, vol. 107, no. ST11, (November 1981): 2234-2270.

Tables

Table 2.1 Comparison of Test to Predicted Shear Capacities (Hawkins et al., 2005)

	2002 Standard $\frac{V_{test}}{V_{pred}}$	2004 LRFD $\frac{V_{test}}{V_{pred}}$	1979 Interim $\frac{V_{test}}{V_{pred}}$
Number of Beams	85	85	85
Mean	1.318	1.243	1.09
STDEV	0.206	0.174	0.417
COV	0.156	0.14	0.383
Probability of $\frac{V_{test}}{V_{pred}} < 1$	6.2%	8.1%	41.3%

Table 3.1 Predicted Ultimate Shear Capacity (V_n)

	2004 LRFD* (kips)	2002 Standard* (kips)	1979 Interim* (kips)	Strut and Tie (kips)
With Deck	240 (at midspan)	276 (near support)	166 (near support)	223
Without Deck	191 (at midspan)	236 (at midspan)	136 (near support)	203

*These values were from the cross-section with the lowest calculated shear capacity in Figure 3.6, Figure 3.7, and Figure 3.10.

Table 3.2 Load and Strength Capacity Reduction Factors

	Dead Load Factor	Live Load Factor	Strength Capacity Reduction Factor ϕ
2004 LRFD	1.25*/1.50**	1.75	0.9
2002 Standard	1.3	1.3(1.67) = 2.17	0.9
1979 Interim	1.3	1.3(1.67) = 2.17	0.9

*Applies to components and attachments

**Applies to wearing surfaces and utilities

Table 3.3 Stirrup Spacing

	Required Stirrup Spacing			Provided Spacing (in)
Distance from the support (ft)	2004 LRFD (in)	2002 Standard (in)	1979 Interim (in)	
0-9	11 (9)	13	20*	21
9-17	13 (10)	24	20*	21
17-26	22 (16)	24	20*	21
26-35	24	23	30 (21)	21
35-44	24	24	30 (21)	21

Note: numbers in parentheses were the stirrup spacing required for horizontal shear
*This was the stirrup spacing required at the critical section, according to the 1979 Interim, which was located 22 ft. from the support.

Table 4.1 Types of Instrumentation

Instrumentation	**Manufacturer**	**Model**	**Description**
LVDTs	Schaevitz	1000 HR 2000 HR 5000 HR	Travel, ± 1.0 in Travel, ± 2.0 in Travel, ± 5.0 in
Rosette Strain Gages	TML	Texas Measurements FRA-6-11-5LT	Gage length, 6 mm
Horizontal Strain Gages	TML	Texas Measurements PL-60-11-5LT	Gage length, 60 mm
Dynamic Coordinate Measurement Machine	Krypton	K600 system	System includes LEDs, CCD cameras, and controller

Table 4.2 Coordinates of the Surface Mounted Strain Gages

Horizontal Gage	x (in.)	y (in.)	Rosette Gage	x (in.)	y (in.)
*L1	42	58.5	R1	65	33.5
L2	42	50	R2	75	33.5
L3	42	39	R3	85	33.5
L4	42	28.5	R4	95	33.5
L5	42	18	R5	105	33.5
L6	42	4	R6	115	33.5
L7	65.4	0	R7	125	33.5
L8	61	0	R8	135	28.5
L9	56.7	0	R9	135	23.5
L10	52.3	0	R10	145	33.5
L11	48	0	R11	145	28.5
L12	43.6	0	R12	145	23.5
L13	39.2	0	R13	155	33.5
L14	34.9	0	R14	155	28.5
L15	30.5	0	R15	155	23.5
L16	26.1	0	R16	160	23.5
L17	21.8	0			
L18	17.4	0			
L19	13.1	0			
L20	8.7	0			
L21	4.4	0			
L22	0	0			
L23	-4.4	0			

*L1 was not installed on the specimen with no bridge deck.
x = distance from centerline of applied load (positive toward the roller support)
y = distance from bottom of specimen

Table 4.3 Coordinates of the Krypton LEDs

LED	x (in.)	y (in.)	LED	x (in.)	y (in.)
*1	0	39	28	90	39
*2	0	28.5	29	90	28.5
*3	0	18	30	90	18
*4	10	39	31	100	39
*5	10	28.5	32	100	28.5
*6	10	18	33	100	18
*7	20	39	*34	110	39
*8	20	28.5	*35	110	28.5
*9	20	18	*36	110	18
10	30	39	*37	120	39
11	30	28.5	*38	120	28.5
12	30	18	*39	120	18
13	40	39	*40	130	39
14	40	28.5	*41	130	28.5
15	40	18	*42	130	18
16	50	39	*43	140	39
17	50	28.5	*44	140	28.5
18	50	18	*45	140	18
19	60	39	*46	150	39
20	60	28.5	*47	150	28.5
21	60	18	*48	150	18
22	70	39	*49	160	39
23	70	28.5	*50	160	28.5
24	70	18	*51	160	18
25	80	39	*52	170	39
26	80	28.5	*53	170	28.5
27	80	18	*54	170	18

*These LEDS were not used on Specimen II.
x = distance from centerline of applied load (positive toward the roller support)
y = distance from bottom of specimen

Table 4.4 Coordinates of the DEMEC Points

DEMEC Point	x (in.)	y (in.)	DEMEC Point	x (in.)	y (in.)
1	0	4	13	96	4
2	8	4	14	104	4
3	16	4	15	112	4
4	24	4	16	120	4
5	32	4	17	128	4
6	40	4	18	136	4
7	48	4	19	144	4
8	56	4	20	152	4
9	64	4	21	160	4
10	72	4	22	168	4
11	80	4	23	176	4
12	88	4			

x = distance from centerline of applied load (positive toward the roller support)
y = distance from bottom of specimen

Table 5.1 Nominal and Measured Material Properties

Material Property	Nominal Value	Measured Value	Percent Change
Girder concrete compressive strength f_c'	6,000 psi	10,130 psi	68.8%
Bridge deck concrete compressive strength $f_{c\,d}'$	4,000 psi	5,690 psi	42.3%
Girder concrete modulus of elasticity E_c	*4,415 ksi	5,050 ksi	14.4%
Stirrup yield strength f_{sy}	60 ksi	67.3 ksi	12.2%
2004 LRFD Effective Prestressing f_{pe}	137.5 ksi	125.3 ksi	-8.9%
2002 Standard Effective Prestressing f_{pe}	139.1 ksi	125.3 ksi	-9.9%

* Based on $57{,}000\sqrt{f_c'}$

Table 5.2 Effect of the Measured f'_c on the Predicted Shear Capacity

		V_{pred} (kips) All nominal properties	V_{pred} (kips) Measured f_c'*	Percent Change
Specimen I (with bridge deck)	2004 LRFD	237	255	7.6%
	2002 Standard	288	325	12.8%
	1979 Interim	178	178	0%
	Strut and Tie	223	262	17.4%
Specimen II (no bridge deck)	2004 LRFD	190	203	6.8%
	2002 Standard	234	247	5.6%
	1979 Interim	146	146	0%
	Strut and Tie	203	228	12.3%

Note: Capacities from the cross-section under the applied load
*$f_c'_d$ used for the bridge deck

Table 5.3 Effect of the Measured f_c' on the 2004 LRFD Parameters

	All nominal properties			Nominal properties with measured f_c'*		
	d_v (in)	θ (degrees)	β	d_v (in)	θ (degrees)	β
Specimen I (with deck)	47.68	23.4	3.12	48.31	25.4	3.09
Specimen II (no deck)	39.22	24.5	3.04	39.22	26.6	2.94

Note: From the cross-section under the applied load
*$f_c'_d$ used for the bridge deck

Table 5.4 Effect of the Measured f_c' on the 2002 Standard Parameters

Specimen I (with bridge deck)	$3.5\sqrt{f_c'}$ (psi)	$0.3f_{pc}$* (psi)	V_{cw} (kips)
All nominal Properties	271	231	228
Nominal properties, with measured f_c'**	352	237	266

*f_c' affects the depth of the neutral axis, which affects f_{pc}
**f_{cd}' used for the bridge deck

Specimen II (no bridge deck)	$6\sqrt{f_c'}$ (psi)	f_{pe} (psi)	M_{cr} (kip-ft)	$0.6\sqrt{f_c'}bd$ (kips)	V_d (kips)	$\frac{V_i M_{cr}}{M_{max}}$ (kips)	V_{ci} (kips)
All nominal properties	465	2,403	2,323	16.2	7.4	160.2	184
Nominal Properties, with measured f_c'	604	2,403	2,445	21.1	7.4	168.6	197

Note: Parameters From the Cross-section Under the Applied Load

Table 5.5 Effect of the Measured E_c on the Predicted Shear Capacity

		V_{pred} (kips) All nominal properties	V_{pred} (kips) Measured E_c	Percent Change
Specimen I (with bridge deck)	2004 LRFD	237	237	0%
	2002 Standard	288	293	1.7%
	1979 Interim	178	178	0%
	Strut and Tie	223	223	0%
Specimen II (no bridge deck)	2004 LRFD	190	190	0%
	2002 Standard	234	234	0%
	1979 Interim	146	146	0%
	Strut and Tie	203	203	0%

Note: Capacities from the cross-section under the applied load

Table 5.6 Effect of the Measured f_{sy} on the Predicted Shear Capacity

		V_{pred} (kips) All nominal properties	V_{pred} (kips) Measured f_{sy}	Percent Change
Specimen I (with bridge deck)	2004 LRFD	237	243	2.5%
	2002 Standard	288	296	2.8%
	1979 Interim	178	189	6.2%
	Strut and Tie	223	244	9.4%
Specimen II (no bridge deck)	2004 LRFD	190	194	2.1%
	2002 Standard	234	240	2.6%
	1979 Interim	146	157	7.5%
	Strut and Tie	203	223	9.9%

Note: Capacities from the cross-section under the applied load

Table 5.7 Effect of the Measured f_{sy} on the 2004 LRFD Parameters

	All nominal Properties		Nominal properties, with measured f_{sy}	
	θ (degrees)	β	θ (degrees)	β
Specimen I (with bridge deck)	23.4	3.12	24.3	2.99
Specimen II (no bridge deck)	24.5	3.04	25.5	2.92

Note: From the cross-section under the applied load

Table 5.8 Effect of the Measured f_{pe} on the Predicted Shear Capacity

		V_{pred} (kips) All nominal properties	V_{pred} (kips) Measured f_{pe}	Percent Change
Specimen I (with bridge deck)	2004 LRFD	237	235	-0.8%
	2002 Standard	288	278	-3.6%
	1979 Interim	178	178	0%
	Strut and Tie	223	222	-0.5%
Specimen II (no bridge deck)	2004 LRFD	190	188	-1.1%
	2002 Standard	234	219	-6.8%
	1979 Interim	146	146	0%
	Strut and Tie	203	201	-1.0%

Note: Capacities from the cross-section under the applied load

Table 5.9 Combined Effect of all the Measured Material Properties on the Predicted Shear Capacity

		V_{pred} (kips) All nominal properties	V_{pred} (kips) All measured properties	Percent Change
Specimen I (with bridge deck)	2004 LRFD	237	259	9.3%
	2002 Standard	288	316	9.7%
	1979 Interim	178	189	6.2%
	Strut and Tie	223	281	26%
Specimen II (no bridge deck)	2004 LRFD	190	204	7.4%
	2002 Standard	234	238	1.7%
	1979 Interim	146	157	7.5%
	Strut and Tie	203	246	21.2%
			Average	11.2%

Note: Capacities from the cross-section under the applied load

Table 6.1 Shear Test Results

(From the cross-section under the applied load)

		V_{pred} (kips) (Measured material properties)	V_{test} (kips) (Including dead load)	$\frac{V_{test}}{V_{pred}}$
Specimen I (with bridge deck)	2004 LRFD	259	392	1.51
	2002 Standard	316		1.24
	1979 Interim	189		2.07
	Strut and Tie	281		1.40
Specimen II (no bridge deck)	2004 LRFD	204	329	1.61
	2002 Standard	238		1.38
	1979 Interim	157		2.09
	Strut and Tie	246		1.34

Table 6.2 2004 LRFD θ and β for Sections with Transverse Reinforcement

$\frac{v_u}{f_c'}$	ε_x * 1000								
	≤-0.20	≤-0.10	≤-0.05	≤0	≤0.125	≤0.25	≤0.50	≤0.75	≤1.00
≤0.075	22.5 6.32	20.4 4.75	21.0 4.10	21.8 3.75	24.3 3.24	26.6 2.94	30.5 2.59	33.7 2.38	36.4 2.23
≤0.100	18.1 3.79	20.4 3.38	21.4 3.24	22.5 3.14	24.9 2.91	27.1 2.75	30.8 2.50	34.0 2.32	36.7 2.18
≤0.125	19.9 3.18	21.9 2.99	22.8 2.94	23.7 2.87	25.9 2.74	27.9 2.62	31.4 2.42	34.4 2.26	37.0 2.13
≤0.150	21.6 2.88	23.3 2.79	24.2 2.78	25.0 2.72	26.9 2.60	28.8 2.52	32.1 2.36	34.9 2.21	37.3 2.08
≤0.175	23.2 2.73	24.7 2.66	25.5 2.65	26.2 2.60	28.0 2.52	29.7 2.44	32.7 2.28	35.2 2.14	36.8 1.96
≤0.200	24.7 2.63	26.1 2.59	26.7 2.52	27.4 2.51	29.0 2.43	30.6 2.37	32.8 2.14	34.5 1.94	36.1 1.79
≤0.225	26.1 2.53	27.3 2.45	27.9 2.42	28.5 2.40	30.0 2.34	30.8 2.14	32.3 1.86	34.0 1.73	35.7 1.64
≤0.250	27.5 2.39	28.6 2.39	29.1 2.33	29.7 2.33	30.6 2.12	31.3 1.93	32.8 1.70	34.3 1.58	35.8 1.5

Table 6.3 Longitudinal Strain for Various Gage Lengths for the Cross-section 60 in. from the Applied Load

	Longitudinal Strain		
	20 in. Gage Length (με)	40 in. Gage Length (με)	60 in. Gage Length (με)
Top Krypton LED	-336	408	363
Middle Krypton LED	765	596	361
Bottom Krypton LED	672	185	501
DEMEC points	1,245	1,299	1,336

Table 6.4 Modified Predicted Shear Capacity

	2002 Standard V_c (kips) (Measured material properties)	2004 LRFD V_s (kips) (Measured material properties)	Modified V_{pred}*	V_{test} (kips) (Including dead load)	$\frac{V_{test}}{V_{pred}}$
Specimen I	243	126	369	392	1.06
Specimen II	183	98	281	329	1.17

*V_c of 2002 Standard and V_s of 2004 LRFD

Table 7.1 Range of Girder Parameters

Parameter	**Range**
Depth	36 in. - 54 in.
Span Length	40 ft - 100 ft
Girder f_c'	5 ksi - 6 ksi
Girder spacing	7 ft - 14 ft

Table 7.2 Girder Information from Selected Mn/DOT Bridges

Girder from: Mn/DOT Bridge No.	Year Built	Depth (in)	Span Length (ft)	Girder f_c' (ksi)	Girder Spacing (ft)	Number of Strands*	Grade of Strands** (ksi)	Strand Diameter (in)
27068a	1981	36	43	5	10.8	18(6)	270(Lowlax)	0.5
27068b	1981	36	57	5	7.2	20(4)	270(Lowlax)	0.5
83030	1975	36	54	6	9.5	26(8)	270(SR)	0.5
48010	1978	45	43	5	12.5	16(4)	270(SR)	0.5
83022	1975	45	57	5	10.8	24(6)	270(SR)	0.5
49016	1974	45	76	5.1	7.7	32(8)	270(SR)	0.5
31019	1976	45	59	6	13.1	34(8)	270(SR)	0.5
46004	1981	45	76	6	8.9	38(8)	270(SR)	0.5
73872a	1976	54	58	5	14.7	29(9)	270(SR)	0.5
73872b	1976	54	79	5	11	44(12)	270(SR)	0.5
25013	1982	54	77	5.9	13.5	48(12)	270(SR)	0.5
61001	1981	54	95	6	7.3	43(9)	270(SR)	0.5

*Number in parenthesis was the number of draped strands

**Lowlax = low relaxation strands; SR = stress relieved strands

Table 7.3 Parameter Distribution of Selected Mn/DOT Bridges

Girder from: Mn/DOT Bridge No.	Depth (in)	Span Length (40 ft)	Span Length (60ft)	Span Length (80 ft)	Span Length (100 ft)	Girder f_c' (5 ksi)	Girder f_c' (6 ksi)	Girder Spacing (8 ft)	Girder Spacing (10 ft)	Girder Spacing (>12 ft)
27068a	36	43				5			10.8	
27068b	36		57			5		7.2		
83030	36		54				6		9.5	
48010	45	43				5				12.5
83022	45		57			5			10.8	
49016	45			76		5.1		7.7		
31019	45		59				6			13.1
46004	45			76			6	8.9		
73872a	54		58			5				14.7
73872b	54			79		5			11	
25013	54			77			5.9			13.5
61001	54				95		6	7.3		

Table 7.4 Required Stirrup Spacing; 1979 Interim Shear Provisions

Girder from: Mn/DOT Bridge No.	Spacing from 0.25*L* to the support* (in)	Spacing at 0.3L* (in)	Spacing at 0.4L* (in)	Spacing at 0.5L* (in)
27068a	17(21)	20(21)	21(21)	21(38)
27068b	21(21)	21(21)	21(21)	21(31)
83030	17(12)	20(18)	21(18)	21(18)
48010	20(21)	21(21)	21(21)	21(21)
83022	20(18)	21(18)	21(22)	21(22)
49016	21(21)	21(21)	21(21)	21(21)
31019	14(15)	17(21)	21(33)	21(33)
46004	20(15)	21(15)	21(18)	21(18)
73872a	16(18)	20(18)	21(18)	21(18)
73872b	19(21)	21(21)	21(21)	21(21)
25013	14(17)	18(22)	21(22)	21(22)
61001	21(22)	21(22)	21(22)	21(22)

L = span length; stirrups were double-leg, #4, Grade 60

*Number in parenthesis was the spacing shown on the bridge construction drawings

Table 7.5 $\frac{\phi V_{n,2002Std}}{V_u}$ at the Critical Section and Tenth Points of the Span Length

	$\frac{\phi V_{n,2002Std}}{V_u}$					
Girder from: Mn/DOT Bridge No.	Critical Section	0.1*L*	0.2*L*	0.3*L*	0.4*L*	0.5*L*
27068a	***0.84***	***0.94***	1.16	1.05	1.16	1.38
27068b	***0.89***	1.09	1.28	1.20	1.29	1.63
83030	***0.91***	1.07	1.11	***0.98***	1.03	1.26
48010	***0.73***	***0.82***	1.09	1.08	1.18	1.41
83022	***0.78***	***0.92***	1.20	1.05	1.11	1.41
49016	***0.96***	1.18	1.18	1.10	1.20	1.63
31019	***0.79***	***0.94***	1.15	1.00	***0.96***	1.16
46004	***0.90***	1.15	1.18	1.05	1.10	1.47
73872a	***0.81***	***0.91***	1.15	1.02	1.07	1.29
73872b	***0.93***	1.11	1.21	1.09	1.14	1.40
25013	***0.88***	1.04	1.16	1.00	***0.97***	1.19
61001	1.09	1.25	1.29	1.20	1.31	2.09

V_u = dead load plus HS20-44 live load.

Table 7.6 $\frac{\phi V_{n,2002Std}}{V_u}$ at the Critical Section Compared to Girder Parameters

Girder from: Mn/DOT Bridge No.	$\frac{\phi V_{n,2002Std}}{V_u}$ Critical Section	Depth (in)	Span Length (40 ft)	Span Length (60ft)	Span Length (80 ft)	Span Length (100 ft)	Girder f_c' (5 ksi)	Girder f_c' (6 ksi)	Girder Spacing (8 ft)	Girder Spacing (10 ft)	Girder Spacing (>12 ft)
27068a	0.84	36	43				5			10.8	
27068b	0.89	36		57			5		7.2		
83030	0.91	36		54				6		9.5	
48010	0.73*	45	43				5				12.5
83022	0.78*	45		57			5			10.8	
49016	0.96	45			76		5.1		7.7		
31019	0.79*	45		59				6			13.1
46004	0.90	45			76			6	8.9		
73872a	0.81	54		58			5				14.7
73872b	0.93	54			79		5			11	
25013	0.88	54			77			5.9			13.5
61001	1.09	54				95		6	7.3		

* Girders with the lowest $\frac{\phi V_{n,2002Std}}{V_u}$

Table 7.7 $\frac{V_s}{V_{n,2002Std}}$ at the Critical Section

Girder from: Mn/DOT Bridge No.	Depth	$\frac{\phi V_{n,2002Std}}{V_u}$	Stirrup Spacing	$\frac{V_s}{V_{n,2002Std}}$ (%)
27068a	36	0.84	17	29
27068b	36	0.89	21	28
83030	36	0.91	17	28
48010	45	0.73	20	29
83022	45	0.78	20	27
49016	45	0.96	21	24
31019	45	0.79	14	31
46004	45	0.90	20	24
73872a	54	0.81	16	28
73872b	54	0.93	19	23
25013	54	0.88	14	27
61001	54	1.09	21	21

Table 7.8 2002 Standard Equation Controlling V_c at each Section of Interest

	$\frac{\phi V_{n,2002Std}}{V_u}$					
Girder from: Mn/DOT Bridge No.	Critical Section	0.1*L*	0.2*L*	0.3*L*	0.4*L*	0.5*L*
27068a	V_{cw} (0.84)	V_{cw} (0.94)	V_{ci} (1.16)	V_{ci} (1.05)	V_{ci} (1.16)	V_{ci} (1.38)
27068b	V_{cw} (0.89)	V_{cw} (1.09)	V_{ci} (1.28)	V_{ci} (1.20)	V_{ci} (1.29)	V_{ci} (1.63)
83030	V_{cw} (0.91)	V_{cw} (1.07)	V_{ci} (1.14)	V_{ci} (0.98)	V_{ci} (1.03)	V_{ci} (1.26)
48010	V_{cw} (0.73)	V_{cw} (0.82)	V_{cw} (1.09)	V_{ci} (1.08)	V_{ci} (1.18)	V_{ci} (1.41)
83022	V_{cw} (0.78)	V_{cw} (0.92)	V_{ci} (1.20)	V_{ci} (1.05)	V_{ci} (1.11)	V_{ci} (1.41)
49016	V_{cw} (0.96)	V_{cw} (1.18)	V_{ci} (1.18)	V_{ci} (1.10)	V_{ci} (1.20)	V_{ci} (1.63)
31019	V_{cw} (0.79)	V_{cw} (0.94)	V_{ci} (1.15)	V_{ci} (1.00)	V_{ci} (0.96)	V_{ci} (1.16)
46004	V_{cw} (0.90)	V_{cw} (1.15)	V_{ci} (1.18)	V_{ci} (1.05)	V_{ci} (1.10)	V_{ci} (1.47)
73872a	V_{cw} (0.81)	V_{cw} (0.91)	V_{ci} (1.15)	V_{ci} (1.02)	V_{ci} (1.07)	V_{ci} (1.29)
73872b	V_{cw} (0.93)	V_{cw} (1.11)	V_{ci} (1.21)	V_{ci} (1.09)	V_{ci} (1.14)	V_{ci} (1.40)
25013	V_{cw} (0.88)	V_{cw} (1.04)	V_{ci} (1.16)	V_{ci} (1.00)	V_{ci} (0.97)	V_{ci} (1.19)
61001	V_{cw} (1.09)	V_{ci} (1.25)	V_{ci} (1.29)	V_{ci} (1.20)	V_{ci} (1.31)	V_{ci} (2.09)

Table 7.9 Evaluation of Eqn (7.3) at the Critical Section

Girder from: Mn/DOT Bridge No.	Radius of Gyration, r (in)	$\frac{y_{tc} - y_t}{r}$ *	$\frac{e}{r}$	$\frac{e(y_{tc} - y_t)}{r^2}$
27068a	11.75	0.95	0.37	0.35
27068b	***11.75***	***0.95***	***0.62***	***0.59***
83030	11.75	0.95	0.41	0.39
48010	14.96	0.88	0.63	0.55
83022	14.96	0.88	0.64	0.56
49016	14.96	0.88	0.57	0.51
31019	14.96	0.88	0.60	0.53
46004	14.96	0.88	0.61	0.54
73872a	18.18	0.84	0.50	0.42
73872b	18.18	0.84	0.52	0.43
25013	18.18	0.84	0.54	0.46
61001	18.18	0.83	0.62	0.51

* This term was evaluated at the web/flange intersection for all but one of the specimens

Figures

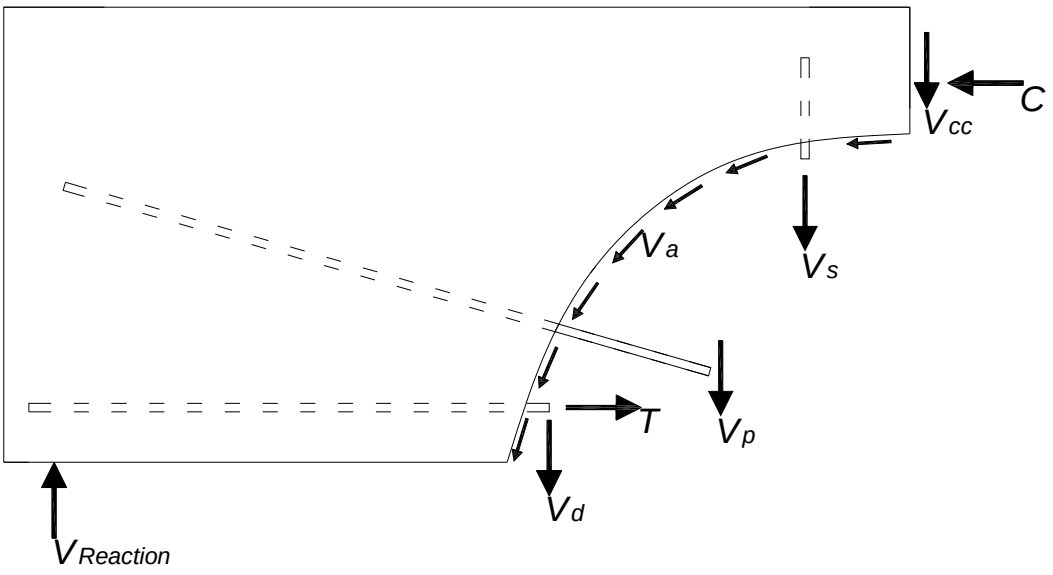

Va: Interface Shear Transfer (Aggregate Interlock)
Vcc: Shear Transfer in Compression Zone
Vd: Dowel Action
Vs: Stirrup Contribution
Vp: Vertical Component of the Prestressing Force

Figure 2.1 Shear Transfer Mechanisms in Cracked Prestressed Concrete Beam

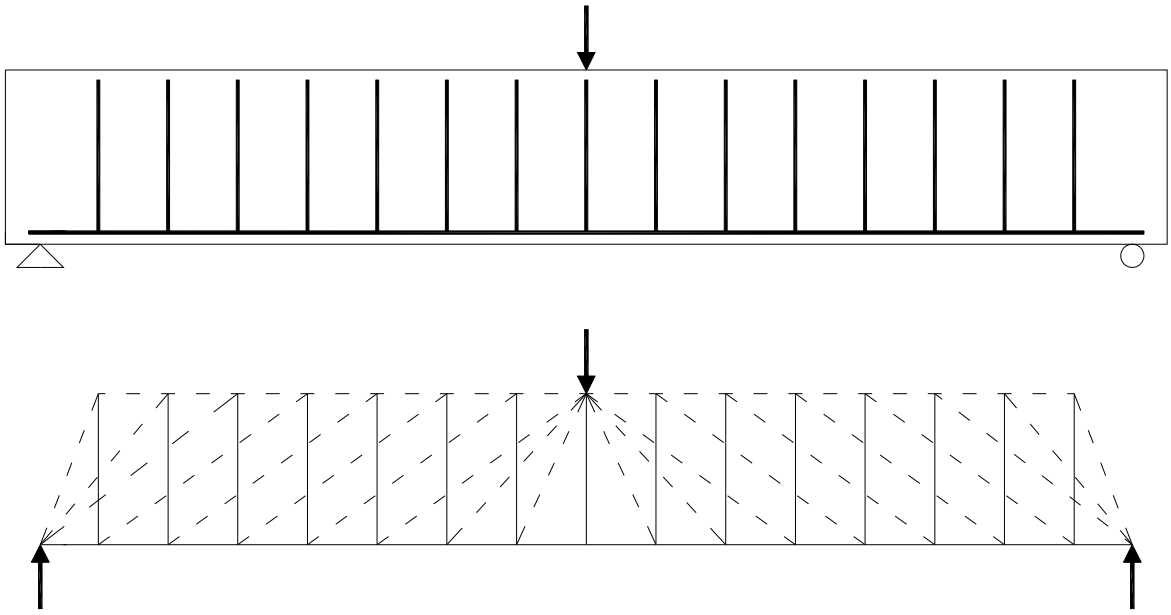

Note: Dashed lines are struts, solid lines are ties

Figure 2.2 Example of a Truss Model

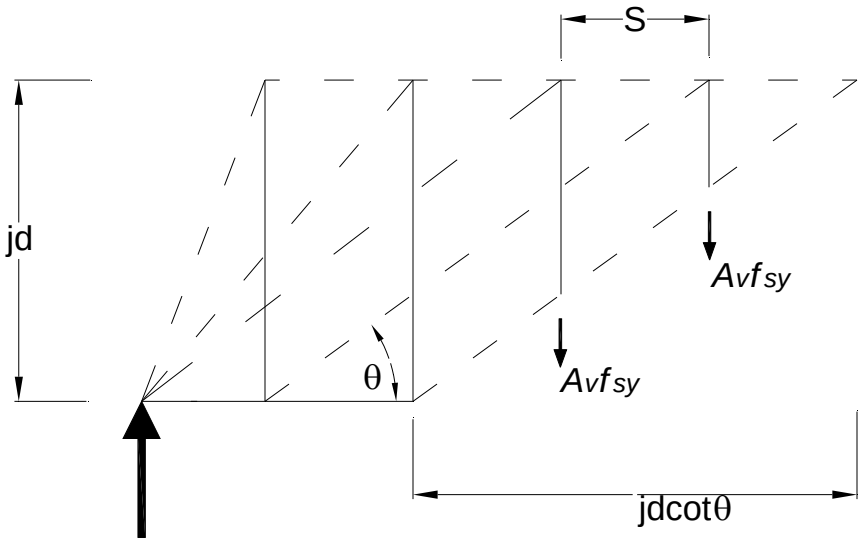

Figure 2.3 Stirrup Contribution to Shear Capacity

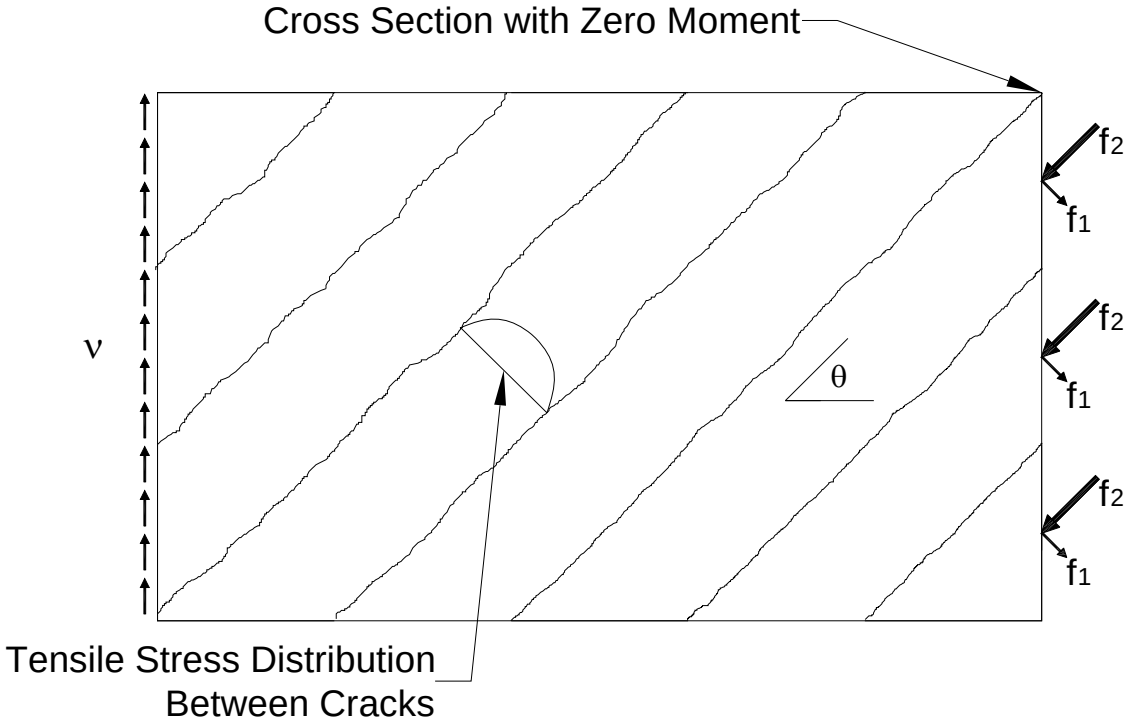

Figure 2.4 Principal Stresses in Cracked Concrete

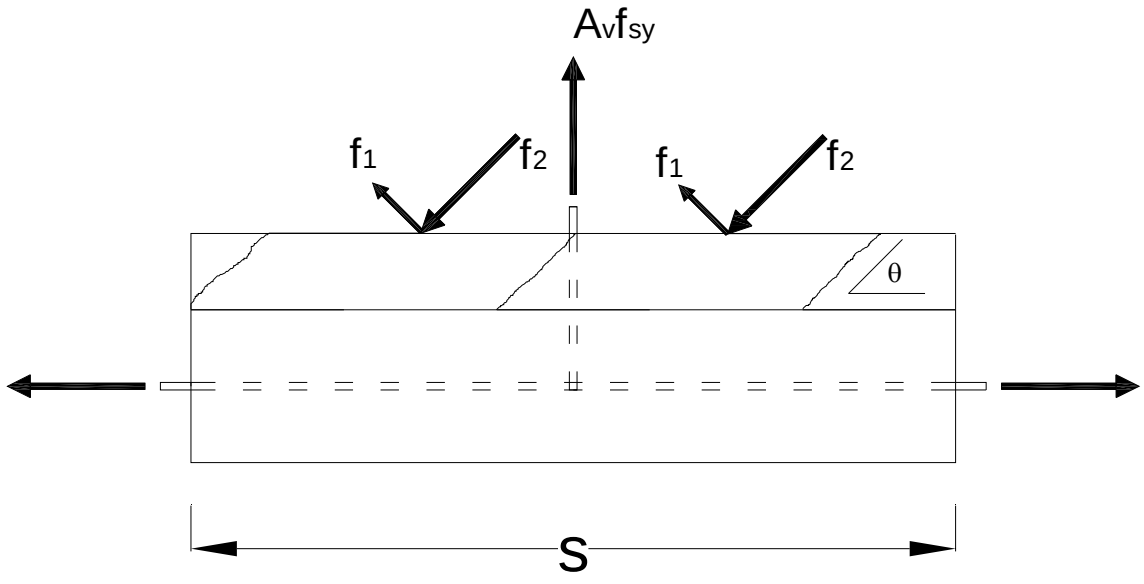

Figure 2.5 Stirrup Contribution (MCFT)

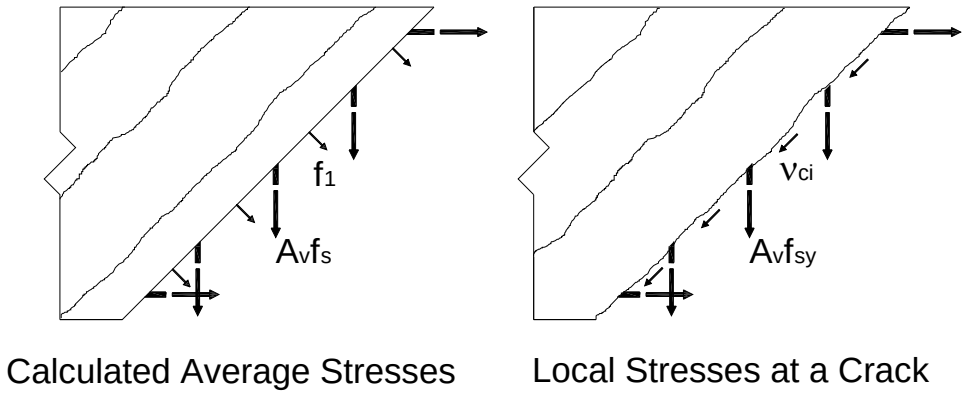

Figure 2.6 Tensile Stresses in Cracked Concrete

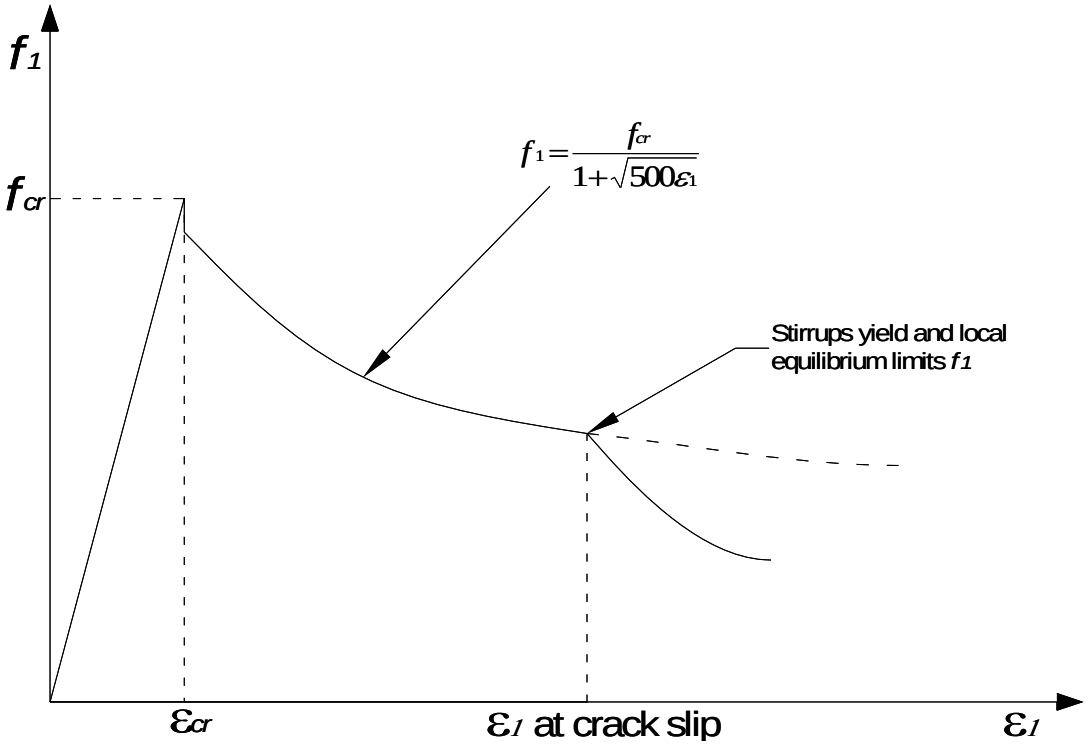

Figure 2.7 Average Tensile Stresses in Cracked Concrete as a Function of ε_1 (Collins et al., 1996)

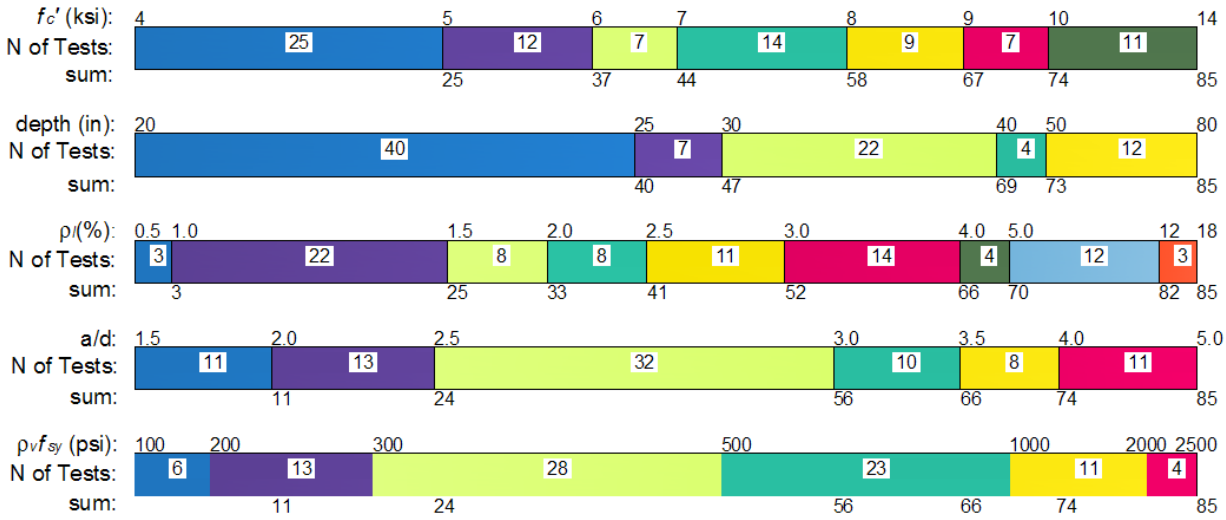

Figure 2.8 Distribution of Member Parameters in the Select Database (Hawkins et al., 2005)

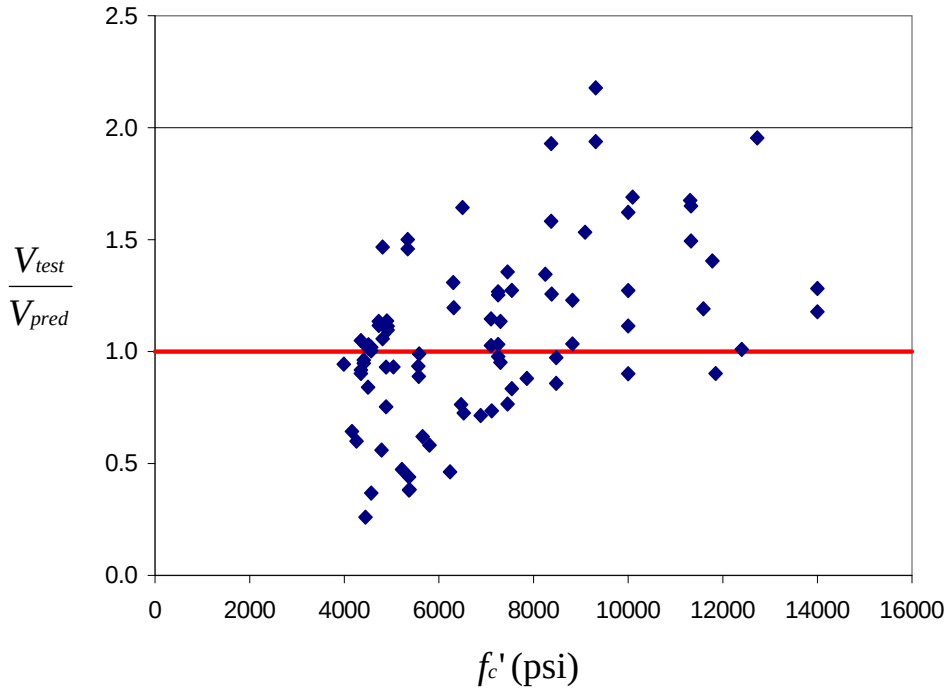

Figure 2.9 1979 Interim V_{test}/V_{pred} vs. f_c' for 85 Prestressed Members (Hawkins et al., 2005)

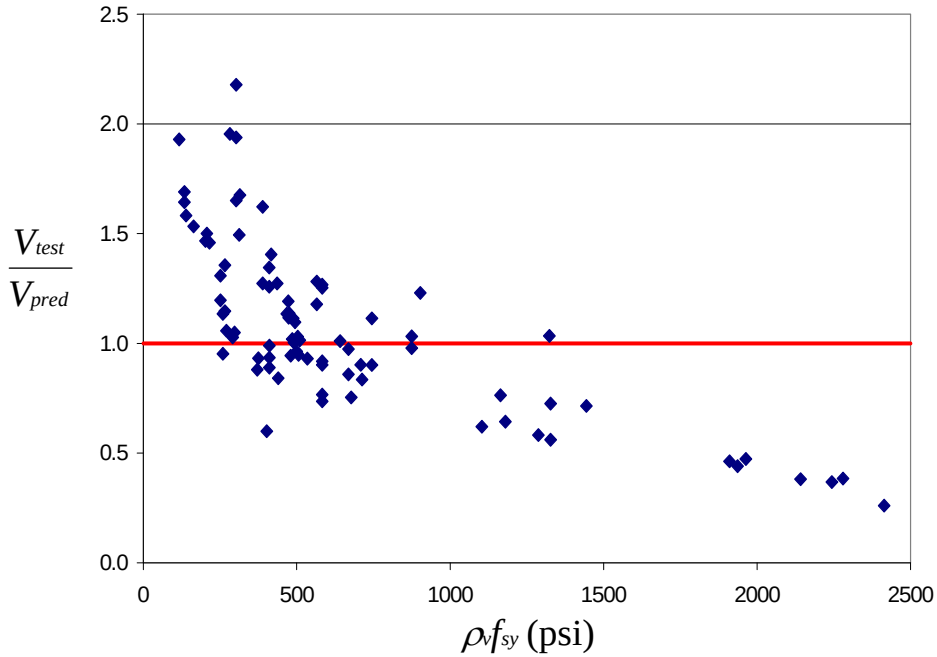

Figure 2.10 1979 Interim V_{test}/V_{pred} vs. Stirrup Reinforcement Ratio for 85 Prestressed Members (Hawkins et al., 2005)

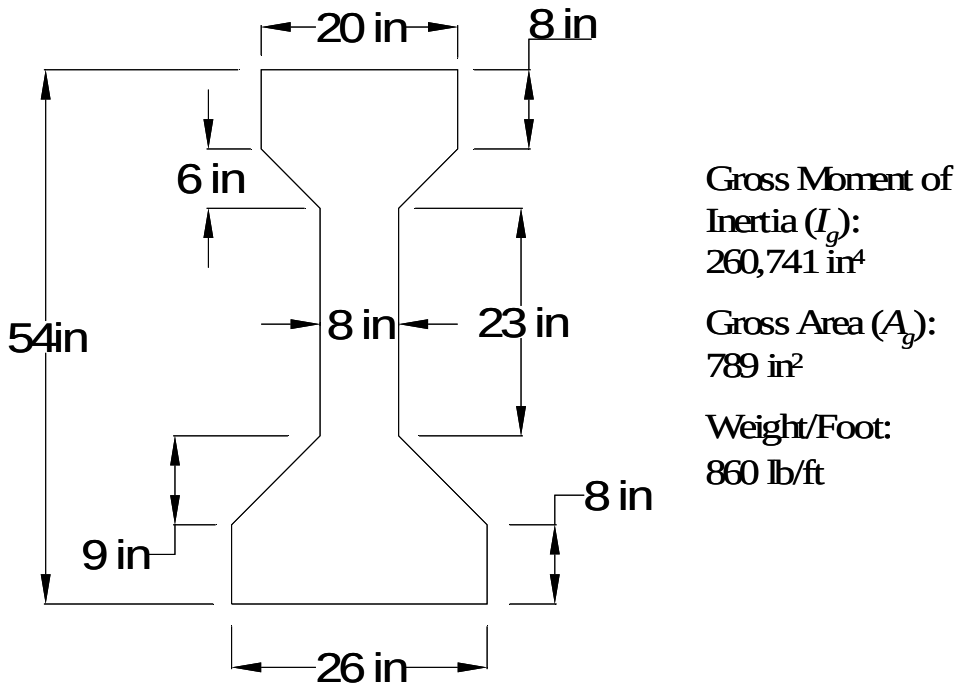

Figure 3.1 Dimensions of Mn/DOT Type 54 Girder

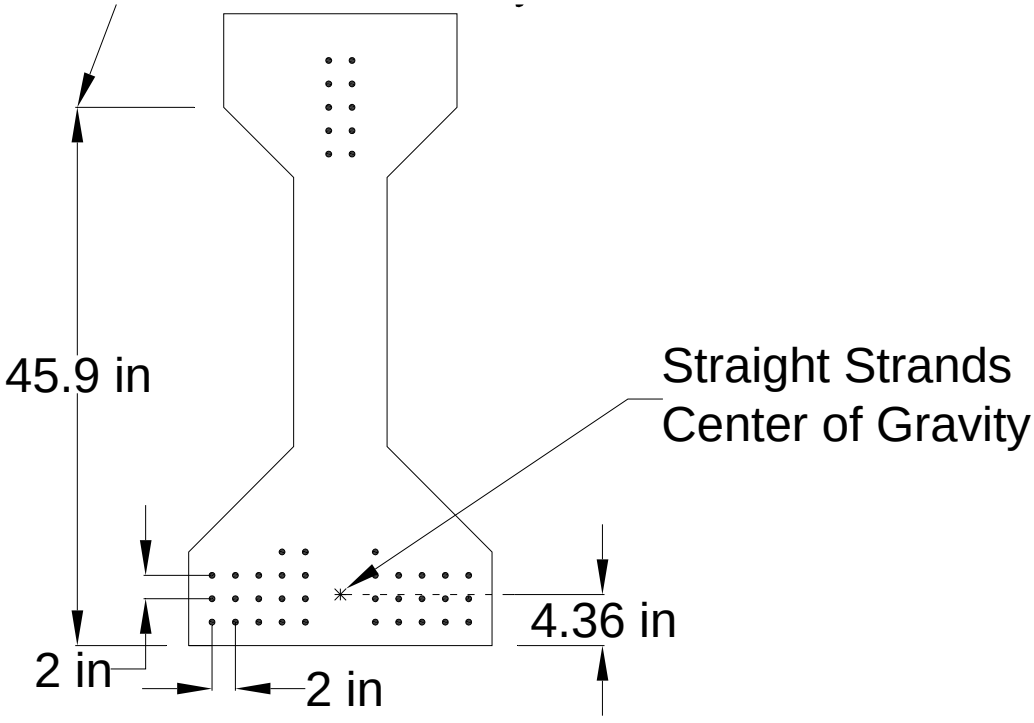

Figure 3.2 Prestressing Strand Pattern at Girder End

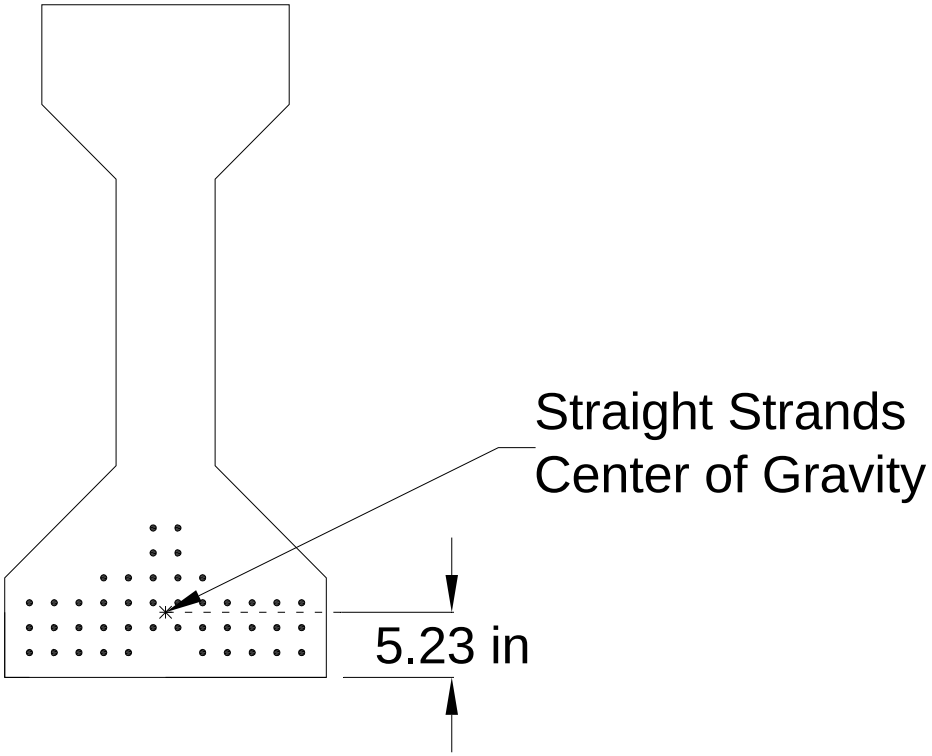

Figure 3.3 Prestressing Strand Pattern at Harp Point

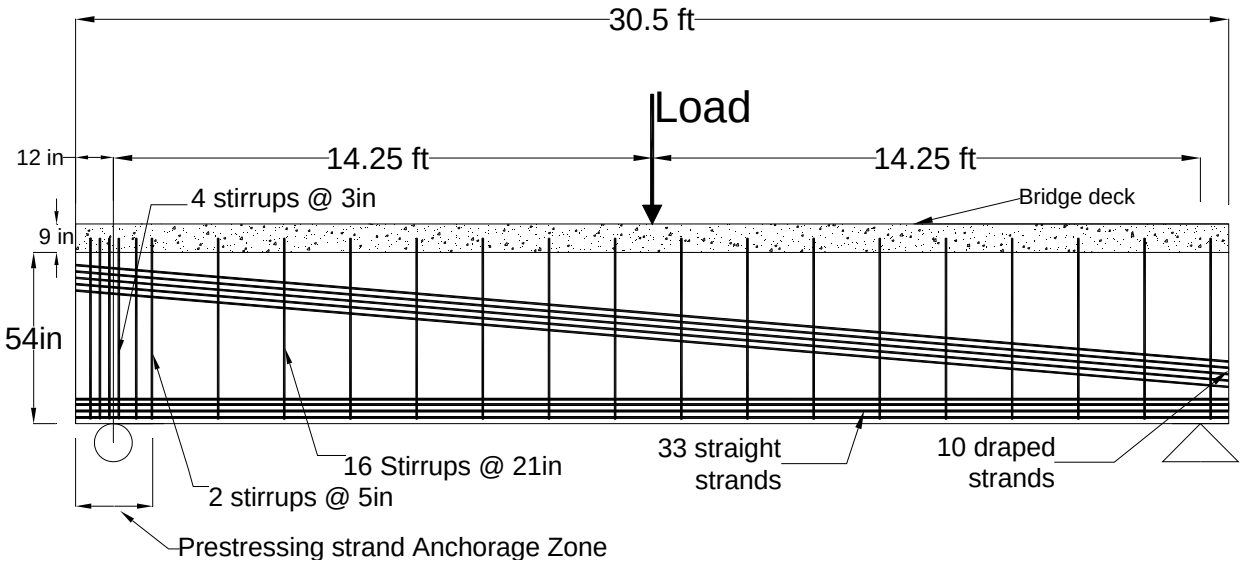

Figure 3.4 Assumed Loading Position for Capacity Calculations

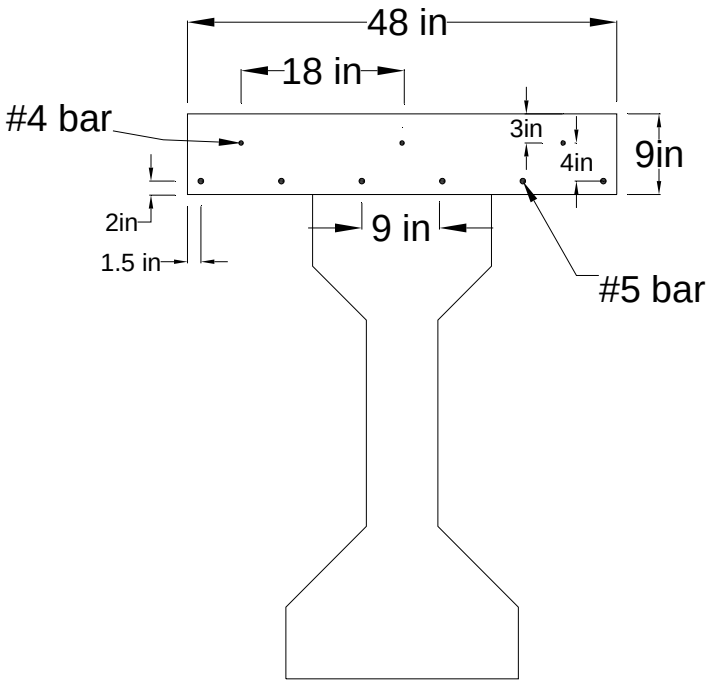

Figure 3.5 Bridge Deck

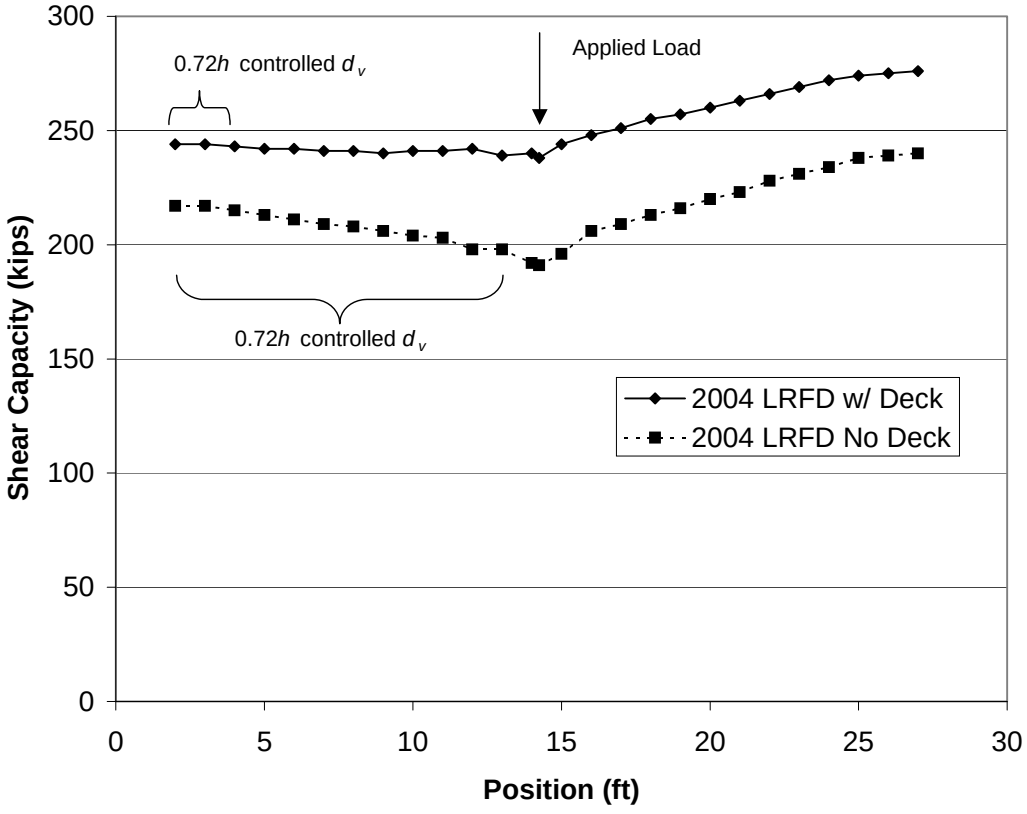

Figure 3.6 Shear Capacity vs. Position (2004 LRFD)

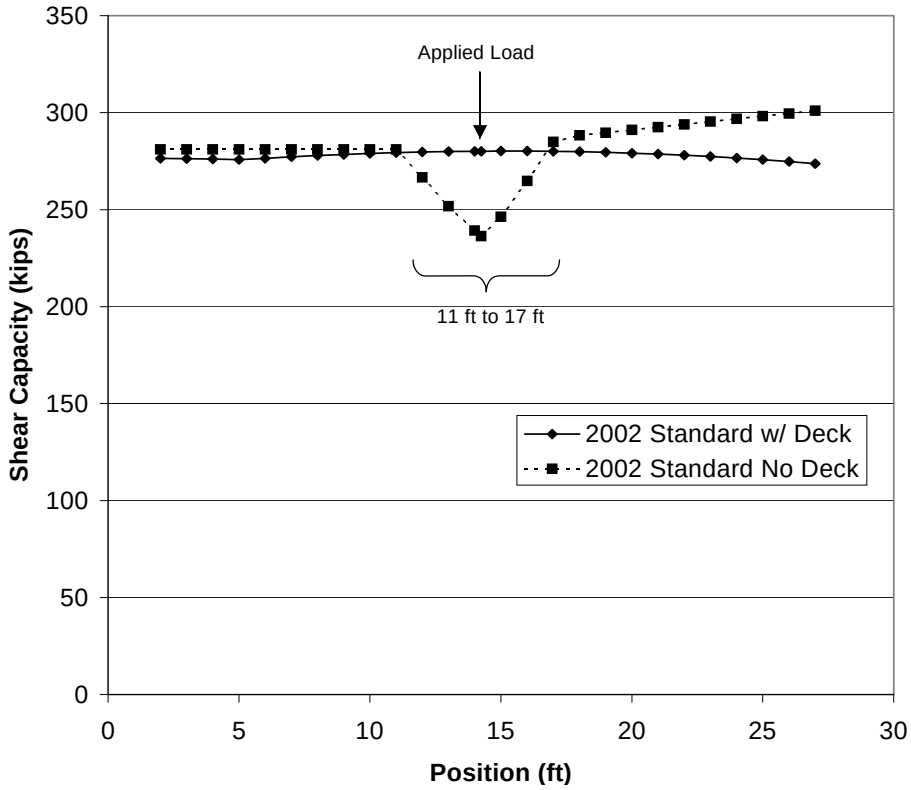

Figure 3.7 Shear Capacity vs. Position (2002 Standard)

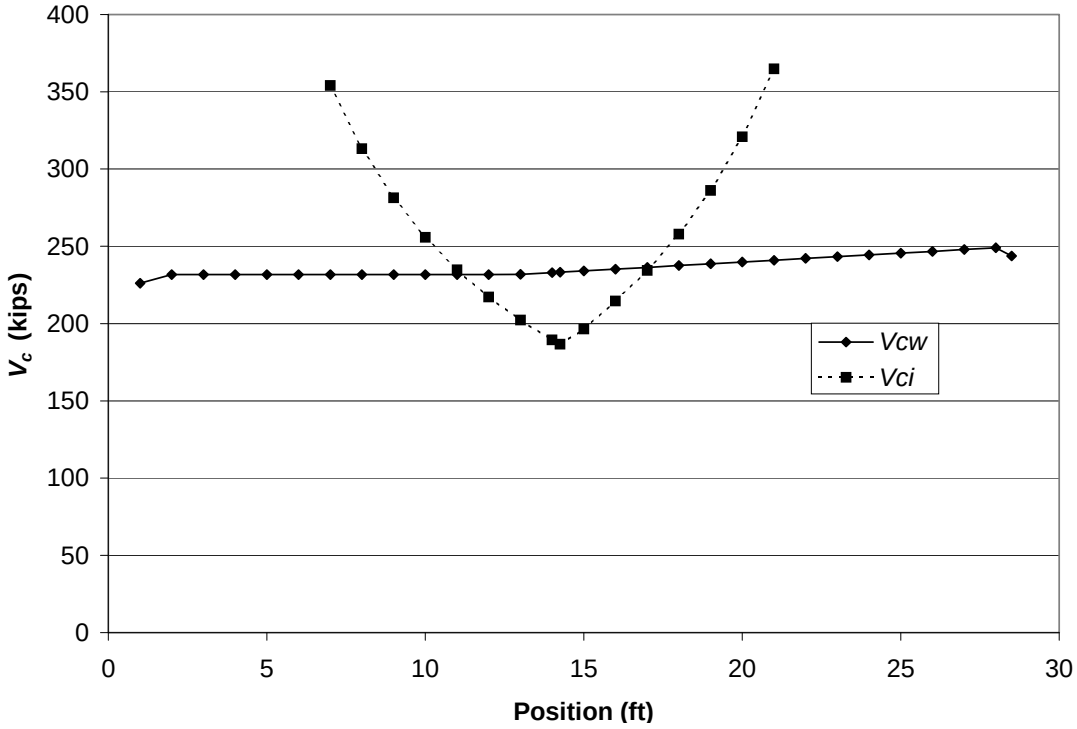

Figure 3.8 V_{ci} and V_{cw} (No Deck, 2002 Standard)

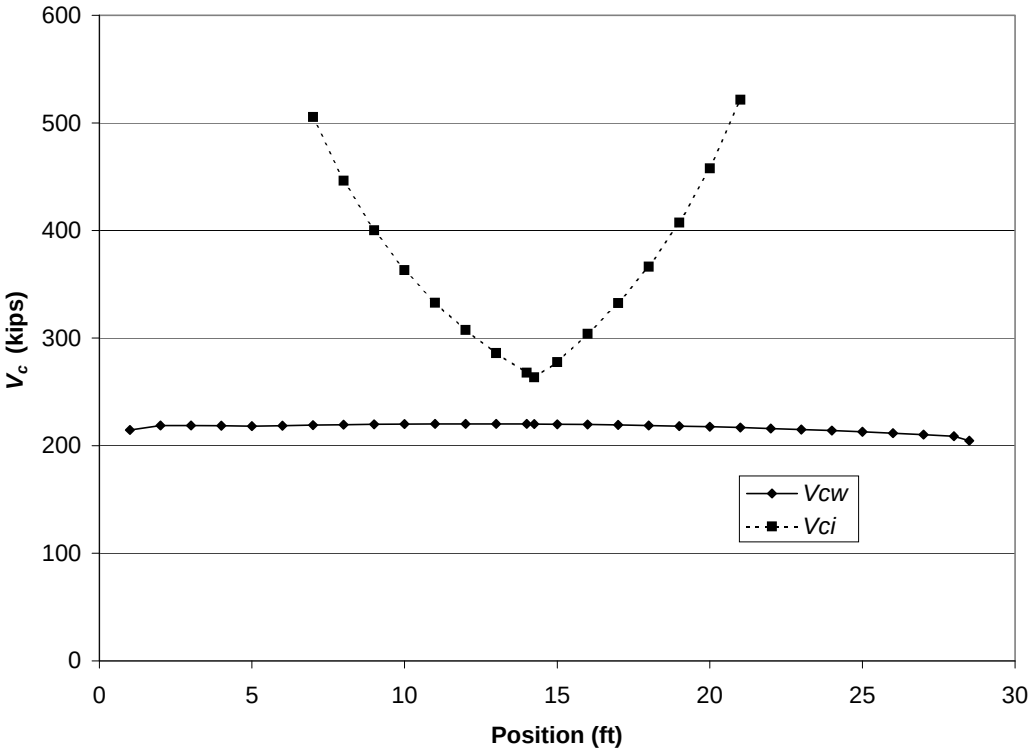

Figure 3.9 V_{ci} and V_{cw} (With Deck, 2002 Standard)

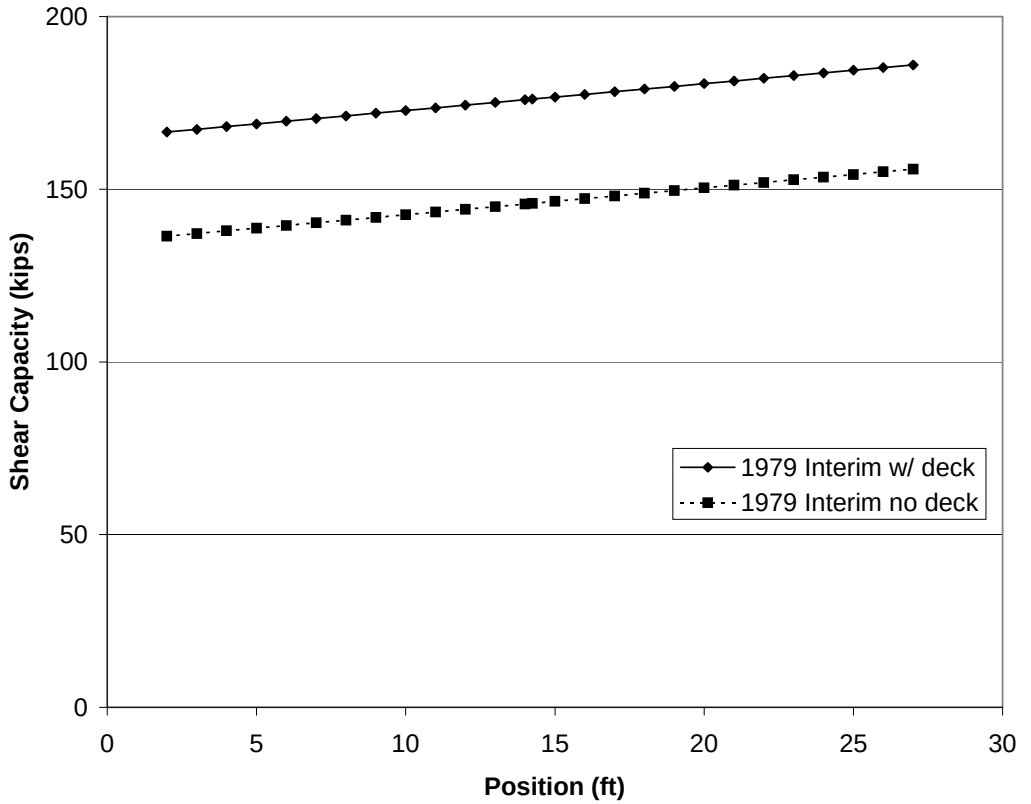

Figure 3.10 Shear Capacity vs. Position (1979 Standard)

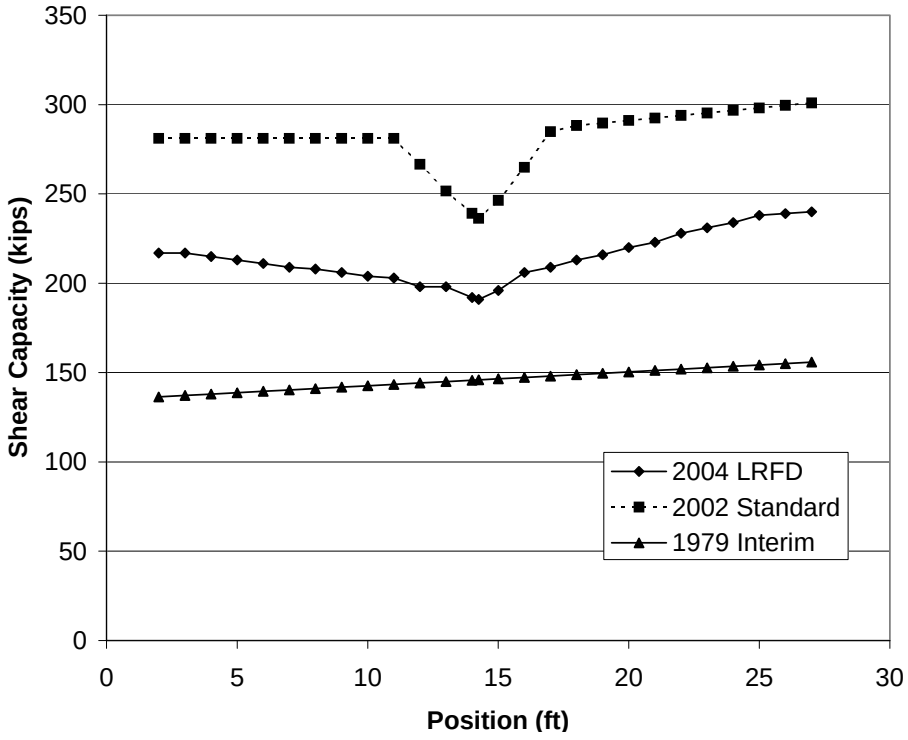

Figure 3.11 Shear Capacity vs. Position (No Deck)

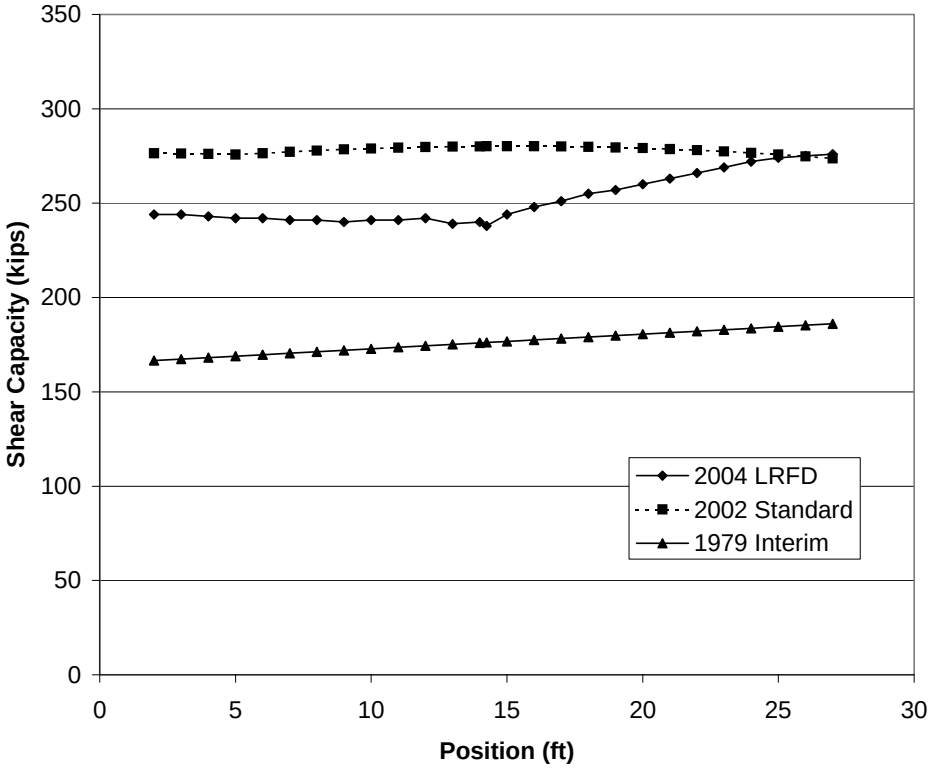

Figure 3.12 Shear Capacity vs. Position (With Deck)

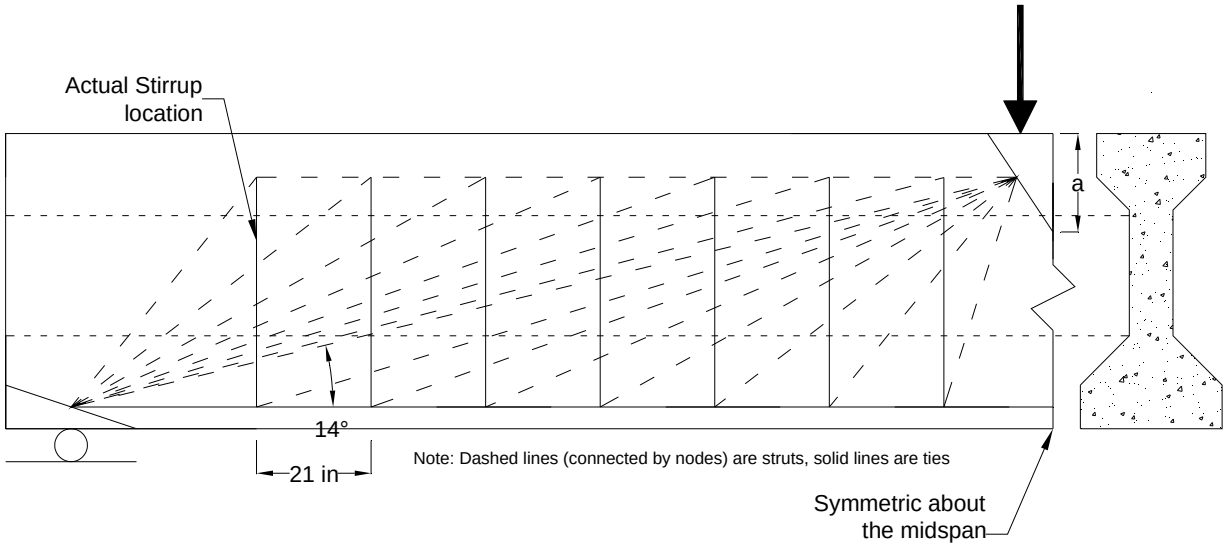

Figure 3.13 Strut and Tie Model for Half of the Beam (no deck)

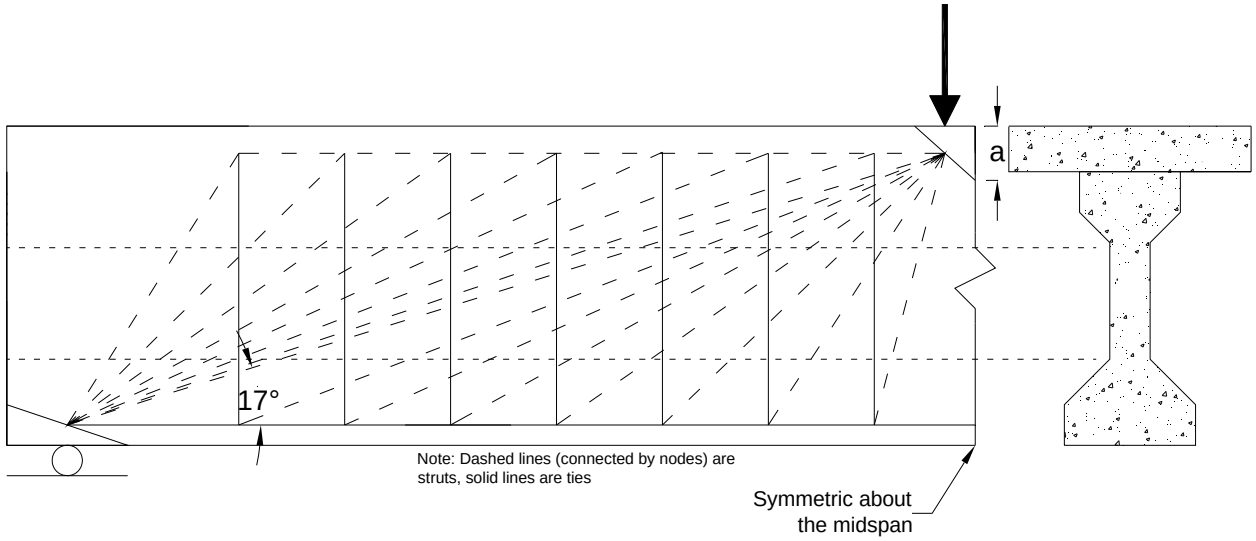

Figure 3.14 Strut and Tie Model for Half of the Beam (with deck)

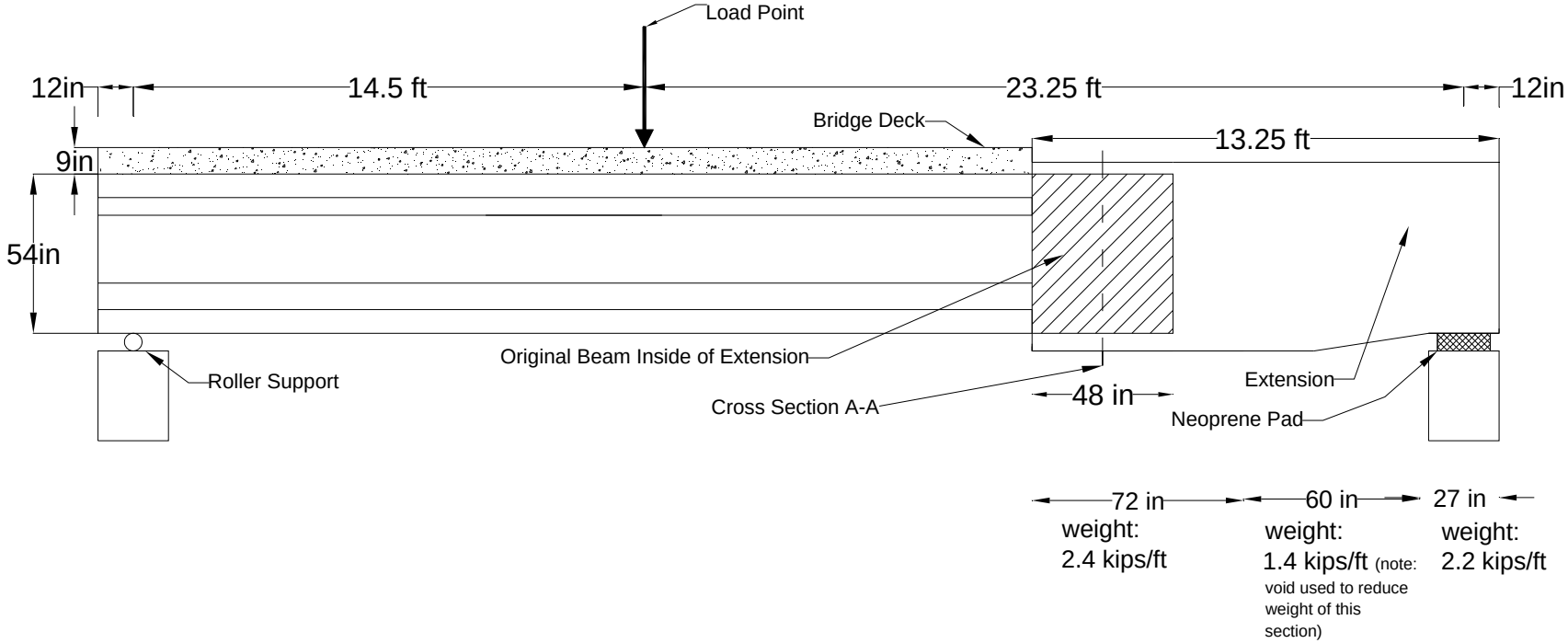

Figure 4.1 Modified Specimen

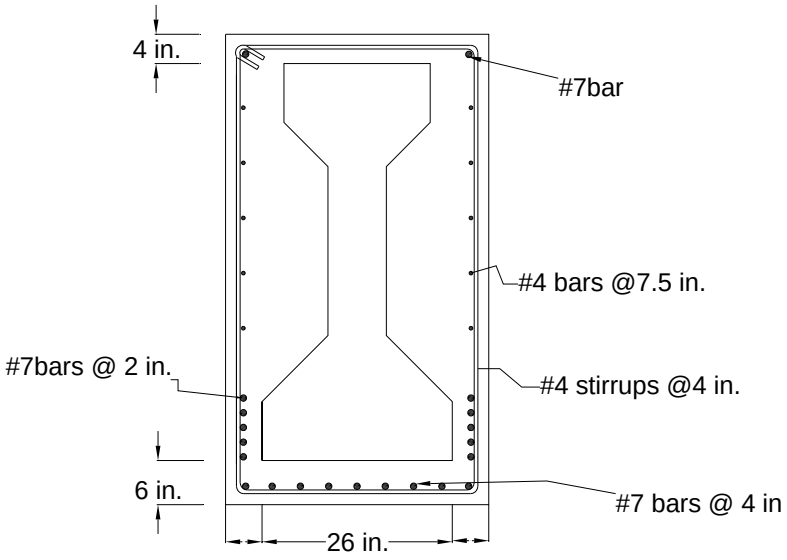

Figure 4.2 Cross-section A-A

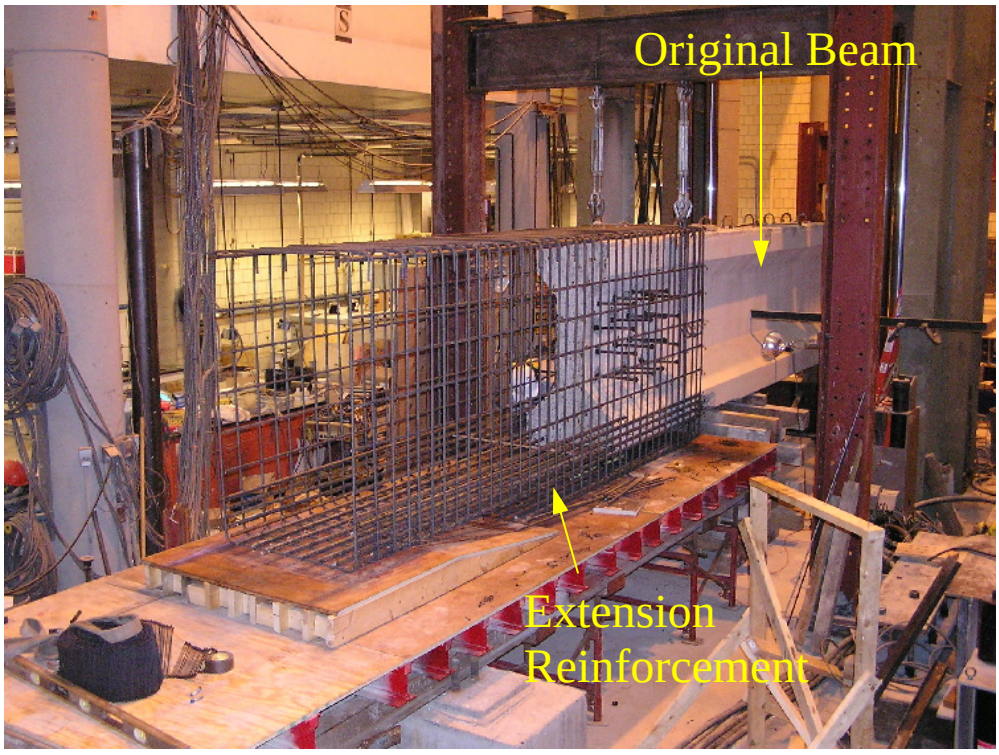

Figure 4.3 Extension Construction: Before Casting

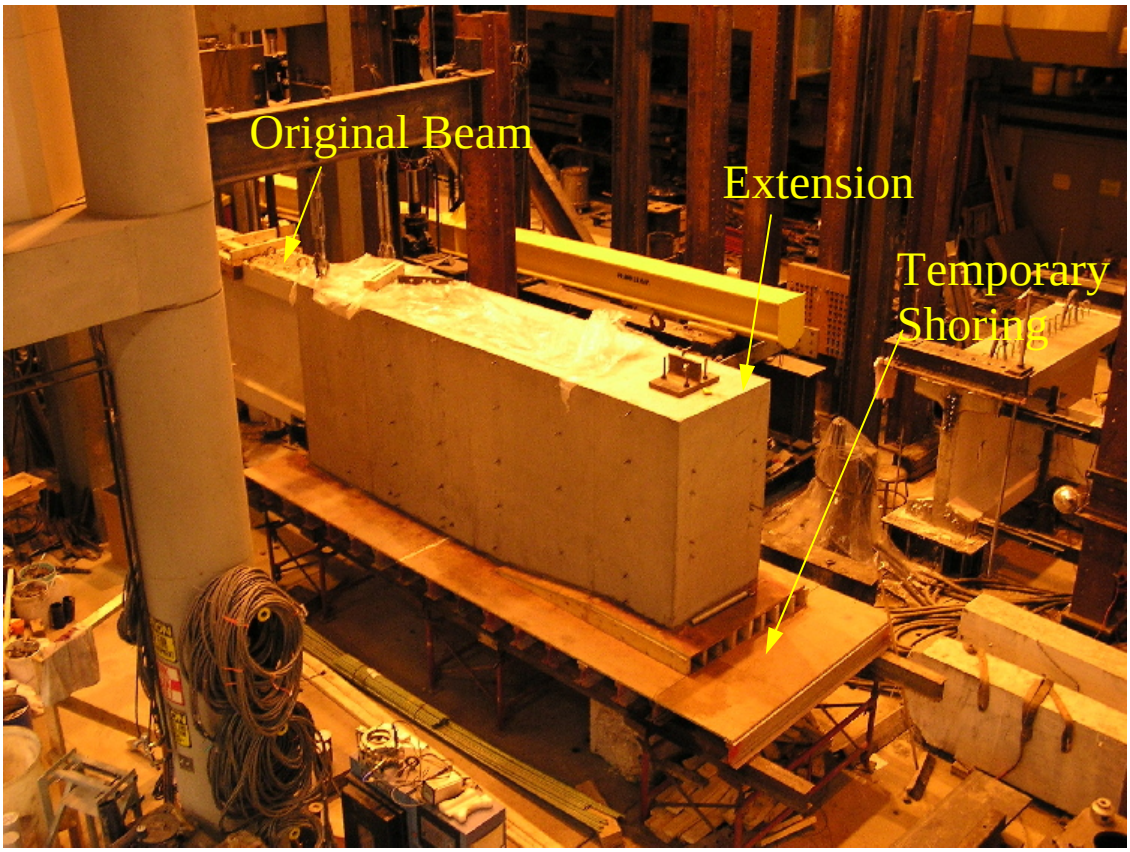

Figure 4.4 Extension Construction: After Casting

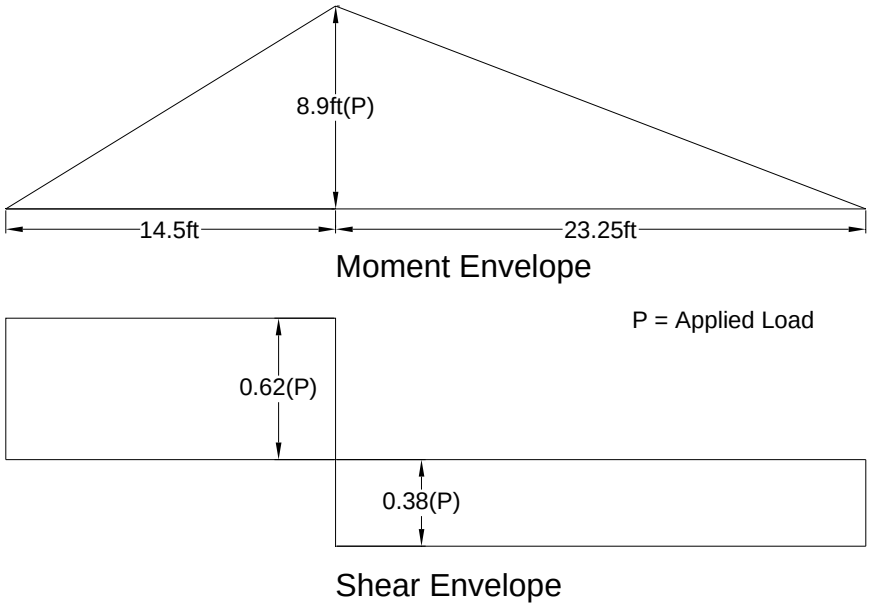

Figure 4.5 Moment and Shear Envelopes, Neglecting Dead Loads

Figure 4.6 Portion of Test Specimen Subjected to Largest Applied Shear

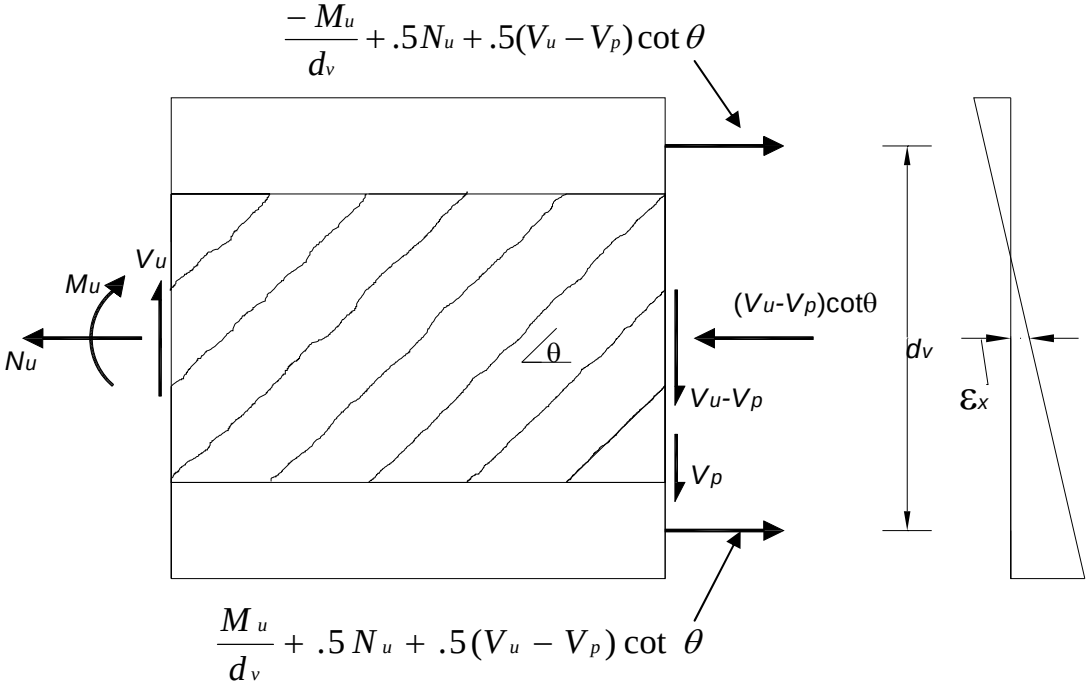

Figure 4.7 Balance of External Forces (AASHTO, 2004)

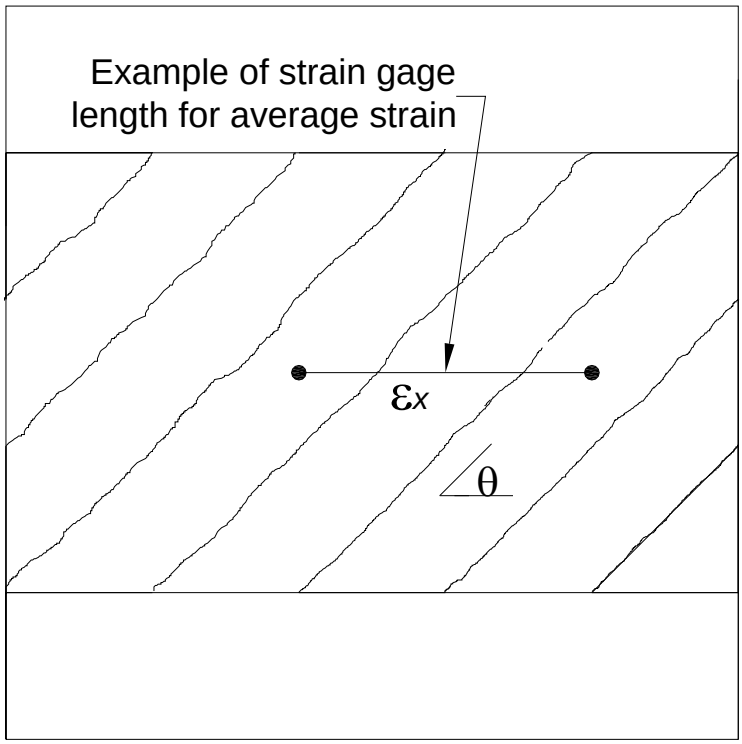

Figure 4.8 Average Longitudinal Strain at Middepth

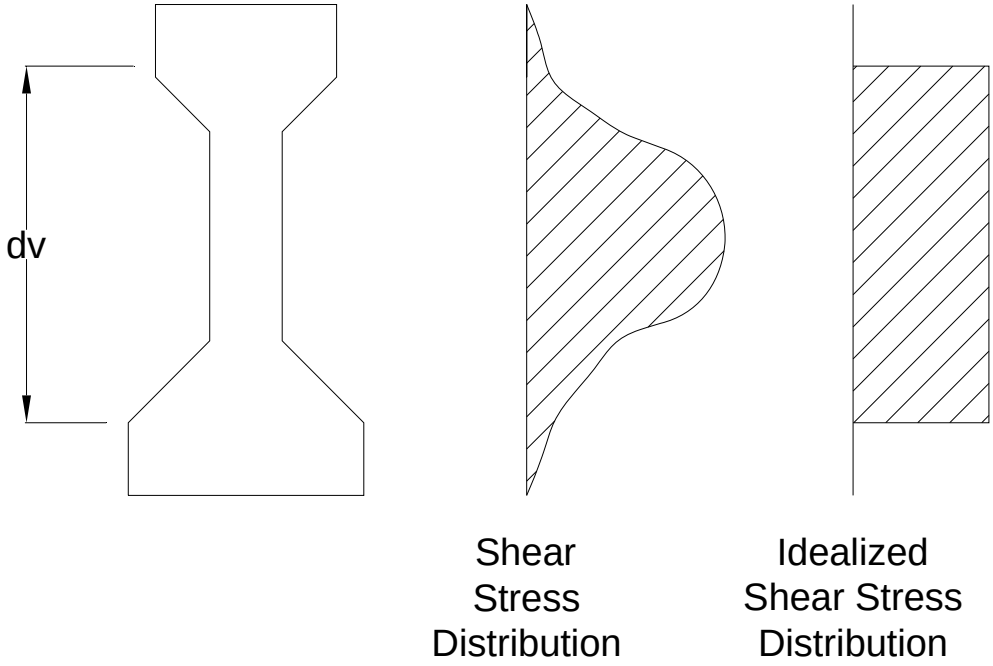

Figure 4.9 Shear Stress Distribution

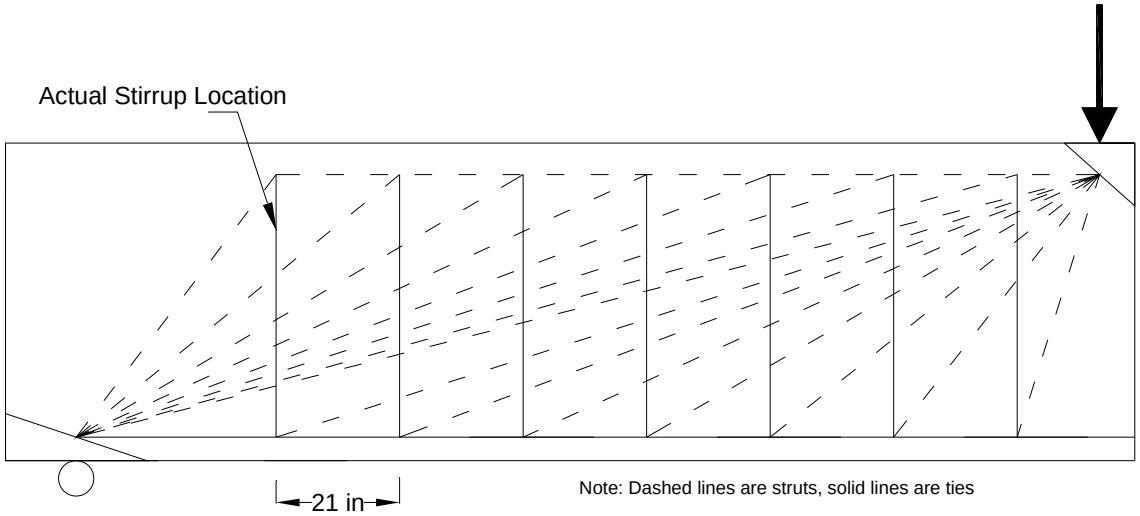

Figure 4.10 Revised Strut and Tie Model to Account for Specimen Modification

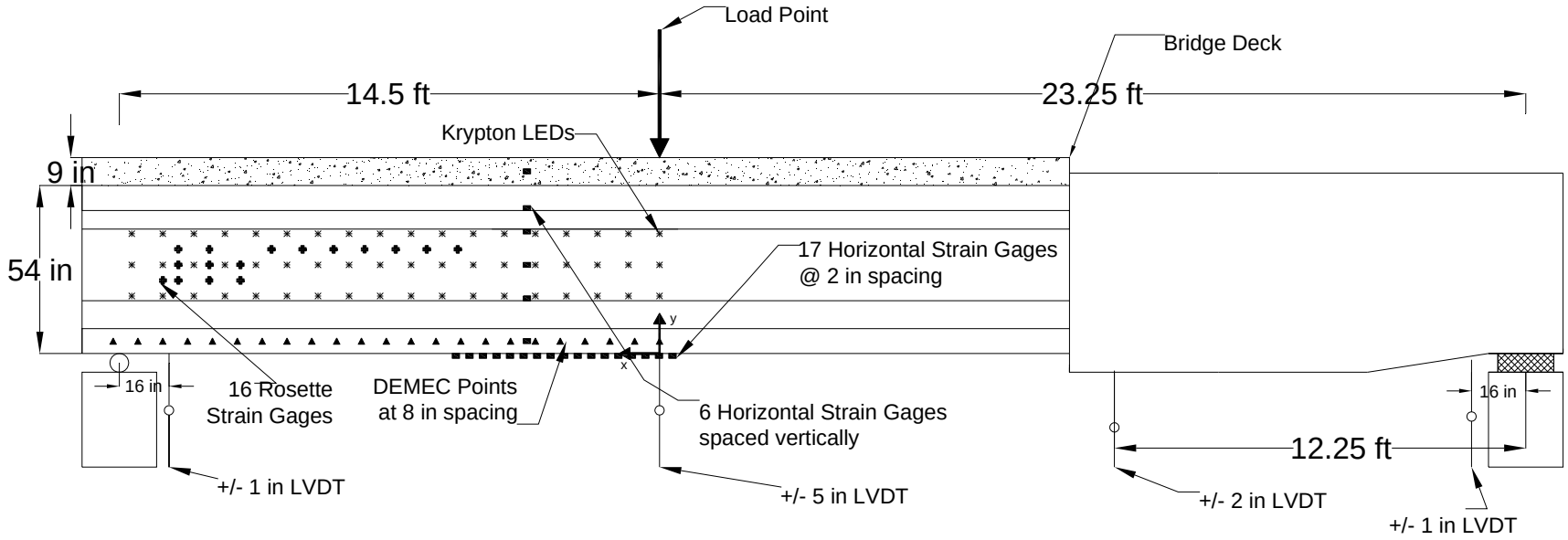

Figure 4.11 Instrumentation Layout

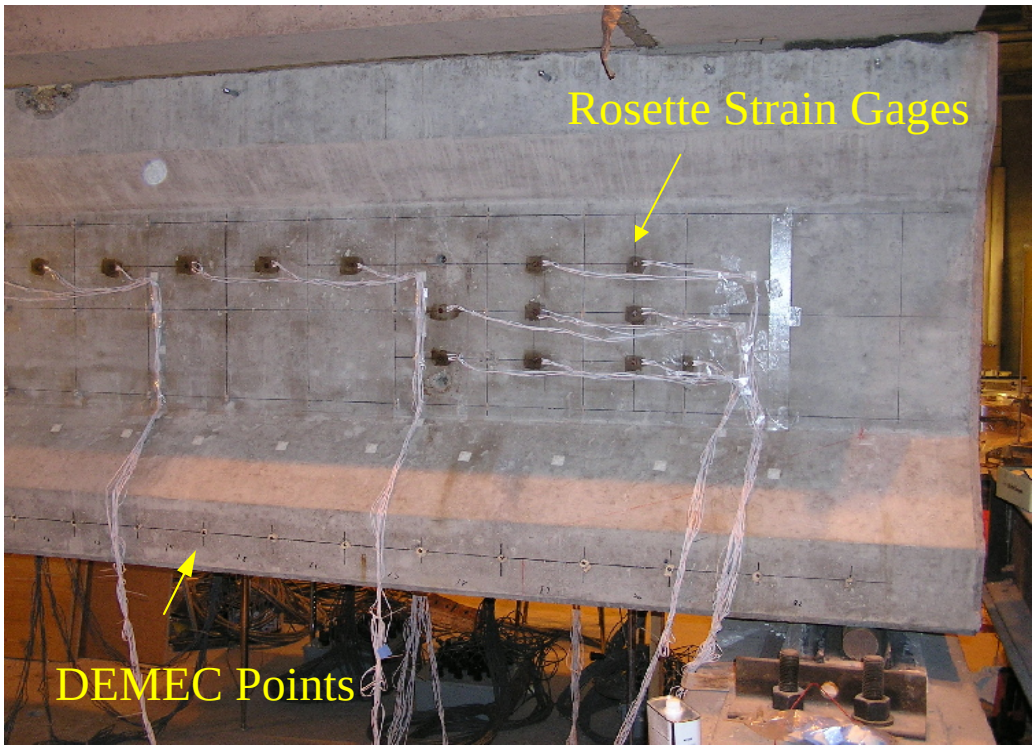

Figure 4.12 Rosette Strain Gages and DEMEC Points

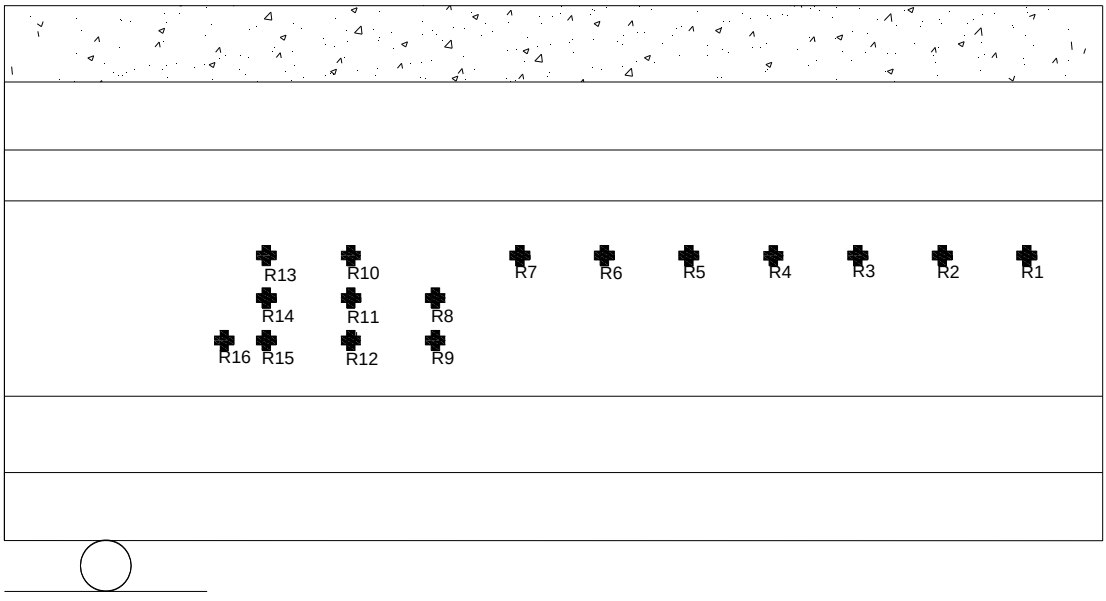

Figure 4.13 Rosette Strain Gage Labels

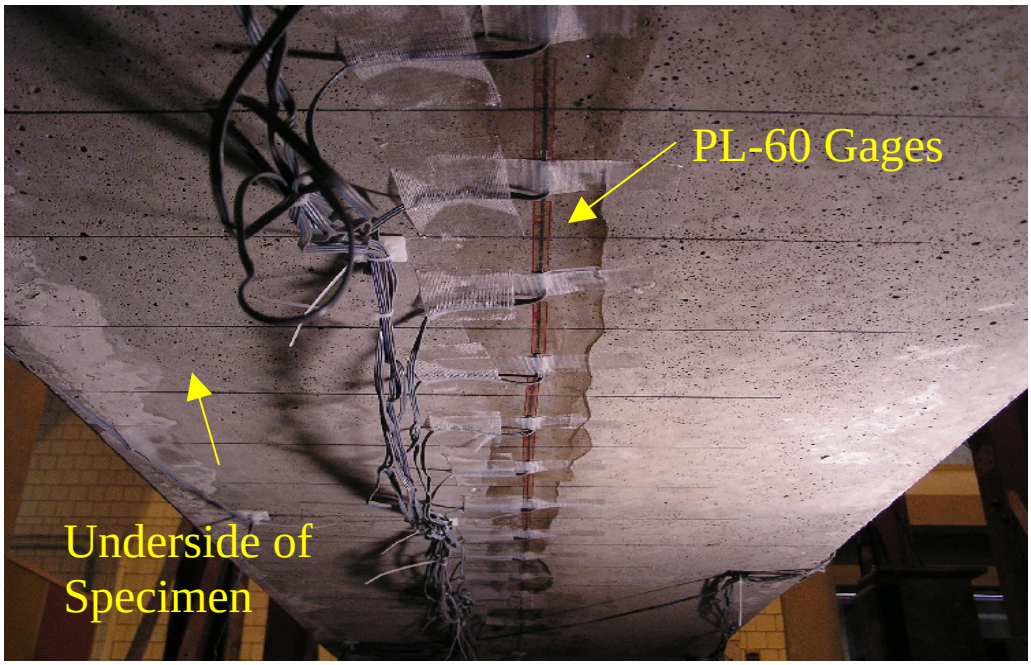

Figure 4.14 Horizontal Strain Gages on Bottom Surface

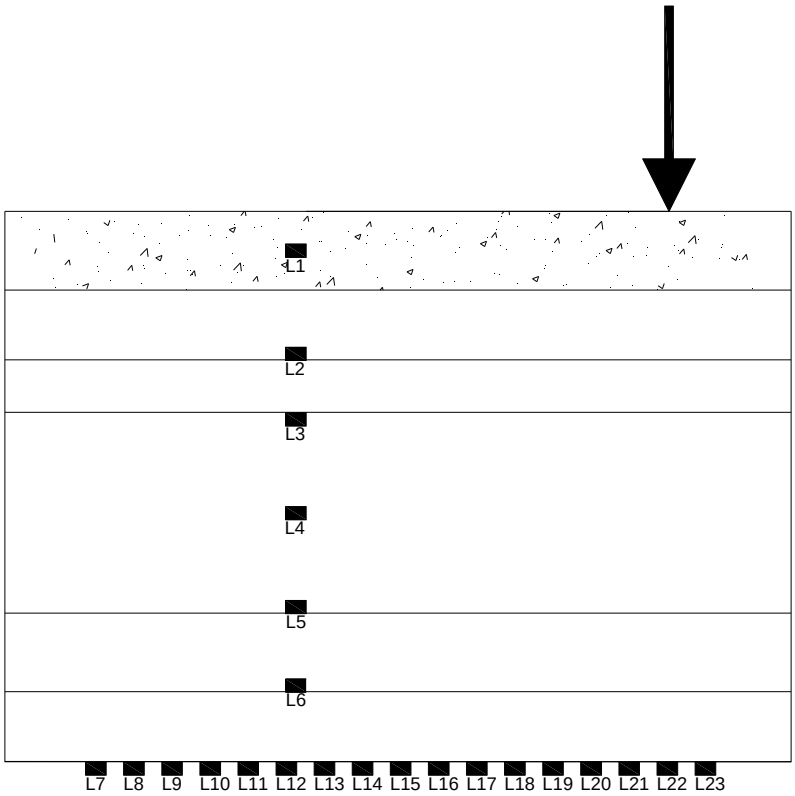

Figure 4.15 Horizontal Strain Gage Labels

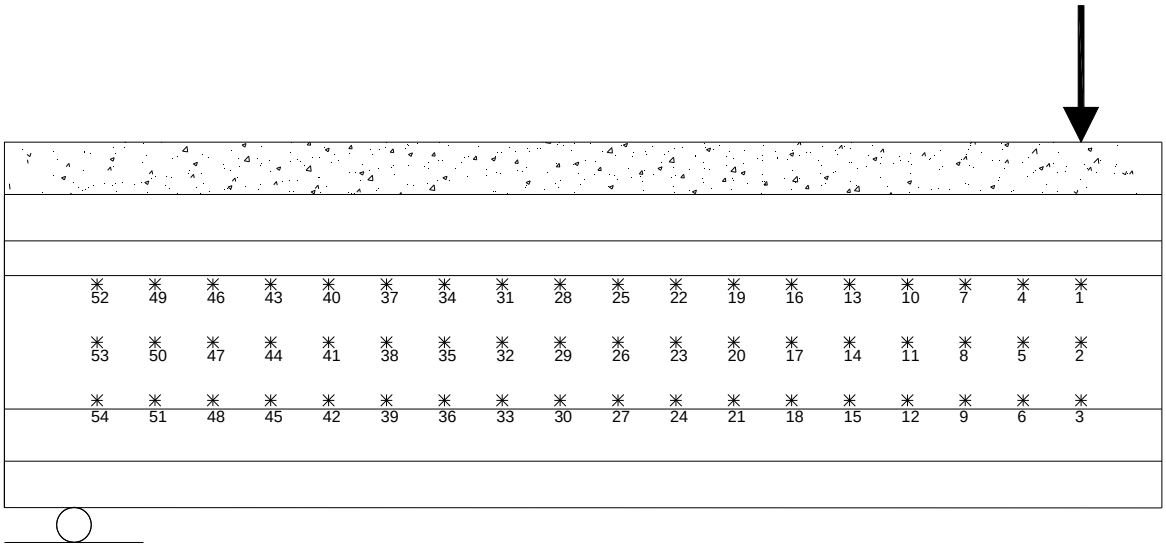

Figure 4.16 Krypton LED labels

Figure 4.17 Krypton Setup up for Specimen I

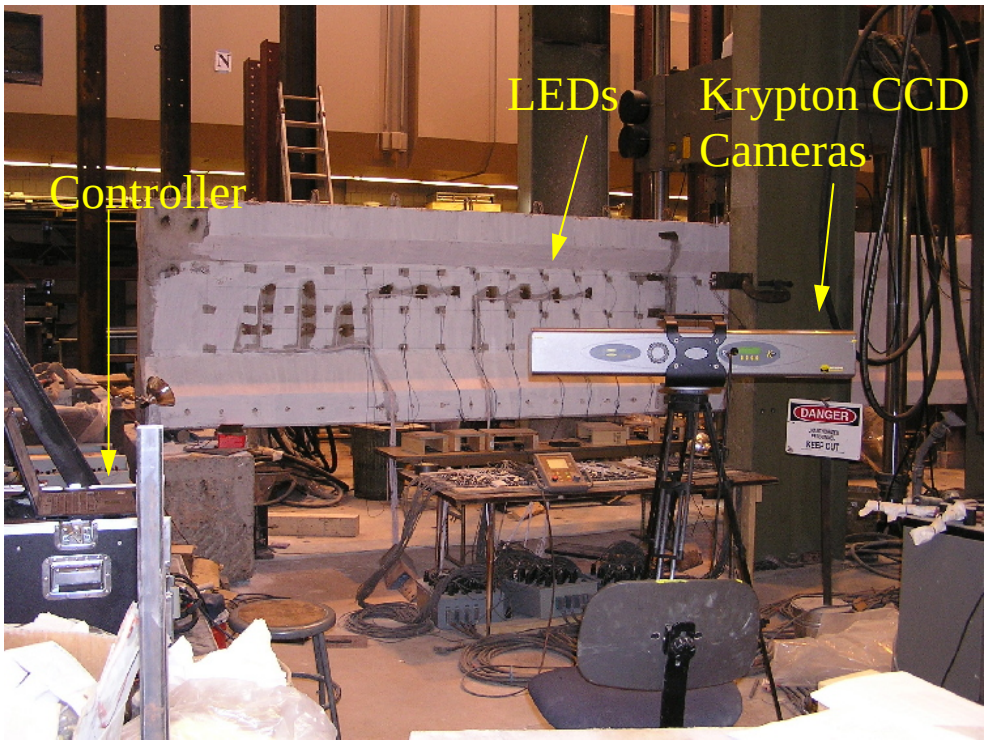

Figure 4.18 Krypton Setup up for Specimen II

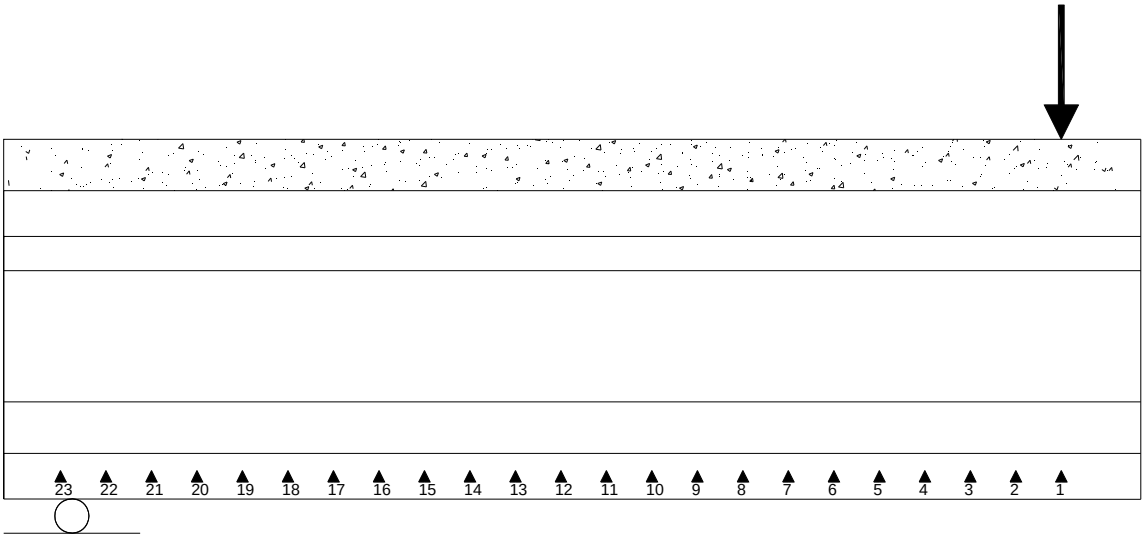

Figure 4.19 DEMEC Point Labels

Figure 4.20 Measurement of DEMEC Points

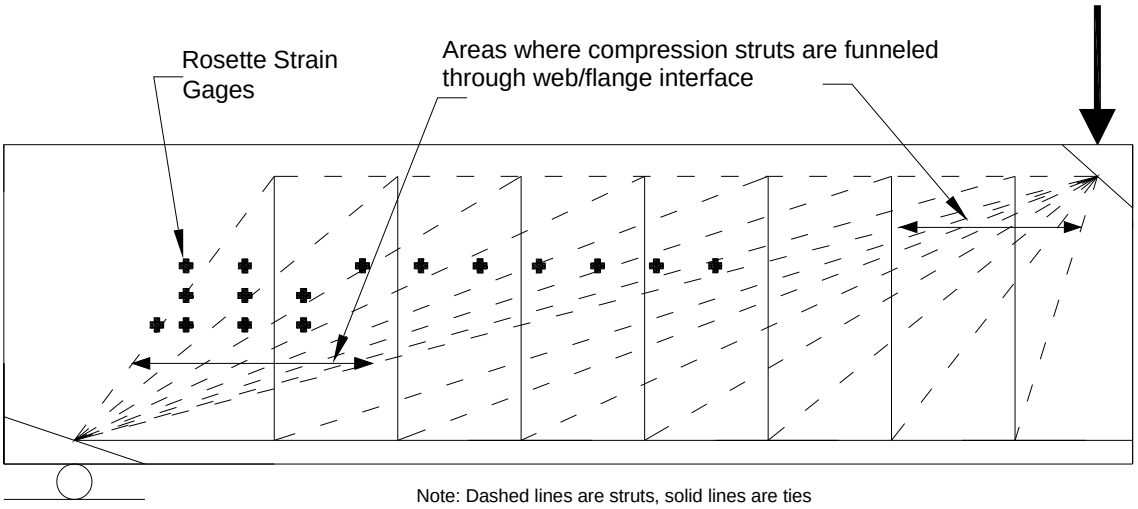

Figure 4.21 Rosette Strain Gages with Strut and Tie Model

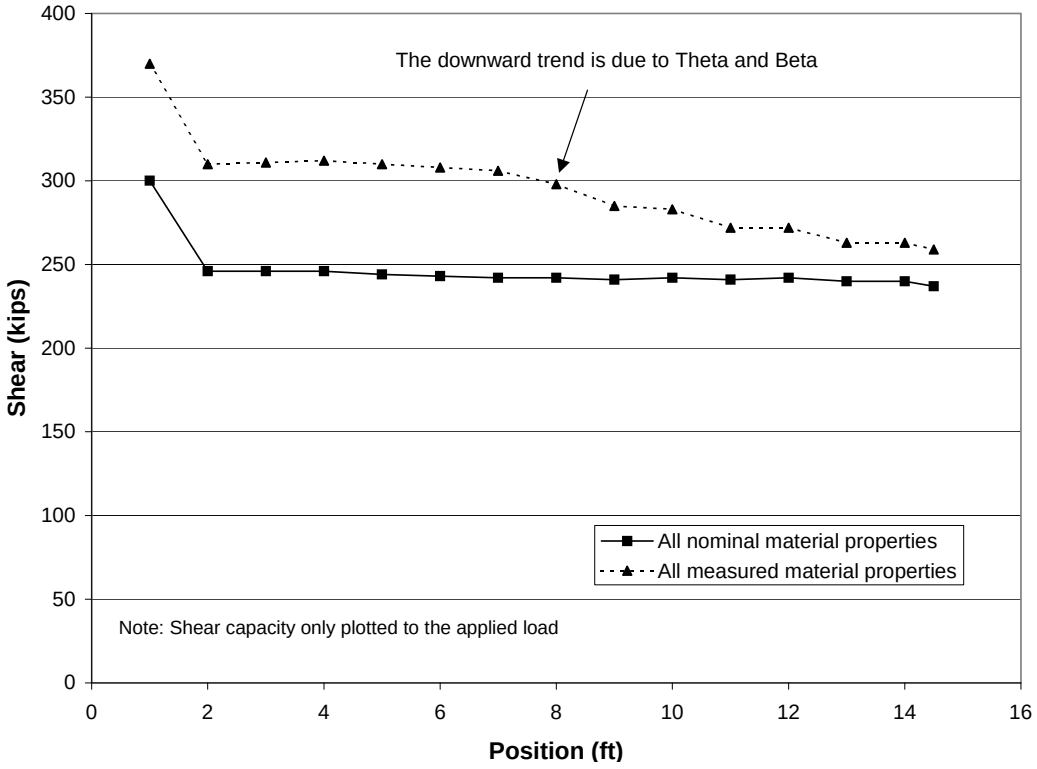

Figure 5.1 2004 LRFD Predicted Shear Capacity Specimen I (with the deck)

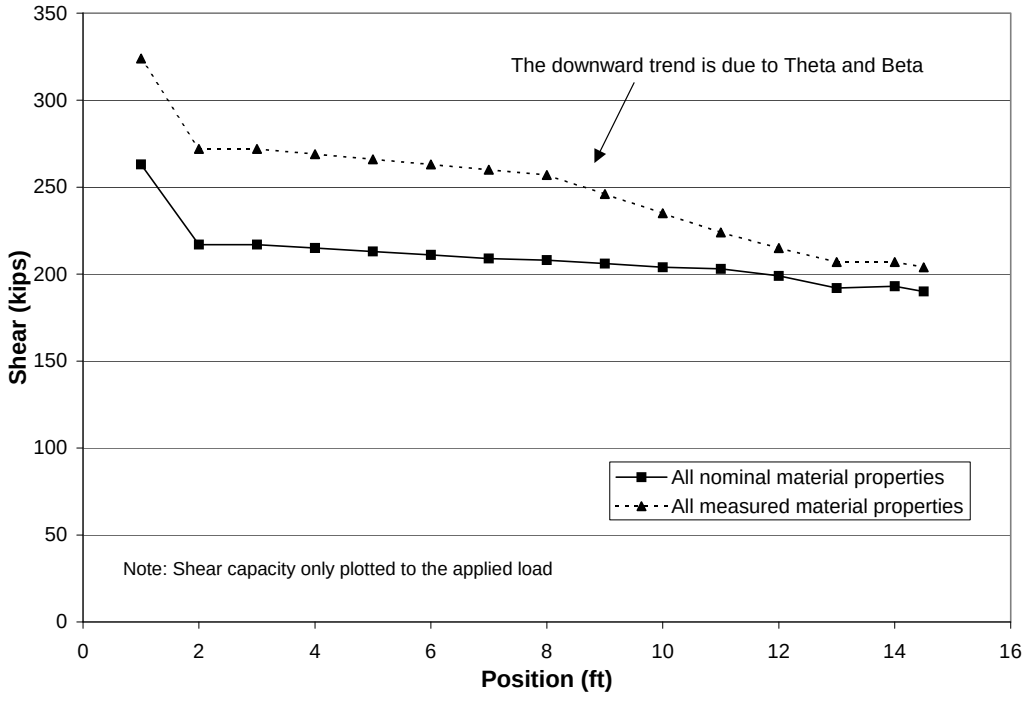

Figure 5.2 2004 LRFD Predicted Shear Capacity Specimen II (no deck)

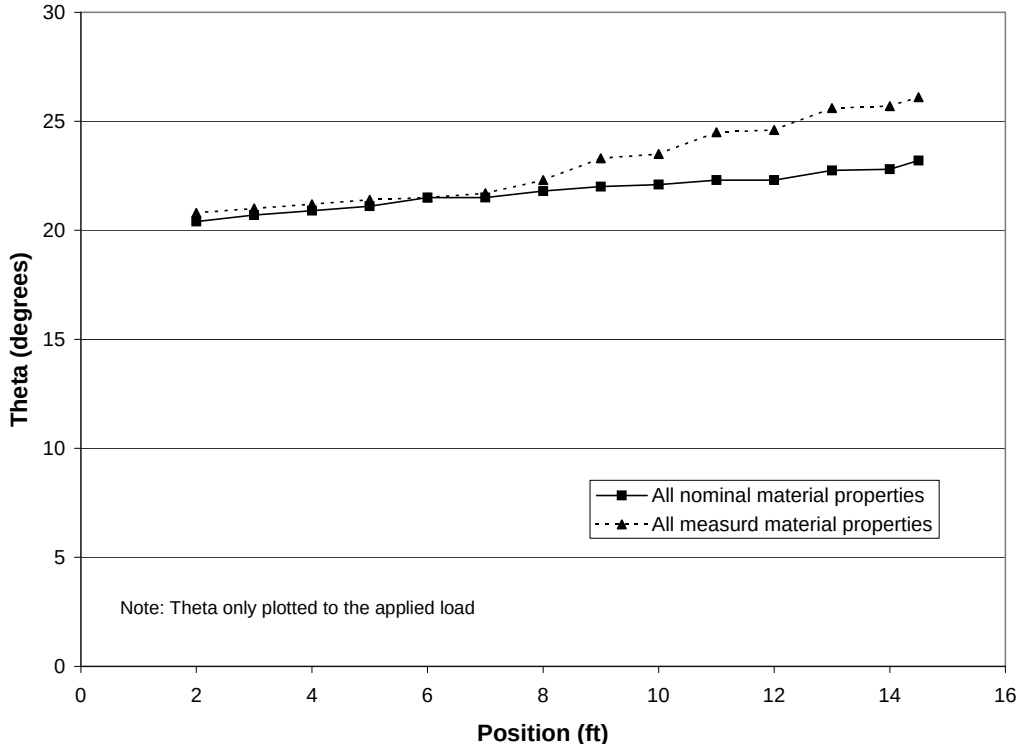

Figure 5.3 θ for Specimen I (with the deck)

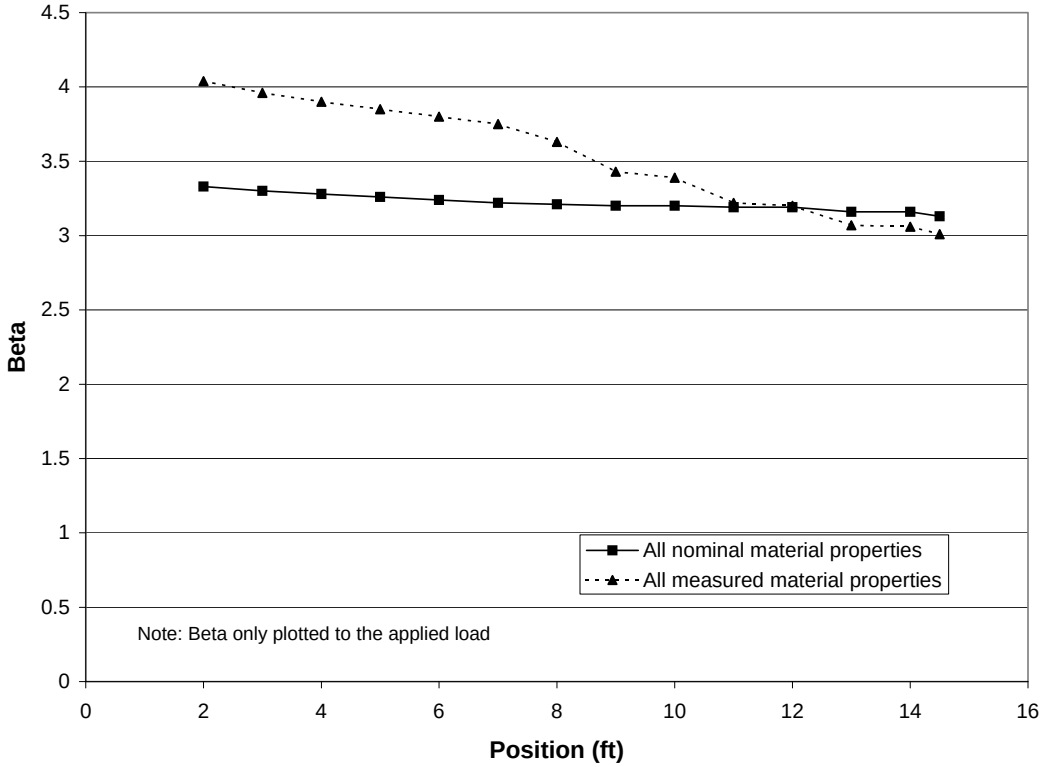

Figure 5.4 β for Specimen I (with the deck)

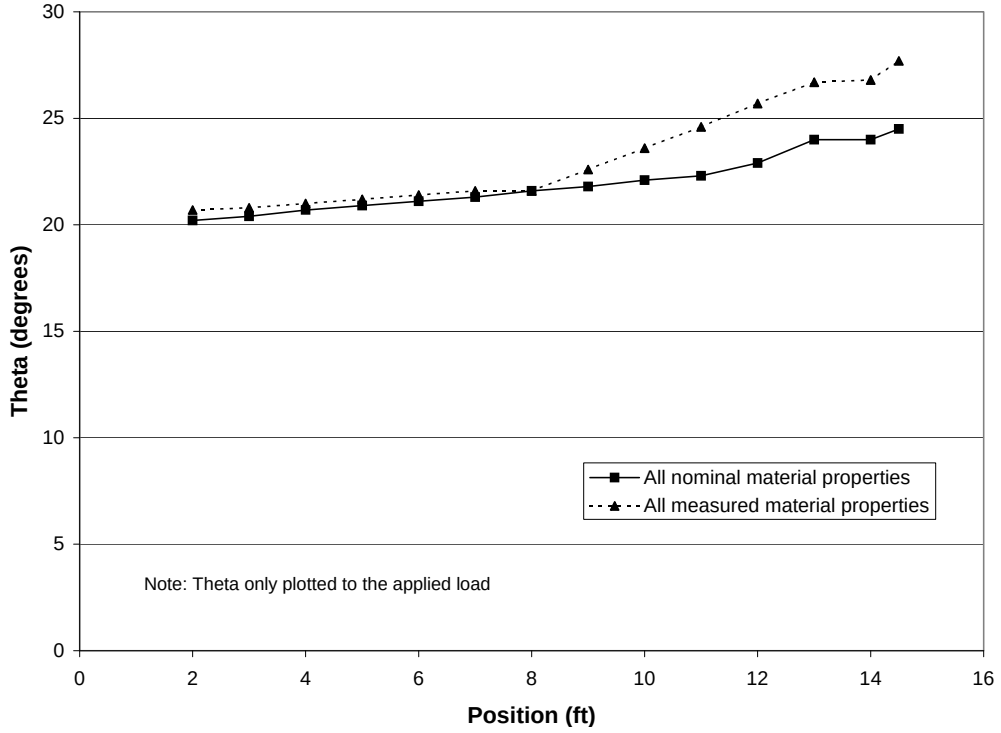

Figure 5.5 θ for Specimen II (no deck)

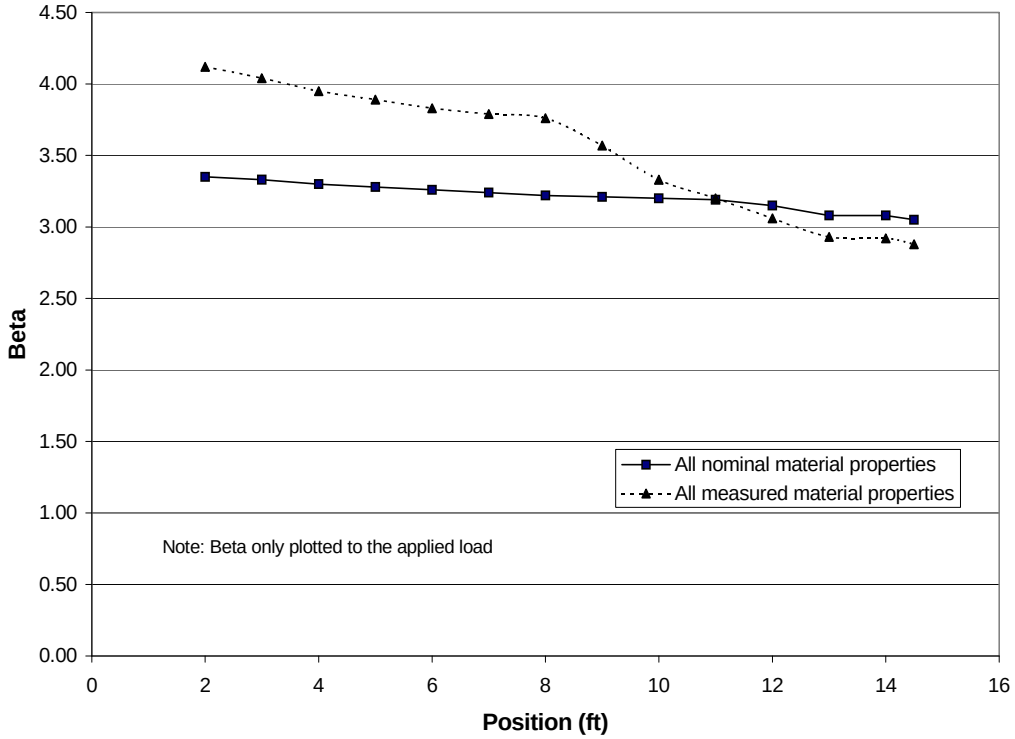

Figure 5.6 β for Specimen II (no deck)

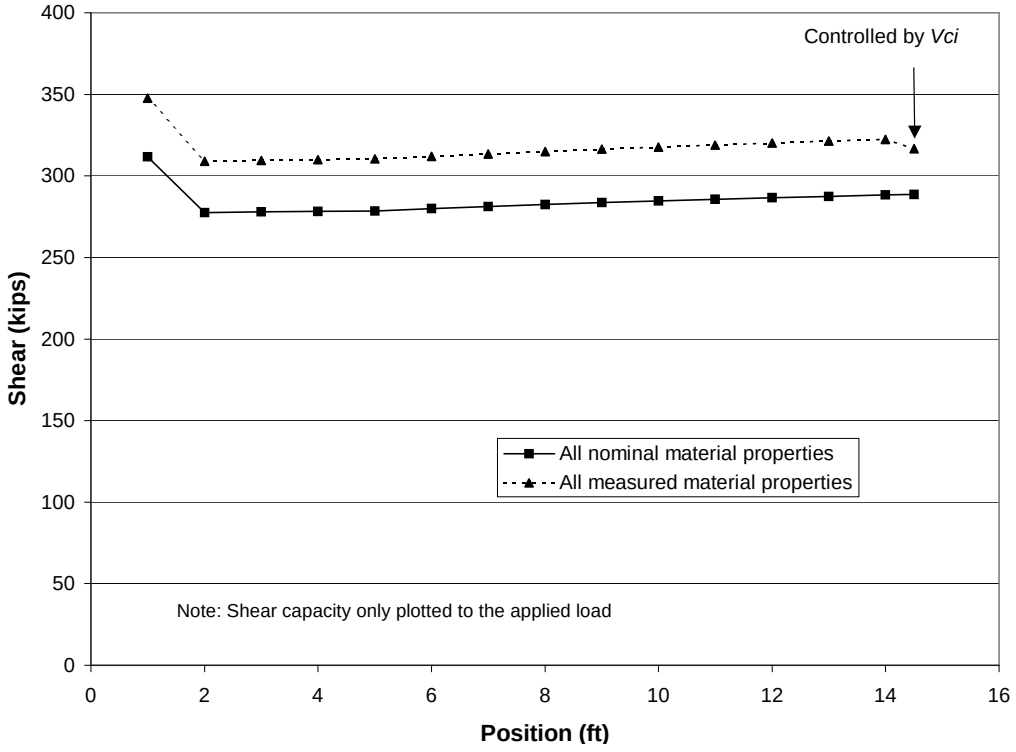

Figure 5.7 2002 Standard Predicted Shear Capacity; Specimen I (with deck)

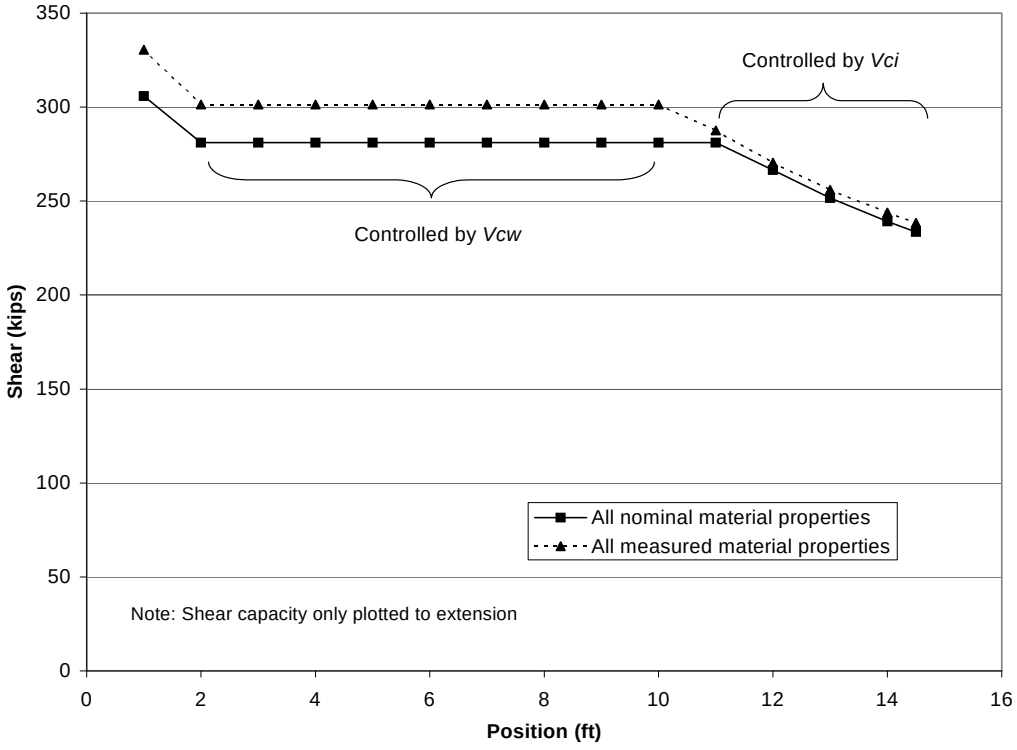

Figure 5.8 2002 Standard Predicted Shear Capacity; Specimen II (no deck)

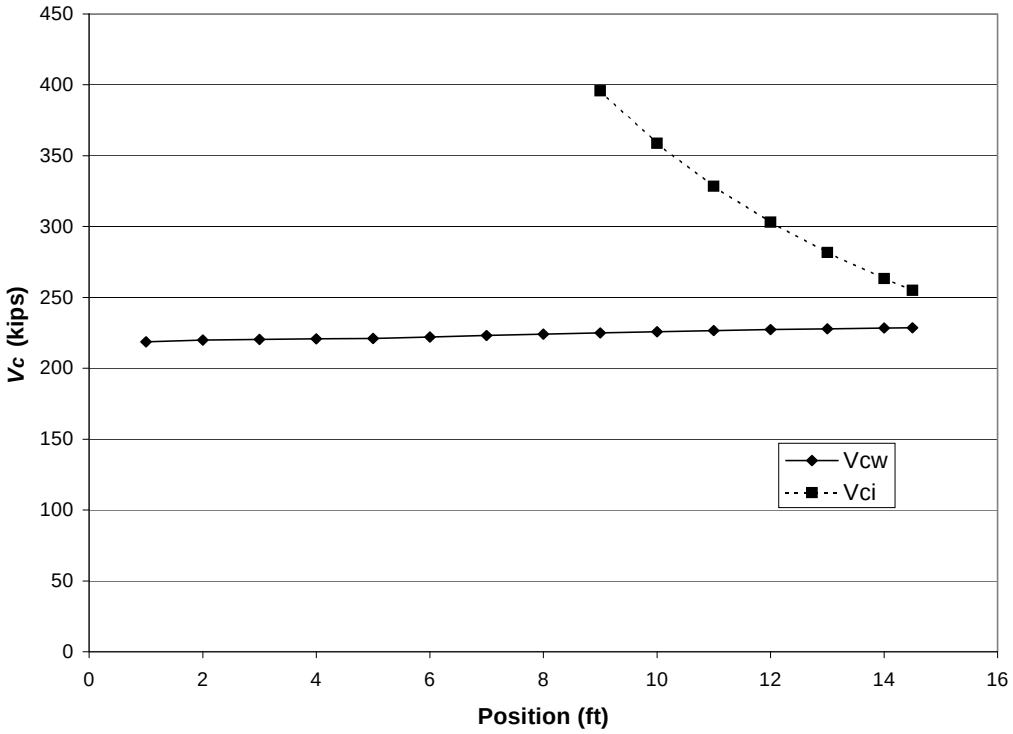

Figure 5.9 V_{ci} and V_{cw} with all Nominal Material Properties; Specimen I

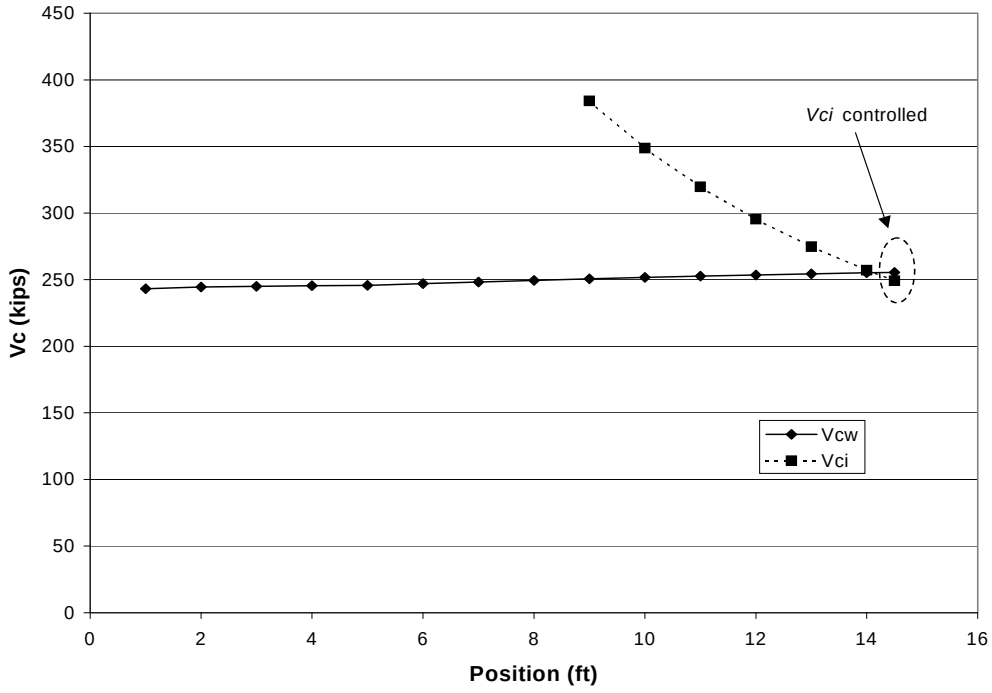

Figure 5.10 V_{ci} and V_{cw} with all Measured Material Properties; Specimen I

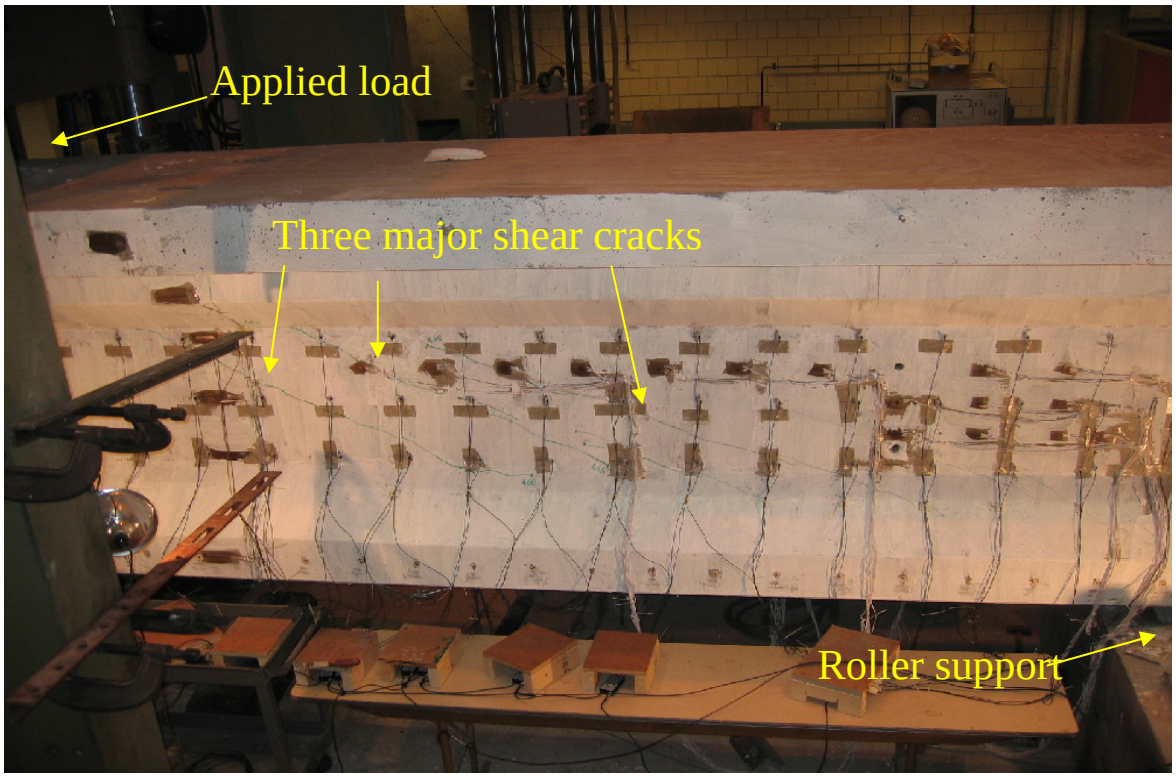

Figure 6.1 Photograph of Initial Web Cracking (Specimen I)

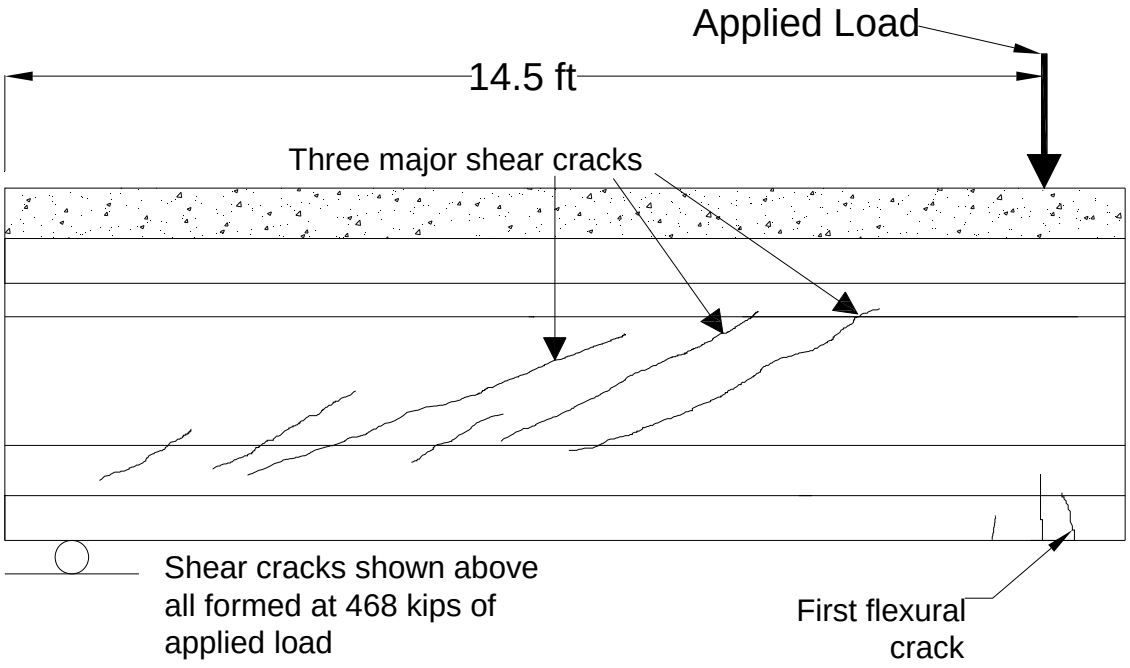

Figure 6.2 Initial Web Cracking (Specimen I)

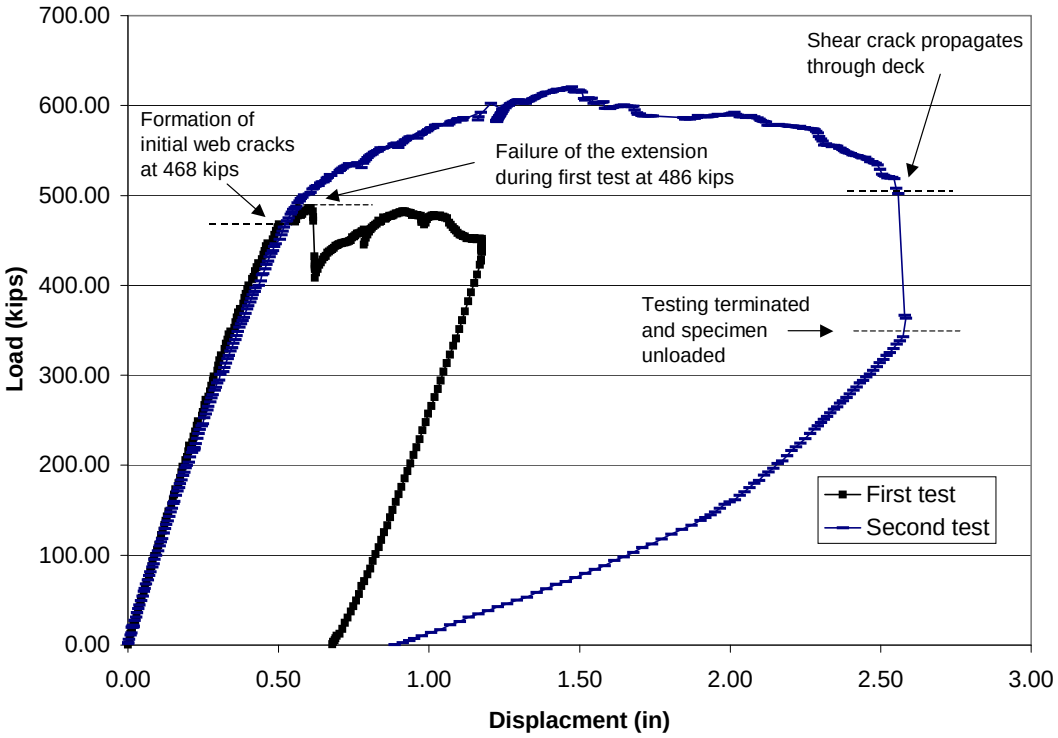

Figure 6.3 Load vs. Displacement (Specimen I)

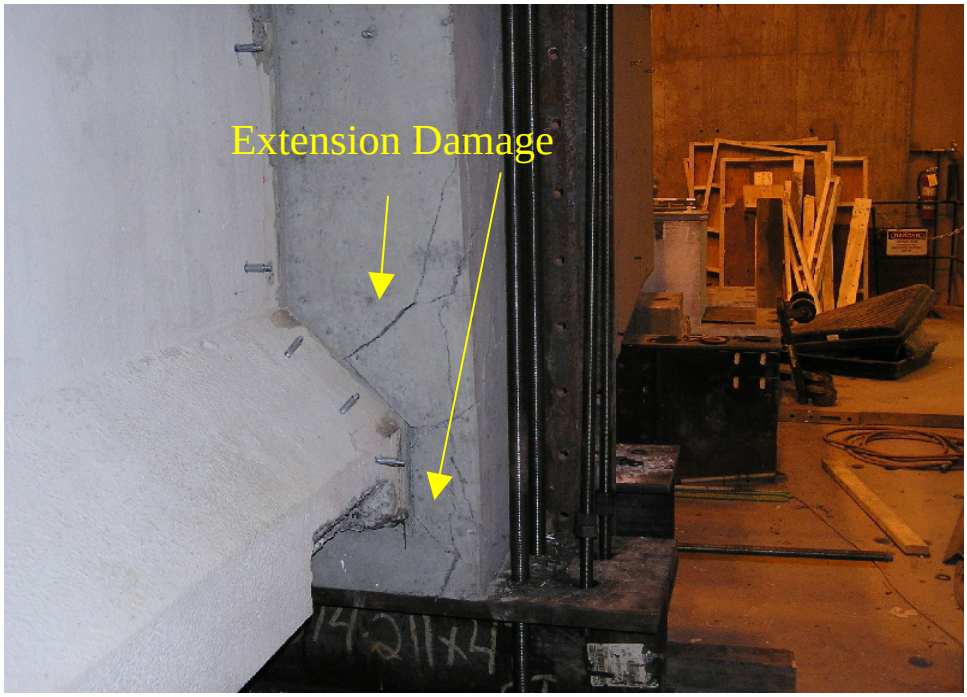

Figure 6.4 Extension Damage (Specimen I)

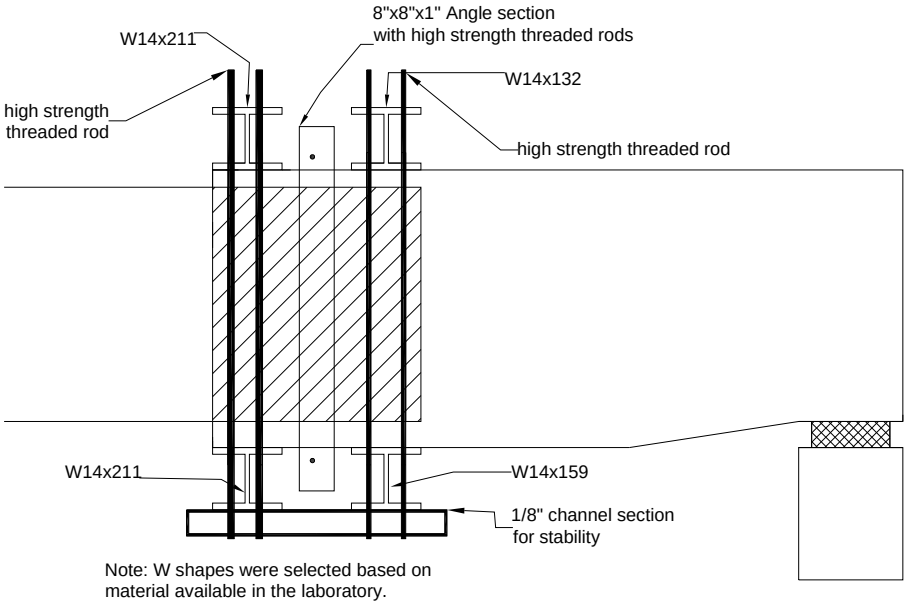

Figure 6.5 Extension Repair

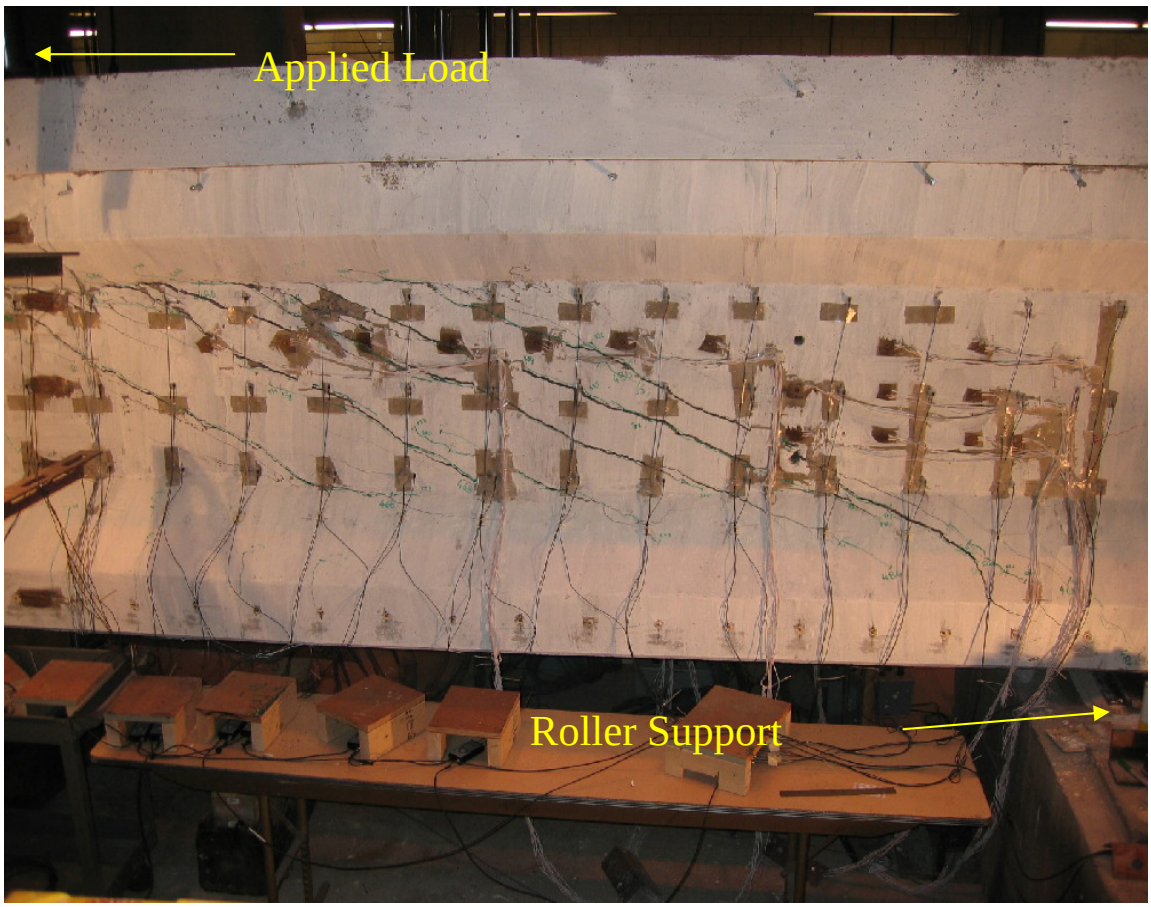

Figure 6.6 Photograph of Cracking at Peak Load (Specimen I)

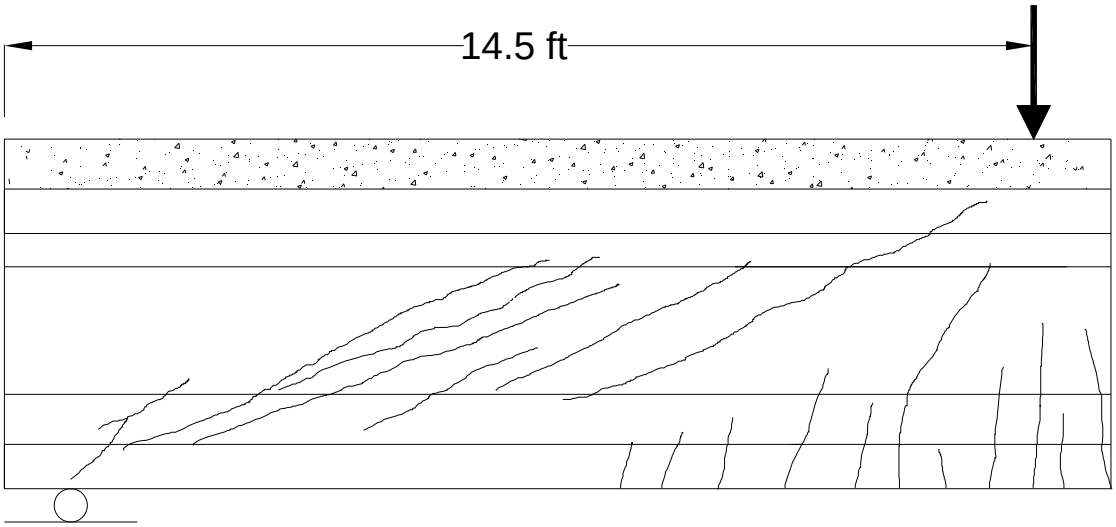

Figure 6.7 Cracking at Peak Load (Specimen I)

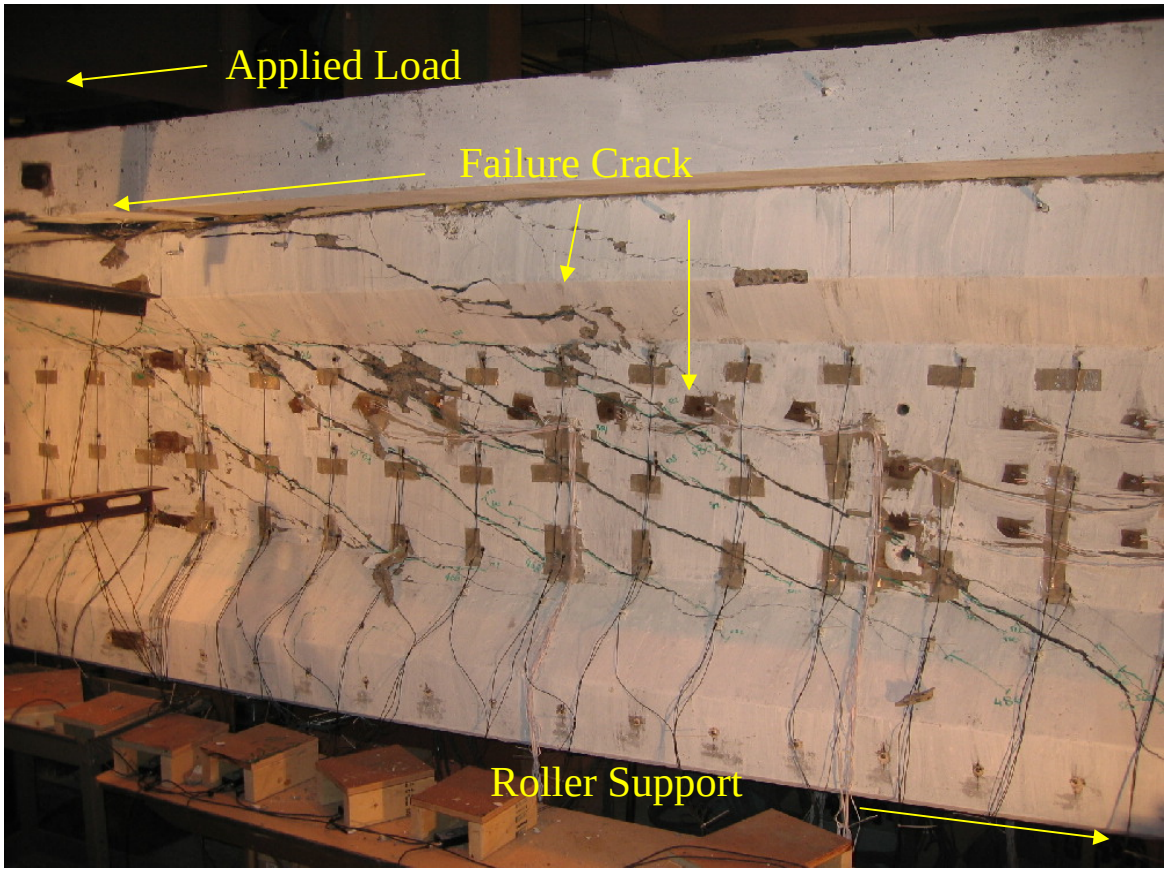

Figure 6.8 Photograph of Cracking at 40% Past Peak Applied Load (Specimen I)

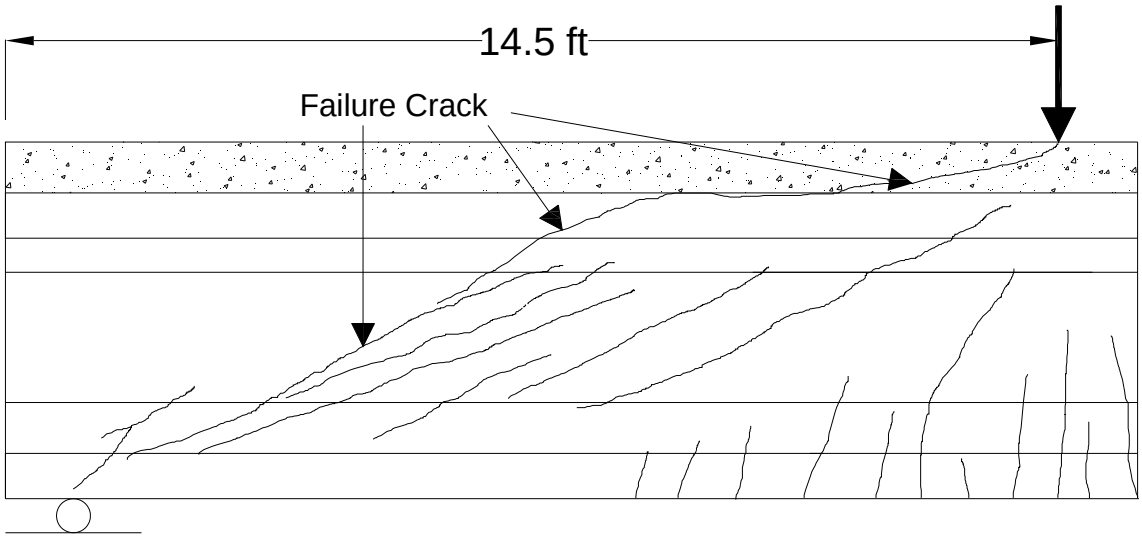

Figure 6.9 Cracking at 40% Past Peak Applied Load (Specimen I)

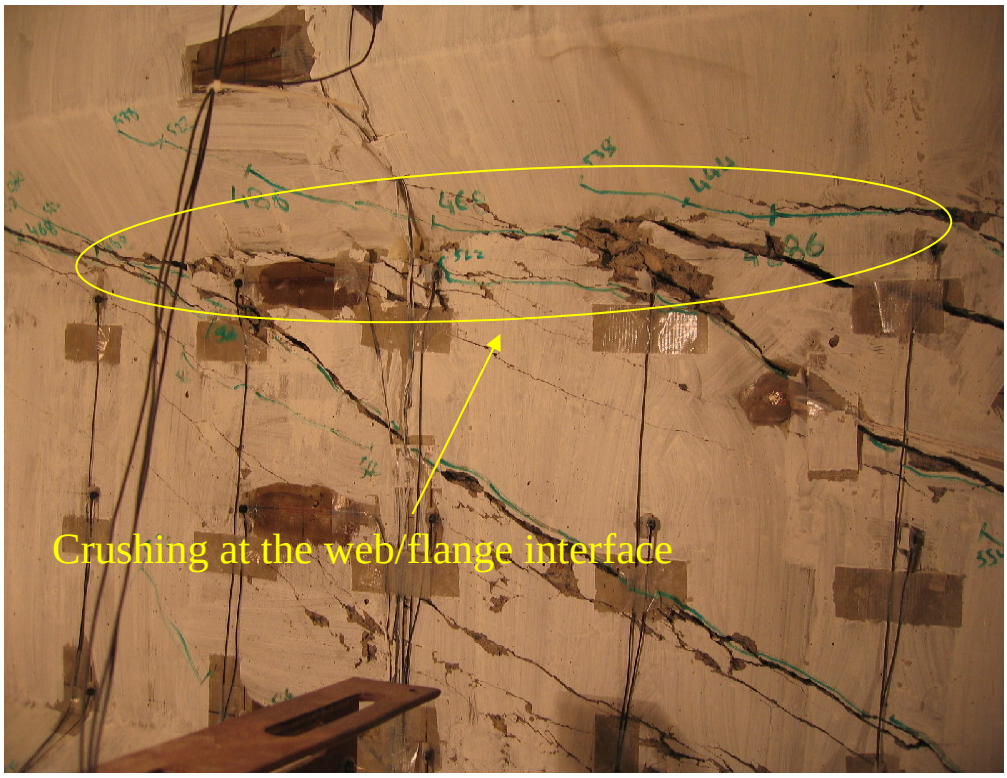

Figure 6.10 Crushing at the Web/Flange Interface (Specimen I)

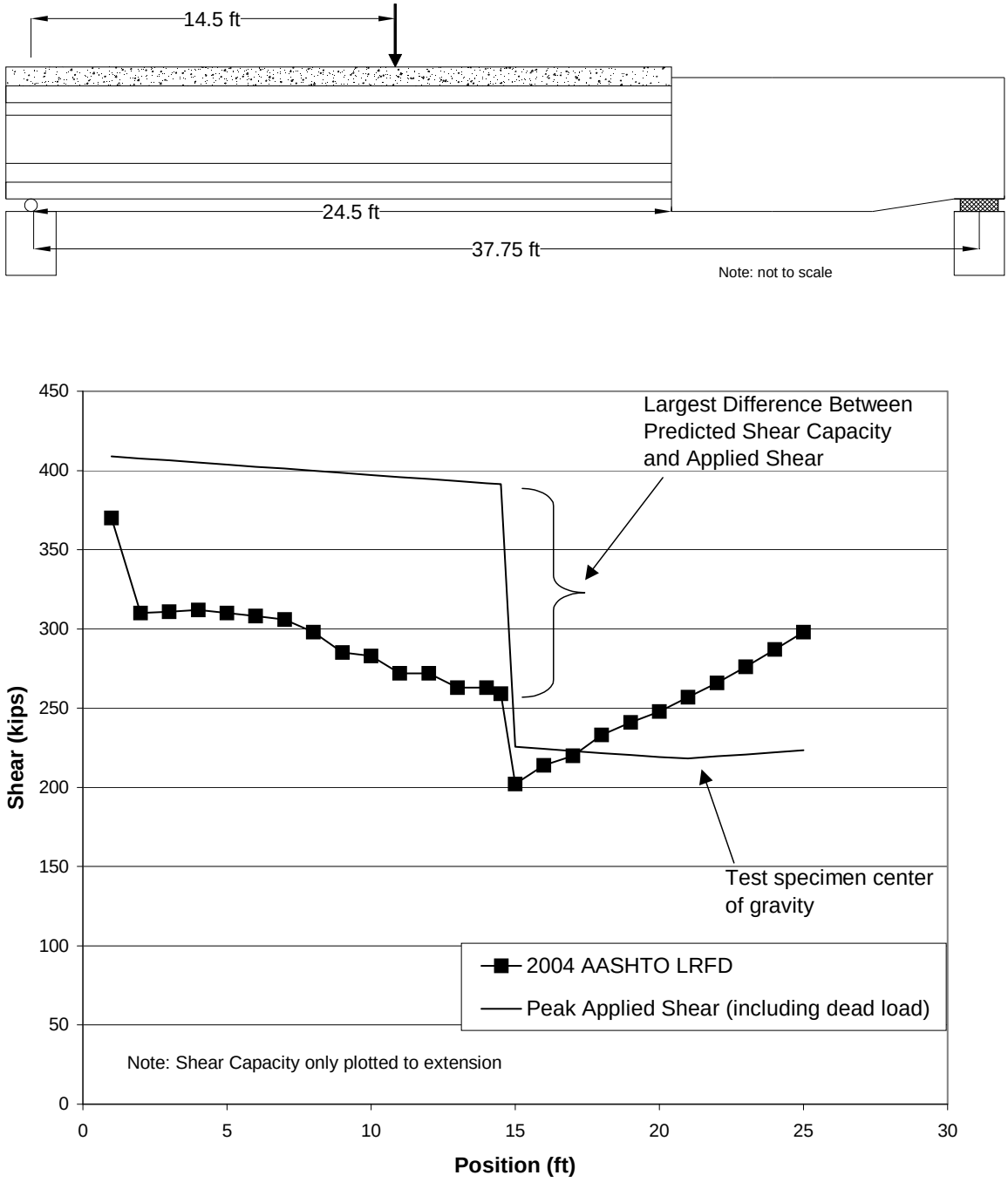

Figure 6.11 AASHTO 2004 LRFD Predicted Shear Capacity vs. Position (Specimen I)

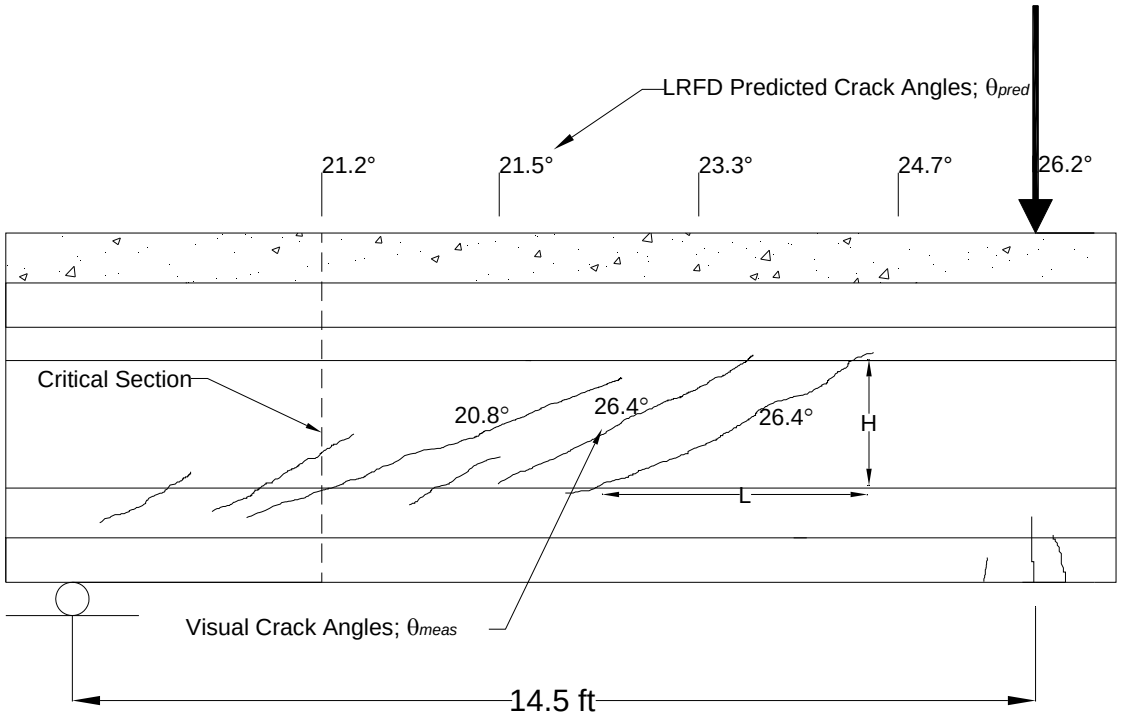

Figure 6.12 Visual Crack Angle Measurements at First Cracking

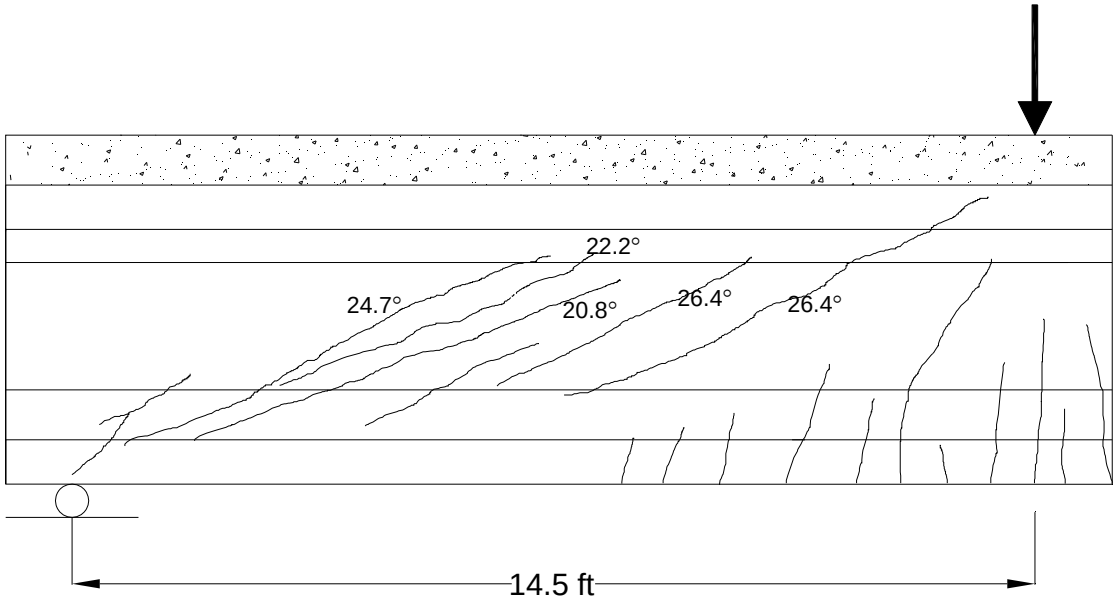

Figure 6.13 Visual Crack Angle Measurements at Peak Load

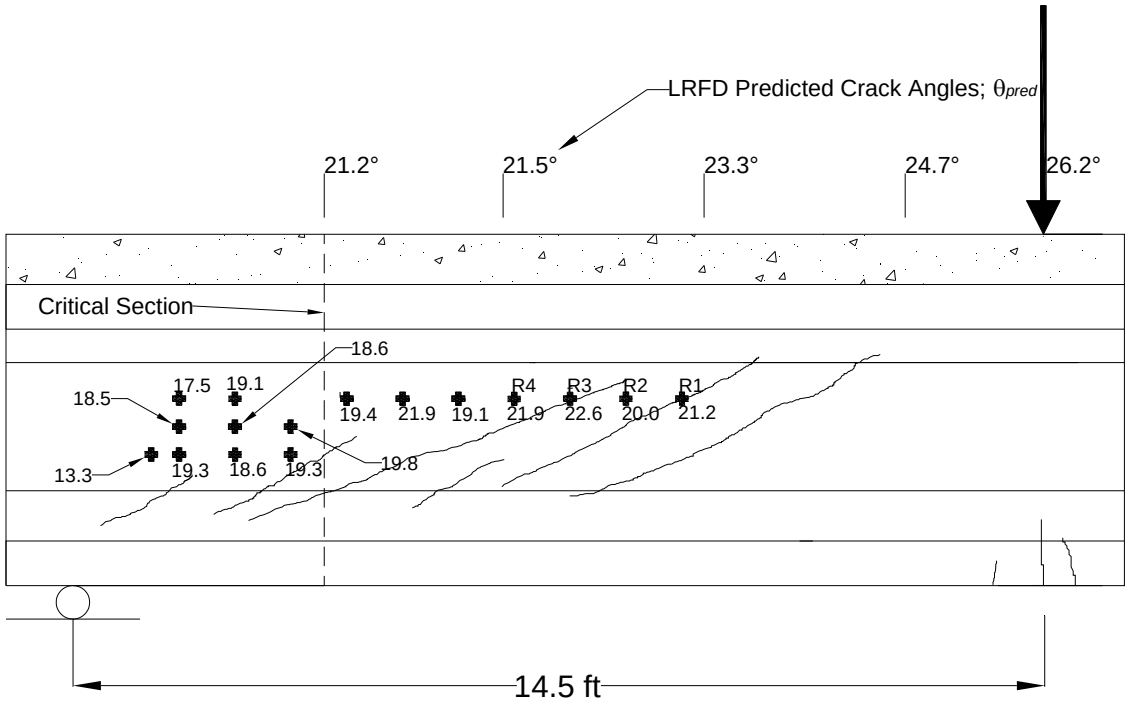

Figure 6.14 Rosette Crack Angle Measurements at First Cracking

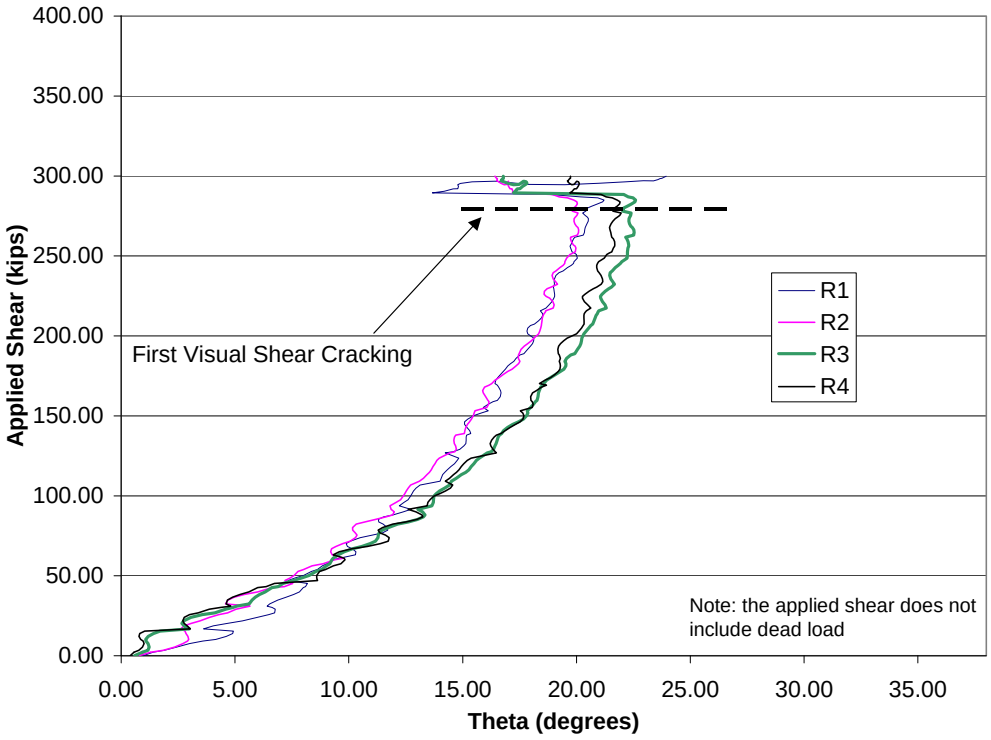

Figure 6.15 θ_{meas} from Four Rosette Strain Gages Closest to Applied Load (First Test, Specimen I)

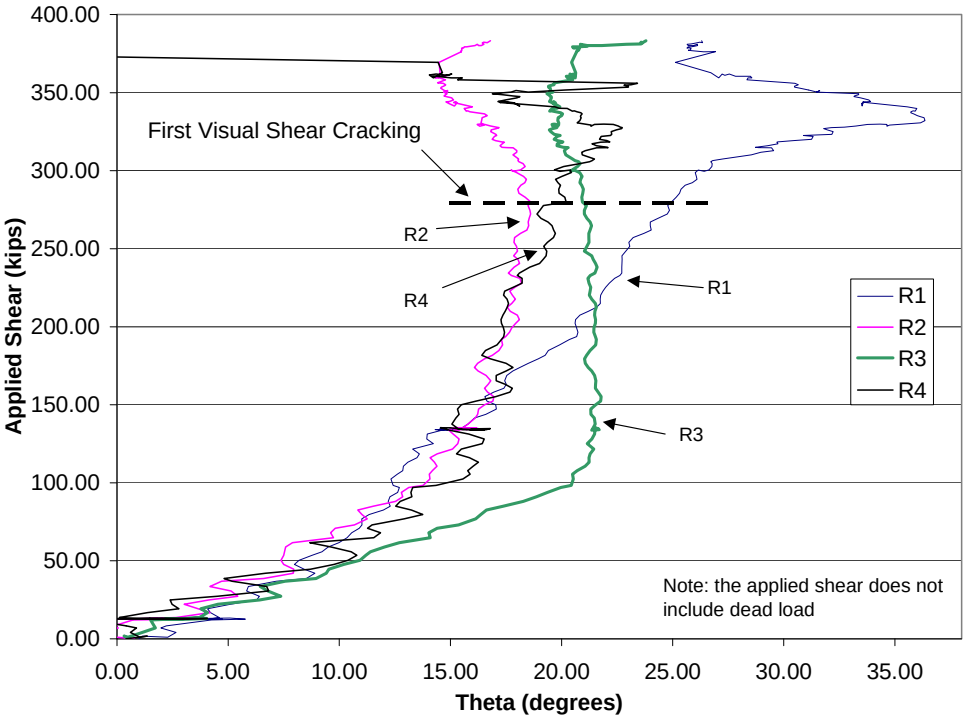

Figure 6.16 θ_{meas} from Four Rosette Strain Gages Closest to Applied Load (Second Test, Specimen I)

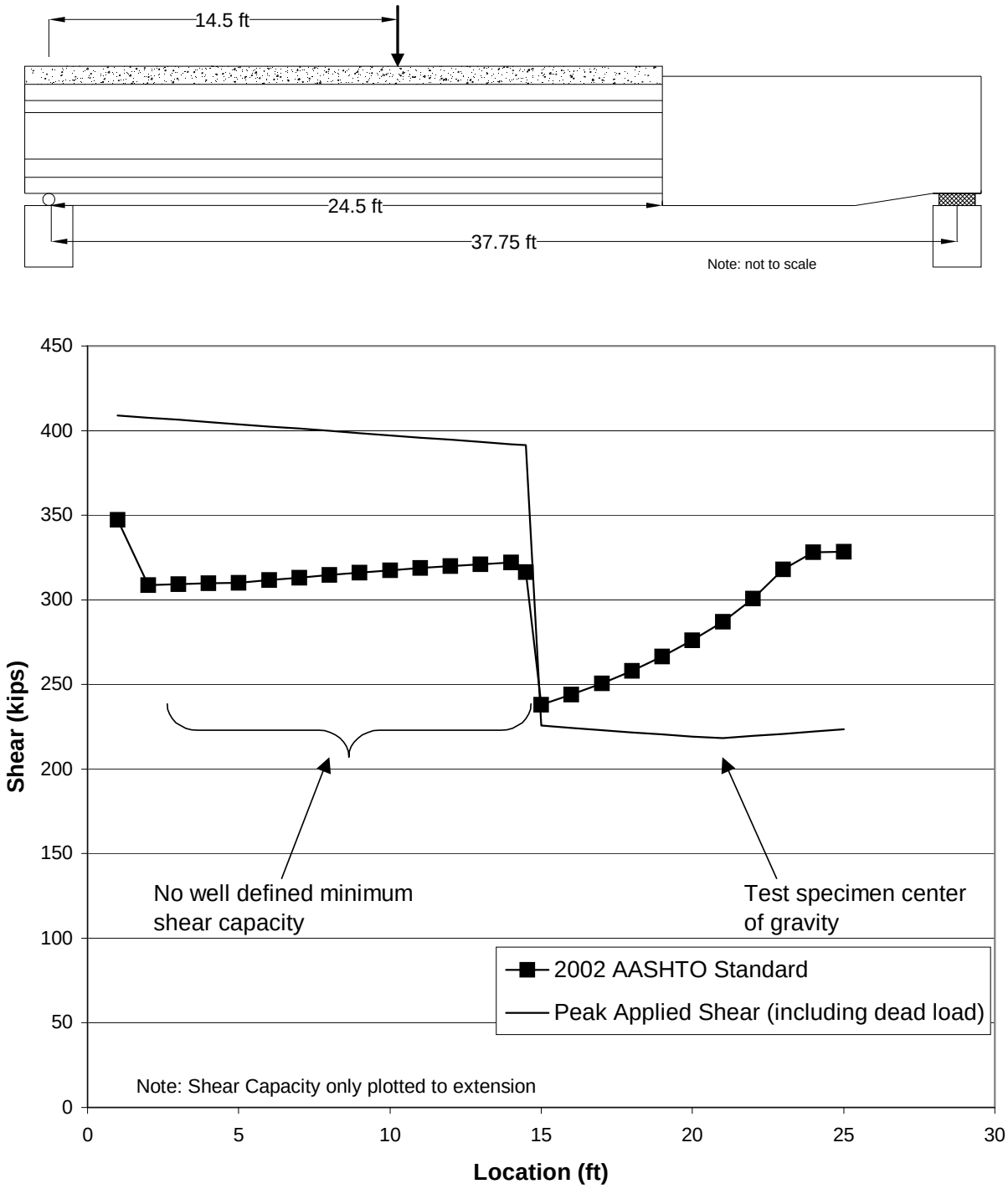

Figure 6.17 AASHTO 2002 Standard Predicted Shear Capacity vs. Position

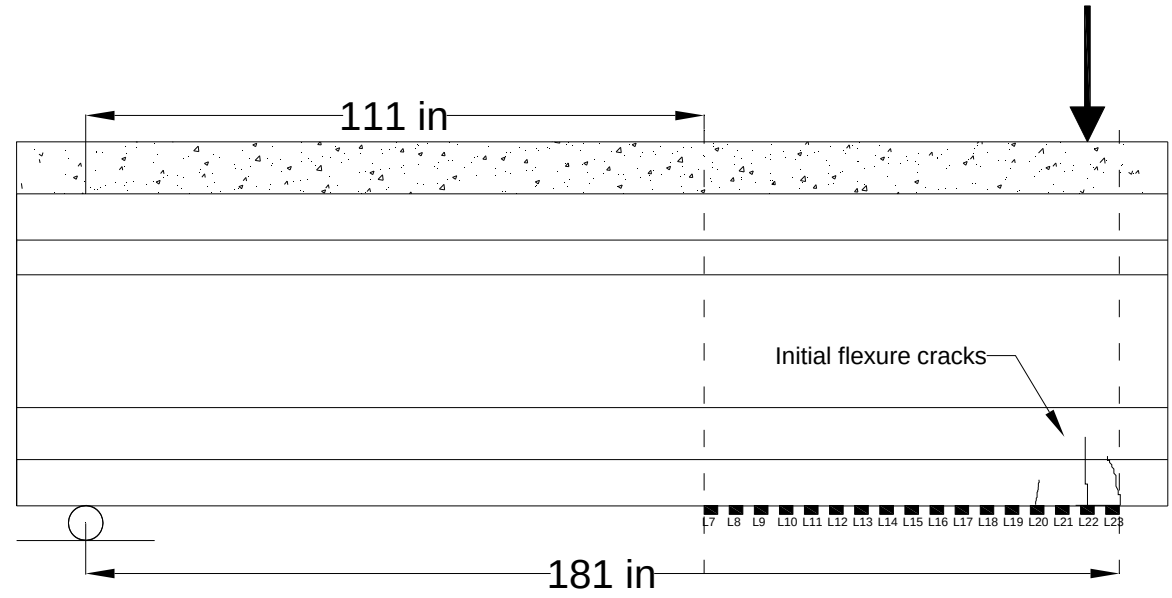

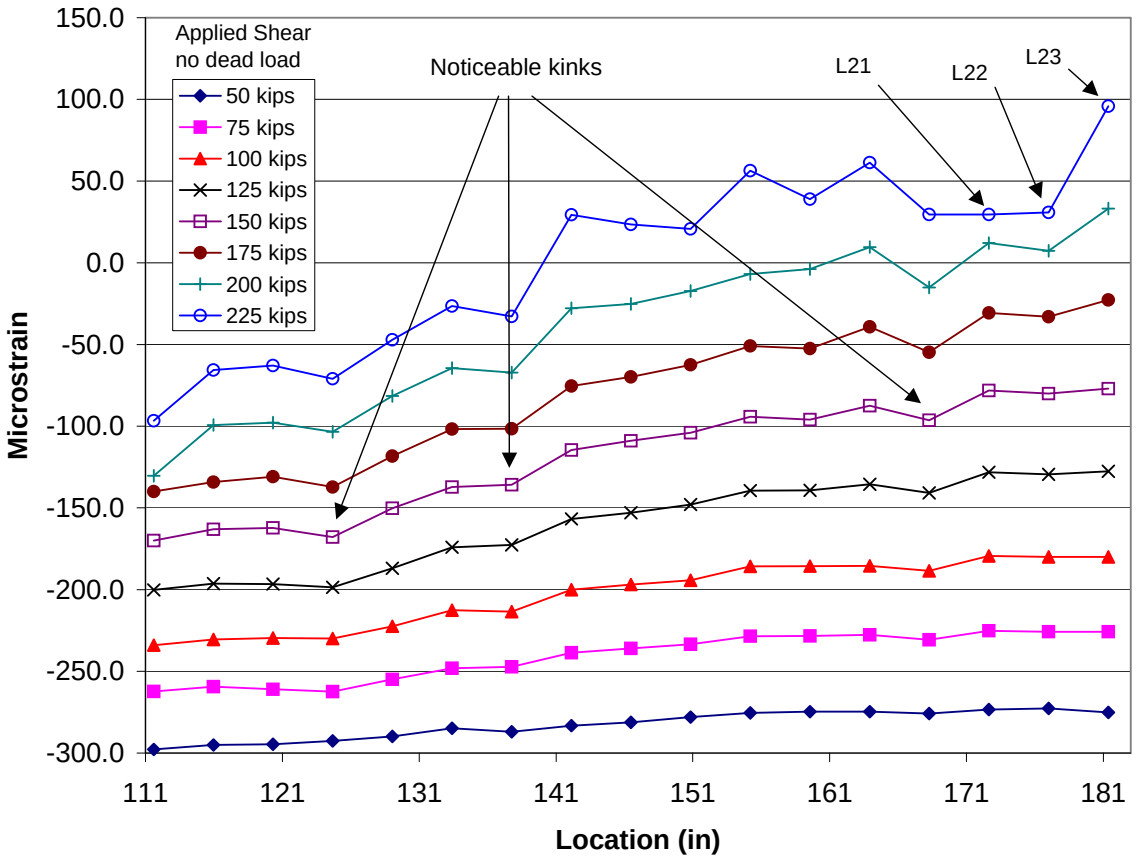

Figure 6.18 Strain Profile Along Bottom Flange (Specimen I)

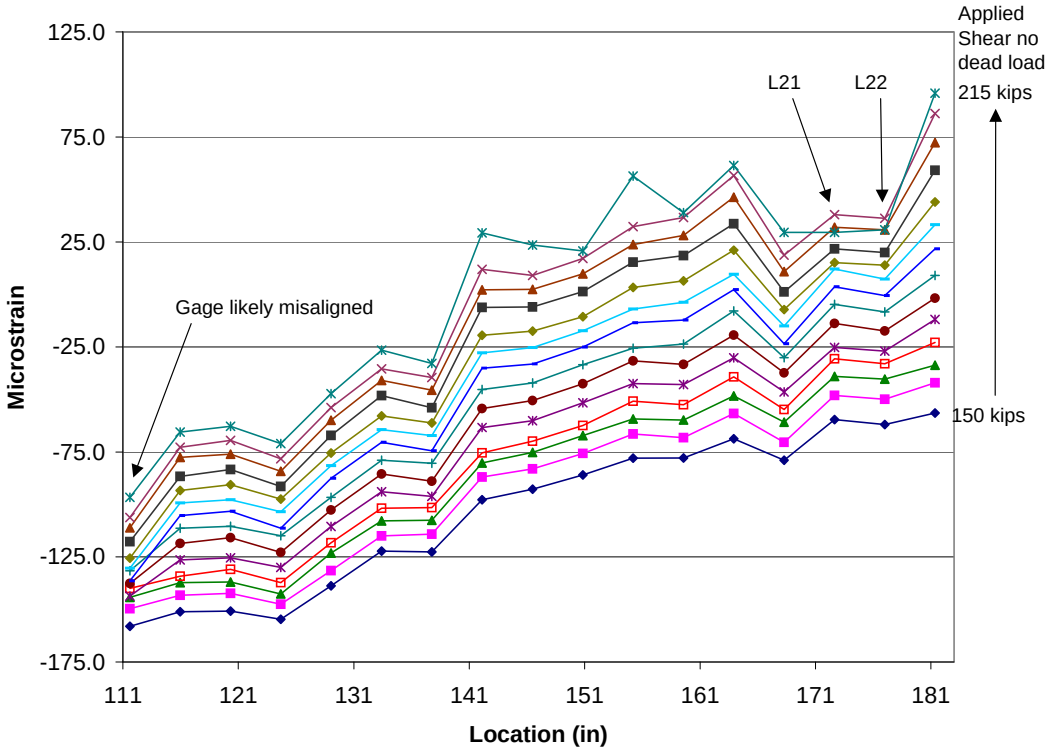

Figure 6.19 Strain Profile in Increments of 5 kips of Applied Shear Between 150 kips and 215 kips

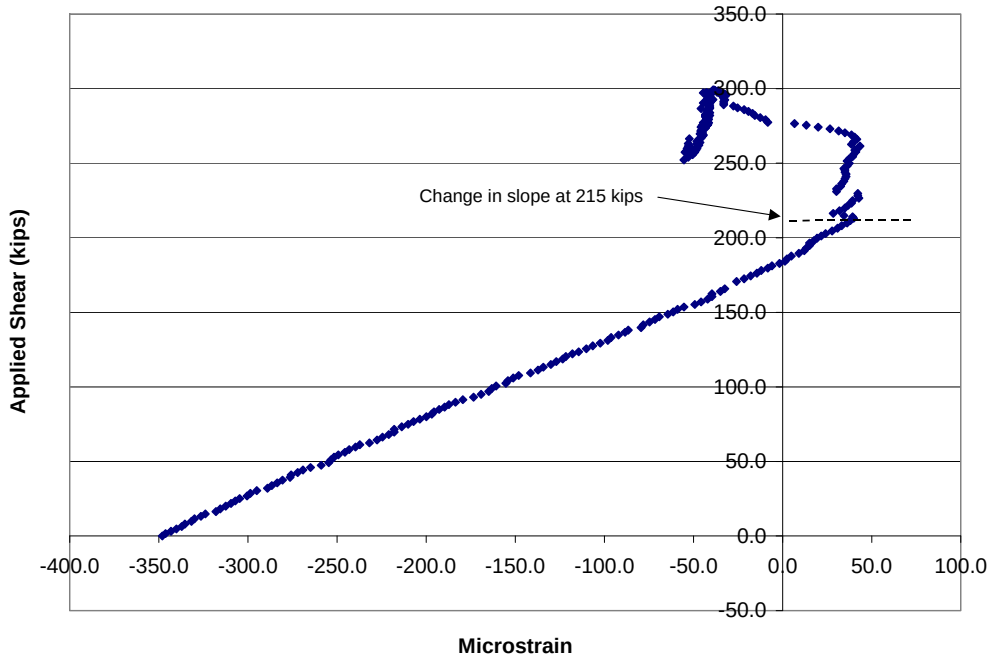

Figure 6.20 Horizontal Gage L21

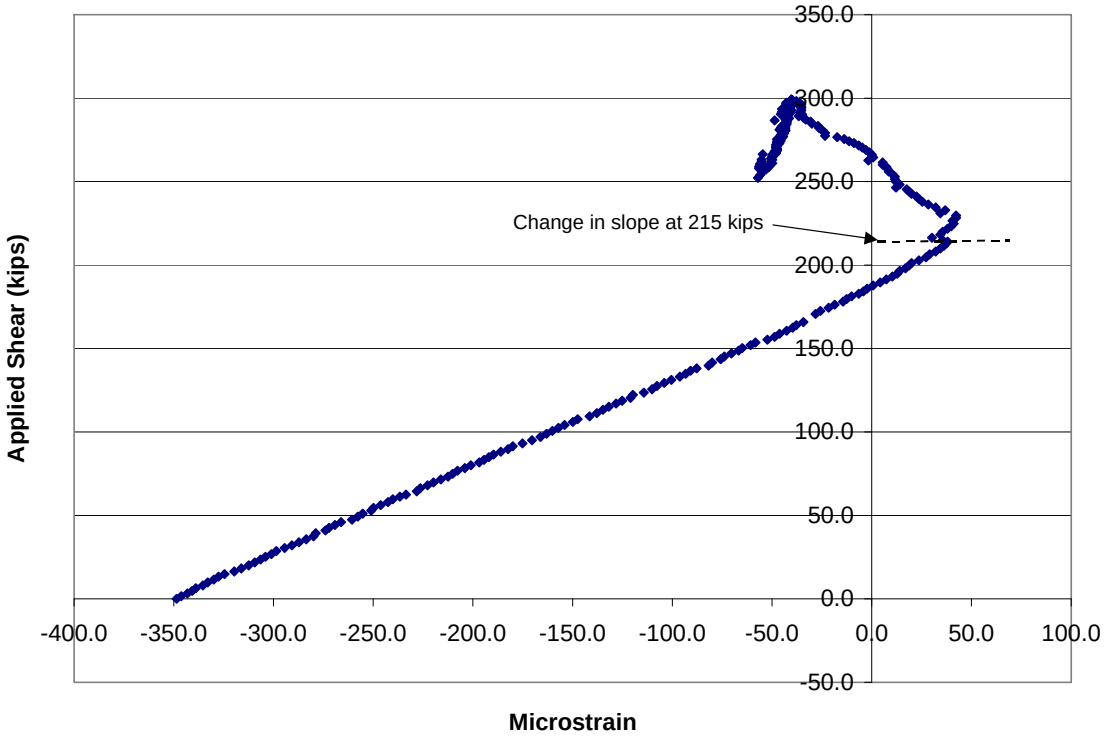

Figure 6.21 Horizontal Gage L22

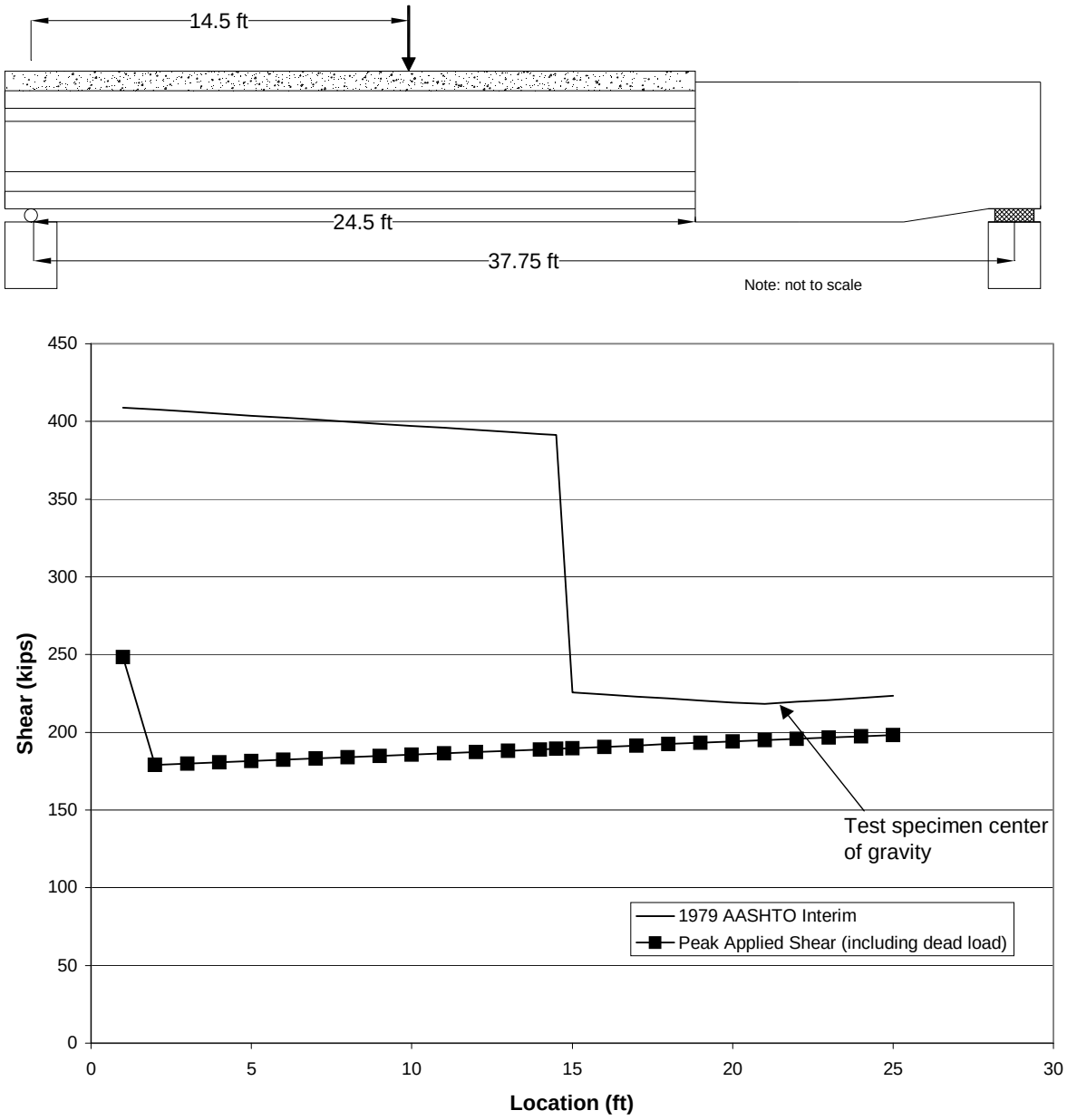

Figure 6.22 AASHTO 1979 Interim Predicted Shear Capacity vs. Position

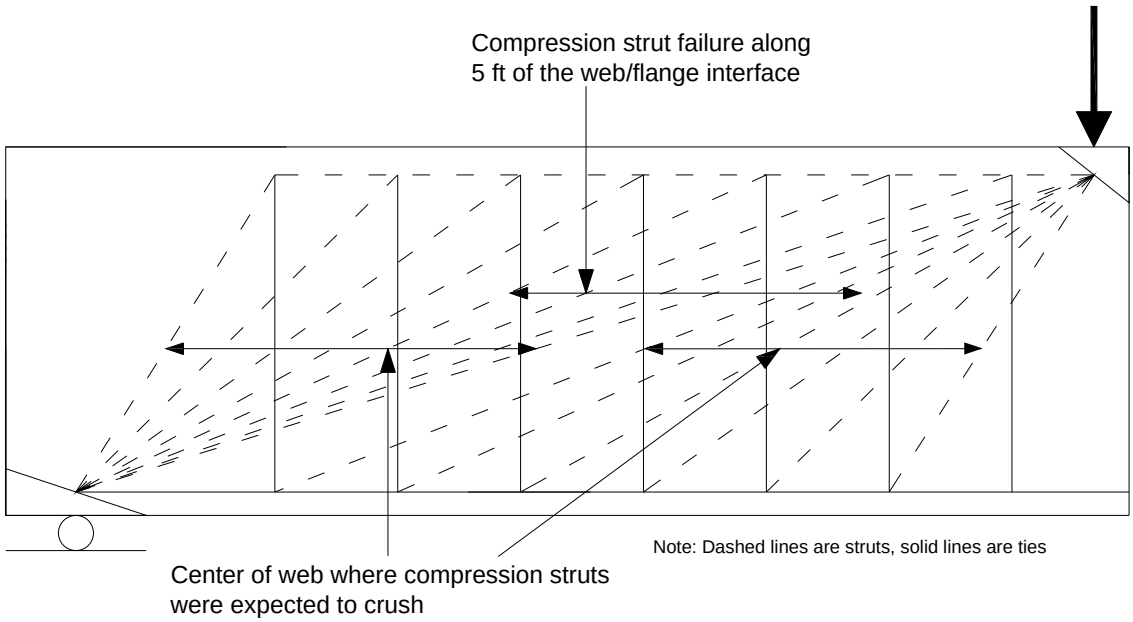

Figure 6.23 Observed Area of Compressive Strut Failure

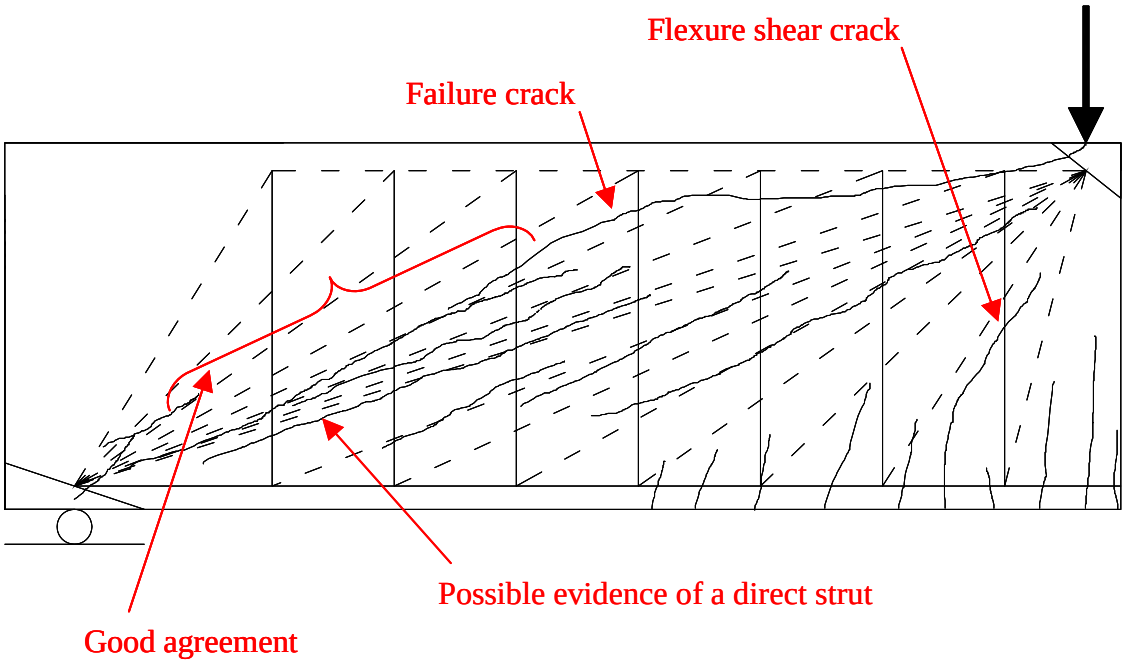

Figure 6.24 Strut and Tie Model and Cracking at 40% Past Peak Applied Load (Specimen I)

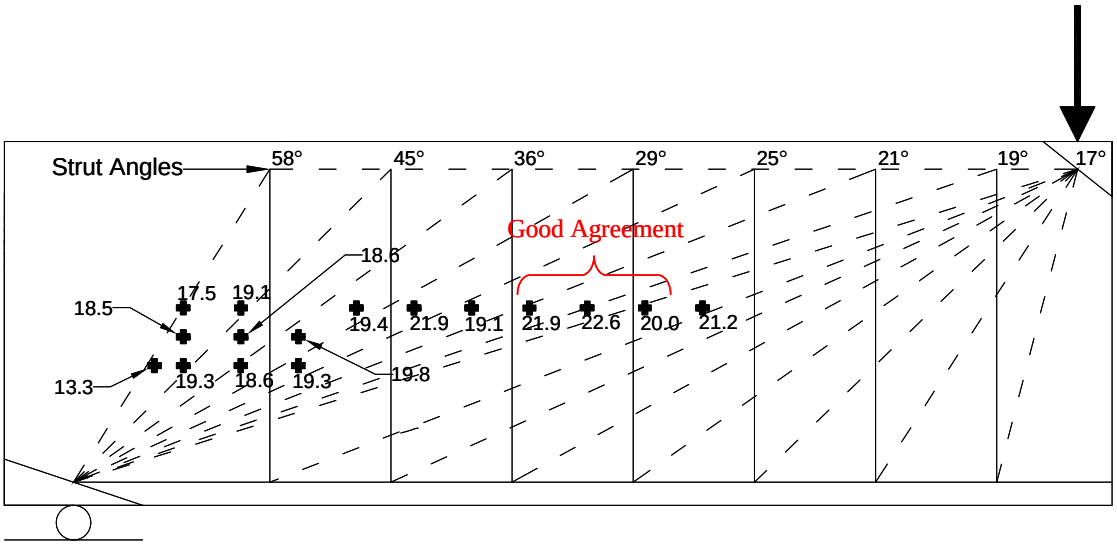

Figure 6.25 Strut and Tie Model With Rosettes at Initial Cracking

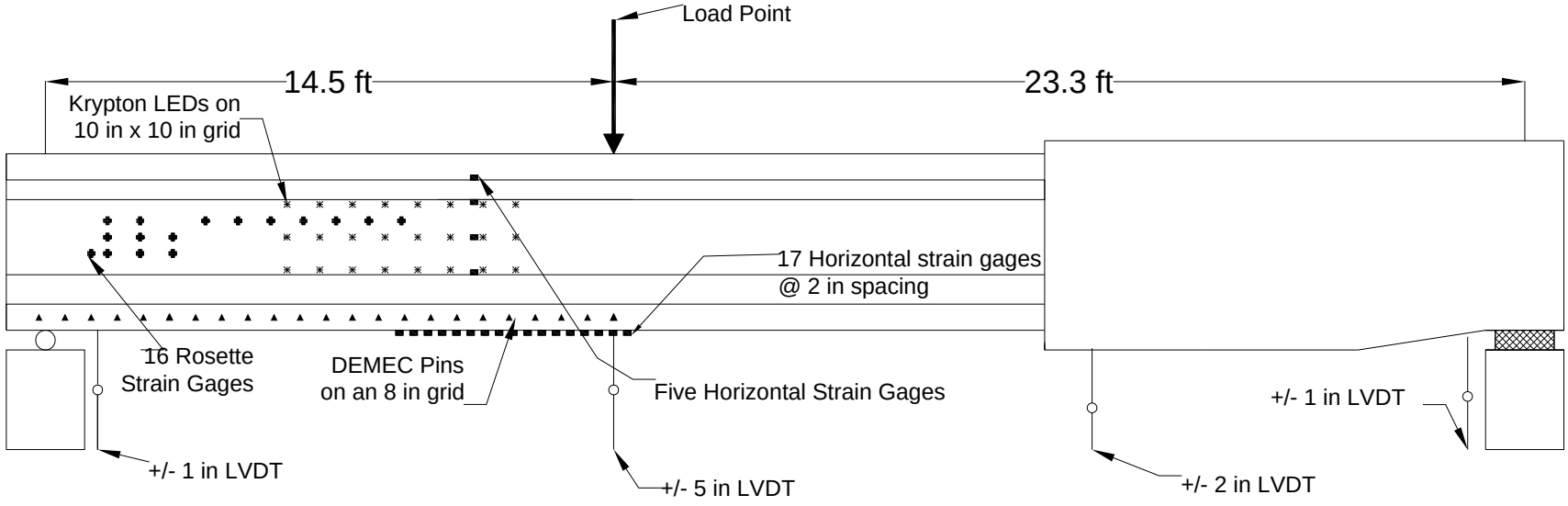

Figure 6.26 Revised Instrumentation Layout (Specimen II)

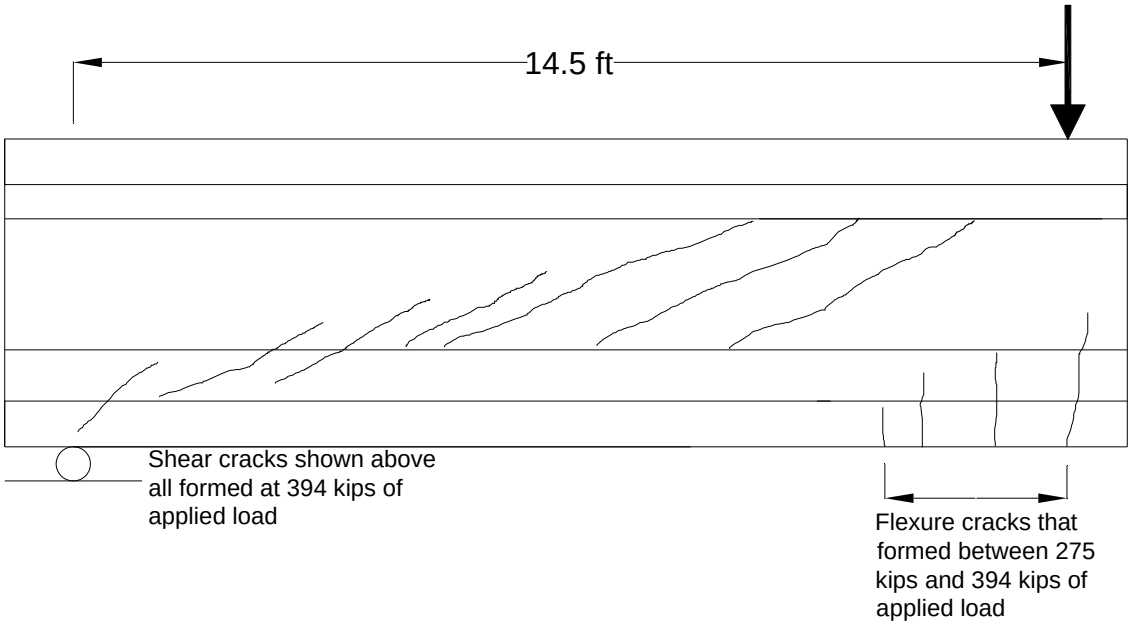

Figure 6.27 Initial Web Cracking (Specimen II)

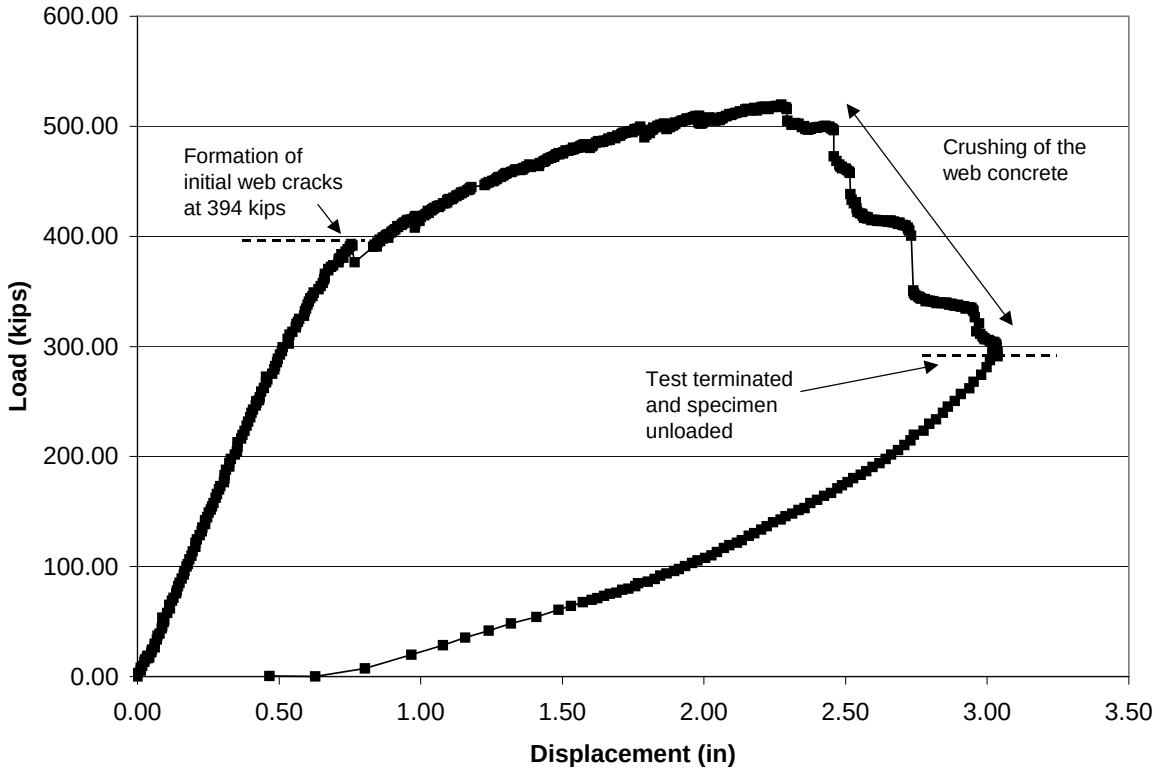

Figure 6.28 Load vs. Displacement (Specimen II)

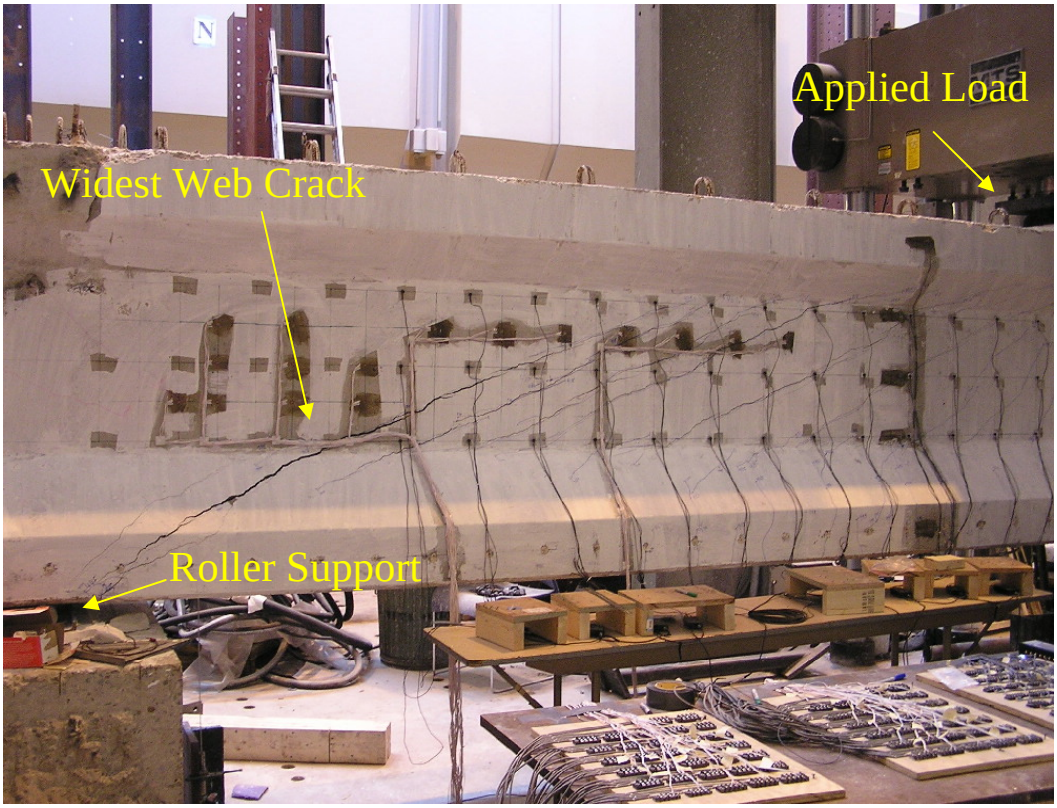

Figure 6.29 Photograph of Cracking at Peak Load (Specimen II)

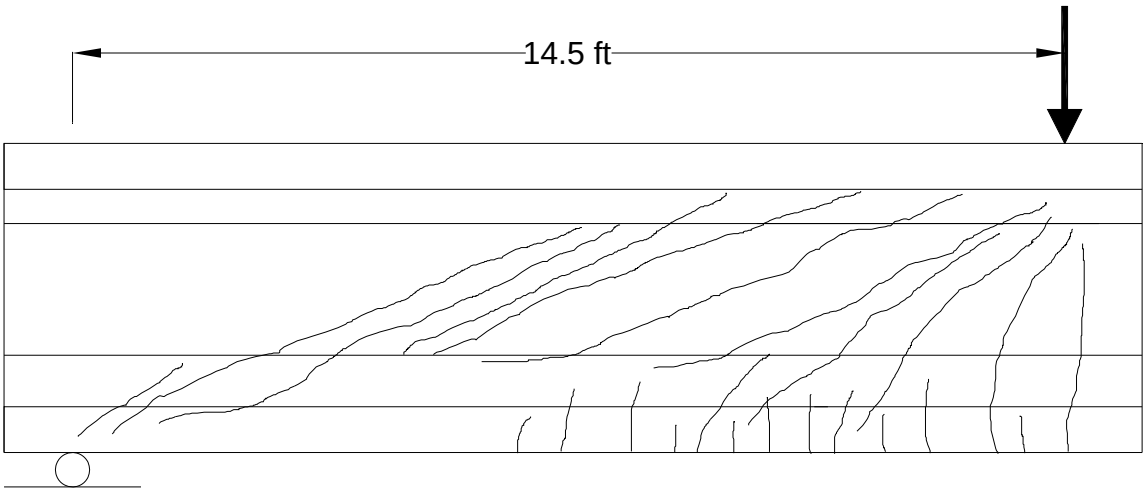

Figure 6.30 Cracking at Peak Load (Specimen II)

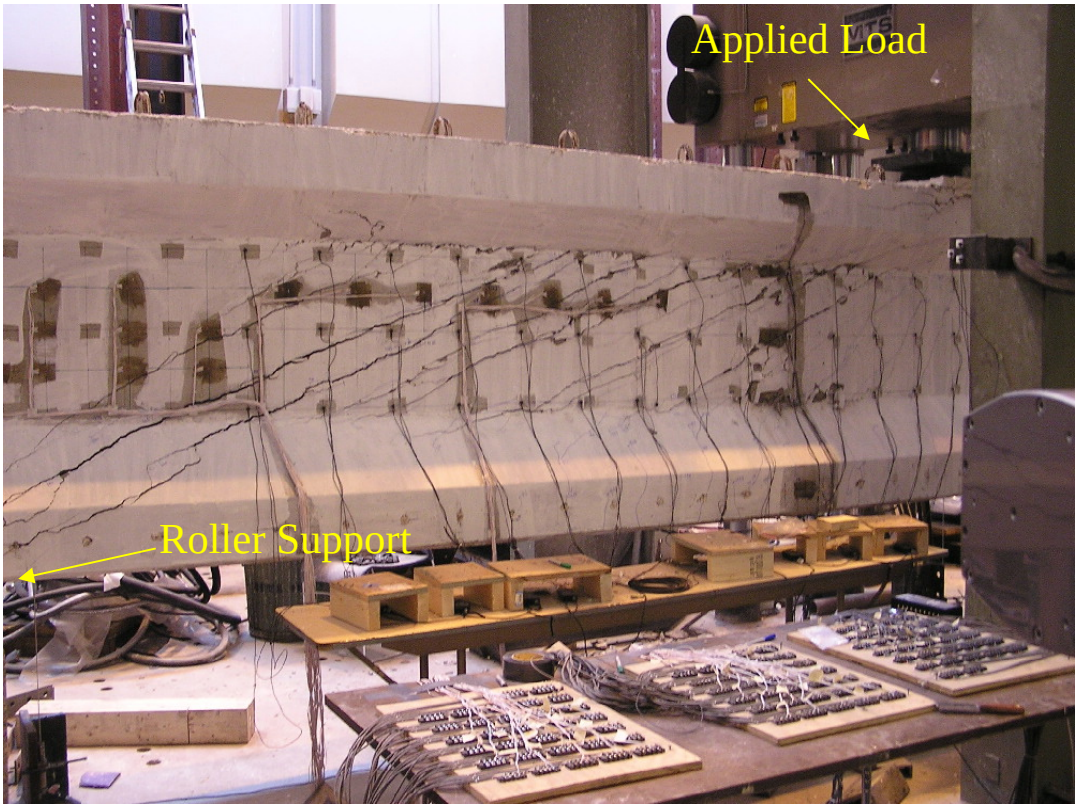

Figure 6.31 Photograph of Cracking at 44% Past Peak Applied Load (Specimen II)

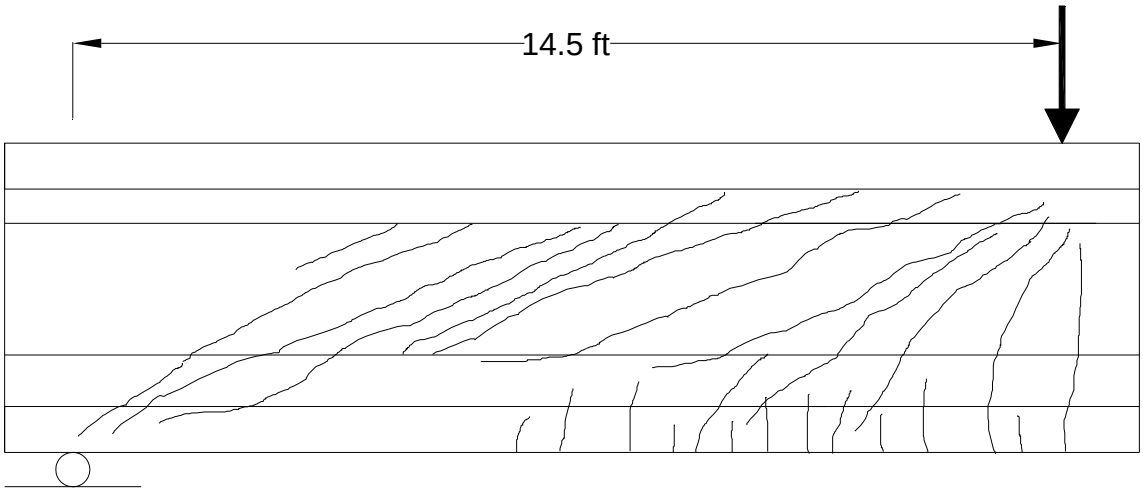

Figure 6.32 Cracking at 44% Past Peak Applied Load (Specimen II)

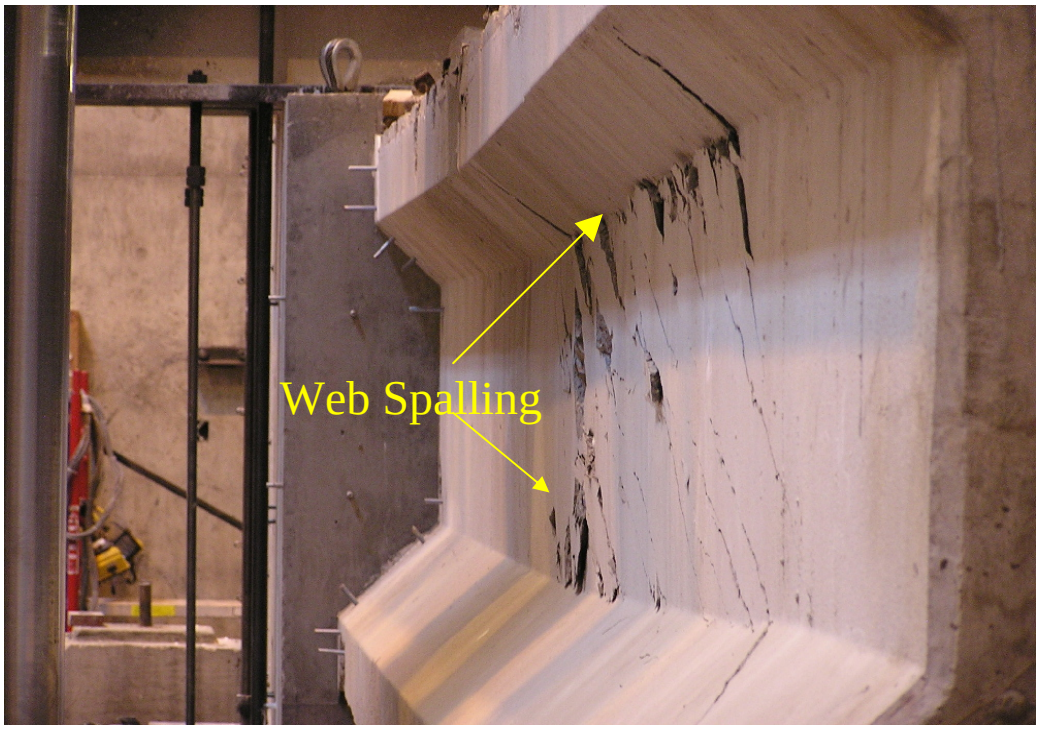

Figure 6.33 Web Crushing (Specimen II)

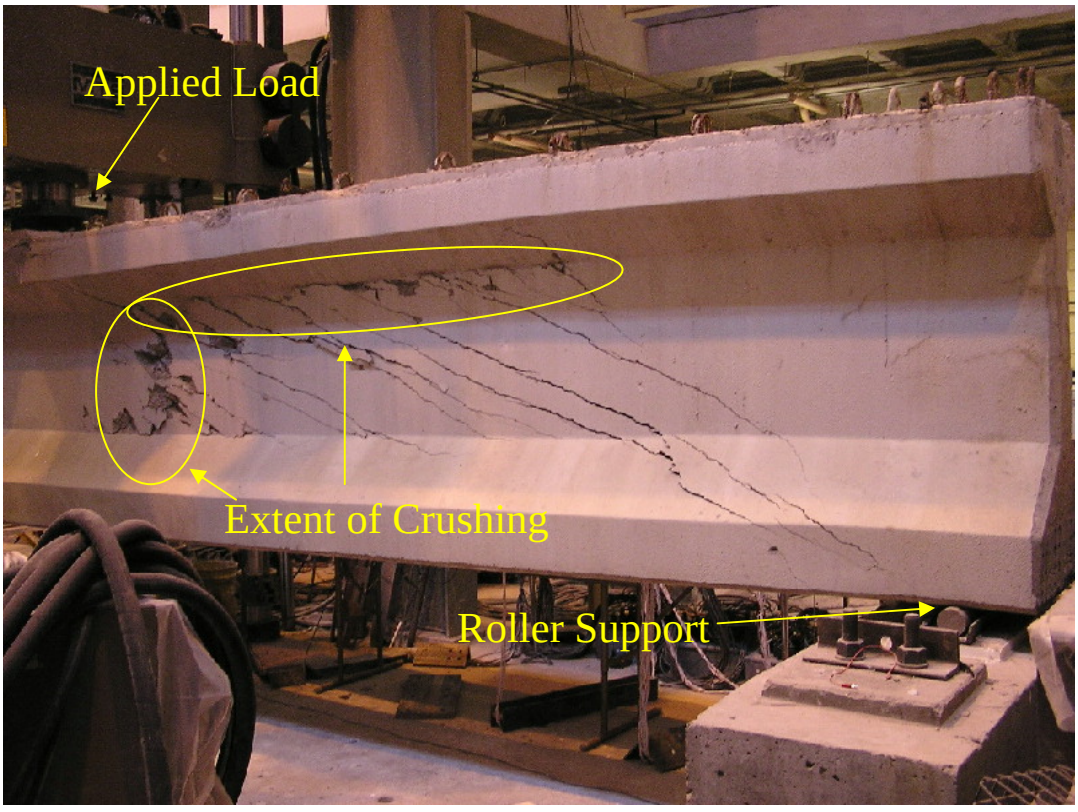

Figure 6.34 Extent of Web Crushing (Specimen II)

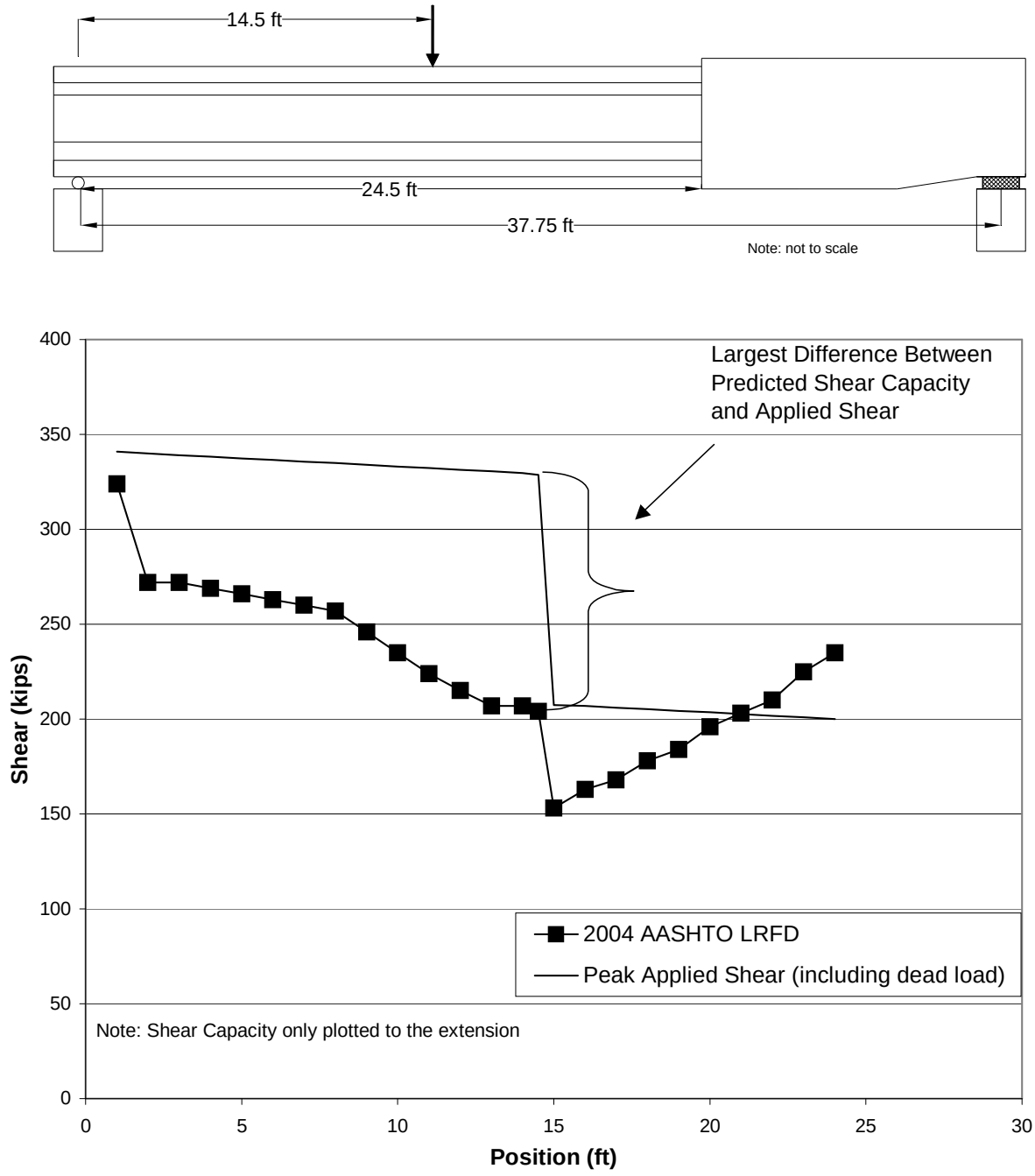

Figure 6.35 AASHTO 2004 LRFD Predicted Shear Capacity vs. Position (Specimen II)

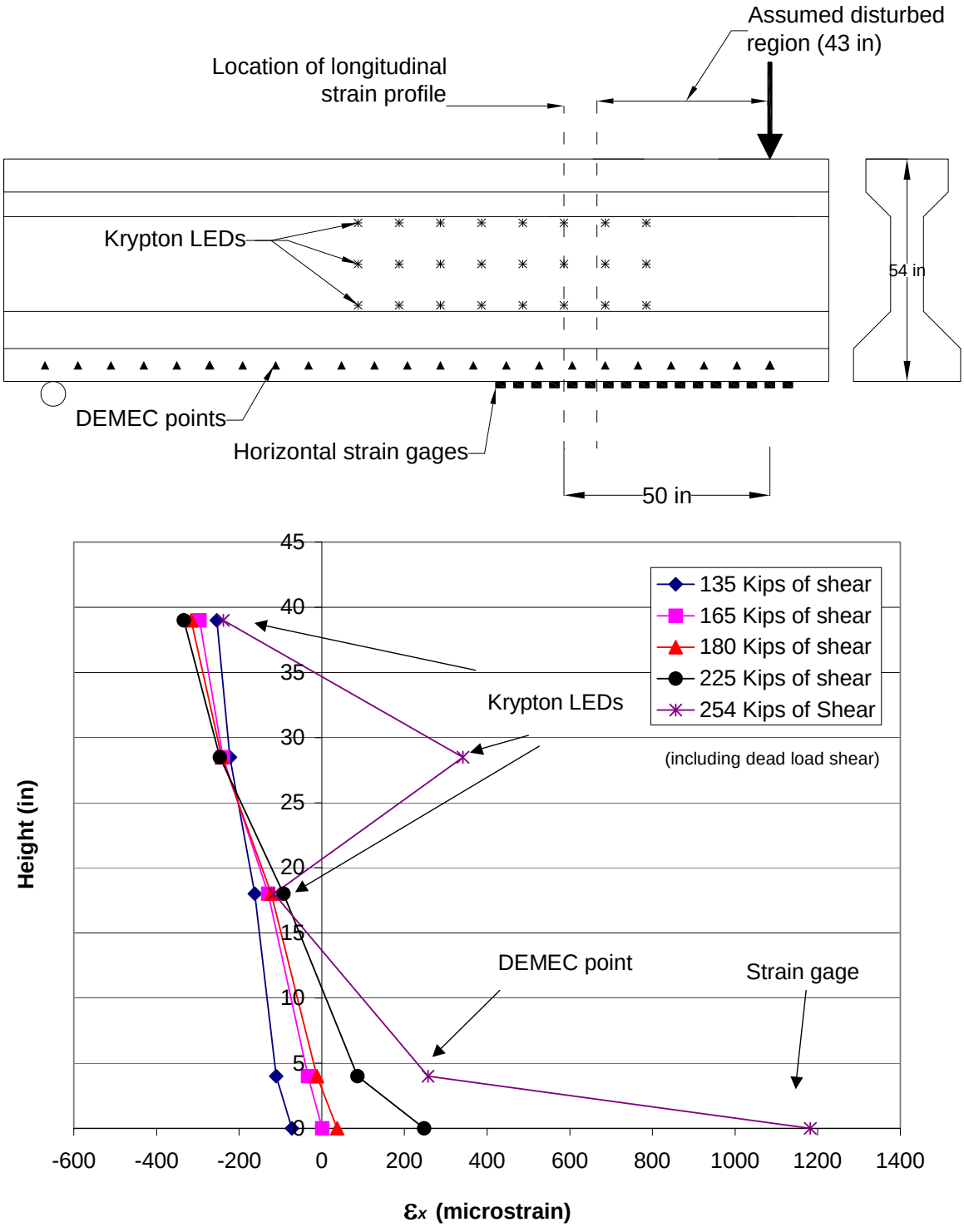

Figure 6.36 Longitudinal Strain Profile 50 in. from Applied Load

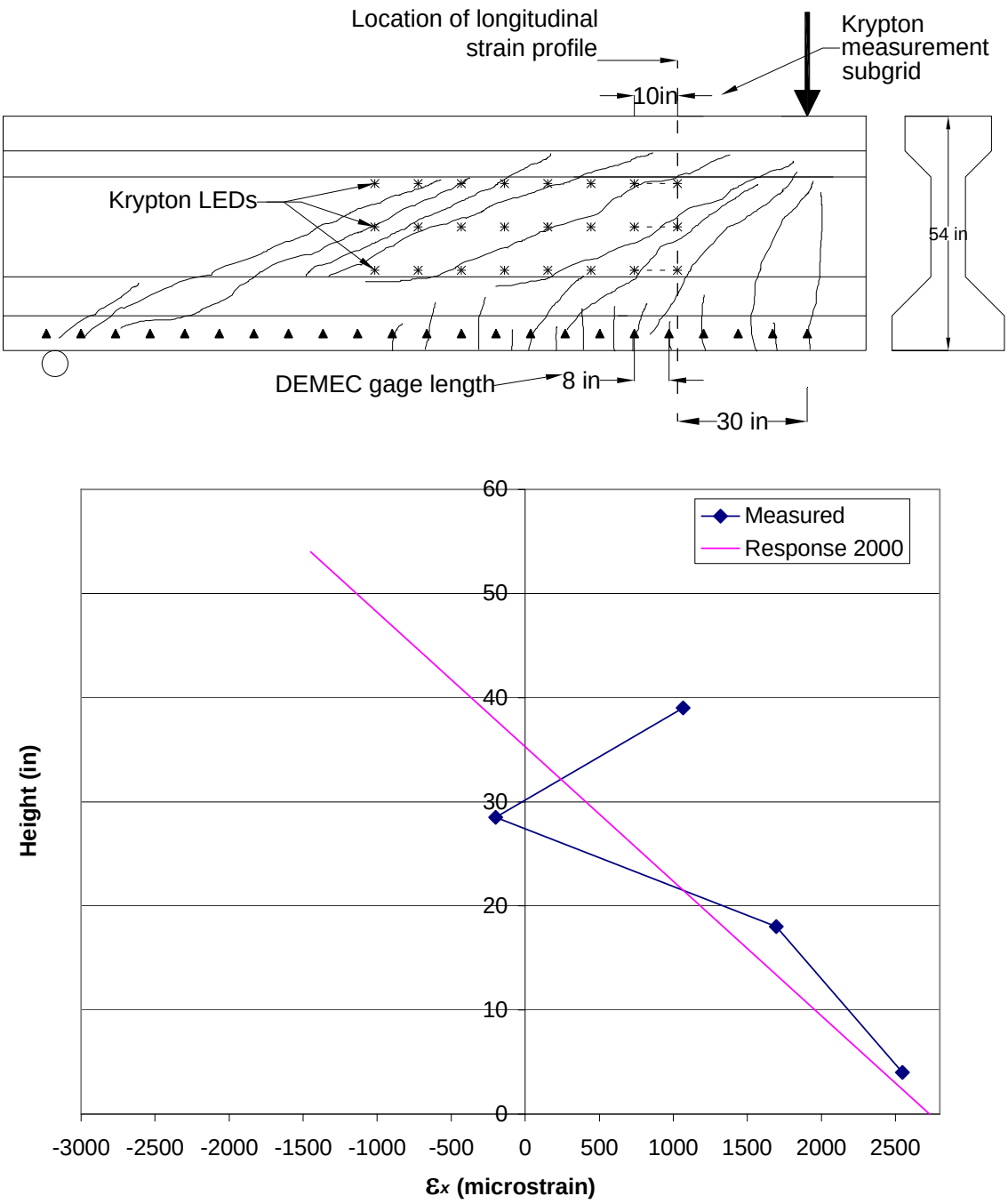

Figure 6.37 Longitudinal Strain Profile 30 in. from Applied Load at Peak Applied Shear

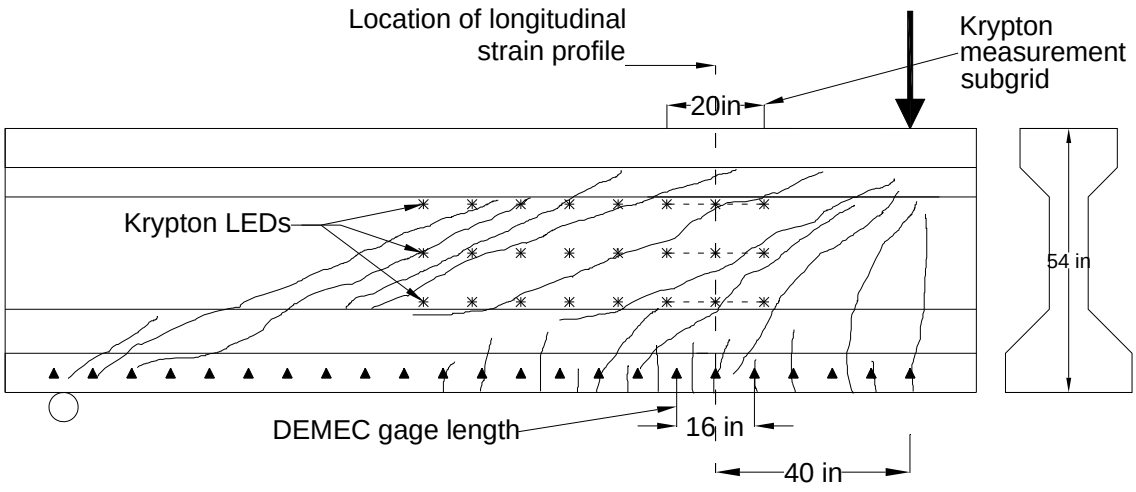

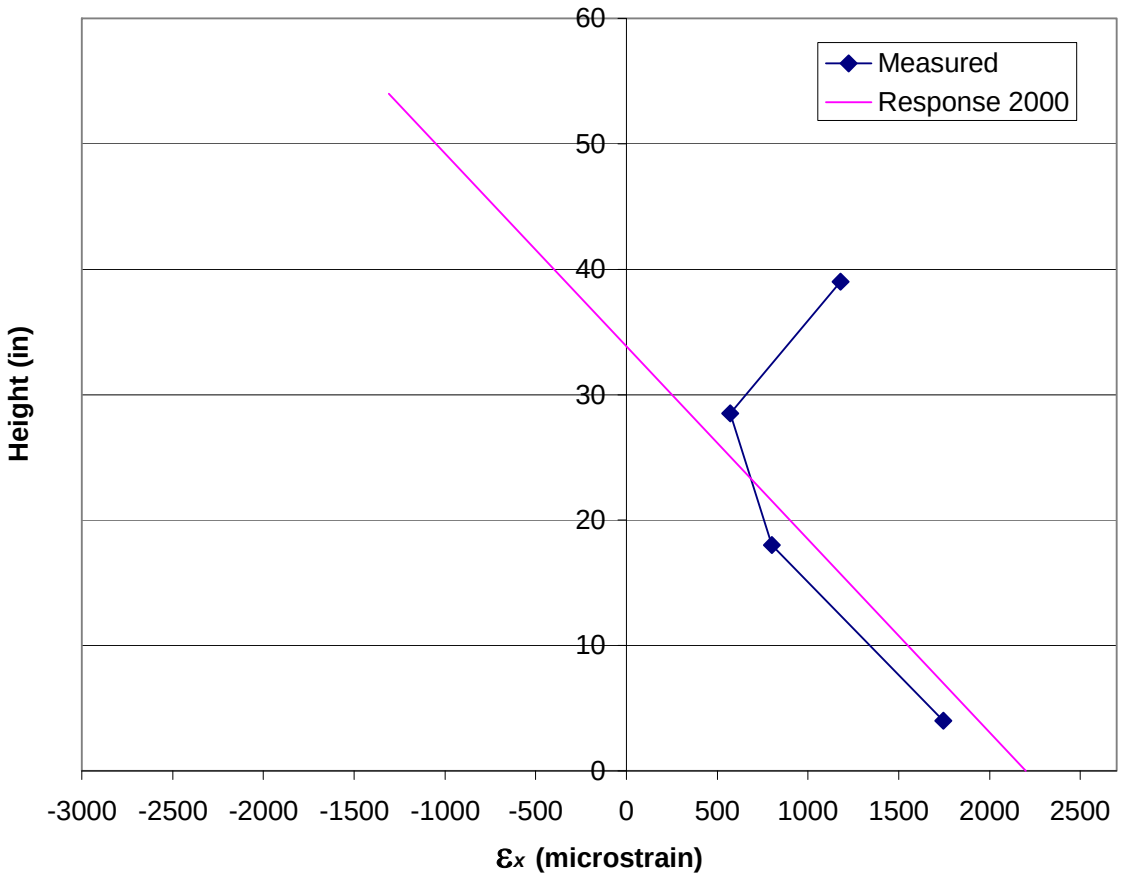

Figure 6.38 Longitudinal Strain Profile 40 in. from Applied Load at Peak Applied Shear

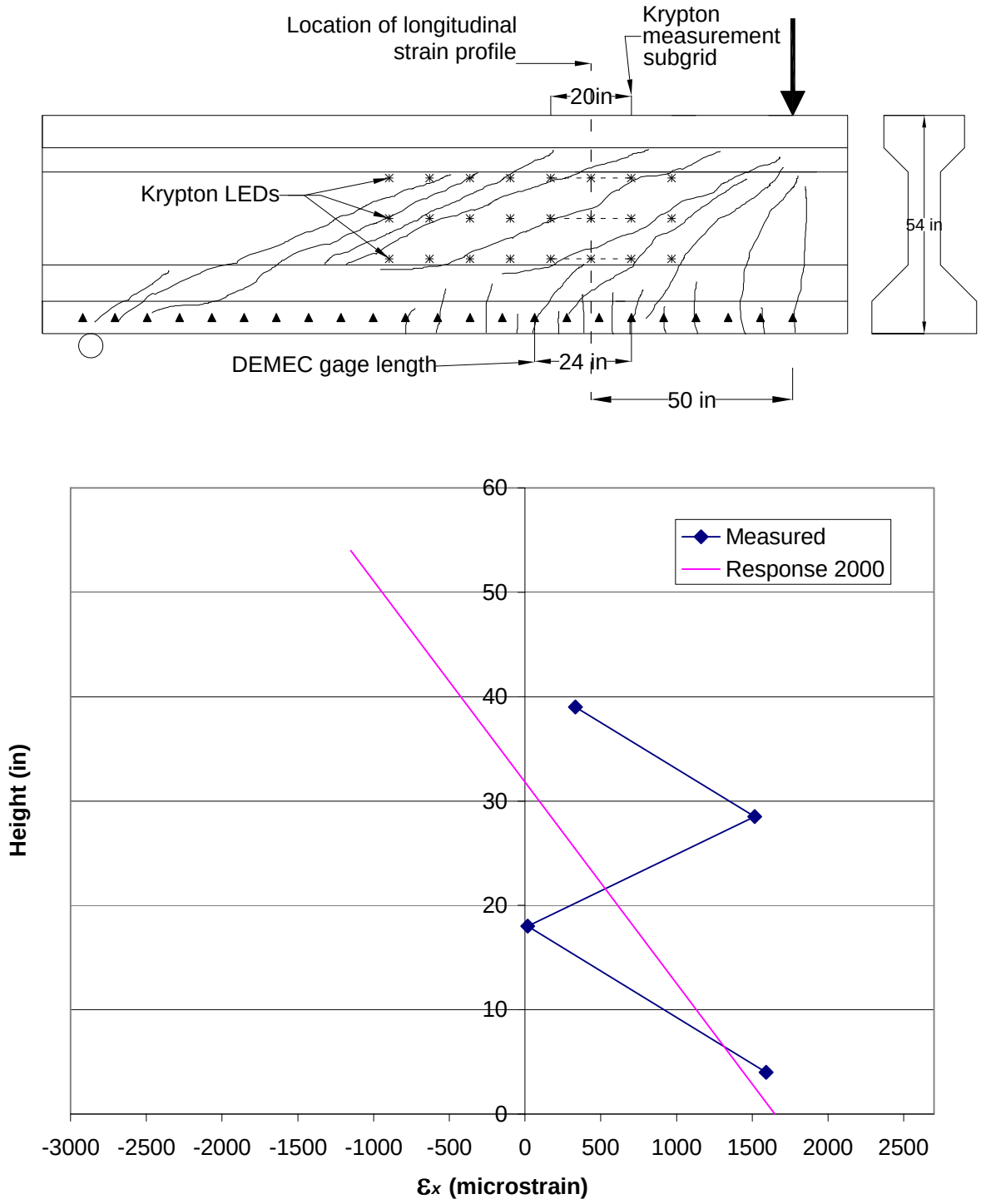

Figure 6.39 Longitudinal Strain Profile 50 in. from Applied Load at Peak Applied Shear

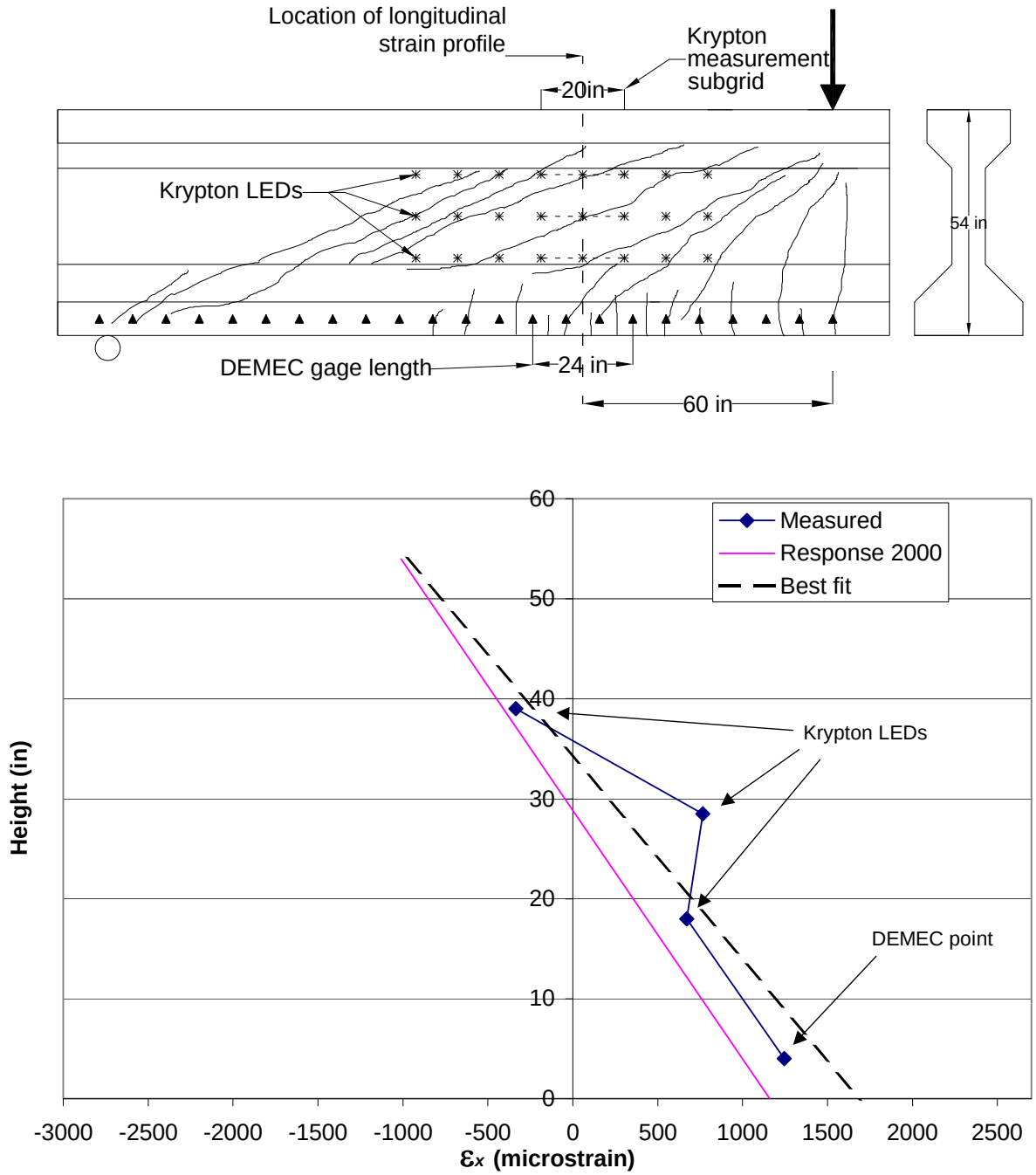

Figure 6.40 Longitudinal Strain Profile 60 in. from Applied Load at Peak Applied Shear

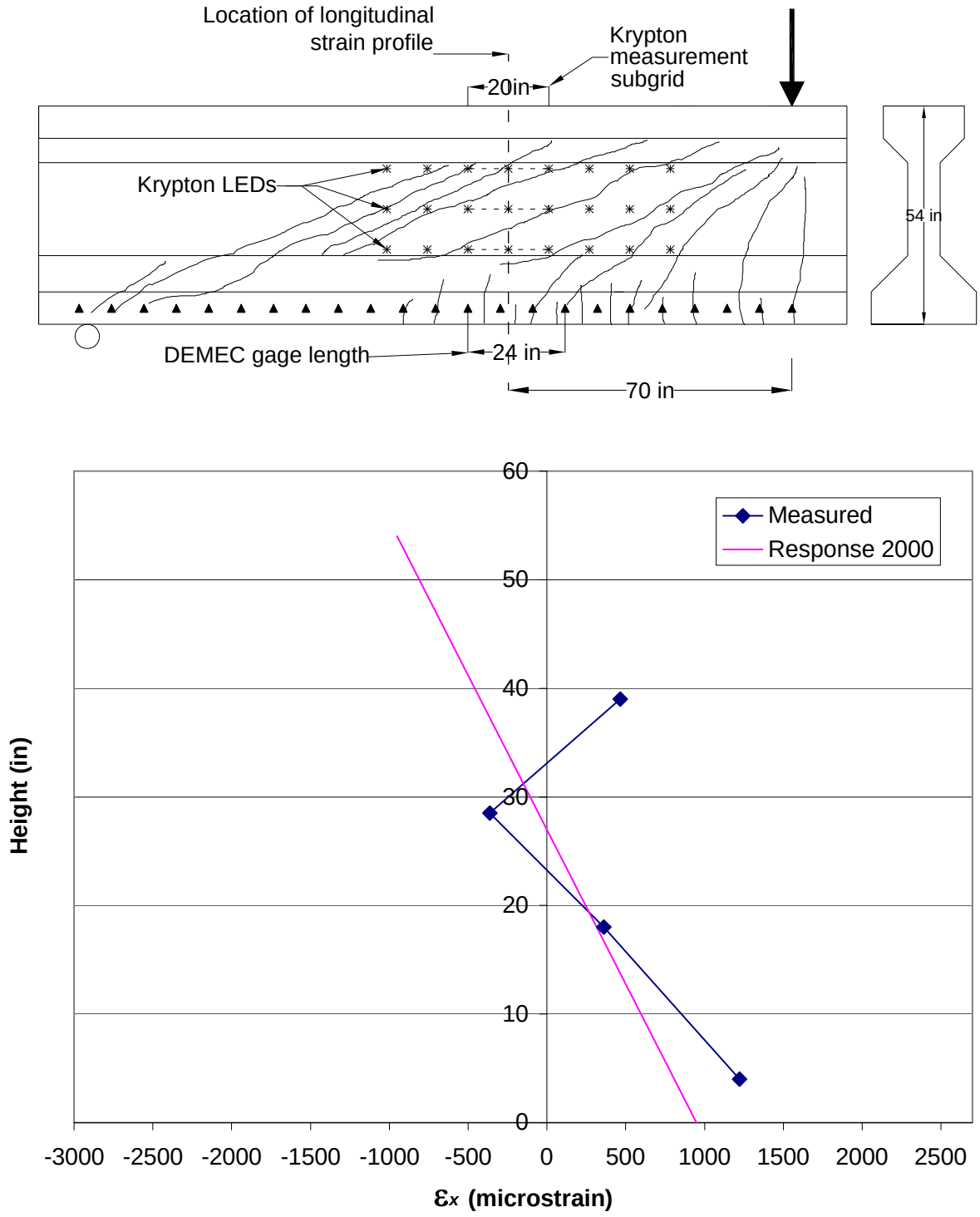

Figure 6.41 Longitudinal Strain Profile 70 in. from Applied Load at Peak Applied Shear

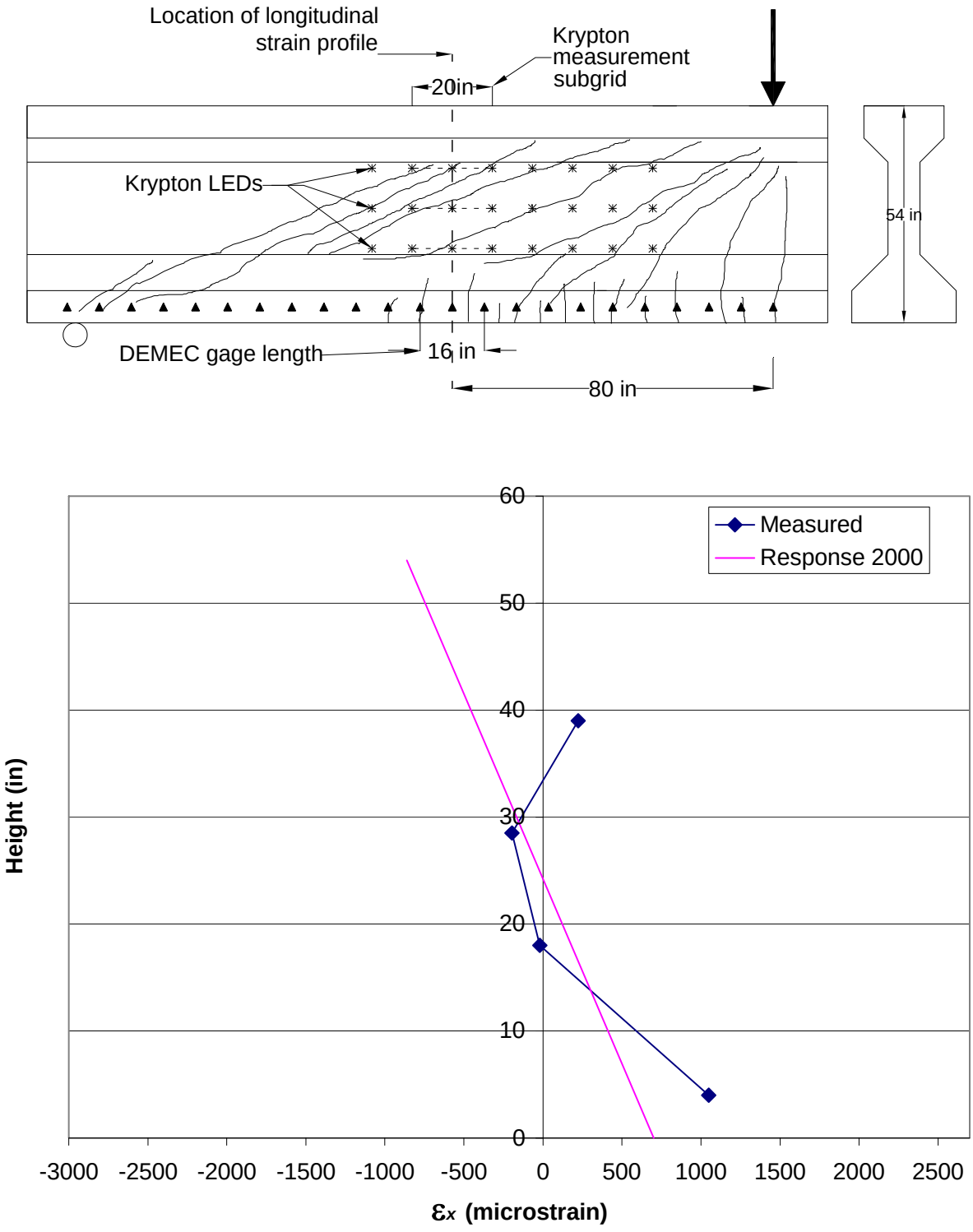

Figure 6.42 Longitudinal Strain Profile 80 in. from Applied Load at Peak Applied Shear

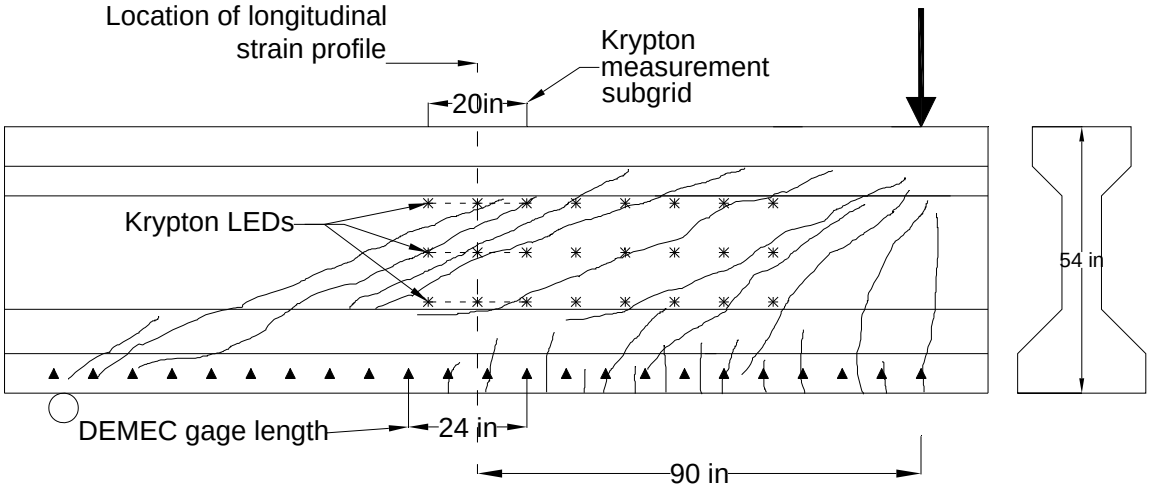

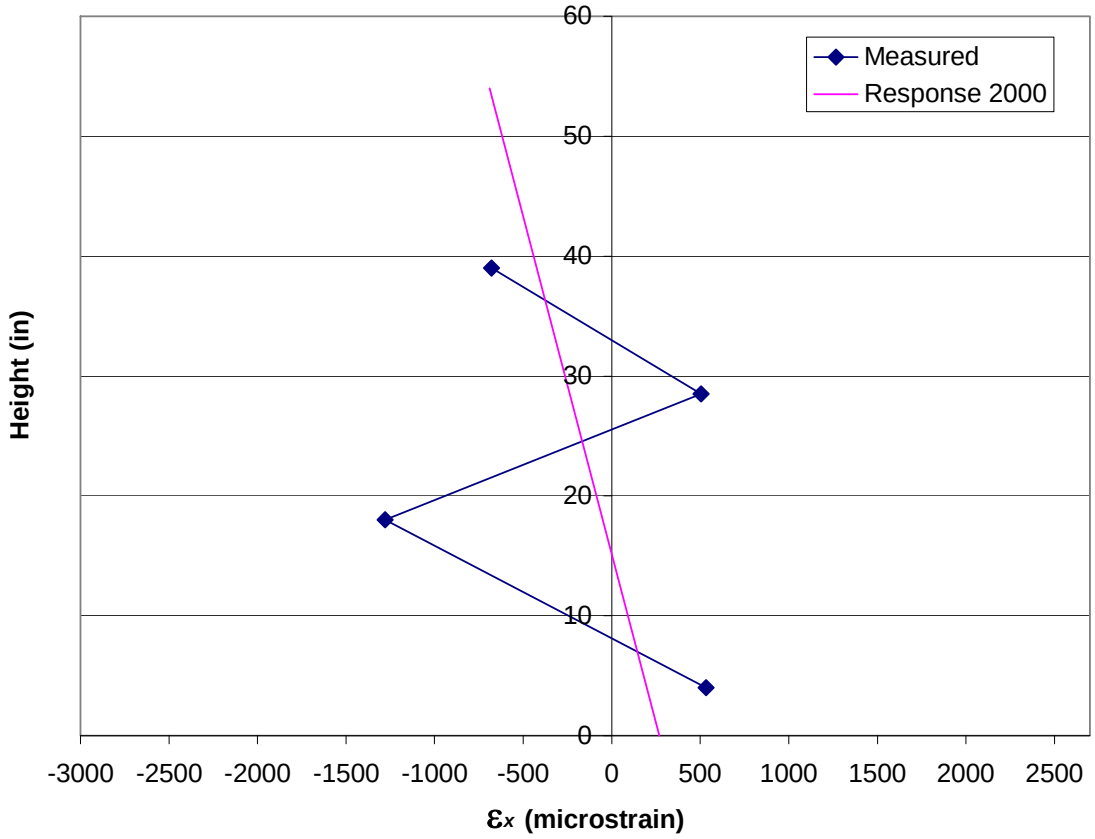

Figure 6.43 Longitudinal Strain Profile 90 in. from Applied Load at Peak Applied Shear

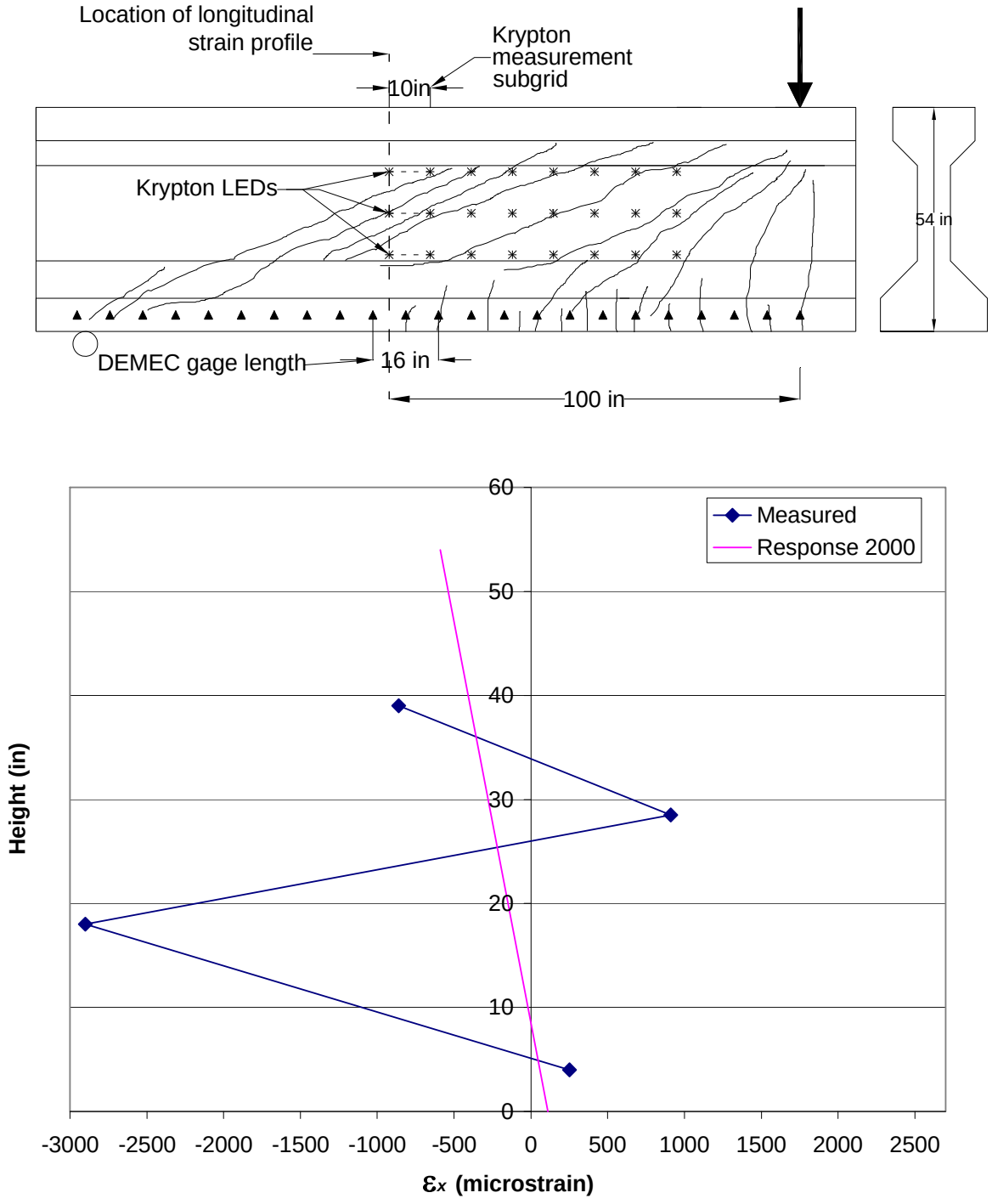

Figure 6.44 Longitudinal Strain Profile 100 in. from Applied Load at Peak Applied Shear

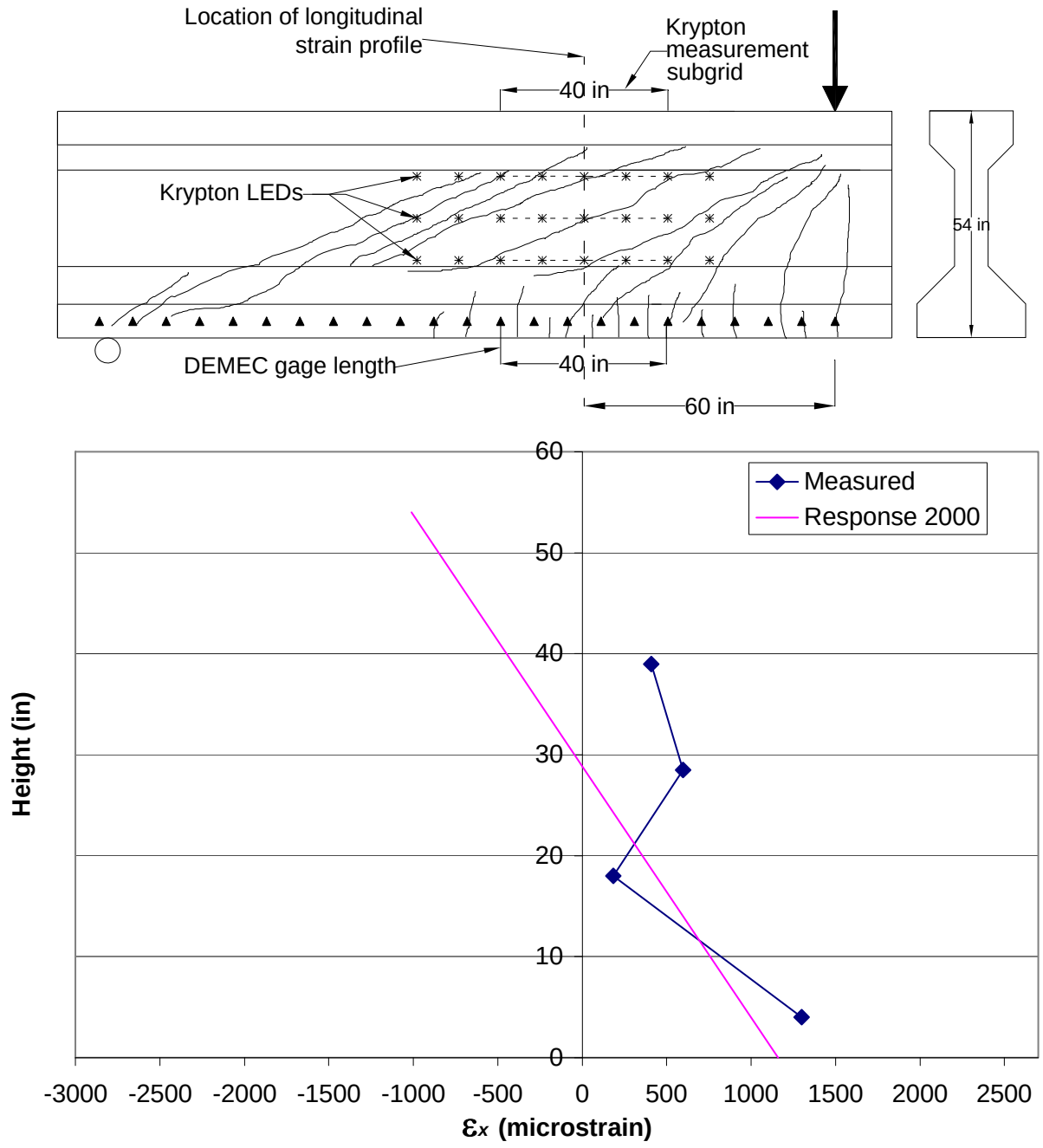

Figure 6.45 Longitudinal Strain Profile 60 in. from Applied Load at Peak Applied Shear with a 40 in. Gage Length

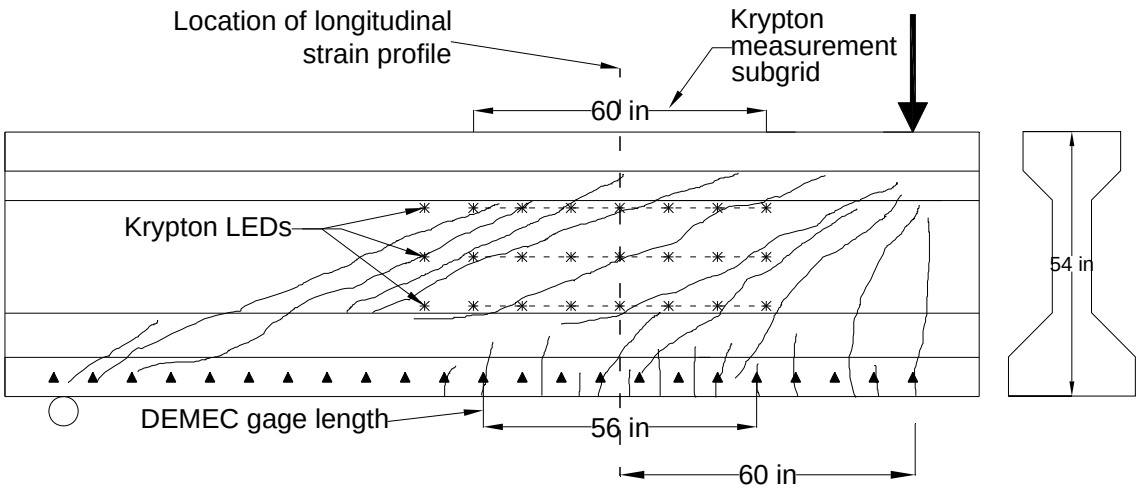

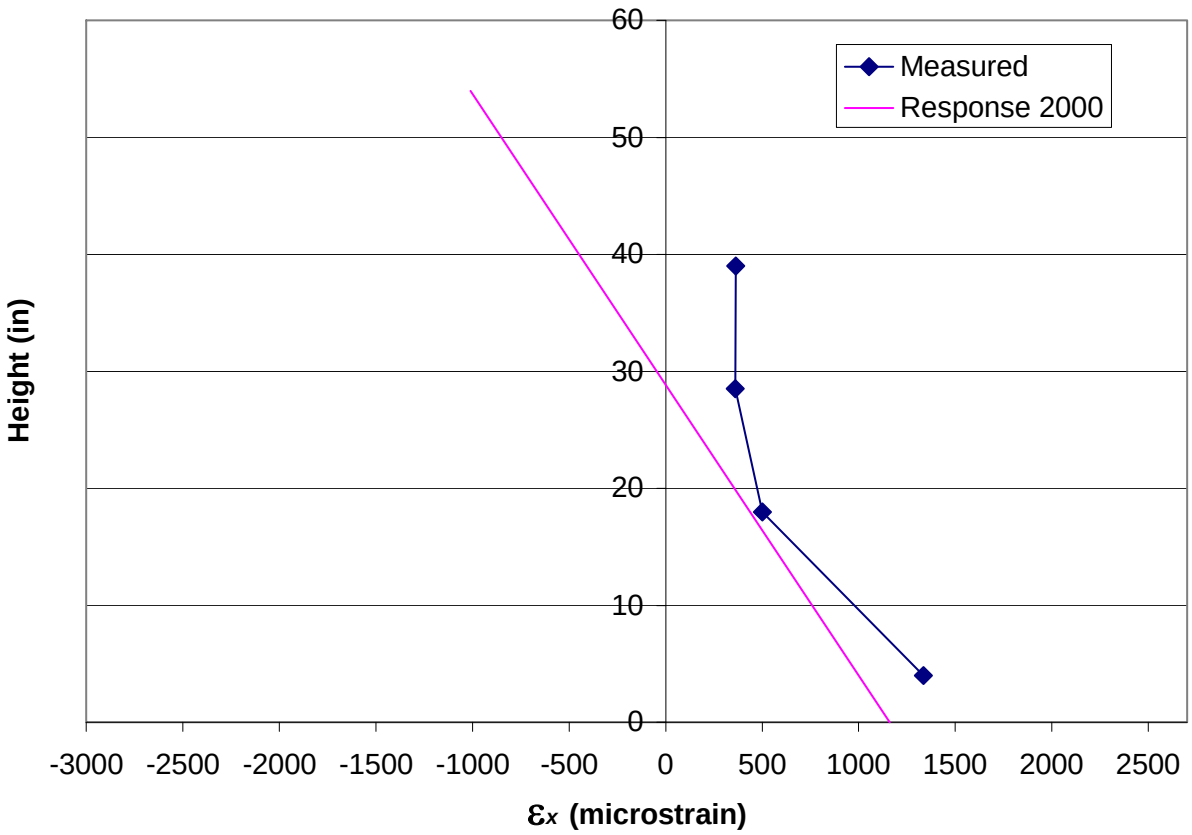

Figure 6.46 Longitudinal Strain Profile 60 in. from Applied Load at Peak Applied Shear with a 60 in. Gage Length

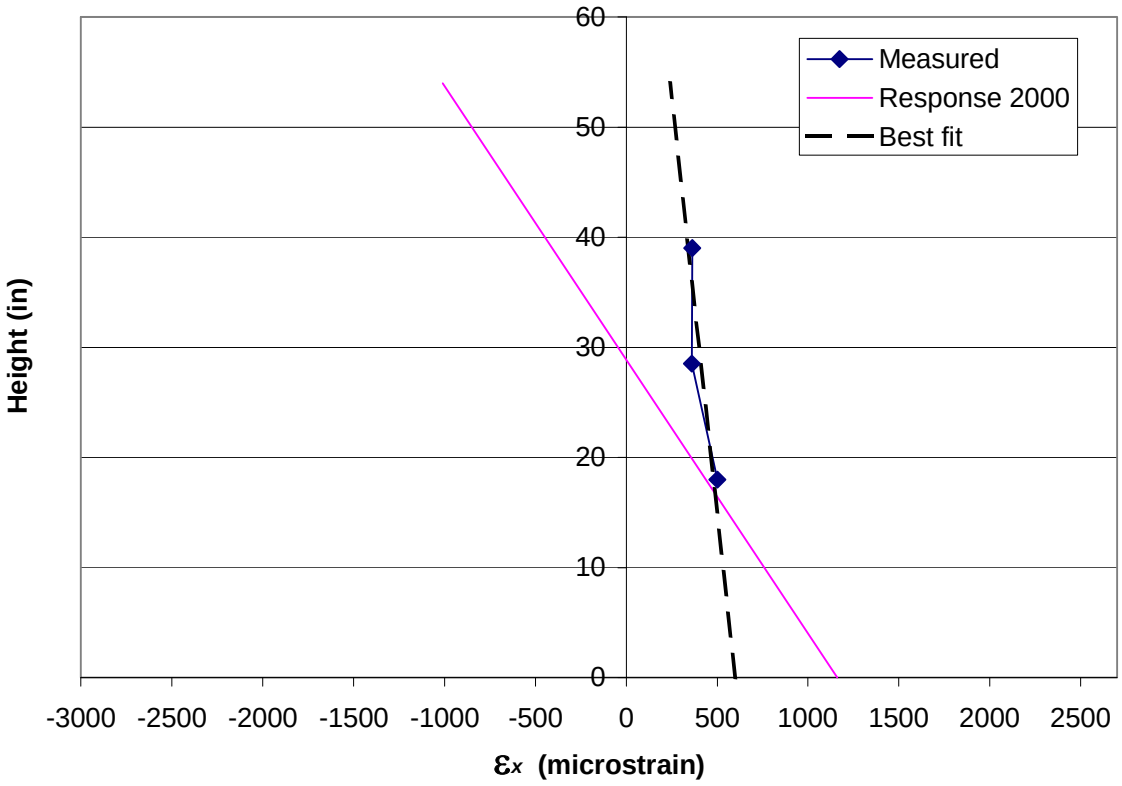

Figure 6.47 Longitudinal Strain Profile from 60 in Gage Length Without DEMEC Strain

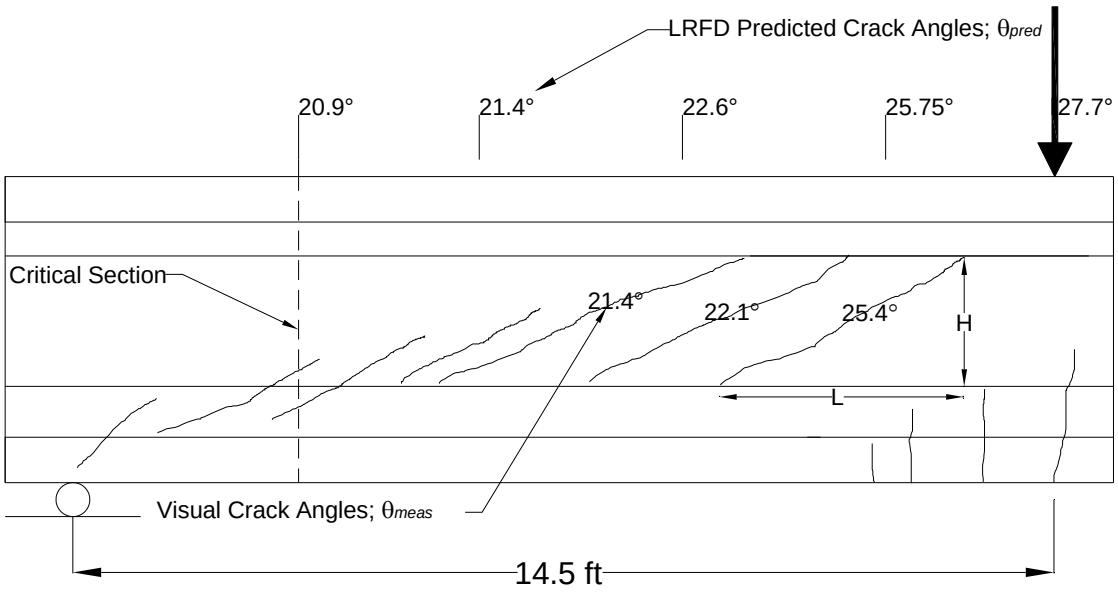

Figure 6.48 Visual Crack Angle Measurements at First Cracking

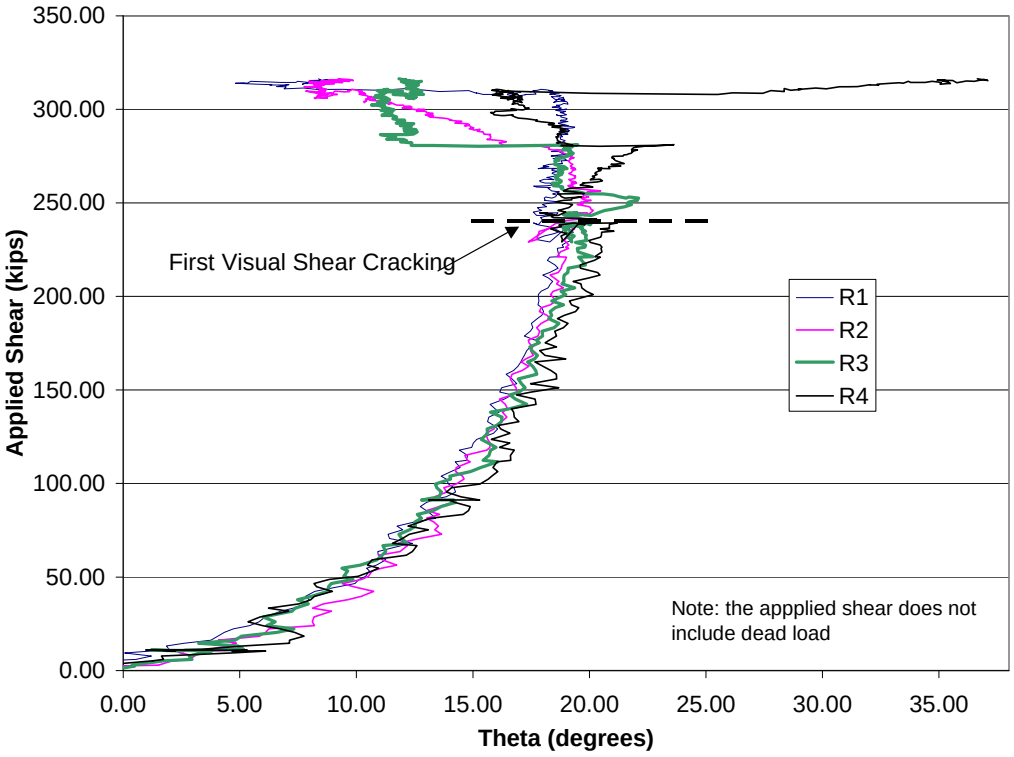

Figure 6.49 θ_{meas} from Four Rosette Strain Gages Closest to Applied Load

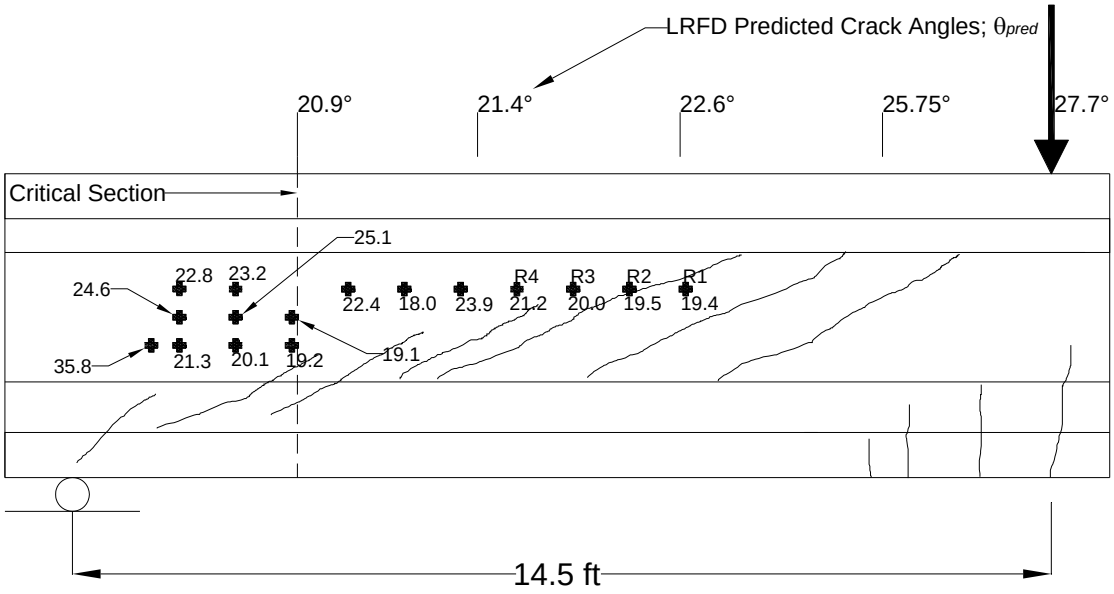

Figure 6.50 Rosette Crack Angle Measurements at First Cracking

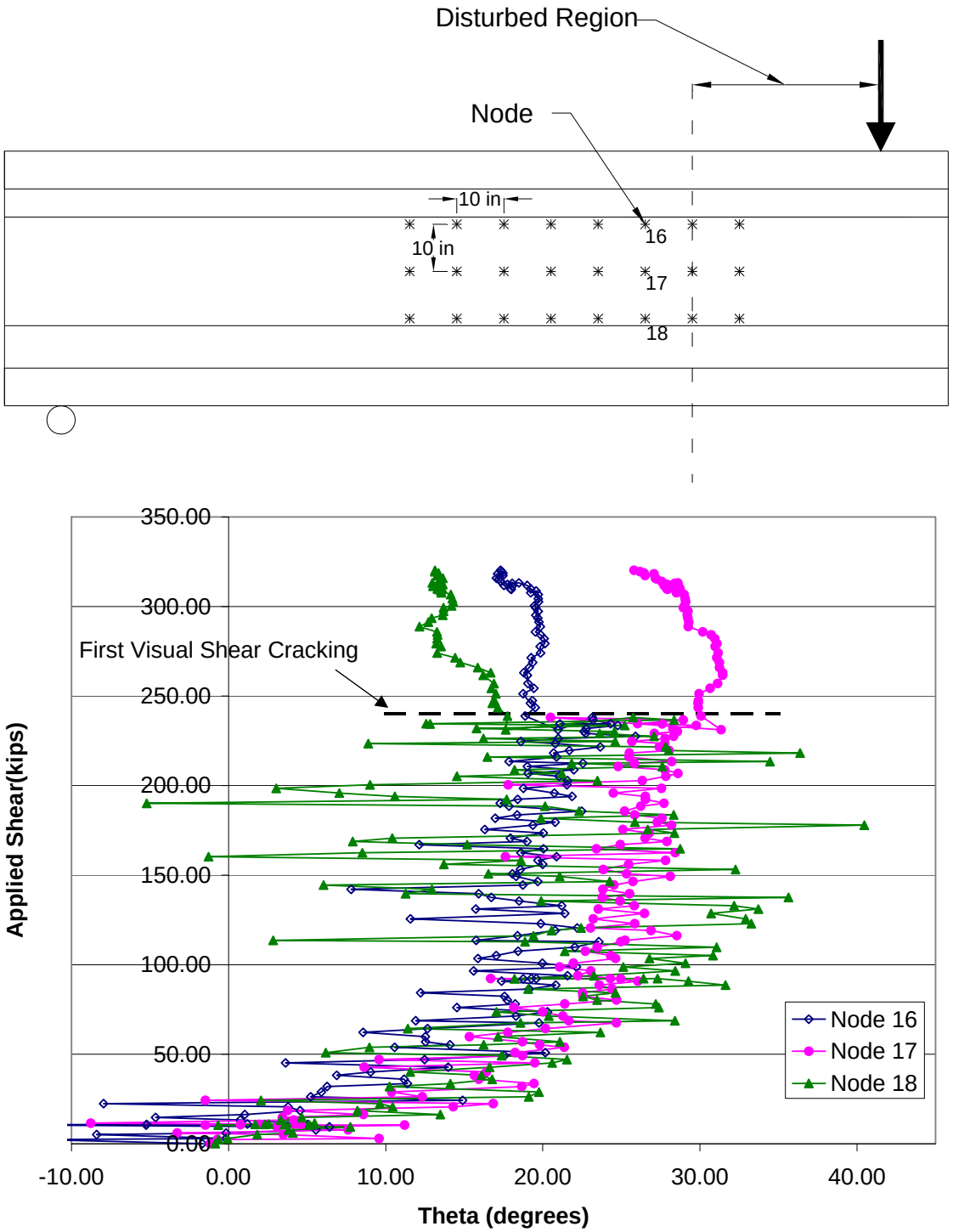

Figure 6.51 Example of θ_{meas} From the Krypton

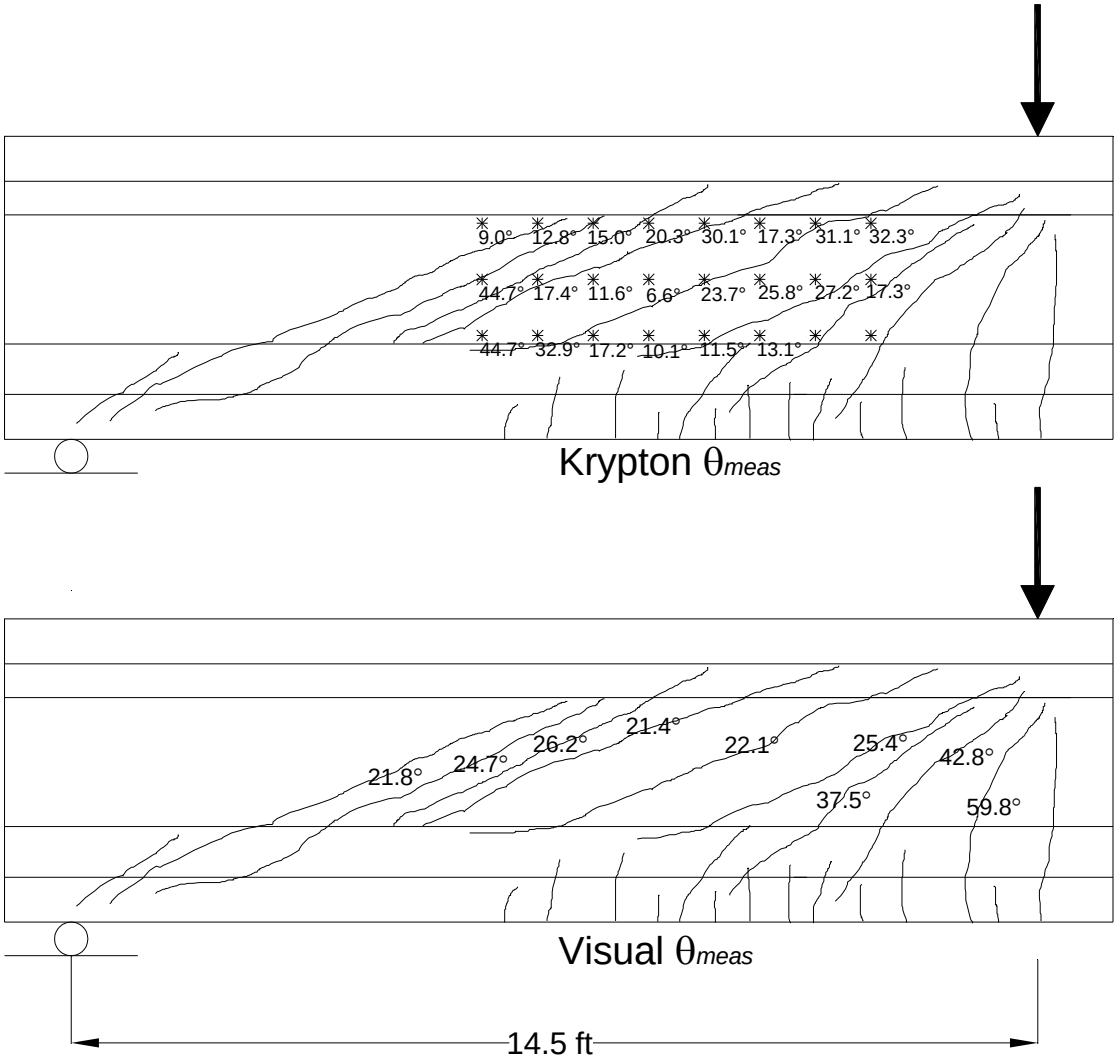

Figure 6.52 Crack Angle Measurements at Peak Load

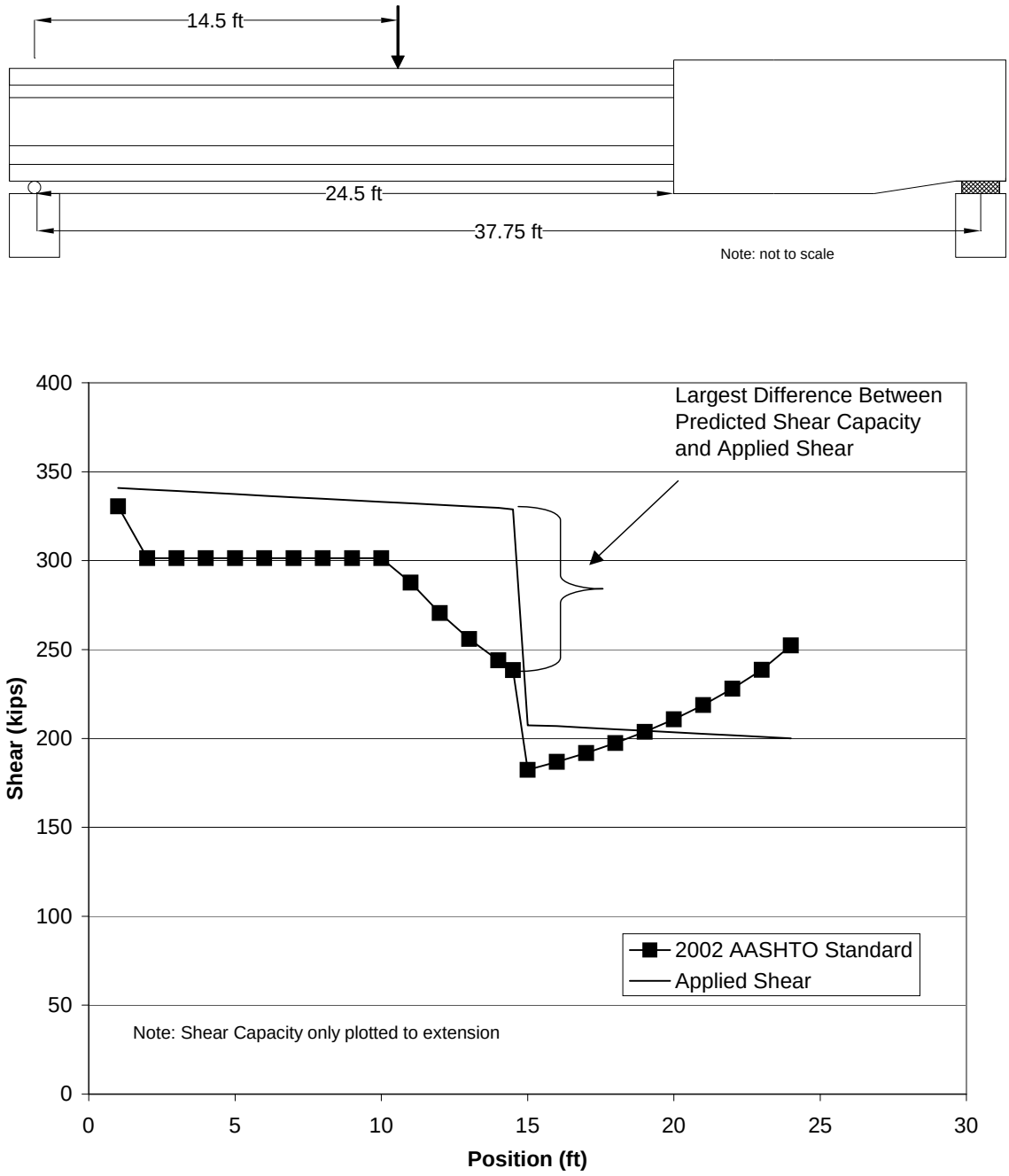

Figure 6.53 AASHTO 2002 Standard Predicted Shear Capacity vs. Position

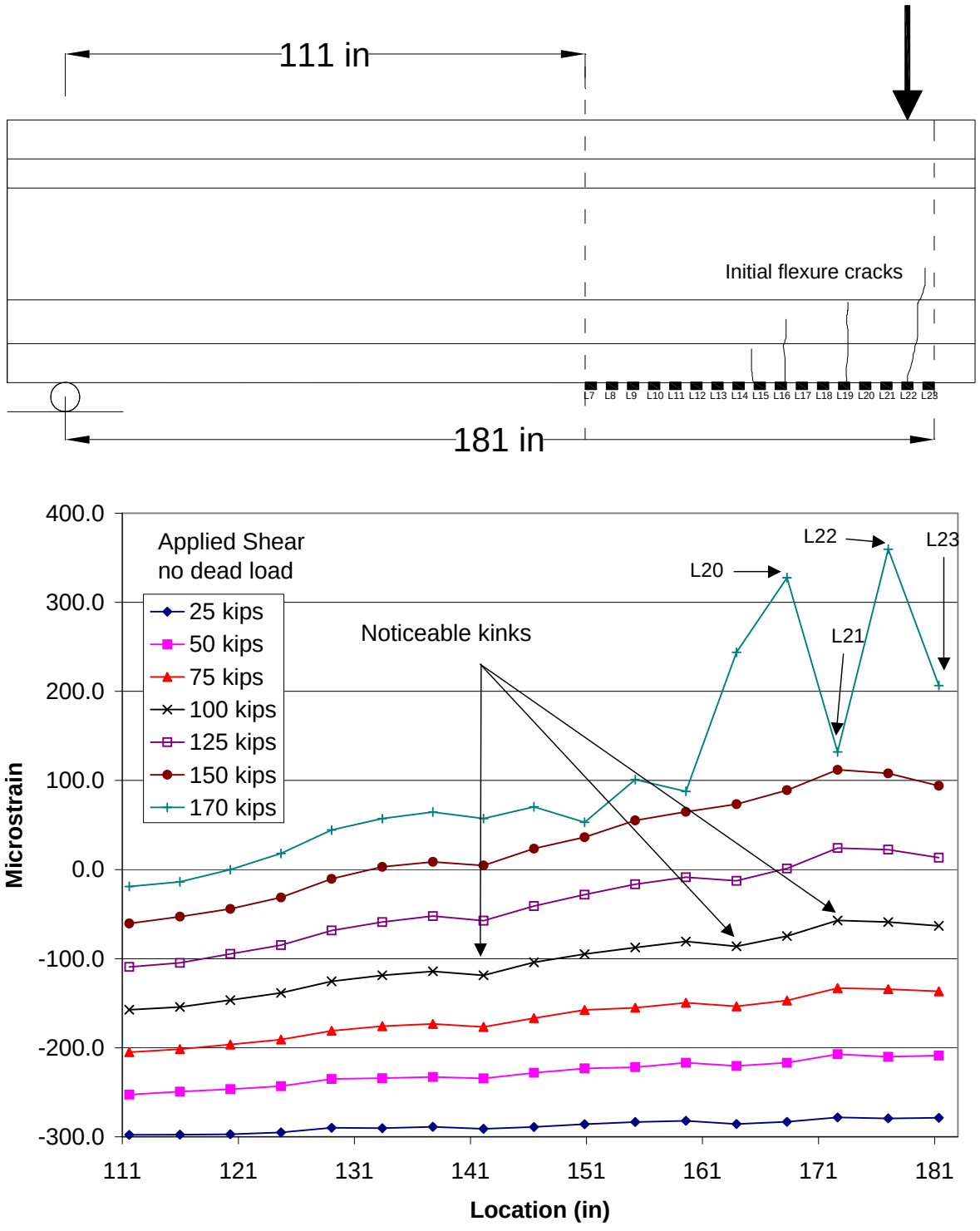

Figure 6.54 Strain Profile Along Bottom Flange (Specimen II)

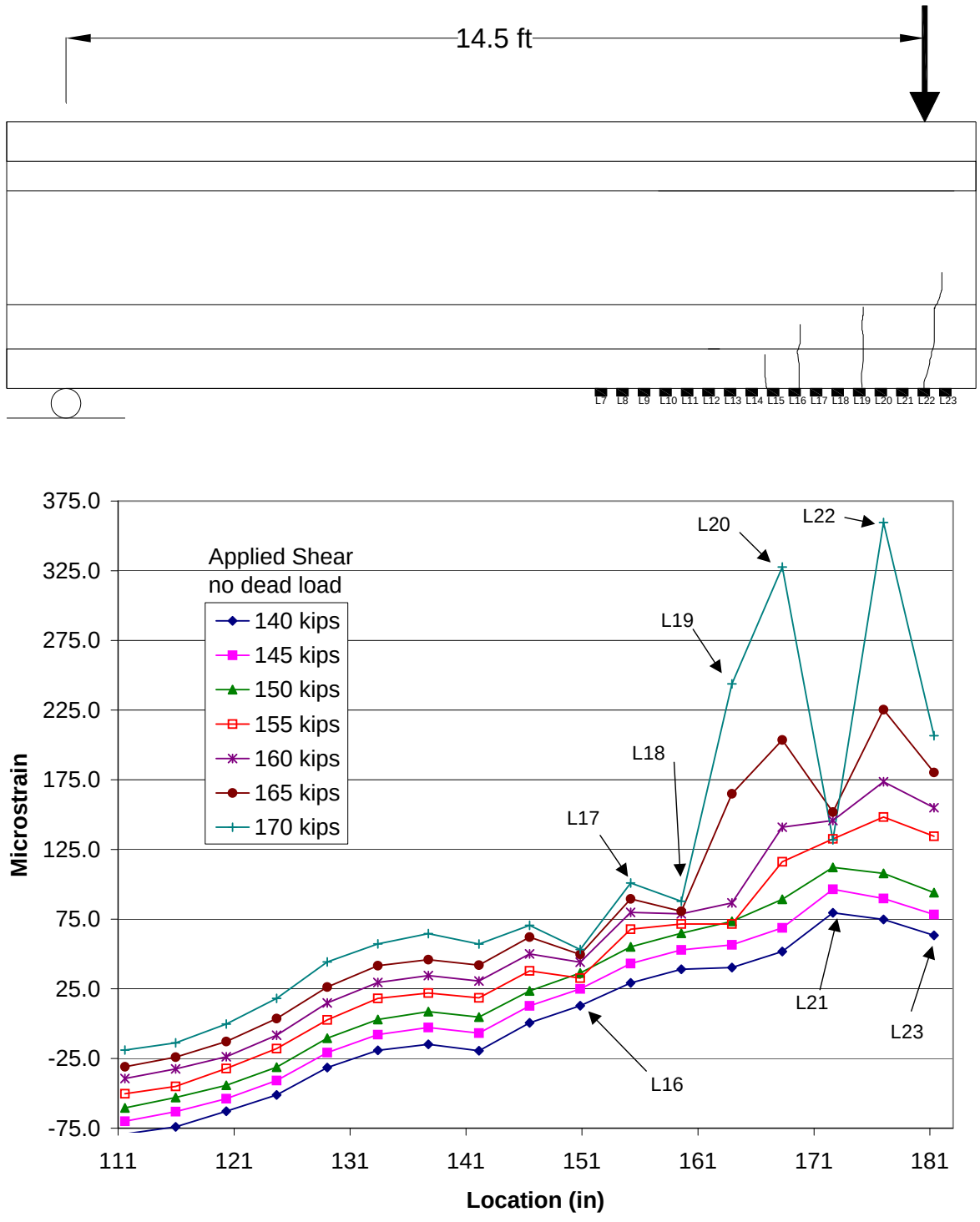

Figure 6.55 Strain Profile Along Bottom Flange (Specimen II)

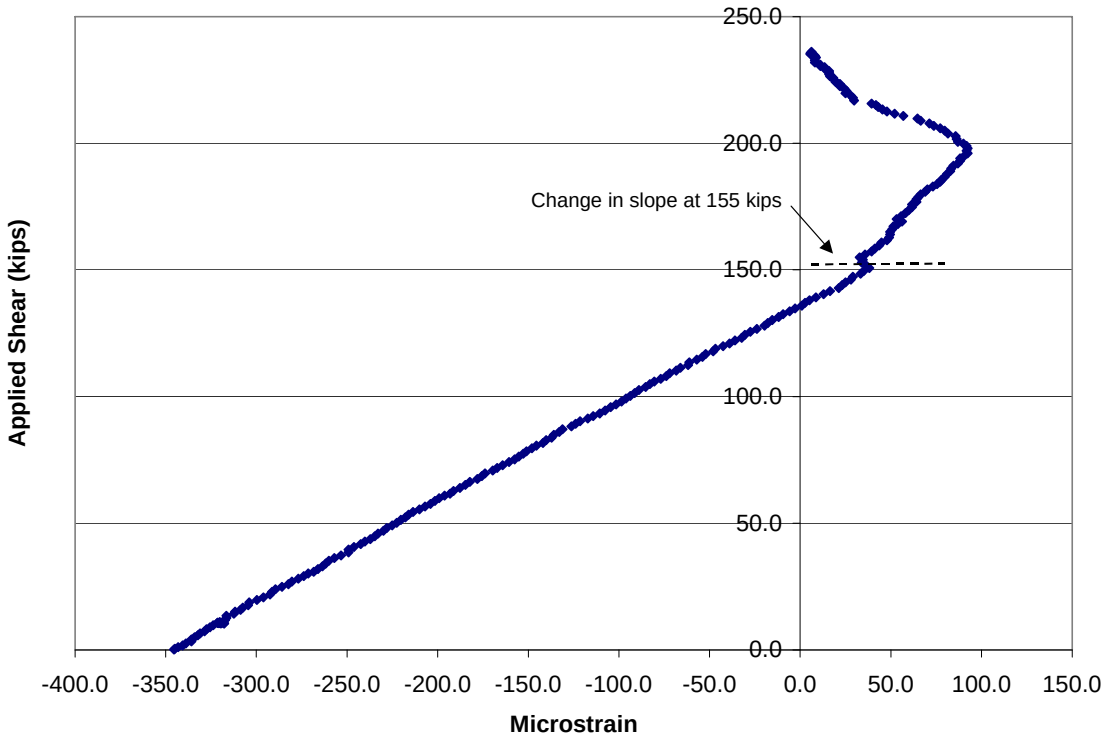

Figure 6.56 Horizontal Gage L16

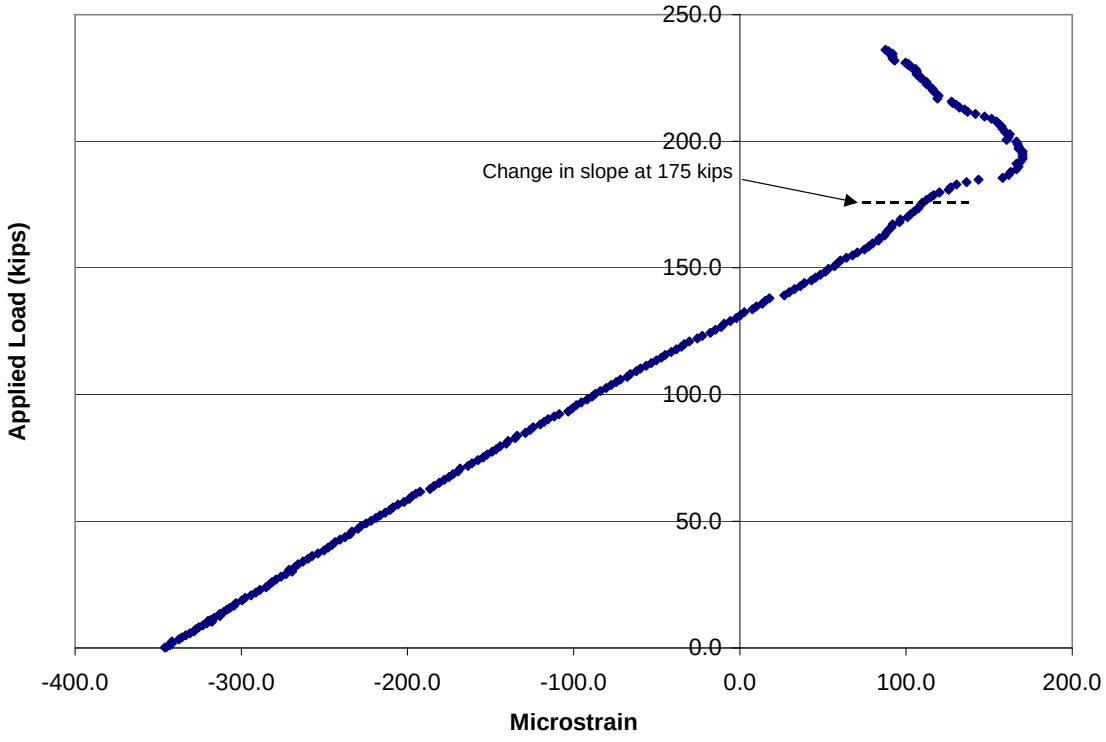

Figure 6.57 Horizontal Gage L17

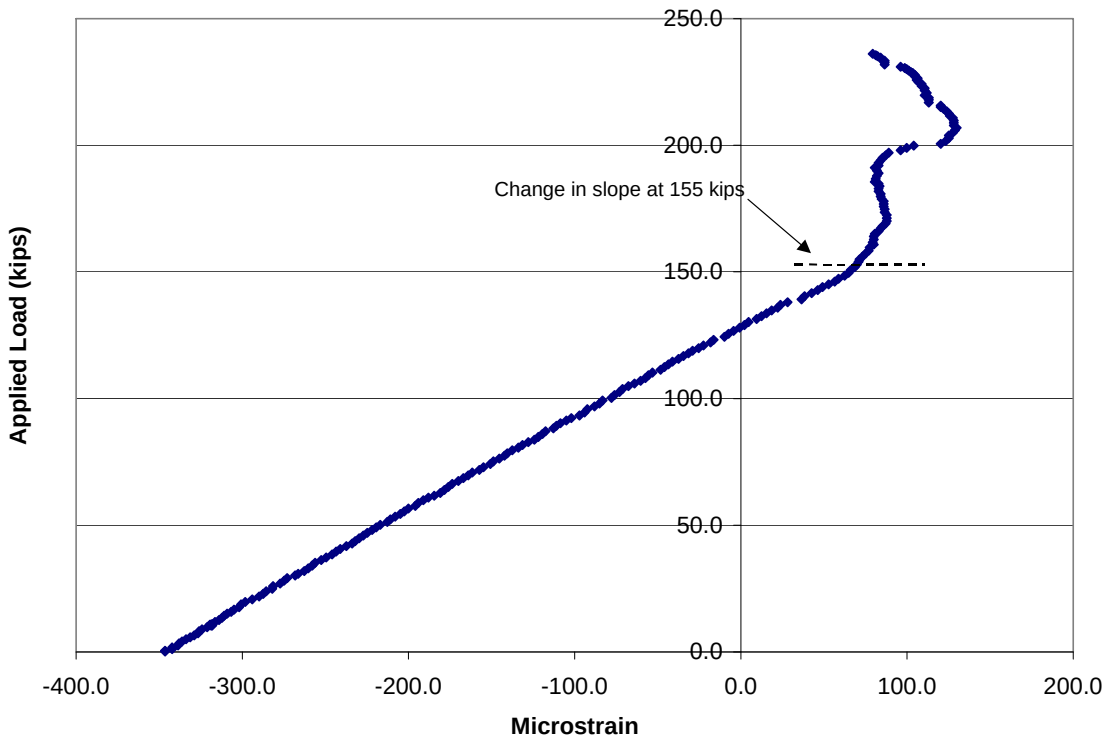

Figure 6.58 Horizontal Gage L18

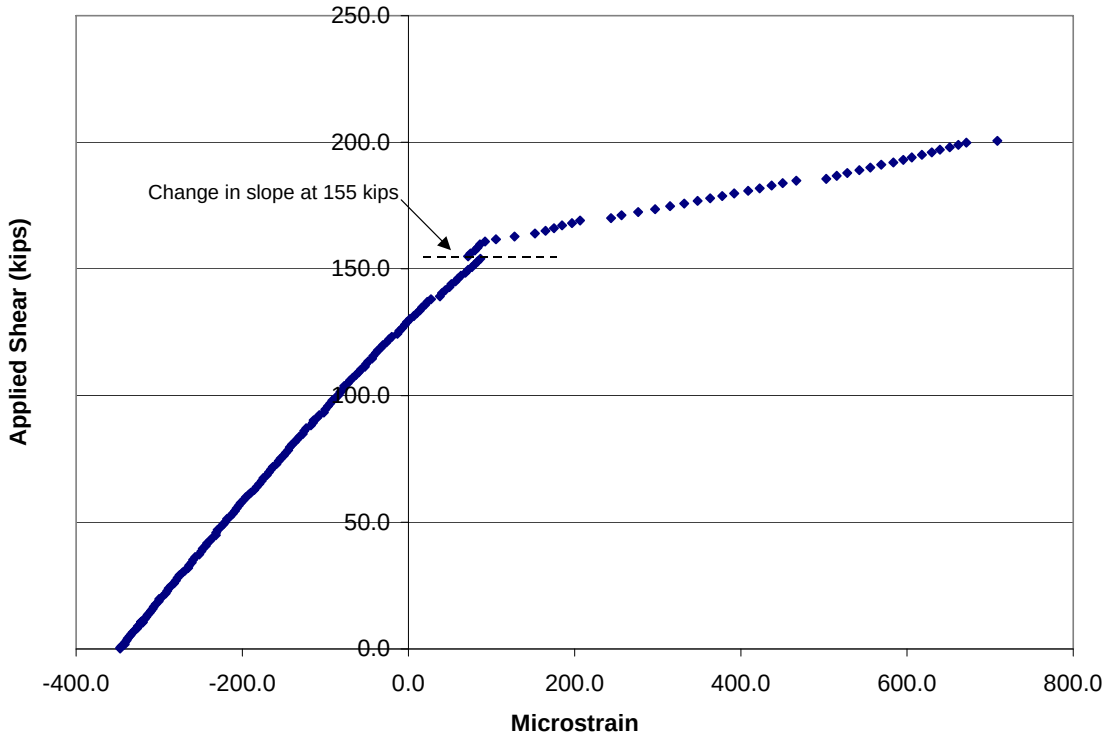

Figure 6.59 Horizontal Gage L19

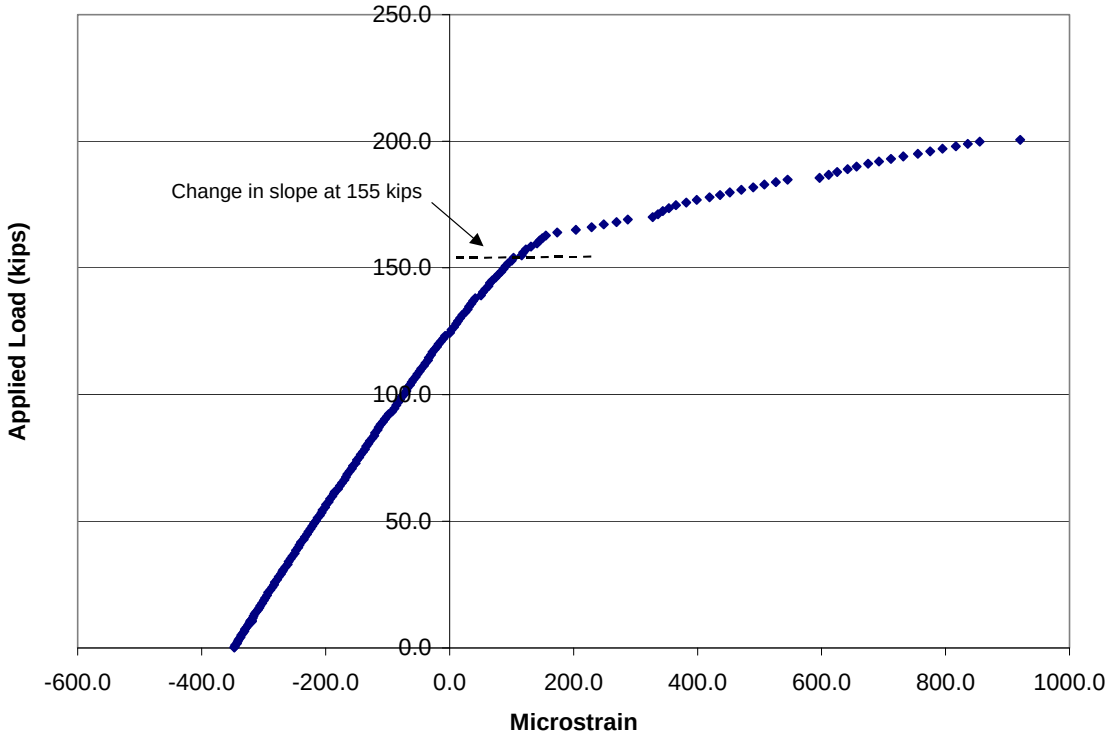

Figure 6.60 Horizontal Gage L20

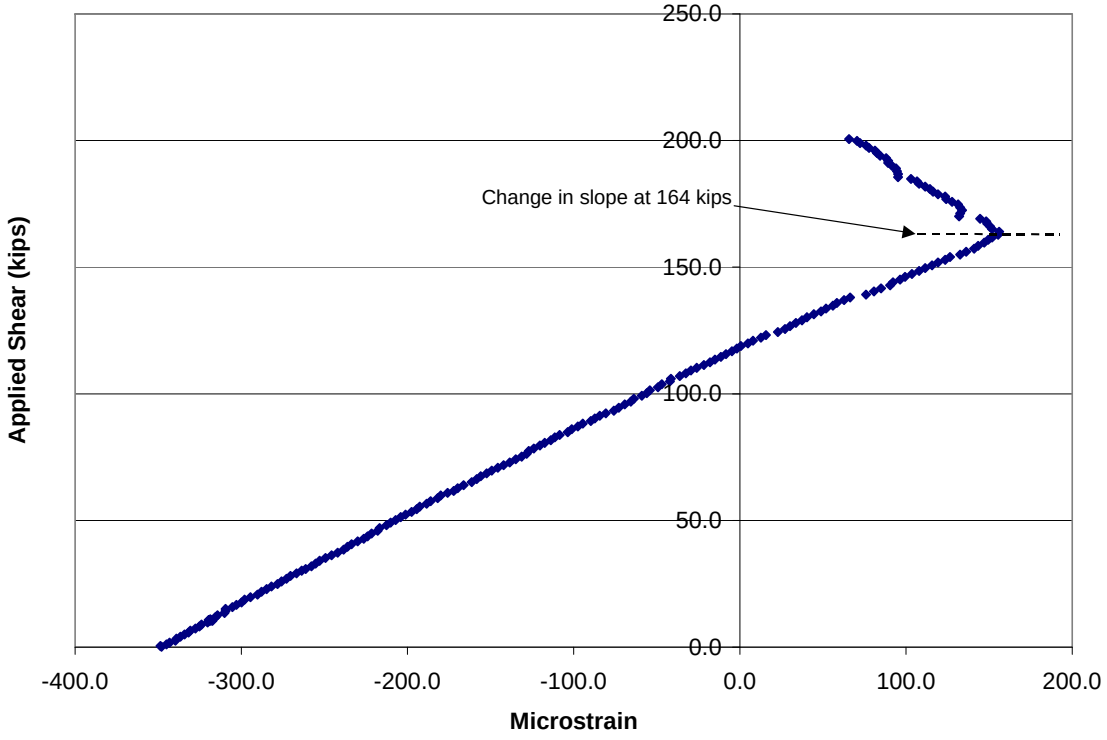

Figure 6.61 Horizontal Gage L21

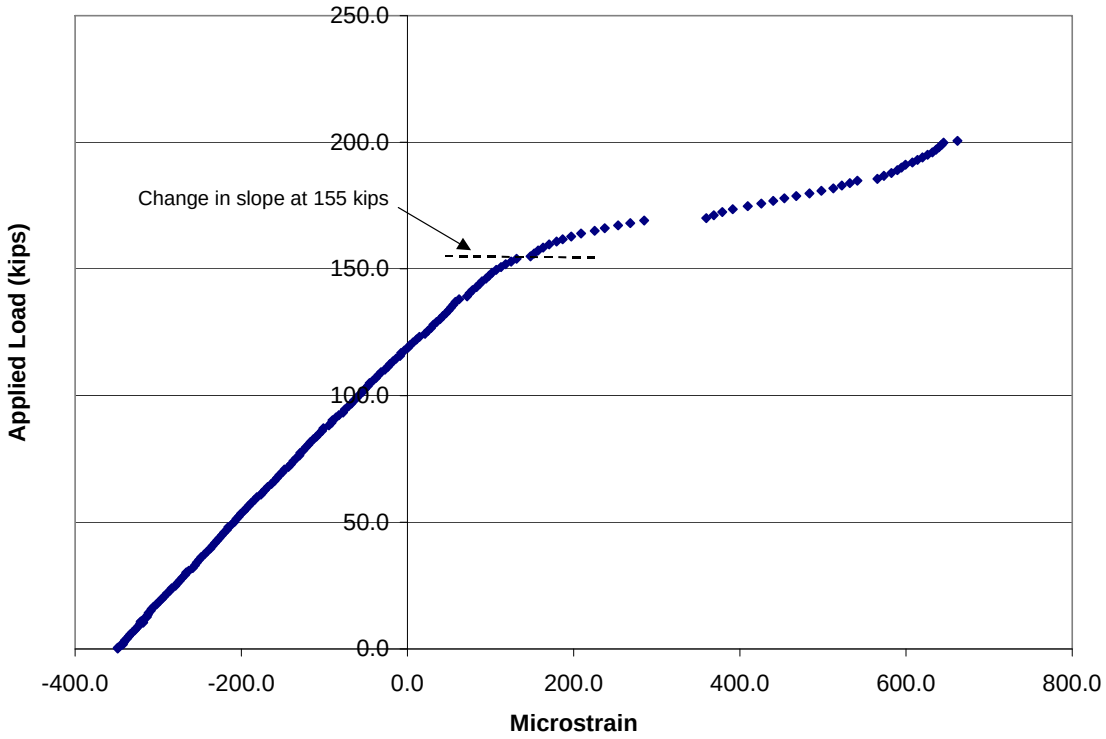

Figure 6.62 Horizontal Gage L22

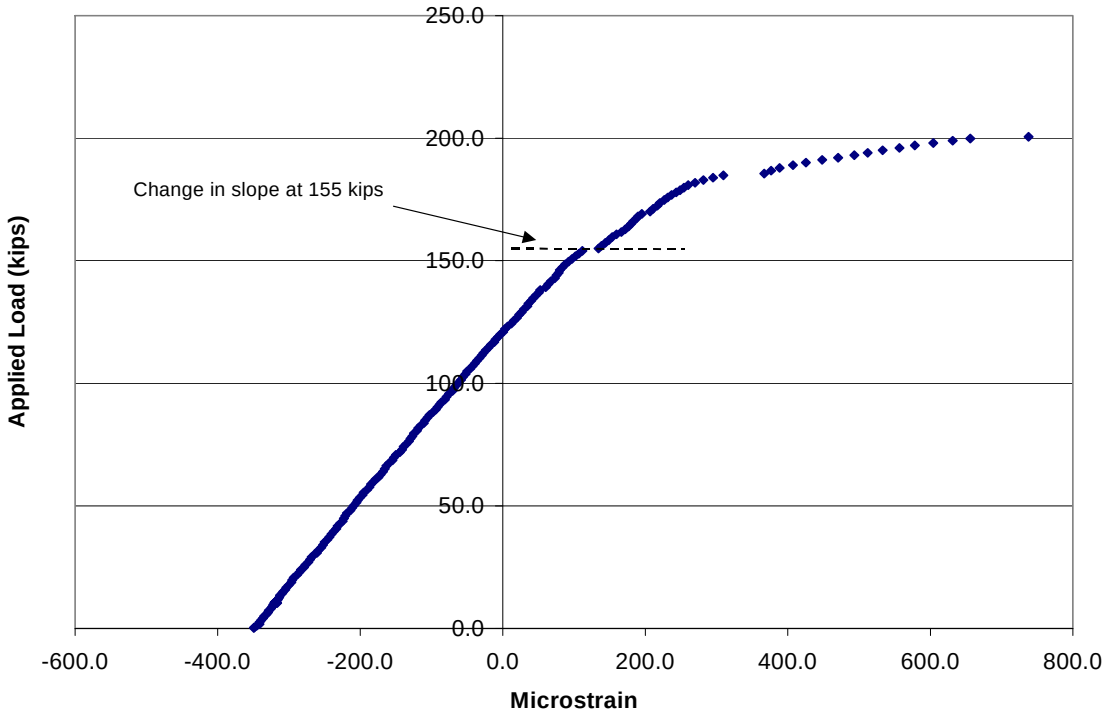

Figure 6.63 Horizontal Gage L23

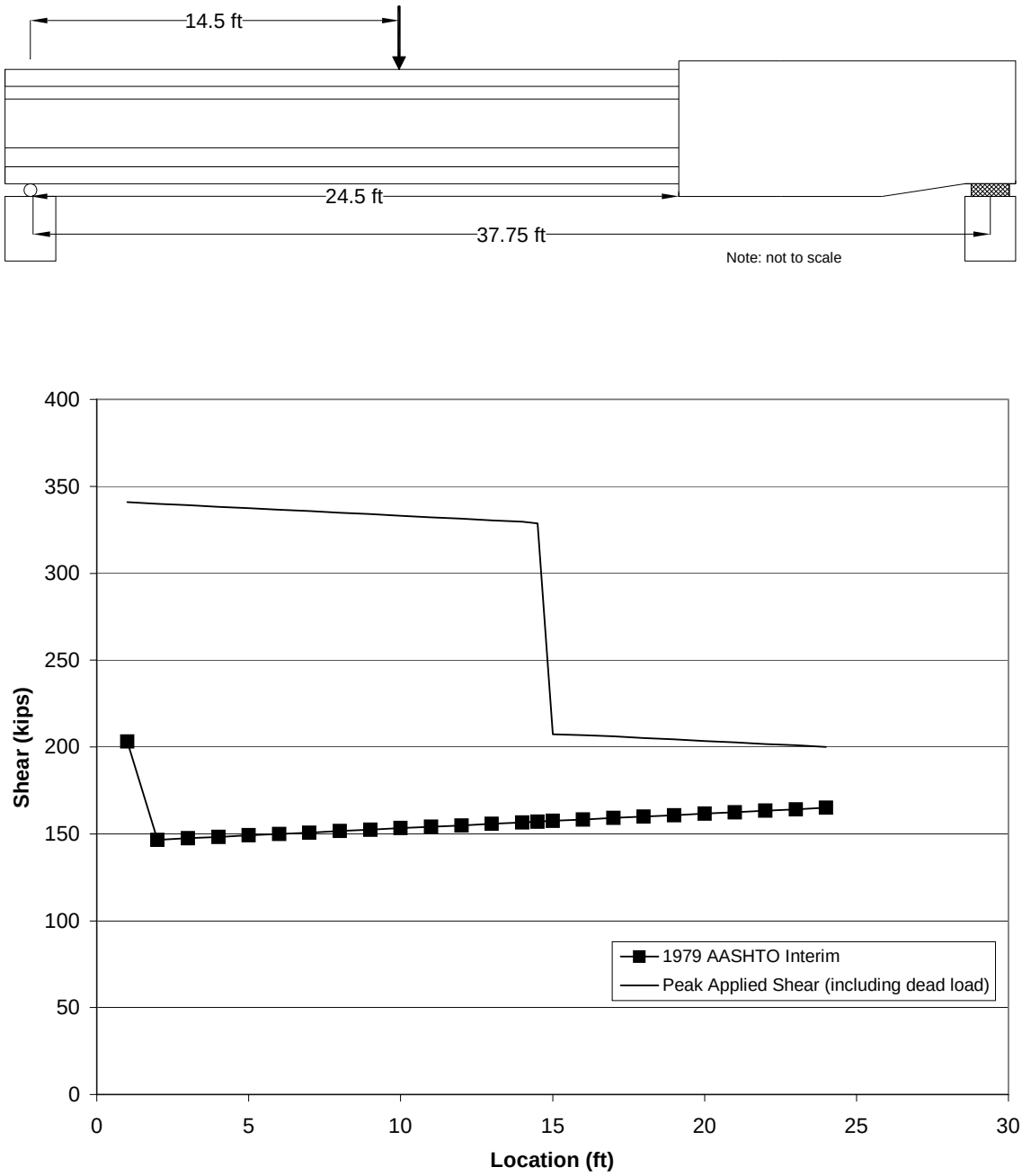

Figure 6.64 AASHTO 1979 Interim Predicted Shear Capacity vs. Position

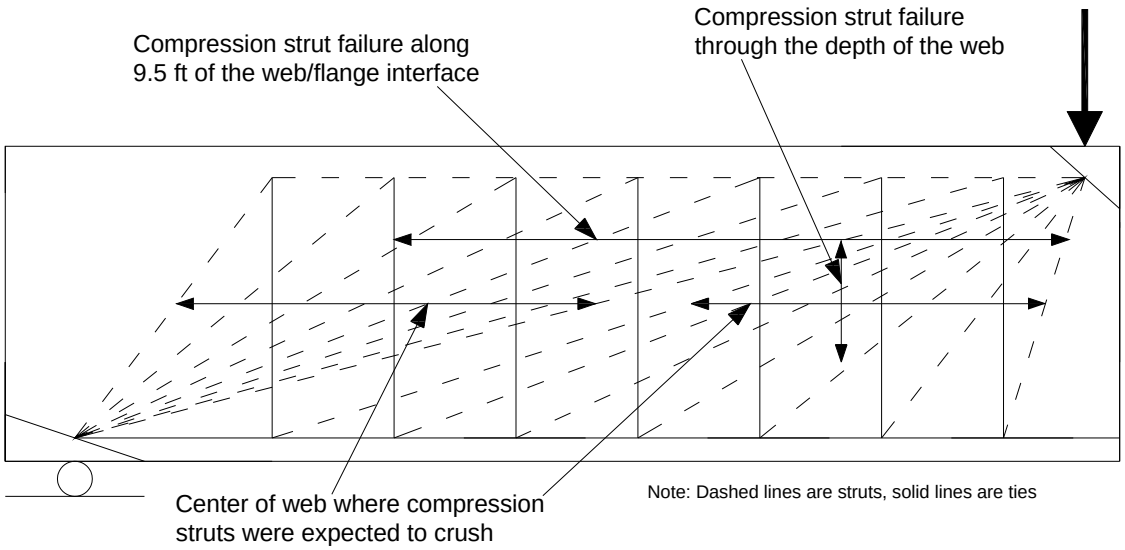

Figure 6.65 Observed Area of Compressive Strut Failure

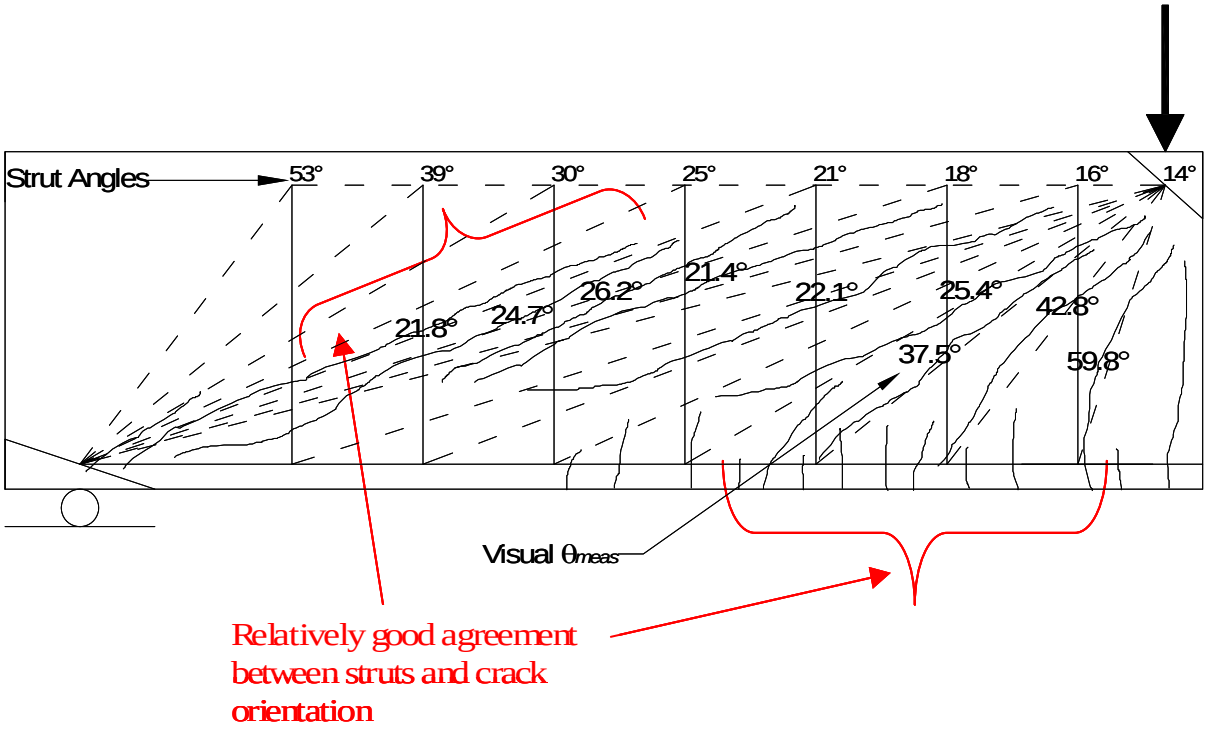

Figure 6.66 Strut and Tie Model and Cracking at 40% Past Peak Applied Load (Specimen II)

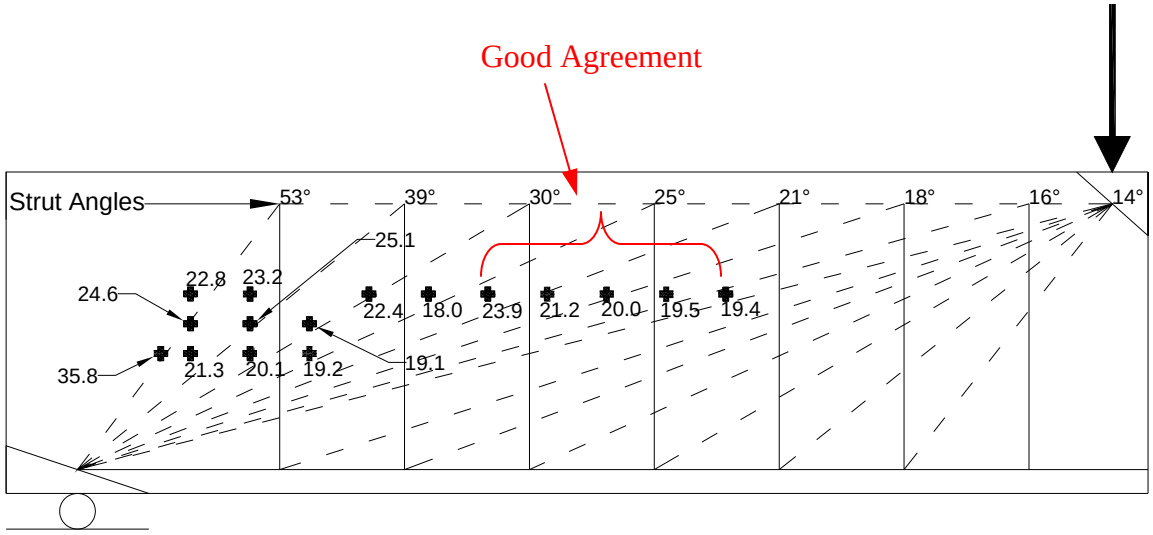

Figure 6.67 Strut and Tie Model With Rosettes at Initial Cracking

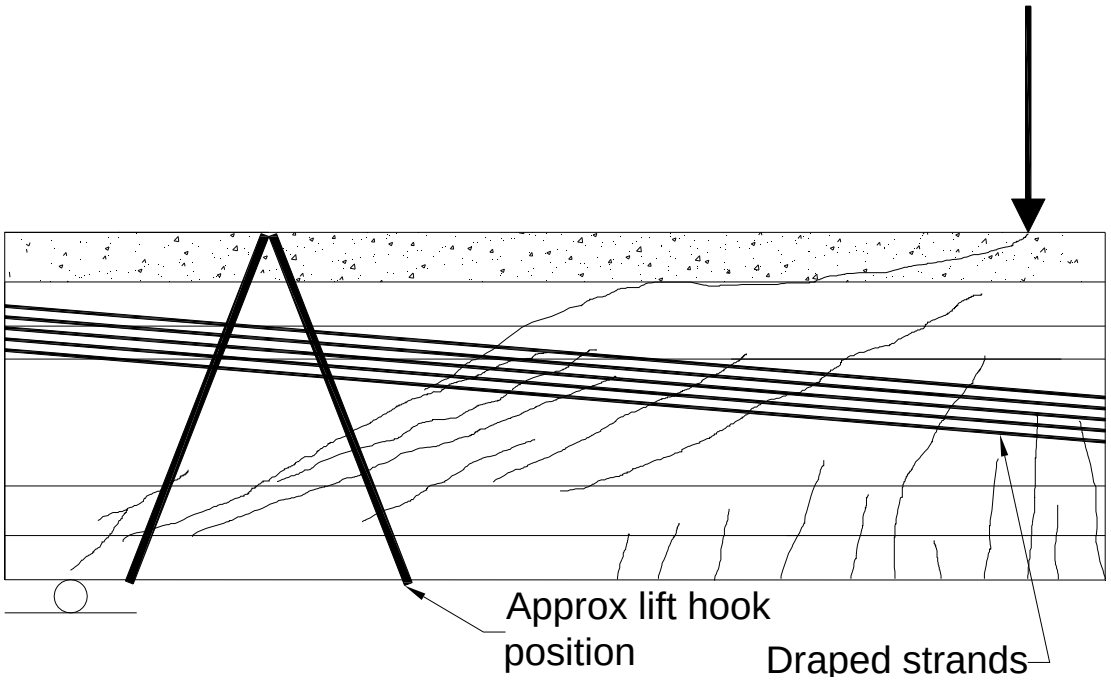

Figure 6.68 Approximate Location of Lift Hook In Specimen I

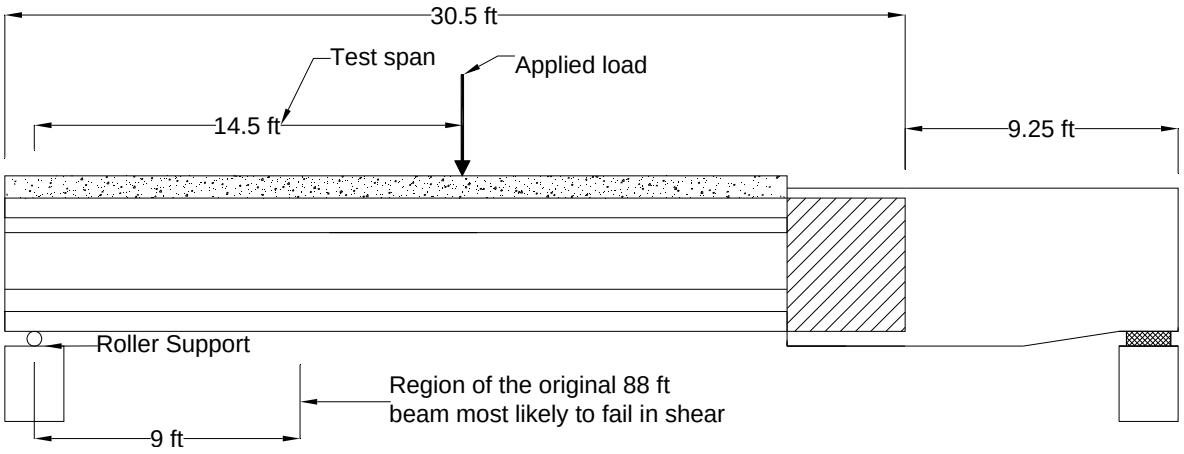

Figure 7.1 Modified Test Specimen

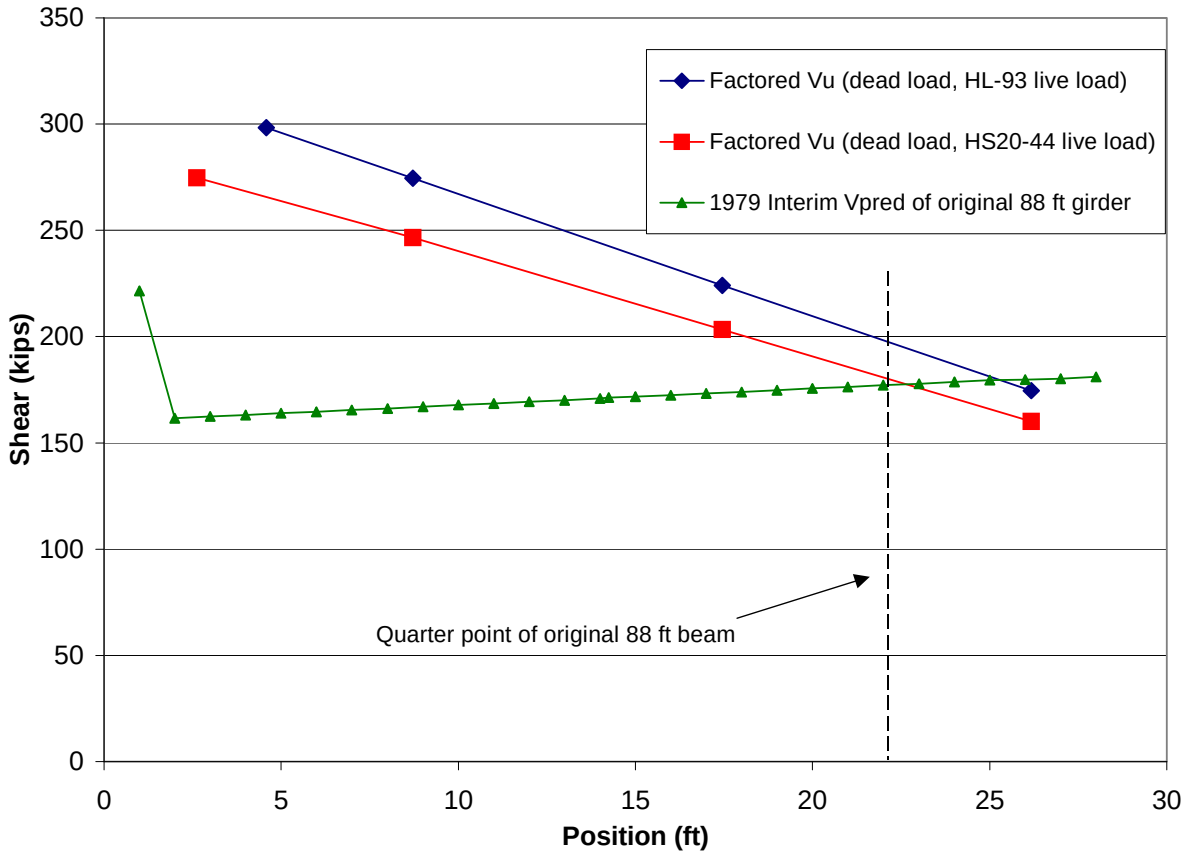

Figure 7.2 1979 Interim Shear Capacity vs. Position

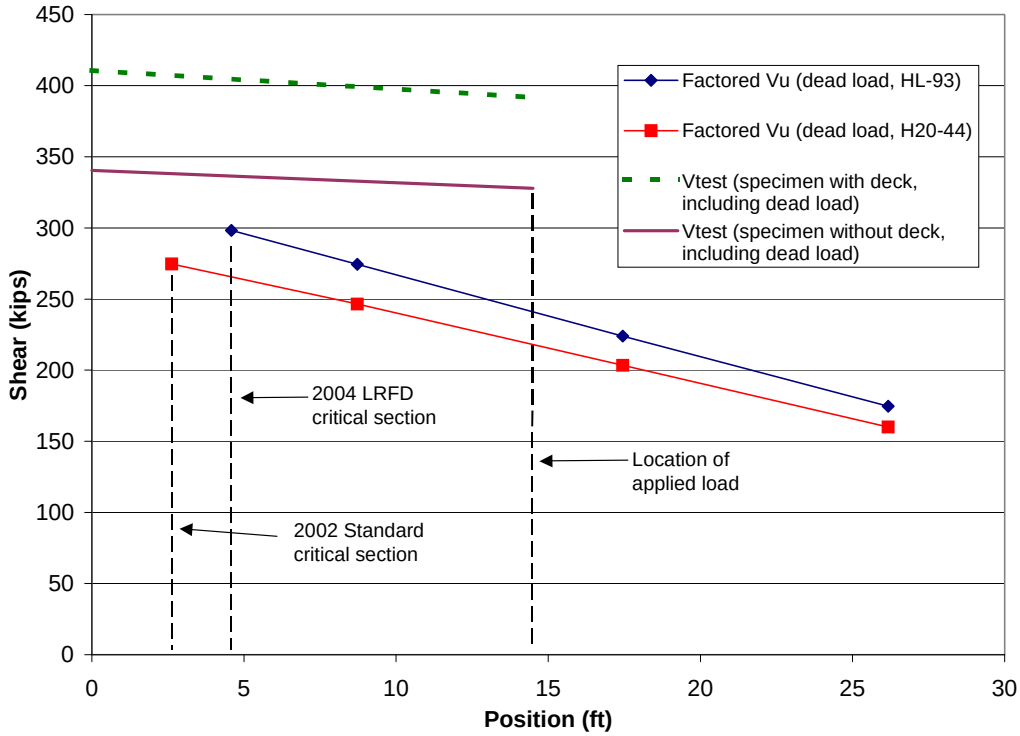

Figure 7.3 Shear Applied to Specimens, and Required Shear Capacity of Original 88 ft Girder

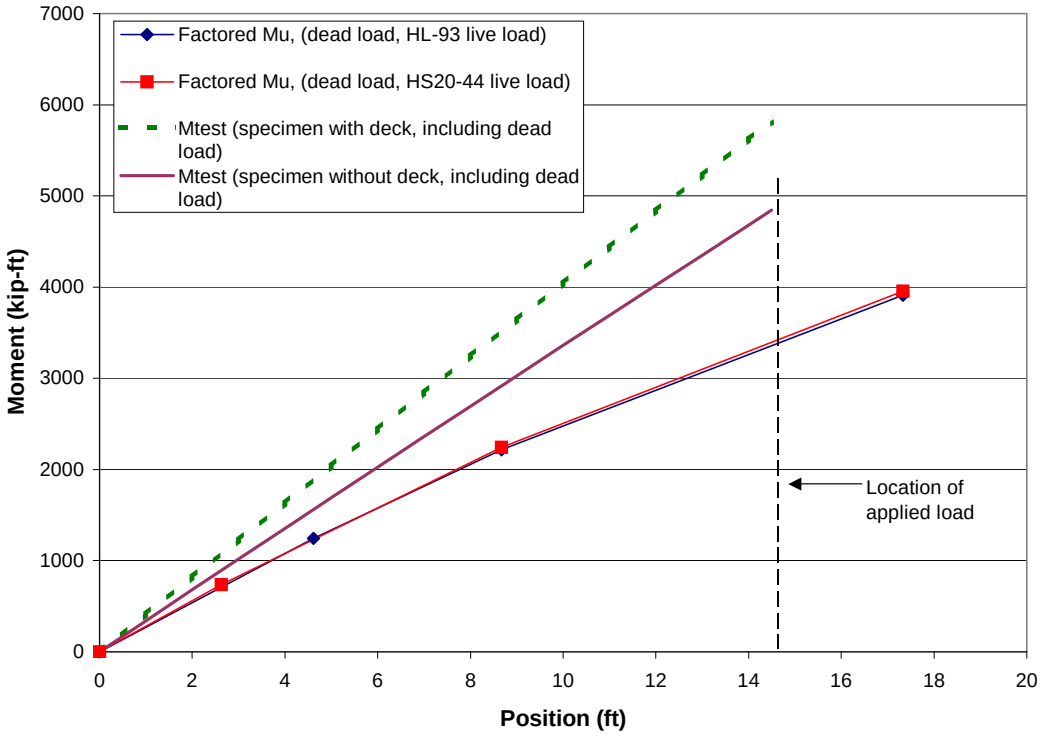

Figure 7.4 Moment Applied to Specimens, and Required Moment Capacity of Original 88 ft Girder

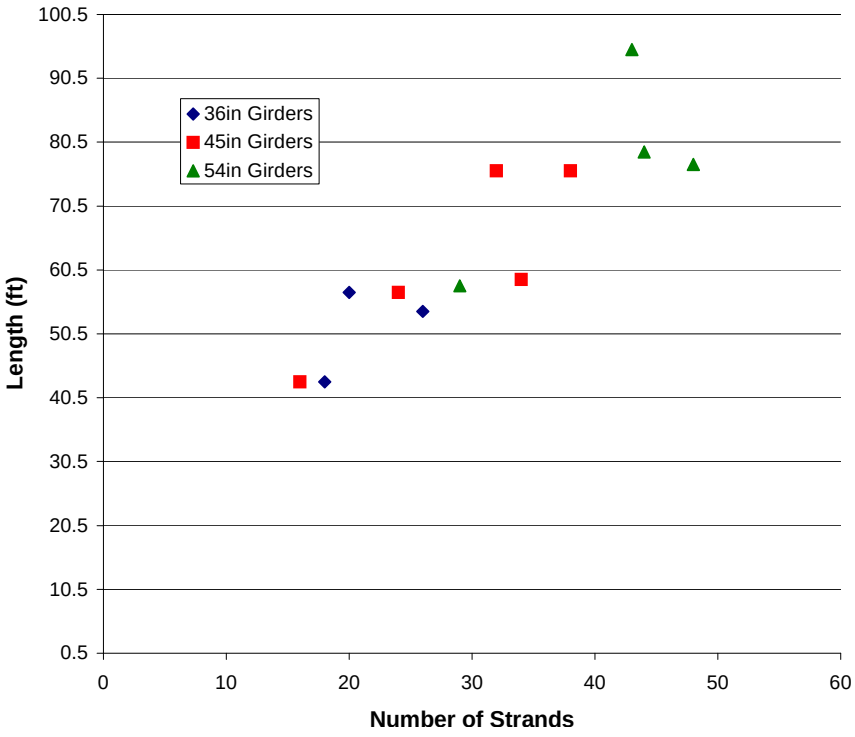

Figure 7.5 Girder Length vs. Number of Prestressing Strands

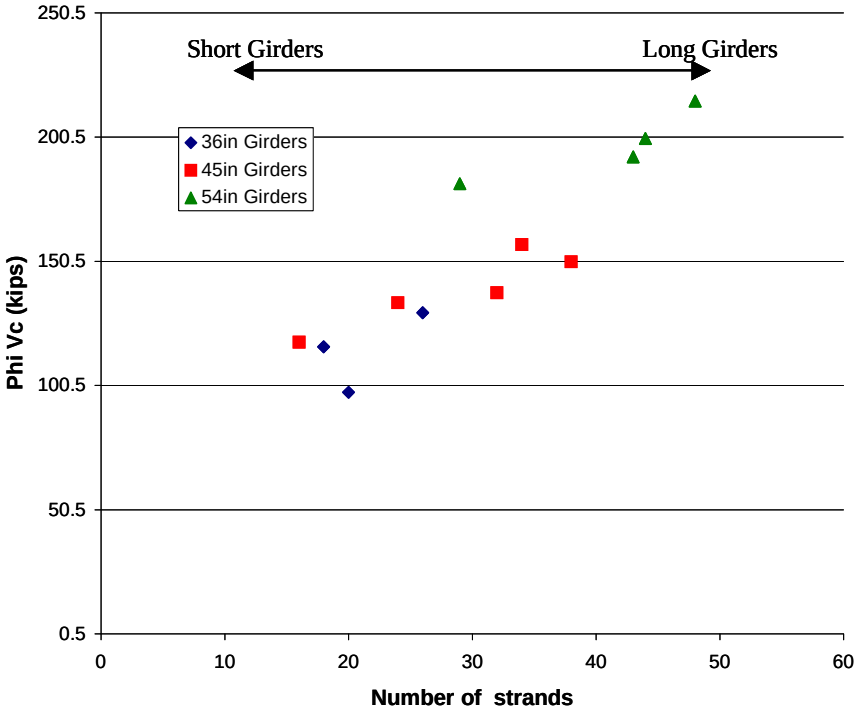

Figure 7.6 ϕV_c at the Critical Section vs. Number of Strands

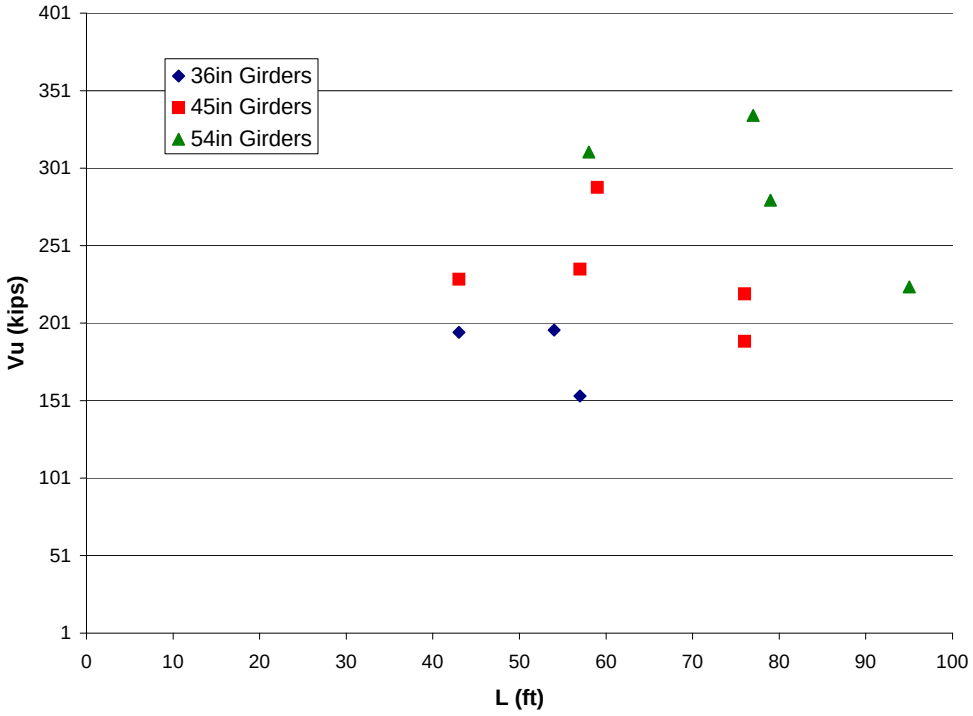

Figure 7.7 V_u at the Critical Section vs. Girder Length (L)

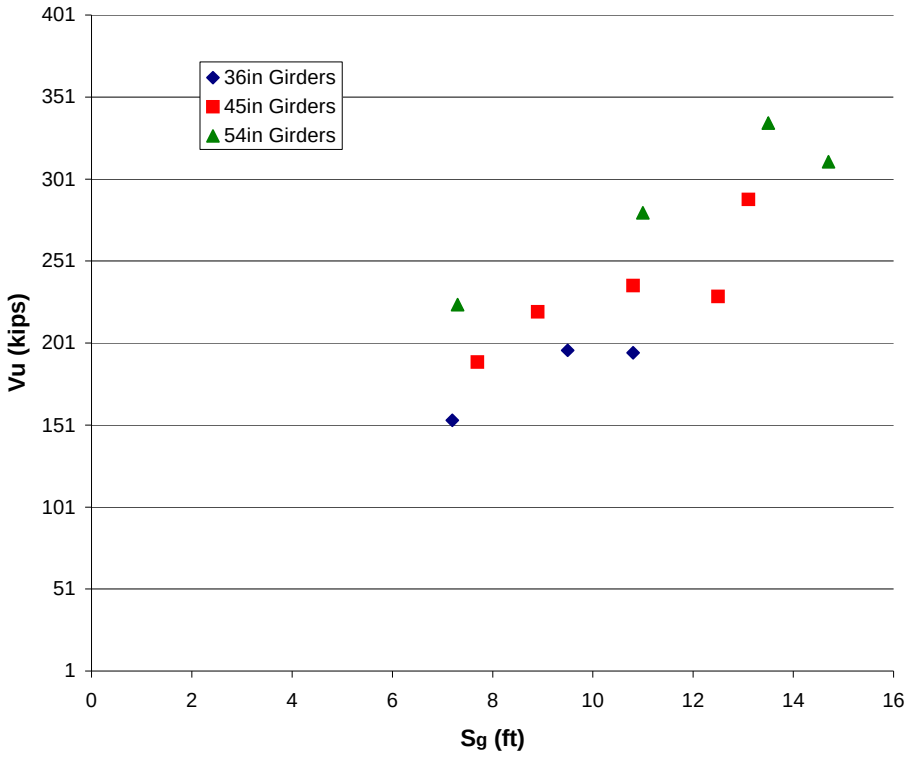

Figure 7.8 V_u at the Critical Section vs. Girder Spacing (S_g)

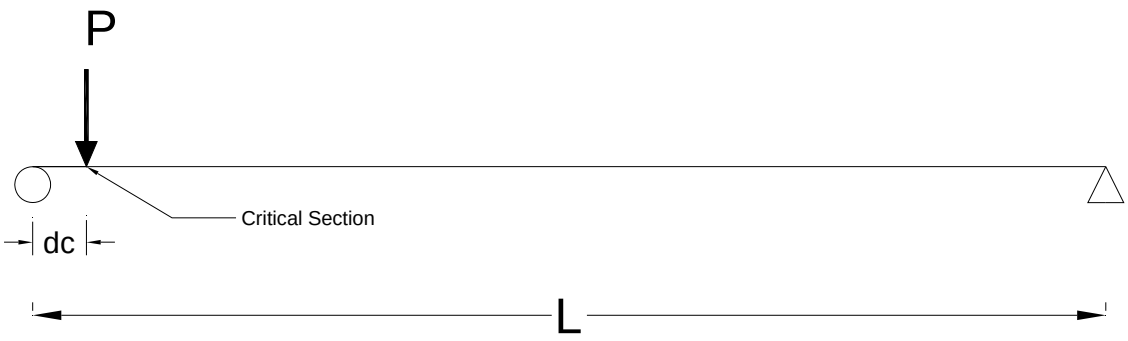

Live Load Shear Demand:

$$V = P\left(\frac{L - dc}{L}\right) = P\left(1 - \frac{dc}{L}\right) = P(1 - \alpha)$$

Figure 7.9 Truck Live Load Shear Demand at the Critical Section

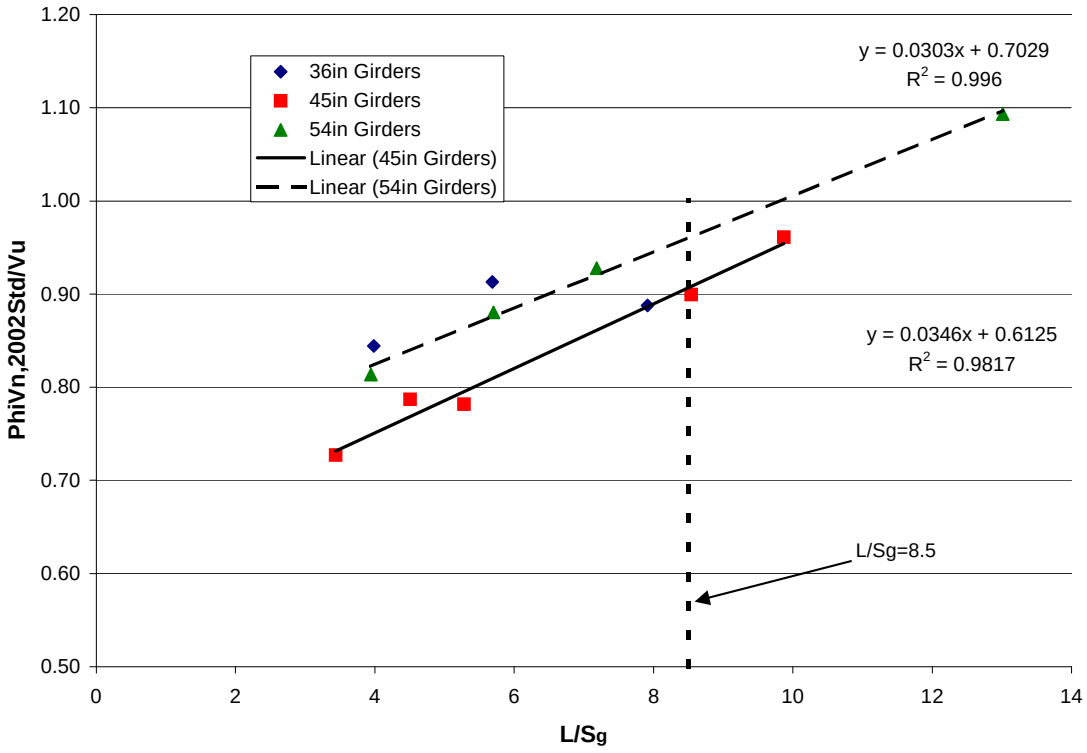

Figure 7.10 $\frac{\phi V_{n,2002Std}}{V_u}$ **at the Critical Section vs.** $\frac{L}{S_g}$

Appendix A
Sample Calculations

A.1 Shear Capacity Calculations

This section contains samples of the shear capacity calculations from the AASHTO 2004 LRFD, 2002 Standard, 1979 Interim, and the Strut and Tie Model. The sample calculations are from the cross-section at midspan for the specimen with a bridge deck (Specimen I), with the loading shown in Figure A.1. Nominal material properties were assumed, and ϕ was taken as 1.0. The calculations for the specimen without a bridge deck were similar to those presented in this section.

A.1.1 AASHTO 2004 LRFD Shear Capacity Calculations at midspan

The 2004 LRFD sample calculations at midspan for Specimen I are presented in this section; refer to Figure A.2 for an illustration of the specimen cross-section. These calculations represent a summary of the calculations performed by the non-iterative spreadsheet used to create shear-moment interaction diagrams for the specimens (Bentz and Collins, 2000a). These interaction diagrams were necessary to calculate the shear capacity of a member with specified shear reinforcement. Material and section properties used in the capacity calculations are given in Table A.1.

Effective stress in the prestressing strands after losses f_{se}

$$f_{se} = f_{po} - (\Delta f_{pES} + \Delta f_{pSR} + \Delta f_{pCR} + \Delta f_{pR2})$$

Loss due to elastic shortening, Δf_{pES}

$$\Delta f_{pES} = \frac{E_p}{E_{ci}} f_{cgp}$$

Stress due to self-weight and prestressing force at transfer, f_{cgp}

According to the 2004 LRFD, this variable must be calculated at the section of maximum moment. Because Specimen I was originally an 88 ft. bridge girder, f_{cgp} was calculated at the midspan of the original girder.

$$f_{cgp} = \frac{0.65 f_{pu}(A_{ps})}{A_g} - \frac{M_{girder}(e_{mid})}{I_g} + \frac{0.65 f_{pu}(A_{ps})(e_{mid}^2)}{I_g}$$

$$= \frac{0.65(270\text{ksi})(6.58\text{in}^2)}{789\text{in}^2} - \frac{\left(\frac{0.86\text{kips/ft}(86\text{ft})^2}{8}\right)(12\text{in/ft})(19.5\text{in})}{260{,}730\text{in}^4}$$

$$+ \frac{0.65(270\text{ksi})(6.58\text{in}^2)(19.5\text{in})^2}{260{,}730\text{in}^4} = 2.436\,\text{ksi}$$

Modulus of Elasticity of concrete at transfer

$$E_{ci} = 33{,}000 w^{3/2} \sqrt{f_{ci}} = 33{,}000(0.155\text{kips/ft}^3)\sqrt{4.6\text{ksi}} = 4{,}319\text{ksi}$$

$$\Delta f_{pES} = \frac{28{,}500\text{ksi}}{4{,}319\text{ksi}}(2.436\text{ksi}) = 16.07\text{ ksi}$$

Loss due to Shrinkage, Δf_{pSR}

$\Delta f_{pSR} = (17\text{-}0.15H)$

where the relative humidity, H, was obtained from Figure 5.4.2.3.3-1 given in the 2004 LRFD.

$\Delta f_{pSR} = (17\text{-}0.15(73)) = 6.05$ ksi

Loss due to Creep, Δf_{pCR}

$\Delta f_{pCR} = 12 f_{cgp} - 7\Delta f_{cdp} > 0$

where Δf_{cdp} is the change in concrete stress at center of gravity of the prestressing strand steel due to permanent loads with the exception of the load acting at the time the prestressing force is applied.

Δf_{cdp}

$$\Delta f_{cdp} = \frac{(M_{deck} + M_{diaphragm})e_{mid}}{I_g} + \frac{(M_{barrier} + M_{wearcourse})e_{midc}}{I_{gc}}$$

$$= \frac{(1{,}105.2\text{kipft} + 9.5\text{kipft})(12\text{in/ft})19.5\text{in}}{260{,}730\text{in}^4} + \frac{(152.1\text{kipft} + 160.9\text{kipft})(12\text{in/ft})37.04\text{in}}{733{,}760\text{in}^4}$$

$$= 1.19\text{ksi}$$

$\Delta f_{pCR} = 12(2.463\text{ksi})\text{-}7(1.19\text{ksi}) = 21.23\text{ksi}$

Loss due to Relaxation, Δf_{pR2}

$\Delta f_{pR2} = 20\text{-}0.4\Delta f_{pES}\text{-}0.2(\Delta f_{pSR}+\Delta f_{pCR}) = 20\text{-}0.4(16.07\text{ksi})\text{-}0.2(6.05\text{ksi}+21.23\text{ksi}) = 8.12\text{ksi}$

$f_{se} = f_{po} - (\Delta f_{pES} + \Delta f_{pSR} + \Delta f_{pCR} + \Delta f_{pR2})$

= 189ksi – (16.07ksi+6.05ksi+21.23ksi+8.12ksi) = 137.53ksi

Effective shear depth, d_v

The effective shear depth, d_v, was the distance between the resultants of the tensile and compressive forces due to flexure:

$$d_v = d_p - \frac{\beta_1 c}{2}$$

Distance to the neutral axis, c

To calculate d_v, the distance to the neutral axis, c, must be known. The distance to the neutral axis, using a modified form of Eqn. (5.7.3.1.1-3) from the 2004 LRFD was (assuming the neutral axis was in the flange as shown in Figure A.2):

$$c = \frac{A_{ps} f_{pu} - 0.85 f_c{}'_d h_d b_d}{0.85 \beta_1 f_c{}' b_f + \frac{k A_{ps} f_{pu}}{d_p}} + h_d$$

where β_1 was 0.75 for the girder concrete, and k was given in the 2004 LRFD as 0.38 for stress relieved prestressing strand.

$$c = \frac{(6.58\text{in}^2)(270\text{ksi}) - 0.85(4\text{ksi})(9\text{in})(48\text{in})}{0.85(0.75)(6\text{ksi})(20\text{in}) + \frac{0.38(6.58\text{in}^2)(270\text{ksi})}{52.52\text{in}}} + 9\text{in} = 12.45\,\text{in}$$

The depth from the extreme compression fiber to the bottom of the top flange was 17 in., so the neutral axis was in the flange as assumed. Because the deck was 9 in., d_v was calculated using the β_1 of 0.85 from the deck:

$$d_v = 52.52\text{in} - \frac{0.85(12.44\text{in})}{2} = 47.23\text{in}$$

however,

$$d_v = \max(0.72h, d_v, 0.9d_p) = \max(0.72(63\text{in}), 47.23\text{in}, 0.9(52.52\text{in})) = 47.27\text{in}$$

Vertical component of the prestressing force V_p

$$V_p = A_{pd} f_{se} \sin(\alpha)$$

where A_{pd} is the area of the draped prestressing strands and α is the angle of the draped prestressing strands.

$$V_p = 10(0.1531\text{in}^2)(137.53\text{ksi})\sin(4.75) = 17.4\text{kips}$$

Required stirrups for the cells in the 2004 LRFD θ and β table

The shear capacity of the specimen was dependent upon the interaction between shear and moment at the cross-section. Thus for every value of longitudinal strain, ε_x, each cell of the θ and β table in Table A.2 represented a specific value of $\frac{v_u}{f_c'}$, in other words a specific value of V_n. A certain amount of shear reinforcement, defined by the term $\frac{A_v f_{sy}}{bs}$, was required for each value of V_n, as shown by the following 2004 LRFD Eqns. (5.8.3.3-3 and 4) for V_c and V_s:

$$V_n = \beta\sqrt{f_c'}bd_v + \frac{A_v f_{sy} d_v \cot\theta}{s}$$

$$v_n = \beta\sqrt{f_c'} + \frac{A_v f_{sy}\cot\theta}{bs}$$

$$\frac{v_n - \beta\sqrt{f_c'}}{\cot\theta} = \frac{A_v f_{sy}}{bs}$$

The value of $\frac{v_n - \beta\sqrt{f_c'}}{\cot\theta}$, and thus the amount of shear reinforcement, $\frac{A_v f_{sy}}{bs}$, required by each cell of the θ and β table is given in Table A.3. In the table, the values in the column labeled "v_n" are $\frac{v_u}{f_c'}$ from Table A.2 multiplied by f_c'. The following is an example of how the values in Table A.3 were calculated:

$$\frac{v_n - \beta\sqrt{f_c'}}{\cot\theta} = \frac{450\text{psi} - 6.32\sqrt{600\text{psi}}}{\cot(22.5)} = -16\text{psi}$$ (first row, second column of Table A.3)

Interpolate θ and β

(the stirrups were double leg #4 bars spaced at 21in)

Provided shear reinforcement = $\frac{A_v f_{sy}}{bs} = \frac{2(0.2\text{in}^2)(60\text{ksi})}{8\text{in}(21\text{in})} = 142.86\text{psi}$

Based on the shear reinforcement provided in Specimen I and the required $\frac{A_v f_{sy}}{bs}$ values in Table A.3, the values of θ and β for each ε_x were interpolated from Table A.2 and are listed in Table A.4.

Determination of V_n for every value of ε_x

The values of θ and β from Table A.4 were used to calculate V_n and M_n, given in Table A.5, for every value of ε_x using the following 2004 LRFD Eqns. (5.8.3.3-1,3 and 4):

$$V_c = \beta\sqrt{f_c'}bd_v$$

$$V_s = \frac{A_v f_{sy} d_v \cot\theta}{s}$$

$$V_n = V_c + V_s + V_p$$

The values in the first column, for example, were calculated as follows:

$$V_c = \beta\sqrt{f_c'}bd_v = 3.47\sqrt{6000\text{psi}}(8\text{in})(47.27\text{in})(1/1000) = 101.6\text{kips}$$

$$V_s = \frac{A_v f_{sy} d_v \cot\theta}{s} = \frac{2(0.2\text{in}^2)(60\text{ksi})(47.27\text{in})\cot(19)}{21} = 156.9\text{kips}$$

$$V_n = 101.6\text{kips} + 156.9\text{kips} + 17.4\text{kips} = 275.9\text{kips}$$

The values of M_n were calculated from the 2004 LRFD Eqn. (5.8.3.4.2-1) for ε_x:

$$\varepsilon_x = \frac{\frac{M_n}{d_v} + 0.5(V_n - V_p)\cot\theta - A_{ps}f_{po}}{2(E_p A_{ps})}$$

$$M_n = (2(\varepsilon_x E_p A_{ps}) - 0.5(V_n - V_p)\cot\theta + A_{ps}f_{po})d_v$$

When the value of ε_x was negative, the following 2004 LRFD Eqn (5.8.3.4.2-3) was used:

$$\varepsilon_x = \frac{\frac{M_n}{d_v} + 0.5(V_n - V_p)\cot\theta - A_{ps}f_{po}}{2(E_c A_c + E_p A_{ps})}$$

$$M_n = (2(\varepsilon_x(E_c A_c + E_p A_{ps})) - 0.5(V_n - V_p)\cot\theta + A_{px}f_{po})d_v$$

where A_{ps} and A_c for the M_n equations were the area of prestressing steel and area of concrete on the flexural tension side of the member, respectively. The flexural tension side of the member is shown in Figure A.3. The following values were used in the equation for ε_x (the value of A_{ps} only includes the draped strands on the flexural tension side of the member at midspan):

$A_{ps} = 5.967\ \text{in}^2$

$A_c = 477\ \text{in}^2$

The value of M_n in the first column, for example, was calculated as follows:

$$M_n = \begin{bmatrix} 2\left\{-\frac{0.2}{1000}\left((4{,}415\text{ksi})(477\text{in}^2) + (28{,}500\text{ksi})(5.967\text{in}^2)\right)\right\} \\ -0.5(275.9\text{kips} - 17.4\text{kips})\cot(19) + 5.967\text{in}^2(189\text{ksi}) \end{bmatrix} 47.27\text{in}\left(\frac{1\text{ft}}{12\text{in}}\right) = -622.4\text{kft}$$

V_n based on the moment to shear ratio

The moment to shear ratio $\frac{M}{V}$ at midspan for the applied loading shown in Figure A.1, neglecting dead load (which was assumed to be negligible for these calculations), was 14.25 ft. This value is between 14.0 ft. and 16.6 ft. in the bottom row of Table A.5, and therefore, V_n is:

$$V_n = 241.2\text{kips} + \frac{223.8\text{kips} - 241.2\text{kips}}{16.6\text{ft} - 14.0\text{ft}}(16.6\text{ft} - 14.25\text{ft}) = 239.5\text{kips}$$

A.1.2 AASHTO 2002 Standard Shear Capacity Calculations at midspan

Sample calculations from the 2002 Standard shear provisions for Specimen I are presented in this section.

Effective stress in the prestressing strands after losses f_{se}

$f_{se} = f_{po} - (\text{ES} + \text{SH} + \text{CR}_c + \text{CR}_s)$

Loss due to elastic shortening, ES

$$\text{ES} = \frac{E_p}{E_{ci}} f_{cir}$$

Stress due to self-weight and prestressing force at transfer, f_{cir}

According to the 2004 LRFD, this variable must be calculated at the section of maximum moment. Because Specimen I was originally an 88 ft. bridge girder, f_{cir} was calculated at the midspan of the original girder.

$$f_{cir} = \frac{0.63 f_{pu}(A_{ps})}{A_g} - \frac{M_{girder}(e_{mid})}{I_g} + \frac{0.63 f_{pu}(A_{ps})(e_{mid}^2)}{I_g}$$

$$= \frac{0.63(270\text{ksi})(6.58\text{in}^2)}{789\text{in}^2} - \frac{\left(\frac{0.86\text{kips/ft}(86\text{ft})^2}{8}\right)(12\text{in/ft})(19.5\text{in})}{260{,}730\text{in}^4}$$

$$+ \frac{0.63(270\text{ksi})(6.58\text{in}^2)(19.5\text{in})^2}{260{,}730\text{in}^4} = 2.34\,\text{ksi}$$

Modulus of Elasticity of concrete at transfer

$$E_{ci} = 33w^{3/2}\sqrt{f_{ci}} = 33(155\text{lb/ft}^3)\sqrt{4{,}600\text{psi}} = 4319\text{ksi}$$

$$ES = \frac{28{,}500\text{ksi}}{4{,}319\text{ksi}}(2.34\text{ksi}) = 15.44\text{ ksi}$$

Loss due to Shrinkage, SH

SH = (17,000-150*H*)

SH = (17,000-150(73)) = 6.05 ksi

Loss due to Creep, CR_c

$CR_c = 12f_{cir} - 7f_{cds}$

where f_{cds} is the change in concrete stress at center of gravity of the prestressing strand steel due to permanent loads with the exception of the load acting at the time the prestressing force is applied.

Δf_{cds}

$$\Delta f_{cds} = \frac{(M_{deck} + M_{diaphragm})e_{mid}}{I_g} + \frac{(M_{barrier} + M_{wearcourse})e_{midc}}{I_{gc}}$$

$$= \frac{(1{,}105.2\text{kipft} + 9.5\text{kipft})(12\text{in/ft})19.5\text{in}}{260{,}730\text{in}^4} + \frac{(152.1\text{kipft} + 160.9\text{kipft})(12\text{in/ft})37.04\text{in}}{733{,}760\text{in}^4}$$

$$= 1.19\text{ksi}$$

$CR_c = 12(2.34\text{ksi})-7(1.19\text{ksi}) = 19.75\text{ksi}$

Loss due to Relaxation, CR_s

$CR_s = 20{,}000-0.4ES-0.2(SH + CR_c) = 20{,}000-0.4(15{,}440\text{psi})-0.2(6{,}050\text{psi} + 19{,}750\text{psi})$

$=8.68\text{ksi}$

$f_{se} = f_{po} - (ES + SH + CR_c + CR_s)$

$= 189\text{ksi} - (15.44\text{ksi}+6.05\text{ksi}+19.75\text{ksi}+8.68\text{ksi}) = 139.1\text{ksi}$

Shear forces and moments at midspan

(no load factors were included in the shear forces and moments)

-Shear force at midspan due to dead load: V_d = 0 kips

-Moment at midspan due to self weight of the girder and deck: M_g+M_d = 133 kip-ft

-Ratio of shear force at midspan, due to externally applied loads occurring simultaneously with M_{max}, and M_{max}: $\frac{V_i}{M_{\max}} = \frac{1}{14.25\text{ft}}$

Distance from the extreme compression fiber to the centroid of the prestressing strand, *d*

$d = \max(d_p, 0.8h) = \max(52.52, 0.8(63\text{in})) = 52.52$ in

Flexure shear capacity V_{ci}

From 2002 Standard Eqn. (9-27):

$$V_{ci} = \max\left(1.7\sqrt{f_c'}bd, 0.6\sqrt{f_c'}bd + V_d + \frac{V_i M_{cr}}{M_{\max}}\right)$$

Minimum V_{ci}

$$V_{ci,\min} = 1.7\sqrt{f_c'}bd = 1.7\frac{\sqrt{6{,}000\text{psi}}}{1{,}000}(8\text{in})(52.52\text{in}) = 55.3\text{kips}$$

Cracking moment, M_{cr}

From 2002 Standard Eqn. (9-28):

$$M_{cr} = \frac{I_{gc}}{y_{tc}}\left(6\sqrt{f_c'} + f_{pe} - f_d\right)$$

Compressive stress in the concrete due to effective prestressing force at extreme tension fiber, f_{pe}

$$f_{pe} = \frac{f_{se}A_{ps}}{A} + \frac{f_{se}A_{ps}ey_t}{I_g} = \frac{(139.1\text{ksi})(6.58\text{in}^2)}{789\text{in}^2} + \frac{(139.1\text{ksi})(6.58\text{in}^2)(14.25\text{in})(24.73\text{in})}{260{,}730\text{in}^4}$$
$$= 2.4 \text{ ksi}$$

Stress due to dead load at extreme tension fiber, f_d

$$f_d = \frac{(M_g + M_d)y_t}{I_g} = \frac{133\text{kipft}(24.73\text{in})}{260{,}730\text{in}^4}\left(12\frac{\text{in}}{\text{ft}}\right) = 0.151\text{ksi}$$

$$M_{cr} = \frac{(541{,}092\text{in}^4)}{35.16\text{in}}\left(\frac{6\sqrt{6{,}000\text{psi}}}{1{,}000} + 2.4\text{ksi} - 0.151\text{ksi}\right)\left(\frac{1\text{ft}}{12\text{in}}\right) = 3{,}477\text{kipft}$$

$$V_{ci} = \max\left(55.3\text{kips}, 0.6\frac{\sqrt{6{,}000\text{psi}}}{1{,}000}(8\text{in})(52.52\text{in}) + 0\text{kips} + \frac{(3{,}477\text{kipft})}{14.25\text{ft}}\right) = 264\text{kips}$$

Flexure shear capacity V_{cw}

From 2002 Standard Eqn. (9-29):

$$V_{cw} = \left(3.5\sqrt{f_c'} + 0.3f_{pc}\right)bd + V_p$$

Vertical component of the prestressing force V_p

$$V_p = A_{pd}f_{se}\sin(\alpha) = 10(0.1531\text{in}^2)(139.1\text{ksi})\sin(4.75) = 17.63\text{kips}$$

Compressive stress in the concrete at the centroid of the cross-section resisting externally applied loads f_{pc}

(y_{tc} was below the top flange)

$$f_{pc} = \frac{f_{se}A_{ps}}{A} - \frac{f_{se}A_{ps}e(y_{tc} - y_t)}{I_g} + \frac{(M_g + M_d)(y_{tc} - y_t)}{I_g}$$

$$f_{pc} = \frac{139.1\text{ksi}(6.58\text{in}^2)}{789\text{in}^2} - \frac{139.1\text{ksi}(6.58\text{in}^2)(14.25\text{in})(35.16\text{in} - 24.73\text{in})}{260{,}730\text{in}^4}\ldots$$
$$+ \frac{133\text{kipft}(35.16\text{in} - 24.73\text{in})}{260{,}730\text{in}^4}\left(12\frac{\text{in}}{\text{ft}}\right) = 0.701\text{ksi}$$

$$V_{cw} = \left(3.5\frac{\sqrt{6{,}000\text{psi}}}{1{,}000} + 0.3(0.701\text{ksi})\right)(8\text{in})(52.52\text{in}) + 17.63\text{kips} = 220\text{kips}$$

Concrete contribution to shear capacity V_c

$V_c = \min(V_{ci}, V_{cw}) = \min(264\text{kips}, 220\text{kips})$

Stirrup contribution to shear capacity V_s

From 2002 Standard Eqn. (9-30):

$$V_s = \frac{A_v f_{sy} d}{s} \le 8\sqrt{f_c'}bd$$

$$V_s = \frac{2(0.2\text{in}^2)(60\text{ksi})(52.52\text{in})}{21\text{in}} \le 8\frac{\sqrt{6{,}000\text{psi}}}{1{,}000}(8\text{in})(52.52\text{in})$$

$$V_s = 60\,\text{kips} \le 260\text{kips}$$

$$V_s = 60\text{kips}$$

Shear capacity V_n

$$V_n = V_c + V_s = 220\text{kips} + 60\text{kips} = 280\text{kips}$$

A.1.3 AASHTO 1979 Interim Shear Capacity Calculations at midspan

This section contains the sample shear capacity calculations at midspan for Specimen I.

Concrete contribution to shear capacity, V_c

There was no minimum value for d, so d has been replaced with d_p in the following equations:

$$V_c = \min(180bjd_p, 0.06\,f_c'bjd_p)$$

Ratio of the distance between the centroid of compression and centroid of tension to the depth, j

$$j = \frac{\left(d_p - \frac{a}{2}\right)}{d_p}$$ where a is the depth of the equivalent rectangular compressive stress block

Depth of the equivalent rectangular compressive stress block, a

$a = 0.85c$

and assuming the depth of the compression block is in the flange of the beam:

$$c = \frac{A_{ps}f_{su} - 0.85\,f_c'{}_d h_d b_d}{\beta_1 f_c' b_f} + h_d$$

where f_{su} is the average stress in the prestressing strand at ultimate.

Average stress in the prestressing strand at ultimate load, f_{su}

$$f_{su} = f_{pu}\left(1 - 0.5\frac{\rho f_{pu}}{f_c'}\right)$$

where ρ is the ratio of prestressing steel:

$$\rho = \frac{A_{ps}}{b_{eff}d_p}$$

because the b_{eff} equations given in the code do not make sense for a composite beam that is not part of a bridge, assume b_{eff} is 48 in.:

$$\rho = \frac{6.58\text{in}^2}{48\text{in}(52.52\text{in})} = 0.0026$$

$$f_{su} = 270\text{ksi}\left(1 - 0.5\frac{0.0026(270\text{ksi})}{6\text{ksi}}\right) = 254.2\text{ksi}$$

$$c = \frac{6.58\text{in}^2(254.2\text{ksi}) - 0.85(4\text{ksi})(9\text{in})(48\text{in})}{0.75(6\text{ksi})(20\text{in})} + 9\text{in} = 11.26\text{in}$$

$$a = 0.85(11.26\text{in}) = 9.58\text{in}$$

$$j = \left(\frac{52.52\text{in} - \frac{9.58\text{in}}{2}}{52.52\text{in}}\right) = 0.91$$

$$V_c = \min\left(\frac{180(8\text{in})(0.91)(52.52\text{in})}{1{,}000}, 0.06(6\text{ksi})(8\text{in})(0.91)(52.52\text{in})\right) = \min(69\text{kips}, 138\text{kips})$$

=69 kips

Stirrup contribution to shear capacity

$$V_s = \frac{2A_v f_{sy} j d_p}{s} = \frac{2(2)(0.2\text{in}^2)(60\text{ksi})(0.91)(52.52\text{in}^2)}{21\text{in}} = 109\text{kips}$$

Shear capacity V_n

$$V_n = V_c + V_s = 69\text{kips} + 109\text{kips} = 178\text{kips}$$

A.1.4 AASHTO Strut and Tie Model Shear Capacity Calculations

The strut and tie model is not a sectional method, rather the shear capacity is dependent upon the limit states of the elements that comprise the model. Figure A.4 shows half of the strut and tie model, which is symmetric about the midspan, of Specimen I. All of the nodes in the figure were located in the top and bottom flanges, which were significantly wider than the web. Therefore, the shear strength of this model was controlled by the yield strength of the stirrups and the strength of the compression struts in the web of the specimen.

Determine the force in each stirrup at yield, F_s

$$F_s = A_v f_{sy} = 2(0.2\text{in}^2)(60\text{ksi}) = 24\text{kips}$$

Determine the compressive strength of the direct strut between the applied load and the support *(F)*

Because of the shallow angle, α_s, the direct strut from the load to the roller support was the most susceptible to failure.

Cross-sectional area of the direct strut, A_{cs}

The cross-sectional area of this strut, A_{cs}, was determined using the nodal dimensions of the node at the roller support in Figure A.4, which was the smaller of the two nodes connecting this strut (and thus conservative), and the width of the web:

$$A_{cs} = (l_a \cos(\alpha_s) + l_b \sin(\alpha_s))b = ((8\text{in})\cos(17°) + (15\text{in})\sin(17°))8\text{in} = 96.28\text{in}^2$$

Limiting compressive stress in the direct strut, f_{cu}

The following is from the 2004 LRFD Eqn. (5.6.3.3.3-1):

$$f_{cu} = \min\left(0.85 f_c', \frac{f_c'}{0.8 + 170\varepsilon_1}\right)$$

Principal tensile strain in the cracked concrete, ε_1

In the following equation, ε_s is the longitudinal tensile strain in the concrete, which was assumed to be 0.0 ksi in the web due to the prestressing force. From the 2004 LRFD Eqn. (5.6.3.3.3-2):

$$\varepsilon_1 = \varepsilon_s + (\varepsilon_s + 0.002)\cot^2 \alpha_s = 0.0 + (0.0 + 0.002)\cot^2(17°) = 0.0214$$

$$f_{cu} = \min\left(0.85(6\text{ksi}), \frac{6\text{ksi}}{0.8 + 170(0.0214)}\right) = \min(5.1\text{ksi}, 1.35\text{ksi}) = 1.35\text{ksi}$$

Therefore, from the 2004 LRFD Eqn. (5.6.3.3.1-1):

$F = A_{cs} f_{cu} = (96.28\text{in}^2)(1.35\text{ksi}) = 130\text{kips}$

Vertical component of the prestressing force, V_p

$V_p = A_{po} f_{se} \sin(\alpha) = 10(0.1531\text{in}^2)(137.53\text{ksi})\sin(4.75) = 17.4\text{kips}$

Shear Capacity V_n

The contribution of the direct strut to shear capacity, V_{ds}, is:

$V_{ds} = F \sin \alpha_s = (130\text{kips})\sin(17°) = 38\text{kips}$

Because V_{ds} was larger than the force in each stirrup at yield, F_s, and the struts connecting the stirrups to the roller support were steeper and thus had larger capacities than the direct strut; the contribution of the struts connecting the stirrups to the roller support were limited by F_s, and the shear capacity of the model was:

$V_n = V_{ds} + (\text{number of stirrups})(F_s) + V_p = 38\text{kips} + (7)(24\text{kips}) + 17.4\text{kips} = 223\text{kips}$

A.2 Design Calculations

Samples of the design calculations discussed in Section 3.5 for the 2004 LRFD, 2002 Standard, and 1979 Interim shear provisions are provided in this section. The design calculations were performed for the original 88 ft. bridge, assuming a girder spacing of 10 ft., and bridge deck height of 9 in. The sample calculations presented in this section are from the critical section as defined by each of the codes. The resistance factor, ϕ, in each of the shear provisions was 0.9 for shear.

A.2.1 AASHTO 2004 LRFD Stirrup Design at the Critical Section

According to the 2004 LRFD, the critical section was d_v from the support, which was taken from the d_v at midspan as 55 in. The 2004 LRFD is an iterative method, however, only the final iteration is shown in this section.

Factored shear force and moment at the critical section

The factored ultimate shear force and moment included the dead load from: girder, deck, diaphragms, barrier, and wearing course; and live load from AASHTO HL-93. These reactions were computed using a Mn/DOT Mathcad sheet.

-Factored ultimate shear force, V_u = 298.3 kips

-Factored ultimate moment, M_u = 1,246.8 kip-ft

Effective flange width of the composite section, b_{eff}

From the 2004 LRFD Section 4.6.2.6.1

b_{eff} = min(0.25(span length), $12h_d$ + 0.5(beam top flange width), average beam spacing)

$$b_{eff} = \min\left(0.25(88\text{ft})\frac{12\text{in}}{\text{ft}}, 12(9\text{in}) + 0.5(20\text{in}), 10\text{ft}\left(\frac{12\text{in}}{\text{ft}}\right)\right) = \min(264\text{in}, 118\text{in}, 120\text{in}) = 118\text{in}$$

Effective shear depth, d_v

$$d_v = d_p - \frac{\beta_1 c}{2}$$

Distance to the neutral axis, c

The distance to the neutral axis, using a modified form of Eqn. (5.7.3.1.1-3) from the 2004 LRFD was (assuming the neutral axis was in the deck):

$$c = \frac{A_{ps} f_{pu}}{0.85\beta_1 f_c' d b_{eff} + \frac{k A_{ps} f_{pu}}{d_p}}$$

$$c = \frac{43(0.1531\text{in}^2)(270\text{ksi})}{0.85(0.85)(4\text{ksi})(118\text{in}) + \frac{0.28(43)(0.1531\text{in}^2)(270\text{ksi})}{50.04\text{in}}} = 5.06\text{in}$$

The height of the deck was 9 in., so the neutral axis was in the deck as assumed.

$$d_v = 50.04\text{in} - \frac{0.85(5.06\text{in})}{2} = 47.89\text{in}$$

however,

d_v = max(0.72h, d_v,0.9d_p) = max(0.72(63in), 47.89in, 0.9(50.06in)) = 47.89in

Vertical component of the prestressing force V_p

$$V_p = A_{pd} f_{se} \sin(\alpha) = 10(0.1531\text{in}^2)(137.53\text{ksi})\sin(4.75) = 17.4\text{kips}$$

Determine θ and β

The quantities $\frac{v_u}{f_c'}$ and ε_x were required to find θ and β from Table A.2. However, because θ was in the equation for ε_x, it was found iteratively. For the final iteration, θ was assumed to be 24.2°.

Ratio of the shear stress to the concrete compressive strength

From the 2004 LRFD Eqn. (5.8.2.9-1):

$$\frac{v_u}{f_c'} = \frac{V_u - \phi V_p}{\phi b d_v f_c'} = \frac{298.3\text{kips} - 0.9(17.4\text{kips})}{0.9(8\text{in})(47.89\text{in})(6\text{ksi})} = 0.137$$

Longitudinal strain, ε_x

The following equation assumes ε_x was negative at the critical section, and only 33 of the prestressing strands were on the flexural tension side of the member.

$$\varepsilon_x = \frac{\frac{M_u}{d_v} + 0.5(V_u - V_p)\cot\theta - A_{ps}f_{po}}{2(E_c A_c + E_p A_{ps})}$$

$$\varepsilon_x = \frac{\frac{1{,}246.8\text{kipft}}{47.89\text{in}}\left(\frac{12\text{in}}{\text{ft}}\right) + 0.5(298.3\text{kips} - 17.4\text{kips})\cot(24.2°) - 33(0.1531\text{in}^2)(189\text{ksi})}{2(4{,}415\text{ksi}(477\text{in}^2) + 28{,}500\text{ksi}(33)(0.1531\text{in}^2))}$$

$$\varepsilon_x = -7.33\times10^{-5}$$

$\varepsilon_x \times 1000 = -0.0733$ (the initial assumption that ε_x was negative was correct)

Using $\frac{v_u}{f_c'}$ of 0.136 and $\varepsilon_x \times 1000$ of –0.0733, θ from Table A.2 was 24.2°, which matched the original guess, and β was 2.78.

Concrete contribution to shear capacity, V_c

$$V_c = 0.0316\beta\sqrt{f_c'}bd_v = 0.0316(2.78)\sqrt{6\text{ksi}}(8\text{in})(47.89\text{in}) = 82.4\text{kips}$$

Required stirrup spacing for double leg #4 reinforcing bars

$$V_u = \phi(V_c + V_s + V_p)$$

$$V_u = \phi\left(V_c + \frac{A_v f_{sy} d_v \cot\theta}{s_{req}} + V_p\right)$$

$$s_{req} = \frac{A_v f_{sy} d_v \cot\theta}{\frac{V_u}{\phi} - V_c - V_p}$$

$$s_{req} = \frac{2(0.2\text{in}^2)(60\text{ksi})(47.89\text{in})\cot(24.2°)}{\frac{298.3\text{kips}}{0.9} - 82.4\text{kips} - 17.4\text{kips}} = 11.04\text{in}$$

Check limits on spacing

From the 2004 LRFD Eqn. (5.8.2.5-1):

$$s_{\max} = \frac{A_v f_{sy}}{0.0316\sqrt{f_c'}b} = \frac{2(0.2\text{in}^2)(60\text{ksi})}{0.0316\sqrt{6\text{ksi}}(8\text{in})} = 38.75\text{in} > s_{req} = 11.04\text{in}$$

Because $v_u \geq 0.125 f_c'$:

$$s_{\max} = \min(12\text{in}, 0.4d_v) = \min(12\text{in}, 0.4(47.89\text{in})) = 12\text{in} > s_{req} = 11.04\text{in}$$

Check interface shear

The factored shear at the critical section from the dead load of the barrier, wearing course, and the HL-93 loading was:

$V_{u,h}$ = 202.9kips

Required stirrup spacing for horizontal shear, s_h

From the 2004 LRFD Eqn. (5.8.4.1-1):

$$\frac{V_{u,h}}{\phi} = cA_{cv} + \mu A_{vf} f_{sy}$$

$$\frac{V_{u,h}}{\phi d_v} = \frac{cA_{cv}}{\text{unit length}} + \frac{\mu A_{vf} f_{sy}}{s_h}$$

$$s_h = \frac{\mu A_{vf} f_{sy}}{\frac{V_{u,h}}{\phi d_v} - \frac{cA_{cv}}{\text{unit length}}}$$

where A_{cv} is the area of concrete engaged in shear transfer, A_{vf} is the area of shear reinforcement crossing the shear plane, c is the cohesion factor (given in the 2004 LRFD

as 0.1ksi for intentionally roughened surfaces), and μ is the friction factor (given in the 2004 LRFD as 1.0 for intentionally roughened surfaces).

$$s_h = \frac{1.0(2)(0.2\text{in}^2)(60\text{ksi})}{\frac{202.9\text{kips}}{0.9(47.89\text{in})} - \frac{0.1\text{ksi}(20\text{in})(1\text{in})}{\text{in}}} = 8.86\text{in}$$

Because s_h was less than s_{req}, the design stirrups spacing was:

s = 8.86in

Check limits on $V_{n,h}$

From the 2004 LRFD Eqns. (5.8.4.1-2 and 3):

$$V_{n,h\,\max} \le \min\left(0.2 f_c' d A_{cv}, 0.8 A_{cv}\right) \le \min\left(\frac{0.2(4\text{ksi})(20\text{in})(1\text{in})}{\text{in}}, \frac{0.8(20\text{in})(1\text{in})}{\text{in}}\right) \le \frac{16\text{kips}}{\text{in}}$$

$$V_{n,h} = \frac{cA_{cv}}{\text{unit length}} + \frac{\mu A_{vf} f_{sy}}{s} = \frac{0.1\text{ksi}(20\text{in})(1\text{in})}{\text{in}} + \frac{1.0(2)(0.2\text{in}^2)(60\text{ksi})}{8.86\text{in}} = 4.71\frac{\text{kips}}{\text{in}}$$

$V_{n,h}$ was less than the maximum, so s = 8.86in was acceptable.

Check limits on V_n

From the 2004 LRFD Eqn. (5.8.3.3-2):

$$V_{n,\max} = 0.25 f_c' b d_v + V_p = 0.25(6\text{ksi})(8\text{in})(47.89\text{in}) + 17.91\text{kips} = 593\text{kips}$$

$$V_n = V_c + V_s + V_p$$

$$V_n = 82.4\text{kips} + \frac{2(0.2\text{in}^2)(60\text{ksi})(47.89\text{in})\cot(24.2°)}{8.86\text{n}} + 17.4 = 389\text{kips} < V_{n,\max}$$

Therefore, at the critical section, the design spacing for #4 stirrups was 8.86in. governed by horizontal shear.

A.2.2 AASHTO 2002 Standard Stirrup Design at the Critical Section

According to the 2002 Standard, the critical section was $\frac{h}{2}$ from the support, or 31.5 in.

Shear forces and moments at the critical section

The factored ultimate shear included the dead load from: girder, deck, diaphragms, barrier, and wearing course; and live load from AASHTO HS20-44. The shear forces and moments were computed using Virtis software.

-Factored ultimate shear force, V_u = 274.7 kips

-Unfactored shear force due to dead load: V_d = 95.7 kips

-Unfactored moment due to self weight of the girder: M_g = 93.8 kip-ft

-Unfactored moment due to self weight of the deck and diaphragm: M_d = 130.8 kip-ft

-Unfactored moment due to self weight of the barrier: M_b = 17.9 kip-ft

-Unfactored moment due to self weight of the wearing course: M_w = 18.9 kip-ft

-Factored shear force due to externally applied loads, occurring simultaneously with M_{max}: V_i = 102 kips

-Factored maximum moment due to externally applied loads: M_{max} = 475 kip-ft

Distance from the extreme compression fiber to the centroid of the prestressing strand, d

$d = \max(d_p, 0.8h) = \max(49.59\text{in}, 0.8(63\text{in})) = 50.4$ in

Flexure shear capacity V_{ci}

From the 2002 Standard Eqn. (9-27):

$$V_{ci} = \max\left(1.7\sqrt{f_c'}bd, 0.6\sqrt{f_c'}bd + V_d + \frac{V_i M_{cr}}{M_{\max}}\right)$$

Minimum V_{ci}

$$V_{ci,\min} = 1.7\sqrt{f_c'}bd = = 1.7\frac{\sqrt{6{,}000\text{psi}}}{1{,}000}(8\text{in})(50.4\text{in}) = 53.1\text{kips}$$

Cracking moment, M_{cr}

From the 2002 Standard Eqn. (9-28)

$$M_{cr} = \frac{I_{gc}}{y_{tc}}\left(6\sqrt{f_c'} + f_{pe} - f_d\right)$$

Compressive stress in the concrete due to effective prestressing force at extreme tension fiber, f_{pe}

$$f_{pe} = \frac{f_{se}A_{ps}}{A} + \frac{f_{se}A_{ps}ey_t}{I_g}$$

Note: e at the critical section was 11.3 in.

$$f_{pe} = \frac{(139.1\text{ksi})(6.58\text{in}^2)}{789\text{in}^2} + \frac{(139.1\text{ksi})(6.58\text{in}^2)(11.3\text{in})(24.73\text{in})}{260{,}730\text{in}^4} = 2.14\text{ksi}$$

Stress due to dead load at extreme tension fiber, f_d

$$f_d = \frac{(M_g + M_d)y_t}{I_g} + \frac{(M_b + M_w)y_{tc}}{I_{gc}}$$

Note: y_{tc} was 42.27 in. with a girder spacing of 10 ft

$$f_d = \left(\frac{(93.8\text{kipft} + 130.8\text{kipft})(24.73\text{in})}{260{,}730\text{in}^4} + \frac{(17.9\text{kipft} + 18.9\text{kipft})(42.27)}{733{,}760\text{in}^4}\right)\times\ldots$$
$$\left(12\frac{\text{in}}{\text{ft}}\right) = 0.281\text{ksi}$$

$$M_{cr} = \frac{(733{,}760\text{in}^4)}{42.27\text{in}}\left(\frac{6\sqrt{6{,}000\text{psi}}}{1{,}000} + 2.14\text{ksi} - 0.281\text{ksi}\right)\left(\frac{1\text{ft}}{12\text{in}}\right) = 3{,}362\text{kipft}$$

$$V_{ci} = \max\left(53.1\text{kips}, 0.6\frac{\sqrt{6{,}000\text{psi}}}{1{,}000}(8\text{in})(50.4\text{in}) + 95.7\text{kips} + \frac{102\text{kips}(3{,}362\text{kipft})}{475\text{kipft}}\right)$$

$$V_{ci} = \max(53.1\text{kips}, 836\text{ kips}) = 836\text{kips}$$

Flexure shear capacity V_{cw}

From the 2002 Standard Eqn. (9-29):

$$V_{cw} = \left(3.5\sqrt{f_c'} + 0.3f_{pc}\right)bd + V_p$$

Vertical component of the prestressing force V_p

$$V_p = A_{pd} f_{se} \sin(\alpha) = 10(0.1531\text{in}^2)(139.1\text{ksi})\sin(4.75) = 17.63$$

Compressive stress in the concrete at the centroid of the cross-section resisting externally applied loads f_{pc}

f_{pc} was calculated at the junction of the web and flange, because the centroid was in the flange. In the following equation, h_f is the distance from the extreme tension fiber to the junction of the web and flange.

$$f_{pc} = \frac{f_{se}A_{ps}}{A} - \frac{f_{se}A_{ps}e(h_f - y_t)}{I_g} + \frac{(M_g + M_d)(h_f - y_t)}{I_g}$$

$$f_{pc} = \frac{139.1\text{ksi}(6.58\text{in}^2)}{789\text{in}^2} - \frac{139.1\text{ksi}(6.58\text{in}^2)(11.3\text{in})(40\text{in} - 24.73\text{in})}{260{,}730\text{in}^4} \ldots$$
$$+ \frac{(93.8\text{kipft} + 130.8\text{kipft})(40\text{in} - 24.73\text{in})}{260{,}730\text{in}^4}\left(12\frac{\text{in}}{\text{ft}}\right) = 0.712\text{ksi}$$

$$V_{cw} = \left(3.5\frac{\sqrt{6{,}000\text{psi}}}{1{,}000} + 0.3(0.712\text{ksi})\right)(8\text{in})(50.4\text{in}) + 17.63\text{kips} = 213\text{kips}$$

Concrete contribution to shear capacity V_c

$V_c = \min(V_{ci}, V_{cw}) = \min(836\text{kips}, 213\text{kips}) = 213\text{kips}$

Required stirrup spacing for double leg #4 reinforcing bars

$$V_u = \phi(V_c + V_s)$$

$$s_{req} = \frac{A_v f_{sy} d}{\frac{V_u}{\phi} - V_c} = \frac{2(0.2\text{in}^2)(60\text{ksi})(50.4\text{in})}{\frac{274.7\text{kips}}{0.9} - 213\text{kips}} = 13.11\text{in}$$

Check limits on spacing

From the 2002 Standard Eqn. (9-31):

$$s_{\max} = \min\left(24\text{in}, \frac{A_v f_{sy}}{50b}\right) = \min\left(24\text{in}, \frac{2(0.2\text{in}^2)(60{,}000\text{psi})}{50(8\text{in})}\right) = 24\text{in}$$

$s_{max} > s_{req}$

Check interface shear

Surface intentionally roughened, and assume minimum ties provided (check of the minimum ties will follow)

$$\frac{V_u}{\phi} = \frac{274.7\text{kips}}{0.9} = 305.2\text{kips}$$

$$V_{n,h} = 350 b_v d_p$$

where b_v is the width of the flange.

$$V_{n,h} = \frac{350(20\text{in})(49.59\text{in})}{1{,}000} = 347.2\text{kips} > \frac{V_u}{\phi}$$

Therefore, as long as the stirrup spacing of 13.11in satisfies the minimum tie requirement for horizontal shear transfer, no additional stirrups are required for horizontal shear.

Check tie spacing requirements for horizontal shear

$$\text{minimum } A_{v,h} = \frac{50 b_v s}{f_{sy}} = \frac{50(20\text{in})(13.11\text{in})}{60{,}000\text{psi}} = 0.219\frac{\text{in}^2}{\text{ft}}$$

$$\text{provided } A_{v,h} = \frac{2(0.2in^2)}{13.11in}\left(12\frac{in}{ft}\right) = 0.366\frac{\text{in}^2}{\text{ft}}$$

s_{max} = min(4(b), 24in) = min(4(8in), 24in) = 24 in

The stirrup spacing of 13.11in meets the horizontal shear requirements of the 2002 Standard shear provisions.

Check limits on V_s

$$V_s = \frac{A_v f_{sy} d}{s} \le 8\sqrt{f_c'}bd$$

$$V_s = \frac{2(0.2\text{in}^2)(60\text{ksi})(50.4\text{in})}{13.11\text{in}} \le 8\frac{\sqrt{6{,}000\text{psi}}}{1{,}000}(8\text{in})(50.4\text{in})$$

$$V_s = 92.2\text{ kips} \le 250\text{kips}$$

$$V_s = 92.2\text{kips}$$

Therefore, at the critical section, the design spacing for #4 stirrups was 13.11in.

A.2.3 AASHTO 1979 Interim Stirrup Design at the Critical Section

According to the 1979 Interim, the critical section was a quarter of the length of the beam from the support, or 22ft.

Shear force at the critical section

The factored ultimate shear included the dead load from: girder, deck, diaphragms, barrier, and wearing course; and live load from AASHTO HS20-44. The shear force was computed using Virtis software.

-Factored ultimate shear force, V_u = 182.3 kips

Concrete contribution to shear capacity, V_c

$V_c = \min(180 b j d_p, 0.06 f_c' b j d_p)$

Ratio of the distance between the centroid of compression and centroid of tension to the depth, j

For rectangular or flanged sections in which the neutral axis lies within the flange, the ultimate flexural strength shall be assumed as:

$$M_u = A_{ps} f_{su} d\left(1 - 0.6\frac{\rho f_{su}}{f'_c}\right)$$

From this equation, it can be inferred that:

$$j = 1 - 0.6\frac{\rho f_{su}}{f'_c}$$

Average stress in the prestressing strand at ultimate load, f_{su}

$$f_{su} = f_{pu}\left(1 - 0.5\frac{\rho f_{pu}}{f_c'}\right)$$

where ρ is the ratio of prestressing steel:

$$\rho = \frac{A_{ps}}{b_{eff} d_p}$$

where b_{eff} is the effective width of the composite flange:

$$b_{eff} = \min\left(\frac{\text{girder length}}{4}, \text{girder spacing}, 12(\text{slab thickness}) + \text{b}\right)$$

$$= \min\left(\frac{88\text{ft}\left(\frac{12\text{in}}{\text{ft}}\right)}{4}, 10\text{ft}\left(\frac{12\text{in}}{\text{ft}}\right), 12(9\text{in}) + 8\right) = \min(264\text{in}, 120\text{in}, 116\text{in}) = 116\text{in}$$

$$\rho = \frac{6.58\text{in}^2}{116\text{in}(54.4\text{in})} = 0.001$$

$$f_{su} = 270\text{ksi}\left(1 - 0.5\frac{0.001(270\text{ksi})}{6\text{ksi}}\right) = 263.9\text{ksi}$$

$$j = 1 - 0.6\left(\frac{0.001(263.9\text{ksi})}{6\text{ksi}}\right) = 0.97$$

$$V_c = \min\left(\frac{180(8\text{in})(0.97)(54.4\text{in})}{1{,}000}, \frac{0.06(6{,}000\text{psi})(8\text{in})(0.97)(54.4\text{in})}{1{,}000}\right) = \min(76\text{kips}, 152\text{kips})$$

$$= 76\text{kips}$$

Required stirrup spacing for double leg #4 reinforcing bars

$$V_u = \phi(V_c + V_s) = \phi\left(V_c + \frac{2A_v f_{sy} j d_p}{s_{req}}\right)$$

$$s_{req} = \frac{2A_v f_{sy} j d_p}{\frac{V_u}{\phi} - V_c} = \frac{2(2)(0.2\text{in}^2)(60\text{ksi})(0.97)(54.4\text{in})}{\frac{182.3\text{kips}}{0.9} - 76\text{kips}} = 20\text{in}$$

Check maximum stirrups spacing

$$s_{\max} = \frac{A_v f_{sy}}{100b} = \frac{2(0.2\text{in}^2)(60{,}000\text{psi})}{100(8\text{in})} = 30\text{in}$$

$s_{\max} > s_{req}$

Check stirrup spacing requirement for interface shear

The minimum area of steel per linear ft. for horizontal shear was two #3 bars spaced at 12in. Therefore, the maximum spacing for double leg #4 stirrups was:

$$\frac{(\text{area of two \#4 bars})}{s_{max}} = \frac{(\text{area of two \#3 bars})}{12\text{in}}$$

$$s_{max} = \frac{2(0.2\text{in}^2)}{\frac{2(0.11\text{in}^2)}{12\text{in}}} = 21.8\text{in}$$

Therefore, at the critical section, the design spacing for #4 stirrups was 20 in.

Table A.1 Material and Section Properties

Material Property	Variable	Value
Girder concrete compressive strength	f_c'	6 ksi
Girder concrete compressive strength at transfer	f_{ci}	4.6 ksi
Deck concrete compressive strength	$f_{c'd}$	4 ksi
Initial jacking stress in the prestressing strand	f_{po}	189 ksi
Yield strength of the prestressing strand	f_{py}	243 ksi
Ultimate strength of the prestressing strand	f_{pu}	270 ksi
Yield strength of the transverse reinforcement	f_{sy}	60 ksi
Modulus of Elasticity of the prestressing strand	E_p	28,500 ksi
Modulus of Elasticity of the girder concrete ($57{,}000\sqrt{f_c'}$)	E_c	4,415 ksi
Section Property	**Variable**	**Value**
Total height	h	63 in
Height of the deck	h_d	9 in
Width of the web	b	8 in
Width of the top flange	b_f	20 in
Width of the bridge deck	b_d	48 in
Area of 43 prestressing strand	A_{ps}	$43(0.1531\text{in}^2) = 6.58\ \text{in}^2$
Moment of Inertia of the noncomposite section	I_g	$260{,}730\ \text{in}^4$
Moment of Inertia of the composite section	I_{gc}	$541{,}092\ \text{in}^4$
Moment of Inertia of the composite section of the original 88 ft bridge girder with 10 ft girder spacing (used in the 2004 LRFD prestressing loss calculations)	I_{gc2}	$733{,}760\ \text{in}^4$
Area of the noncomposite section	A_g	$789\ \text{in}^2$
Eccentricity of the prestressing strands at cross-section under the applied load shown in Figure A.1 (noncomposite section)	e	14.25 in
Eccentricity of the prestressing strands at midspan of the original 88 ft bridge girder (noncomposite section)	e_{mid}	19.5 in
Eccentricity of the prestressing strands at midspan of the original 88 ft bridge girder (composite section with 10 ft girder spacing)	e_{midc}	37.04 in
Distance from the extreme tension fiber to the centroid of the noncomposite section	y_t	24.73 in
Distance from the extreme tension fiber to the centroid of the composite section	y_{tc}	35.16 in

Table A.2 2004 LRFD θ and β for Sections with Transverse Reinforcement

$\frac{v_u}{f_c'}$	ε_x * 1000								
	≤-0.20	≤-0.10	≤-0.05	≤0	≤0.125	≤0.25	≤0.50	≤0.75	≤1.00
≤0.075	22.5	20.4	21.0	21.8	24.3	26.6	30.5	33.7	36.4
	6.32	4.75	4.10	3.75	3.24	2.94	2.59	2.38	2.23
≤0.100	18.1	20.4	21.4	22.5	24.9	27.1	30.8	34.0	36.7
	3.79	3.38	3.24	3.14	2.91	2.75	2.50	2.32	2.18
≤0.125	19.9	21.9	22.8	23.7	25.9	27.9	31.4	34.4	37.0
	3.18	2.99	2.94	2.87	2.74	2.62	2.42	2.26	2.13
≤0.150	21.6	23.3	24.2	25.0	26.9	28.8	32.1	34.9	37.3
	2.88	2.79	2.78	2.72	2.60	2.52	2.36	2.21	2.08
≤0.175	23.2	24.7	25.5	26.2	28.0	29.7	32.7	35.2	36.8
	2.73	2.66	2.65	2.60	2.52	2.44	2.28	2.14	1.96
≤0.200	24.7	26.1	26.7	27.4	29.0	30.6	32.8	34.5	36.1
	2.63	2.59	2.52	2.51	2.43	2.37	2.14	1.94	1.79
≤0.225	26.1	27.3	27.9	28.5	30.0	30.8	32.3	34.0	35.7
	2.53	2.45	2.42	2.40	2.34	2.14	1.86	1.73	1.64
≤0.250	27.5	28.6	29.1	29.7	30.6	31.3	32.8	34.3	35.8
	2.39	2.39	2.33	2.33	2.12	1.93	1.70	1.58	1.5

Table A.3 Required Stirrups for the Cells in the 2004 LRFD θ and β Table

v_n (psi)	ε_x * 1000								
	≤-0.20	≤-0.10	≤-0.05	≤0	≤0.125	≤0.25	≤0.50	≤0.75	≤1.00
450	-16	31	51	64	90	111	147	177	204
600	100	126	137	148	174	198	242	283	321
750	182	208	219	232	261	290	343	394	441
900	268	294	308	321	354	387	450	508	563
1050	359	388	403	418	455	491	560	624	672
1200	458	490	505	521	561	601	667	722	774
1350	565	599	615	632	675	706	762	820	879
1500	684	717	734	752	790	821	882	940	998

Note: the values in this table are $\frac{A_v f_{sy}}{bs}$ which are in terms of psi

Table A.4 Interpolated values of θ and β

v_n (psi)	ε_x * 1000								
	≤-0.20	≤-0.10	≤-0.05	≤0	≤0.125	≤0.25	≤0.50	≤0.75	≤1.00
<450							30.5 2.59	33.7 2.38	36.4 2.23
450				22.5 3.18	24.7 3.03	26.8 2.87			
600	19.0 3.47	20.7 3.3	21.5 3.22						
750									
900									
1050									
1200									
1350									
1500									

Note: these values were interpolated from Table A.2 using the provided $\frac{A_v f_{sy}}{bs}$ of 142.86 psi and the required $\frac{A_v f_{sy}}{bs}$ given in Table A.3.

Table A.5 Calculation of V_n and M_n

Variable	ε_x * 1000								
	≤-0.20	≤-0.10	≤-0.05	≤0	≤0.125	≤0.25	≤0.50	≤0.75	≤1.00
V_c (kips)	101.6	96.6	94.2	93.1	88.8	84.1	75.9	69.8	65.3
V_s (kips)	156.9	143.0	137.2	130.7	117.6	107.1	91.8	81.0	73.3
V_p (kips)	17.4	17.4	17.4	17.4	17.4	17.4	17.4	17.4	17.4
V_n (kips)	275.9	257	248.8	241.2	223.8	208.6	185.1	168.2	156
M_n (kip-ft)	-622.4	1401.1	2388.9	3375.9	3725.1	4031.4	4551.5	5001.6	5411.9
$\frac{M_n}{V_n}$ (ft)	-2.3	5.4	9.6	14.0	16.6	19.3	24.5	29.7	33.9

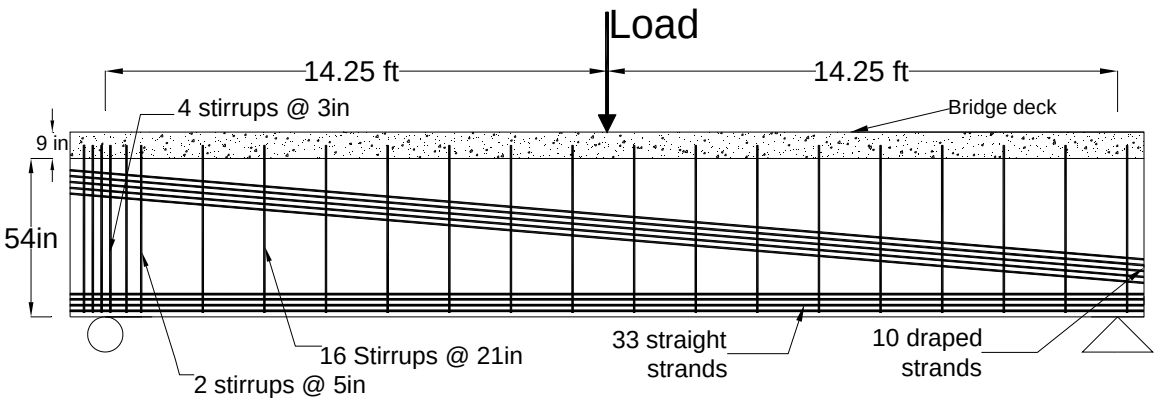

Figure A.1 Loading condition for Sample Calculations

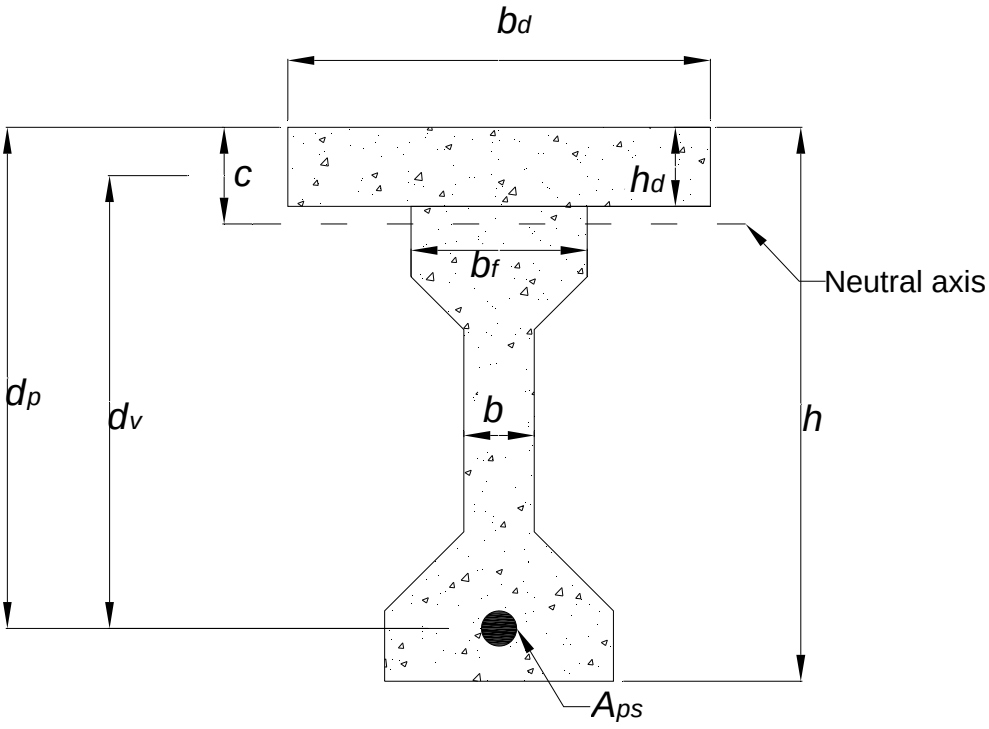

Figure A.2 Cross-section for Sample Calculations

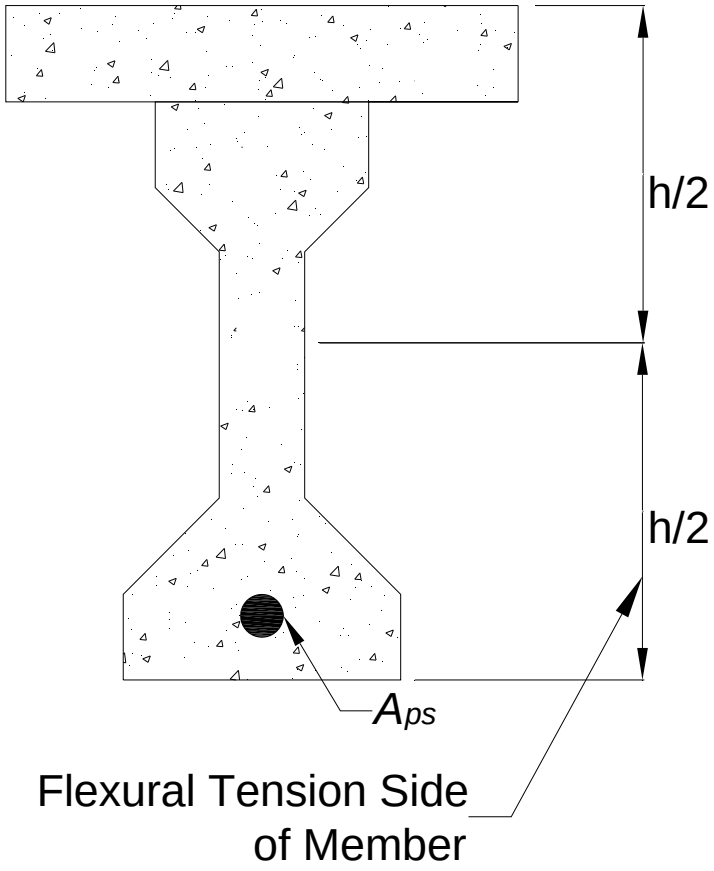

Figure A.3 Flexural Tension Side of Member

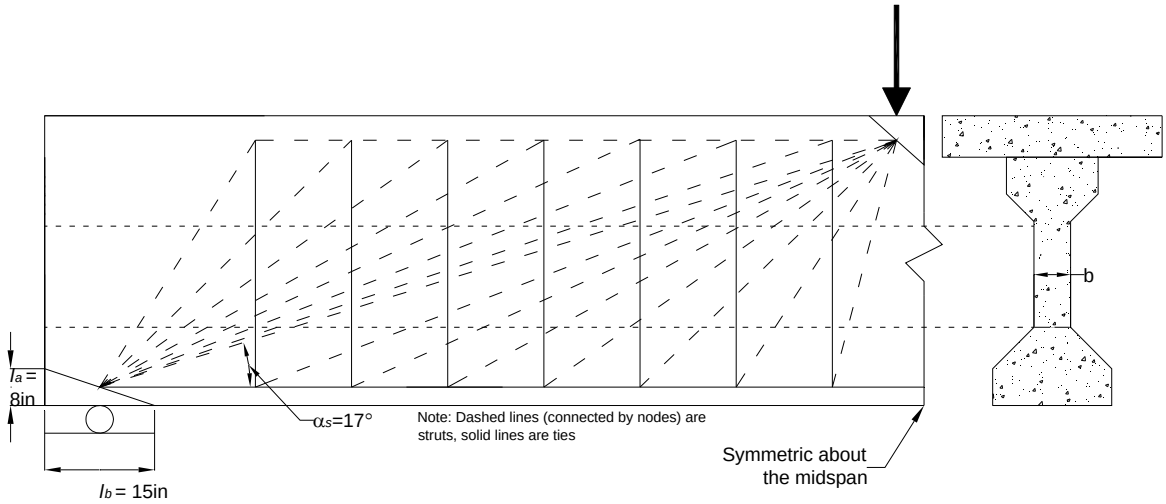

Figure A.4 Strut and Tie Model for Half of the Specimen with a Bridge Deck

Appendix B
Calculation of the Krypton Strains

B.1 Introduction

The Krypton dynamic coordinate measurement system was described in section 4.4.3. The Krypton LEDs were installed in a 10 in. by 10 in. grid pattern shown in Figure B.1. The Krypton system recorded the X, Y, and Z displacements of the LEDs with respect to a static coordinate system established at the center of the Krypton camera. The coordinate system shown in the figure represents the Krypton camera coordinate system. The exact location of the camera coordinate system was unimportant, because the displacement data were only used to calculate strains between LEDs, which required relative displacements. This appendix describes how those strains were calculated.

B.2 Displacement Field Analysis

The LEDs in Figure B.1 form a field of known displacements, from which normal and shear strains could be calculated in the X-Z plane. The field was divided into 10 in. by 10 in., four node quadrilateral elements, which were modeled using isoparametric elements. The analysis procedure presented herein is not limited to 10 in. by 10 in. elements; it applies to any four node quadrilateral combination of LEDs.

If LED installation had been exact, the grid formed would have had perfectly square elements, and the strains between LEDs in the X-Z plane could have been solved for directly. Installation of the LEDs at the grid intersections was as precise as possible; however, it was impossible to form an initial grid with perfect 90° angles. Isoparametric elements were selected to represent the individual elements in Figure B.1, because the initial condition of the grid was considered explicitly in the formulation of the isoparametric elements.

B.2.1 Isoparametric Mapping

The Cartesian coordinate system of a quadrilateral element and its corresponding isoparametric formulation in the natural coordinate system are shown in Figure B.2. The two systems were related through the following equations:

$$x(\xi,\eta) = \sum_{I=1}^{4} X_I N_I(\xi,\eta) \tag{B.1}$$

$$z(\xi,\eta) = \sum_{I=1}^{4} Z_I N_I(\xi,\eta) \tag{B.2}$$

In these equations, N_I represents the linear shape functions of the isoparametric element:

$$N_1 = \frac{1}{4}(1-\xi)(1-\eta) \quad \text{(B.3)} \qquad N_3 = \frac{1}{4}(1+\xi)(1+\eta) \quad \text{(B.5)}$$

$$N_2 = \frac{1}{4}(1+\xi)(1-\eta) \quad \text{(B.4)} \qquad N_4 = \frac{1}{4}(1-\xi)(1+\eta) \quad \text{(B.6)}$$

These equations introduce ξ and η into the X-Z plane through isoparametric mapping. Thus the properties of isoparametric and inverse mapping are:

isoparametric mapping:

$$x = x(\xi,\eta)$$
$$z = z(\xi,\eta) \qquad \text{(B.7)}$$

inverse mapping:

$$\xi = \xi(x,z)$$
$$\eta = \eta(x,z) \qquad \text{(B.8)}$$

From Eqns. (B.7) and (B.8),

$$x \equiv x(\xi(x,z),\eta(x,z))$$
$$z \equiv z(\xi(x,z),\eta(x,z)) \qquad \text{(B.9)}$$

Differentiating these equations with respect to x and z leads to:

$$\begin{aligned} x,_x &= (x,_\xi)(\xi,_x) + (x,_\eta)(\eta,_x) = 1 \\ z,_z &= (z,_\xi)(\xi,_z) + (z,_\eta)(\eta,_z) = 1 \\ x,_z &= (x,_\xi)(\xi,_z) + (x,_\eta)(\eta,_z) = 0 \\ z,_x &= (z,_\xi)(\xi,_x) + (z,_\eta)(\eta,_x) = 0 \end{aligned} \qquad \text{(B.10)}$$

In matrix form, these equations are:

$$\begin{bmatrix} 1 & 0 \\ 0 & 1 \end{bmatrix} = \begin{bmatrix} x,_\xi & x,_\eta \\ z,_\xi & z,_\eta \end{bmatrix} \begin{bmatrix} \xi,_x & \xi,_z \\ \eta,_x & \eta,_z \end{bmatrix} \qquad \text{(B.11)}$$

Jacobian Inverse Jacobian

The derivatives in the Jacobian and its inverse are required to calculate the strains on an element. The Jacobian matrix can be calculated directly from Eqns. (B.1) and (B.2), while the derivatives in the inverse Jacobian are from ξ(x,z) and η(x,z), which are unknown functions. The system of equations above, when solved for the inverse Jacobian, provides the derivatives of ξ(x,z) and η(x,z) without knowing the functions explicitly. This property is a key reason why the isoparametric formulation is valuable in finite element analysis.

Normally the isoparametric formulation is used in finite element analysis to solve the potential energy equation for the displacements of a system caused by an applied load. In this situation, the displacements are known, so the traditional isoparametric formulation can be modified to provide the desired strain data.

B.2.2 Isoparametric Formulation For Strains

If *U* and *V* are displacements in the *X* and *Z* directions, respectively, the mapping equations for these displacements are similar to Eqns. (B.1) and (B.2):

$$U(\xi,\eta) = \sum_{I=1}^{4} U_I N_I(\xi,\eta) \qquad \text{(B.12)}$$

$$V(\xi,\eta) = \sum_{I=1}^{4} V_I N_I(\xi,\eta) \qquad \text{(B.13)}$$

Using inverse mapping, the displacements are:

$$U(x,z) = \sum_{I=1}^{4} U_I \hat{N}_I(x,z) \tag{B.14}$$

$$V(x,z) = \sum_{I=1}^{4} V_I \hat{N}_I(x,z) \tag{B.15}$$

where

$$\hat{N}_I(x,z) = N_I(\zeta(x,z),\eta(x,z)) \tag{B.16}$$

$\hat{N}_I$ contains the equations for $\xi(x,z)$ and $\eta(x,z)$, which, as mentioned previously, are unknown. However, only the derivatives of these two functions, which are known because of the Jacobian, are required to compute the strains.

The normal and shear strains are defined as:

$$\begin{bmatrix} \varepsilon_x \\ \varepsilon_z \\ \gamma_{xz} \end{bmatrix} = \begin{bmatrix} \dfrac{\partial U}{\partial x} \\ \dfrac{\partial V}{\partial z} \\ \dfrac{\partial U}{\partial z} + \dfrac{\partial V}{\partial x} \end{bmatrix} \tag{B.17}$$

Using Eqns. (B.14), (B.15) and (B.17), the strains for the element in Figure B.2 are:

$$\begin{bmatrix} \varepsilon_x \\ \varepsilon_z \\ \gamma_{xz} \end{bmatrix} = \begin{bmatrix} \hat{N}_{1,x} & 0 & \hat{N}_{2,x} & 0 & \hat{N}_{3,x} & 0 & \hat{N}_{4,x} & 0 \\ 0 & \hat{N}_{1,z} & 0 & \hat{N}_{2,z} & 0 & \hat{N}_{3,z} & 0 & \hat{N}_{4,z} \\ \hat{N}_{1,z} & \hat{N}_{1,x} & \hat{N}_{2,z} & \hat{N}_{2,x} & \hat{N}_{3,z} & \hat{N}_{3,x} & \hat{N}_{4,z} & \hat{N}_{4,x} \end{bmatrix} \underline{d} \tag{B.18}$$

Where

$$\underline{d}^T = \begin{bmatrix} U_1 & V_1 & U_2 & V_2 & U_3 & V_3 & U_4 & V_4 \end{bmatrix} \tag{B.19}$$

The nodal displacements in Eqn. (B.19) are defined as:

$$\begin{aligned} U_i &= x_{it} - x_{io} \\ V_i &= z_{it} - z_{io} \end{aligned} \tag{B.20}$$

The subscript "*o*" denotes the value of the *x* and *z* coordinates before load was applied to the specimen. Prior to the shear test, the Krypton system collected data with no load applied to establish the value of x_o and z_o at every LED. The subscript *t* denotes the value of the *x* and *z* coordinates through the shear test.

The derivatives $\hat{N}_{I,x}$ and $\hat{N}_{I,z}$ are evaluated in the following manner:

$$\widehat{N}_{I,x}\Big|_{\substack{x\\z}} = N_{I,\xi}\Big|_{\substack{\xi\\\eta}} \xi_{,x}\Big|_{\substack{x\\z}} + N_{I,\eta}\Big|_{\substack{\xi\\\eta}} \eta_{,x}\Big|_{\substack{x\\z}}$$
$$\widehat{N}_{I,z}\Big|_{\substack{x\\z}} = N_{I,\xi}\Big|_{\substack{\xi\\\eta}} \xi_{,z}\Big|_{\substack{x\\z}} + N_{I,\eta}\Big|_{\substack{\xi\\\eta}} \eta_{,z}\Big|_{\substack{x\\z}} \qquad \text{(B.21)}$$

If the derivatives of the unknown ξ and η functions are replaced with the Jacobian from Eqn. (B.11), the derivatives $\hat{N}_{I,x}$ and $\hat{N}_{I,z}$ become:

$$\widehat{N}_{I,x}\Big|_{\substack{x\\z}} = \frac{1}{J}\left((N_{I,\xi})(z_{,\eta}) - (N_{I,\eta})(z_{,\xi})\right)\Big|_{\substack{\xi\\\eta}}$$
$$\widehat{N}_{I,z}\Big|_{\substack{x\\z}} = \frac{1}{J}\left((-N_{I,\xi})(x_{,\eta}) + (N_{I,\eta})(x_{,\xi})\right)\Big|_{\substack{\xi\\\eta}} \qquad \text{(B.22)}$$

where J is the determinant of the Jacobian; N_I represents Eqns. (B.3-B.6); and the derivatives of the *x* and *z* functions are derivatives of Eqns. (B.1) and (B.2). The values of ξ and η input into Eqn. (B.22) determine the location in the element where strains are computed.

The displacement vector and derivatives on the right hand side of Eqn. (B.18) were dependent upon data collected by the Krypton. To compute the strains at nodes 1-4 in Figure B.2, the initial and displaced Cartesian coordinates of the four nodes were used to determine U_i and V_i, which were input into Eqn. (B.18) through the term $\underline{d}$. The derivatives in Eqn. (B.22) (i.e., $\widehat{N}_{1,x}, \widehat{N}_{1,z}$...) were evaluated at the respective natural coordinates of each node, and input into Eqn. (B.18). This analysis produced the normal and shear strains in the Cartesian coordinate system at each node. When the elements in Figure B.1 shared nodes with adjacent elements, the Krypton strain reported in Chapter 6 was taken as the average from all the elements sharing the node.

It is important to note that this isoparametric formulation did not include the out of plane displacement in the Y-direction. The displacement in this direction was small, and any resulting strains were assumed to be negligible.

B.2.3 Comparison to Elastic Predictions

To evaluate the accuracy of the isoparametric formulation presented in this appendix, the measured strains were compared to predicted strains from elastic analysis. The predicted elastic strains, valid until the specimen cracked, were the result of the prestressing force, dead load moment, and applied moment. The calculated strain from the prestressing force and dead load were superimposed with the measured strain. Only the results from Specimen II are presented in this section, because the Krypton data from Specimen I had large levels of noise and were unusable.

The predicted and measured longitudinal strains from the middle row of LEDs pictured in Figure B.3 are plotted in Figure B.4 through Figure B.11 from zero applied load to initial web shear cracking at 243 kips of applied shear, neglecting dead load. The measured strains were calculated from the Krypton data using the isoparametric formulation presented in this appendix. To reduce noise, the data used to create these plots were processed using a moving average over

every eight data points. These figures show that the predicted and measured longitudinal strains were in good agreement at most of the LEDs until the specimen cracked.

The majority of the measured strains had approximately the same slope and magnitude as the predicted, with a scatter about the mean of roughly ± 15 με. The measured strains from LED 11 had the greatest amount of scatter, approximately ± 40 με, but on average the measured values from this LED were close to the predicted. The magnitude of the measured strains from LED 26 deviated from the prediction by the greatest amount, approximately 70 με at an applied shear of 180 kips, however, the scatter from this LED was minimal. It was difficult to determine exactly why the measured strains from these two LEDs behaved as they did. The LEDs were applied to the specimen in the same manner, and all were exposed to the same conditions during testing. Furthermore, none of the LEDs adjacent to either LED 11 or 26 had measured strains with large scatter or deviation from the predicted strain.

Figure B.12 shows that after cracking the longitudinal strains from the LEDs were nonlinear, and the distribution along the length was non-uniform. The dashed line in the figure denotes the web shear cracking load of 243 kips. Up to this applied shear, the longitudinal strains increased linearly as predicted. The test was conducted in displacement control, so after the web cracked, the applied shear initially dropped before increasing again, as noted in Figure B.12. Beyond initial cracking, the longitudinal strains were highly dependent on the location of the cracks in relation to the Krypton LEDs.

The measured and predicted shear strains from the middle row of LEDs are shown in Figure B.13 through Figure B.20, which serve as further evidence that the measured strains were reasonably similar to the predicted strains in the elastic region of response. The observations regarding scatter about the mean, deviation from the predicted shear strain in the elastic region, and behavior beyond cracking (shown in Figure B.21) were similar to those discussed previously in the analysis of the measured longitudinal strains.

The measured longitudinal and shear strains presented in this section were in reasonable agreement with elastic predictions prior to cracking. This suggests that the isoparametric formulation presented in this appendix, and used to calculate measured strains from the Krypton data, was reasonable.

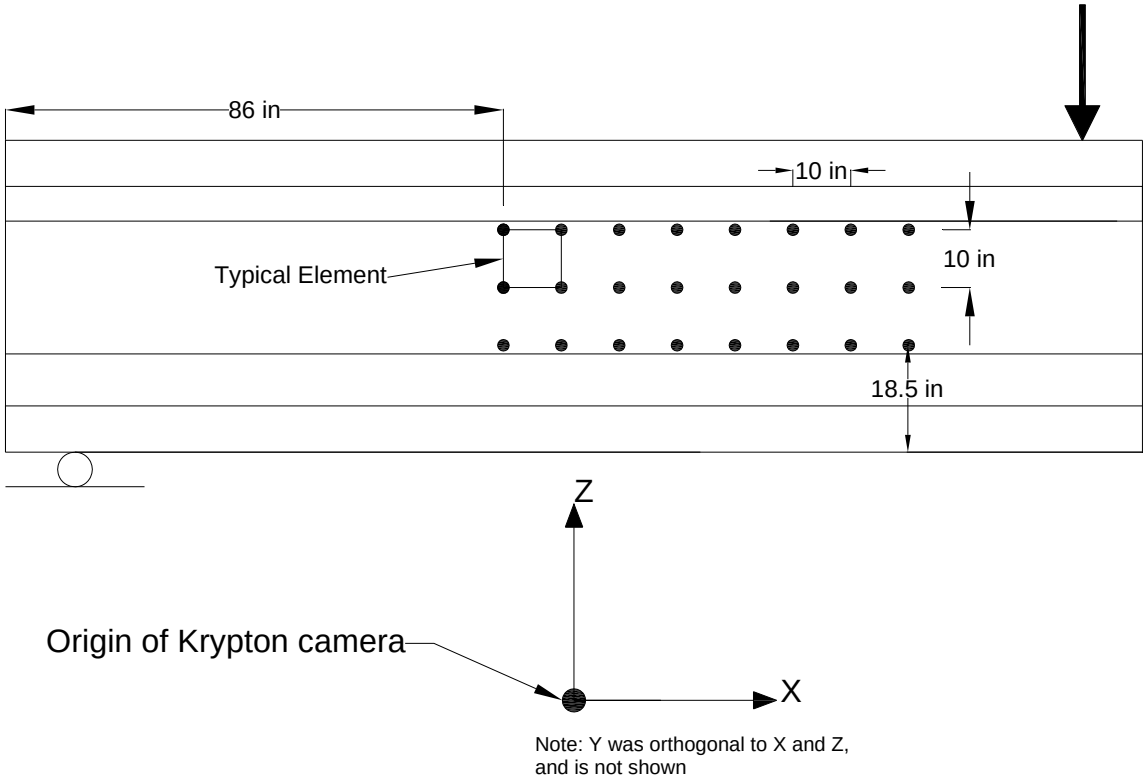

Figure B.1 Krypton Coordinate System

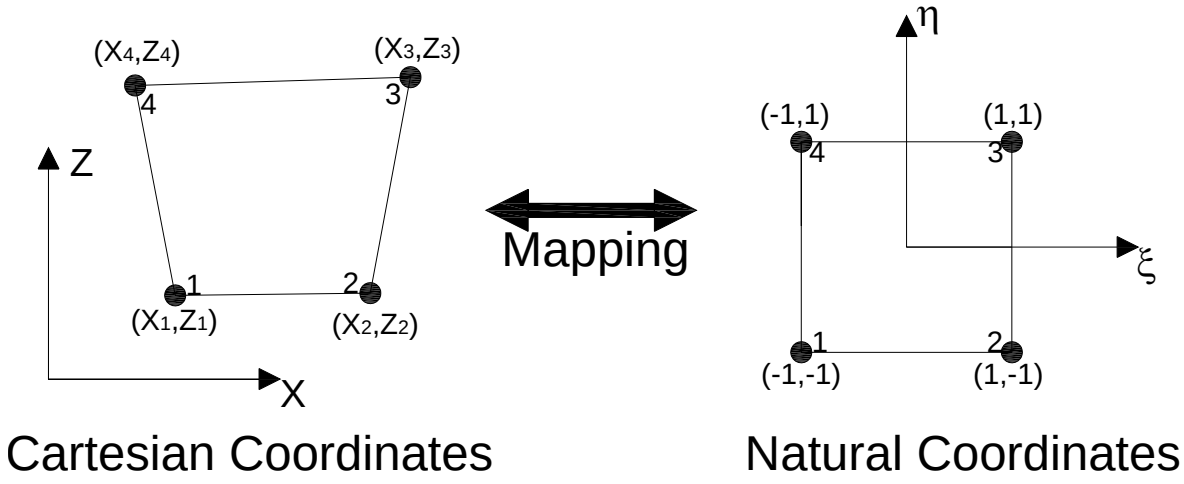

Figure B.2 Coordinate Mapping

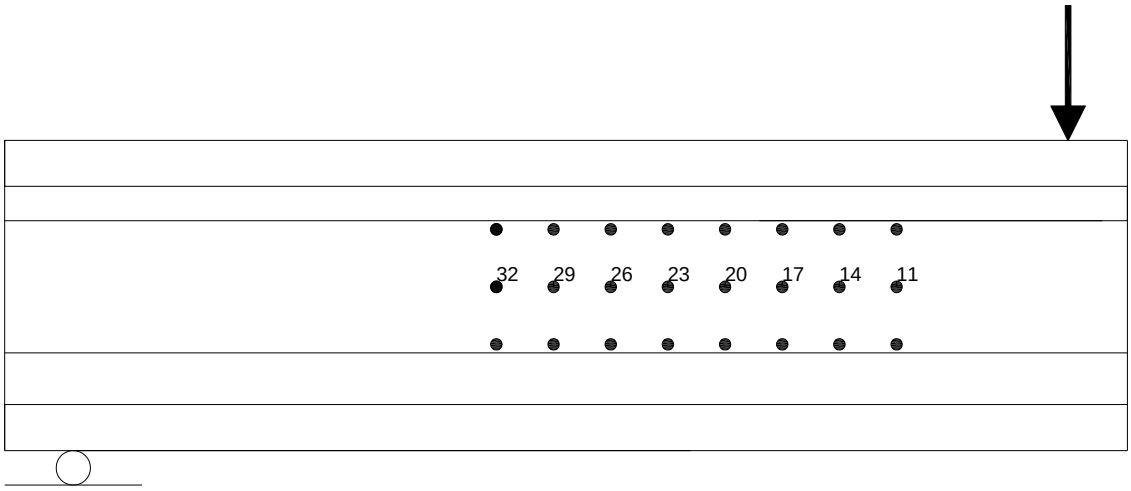

Figure B.3 LED Labels, Specimen II

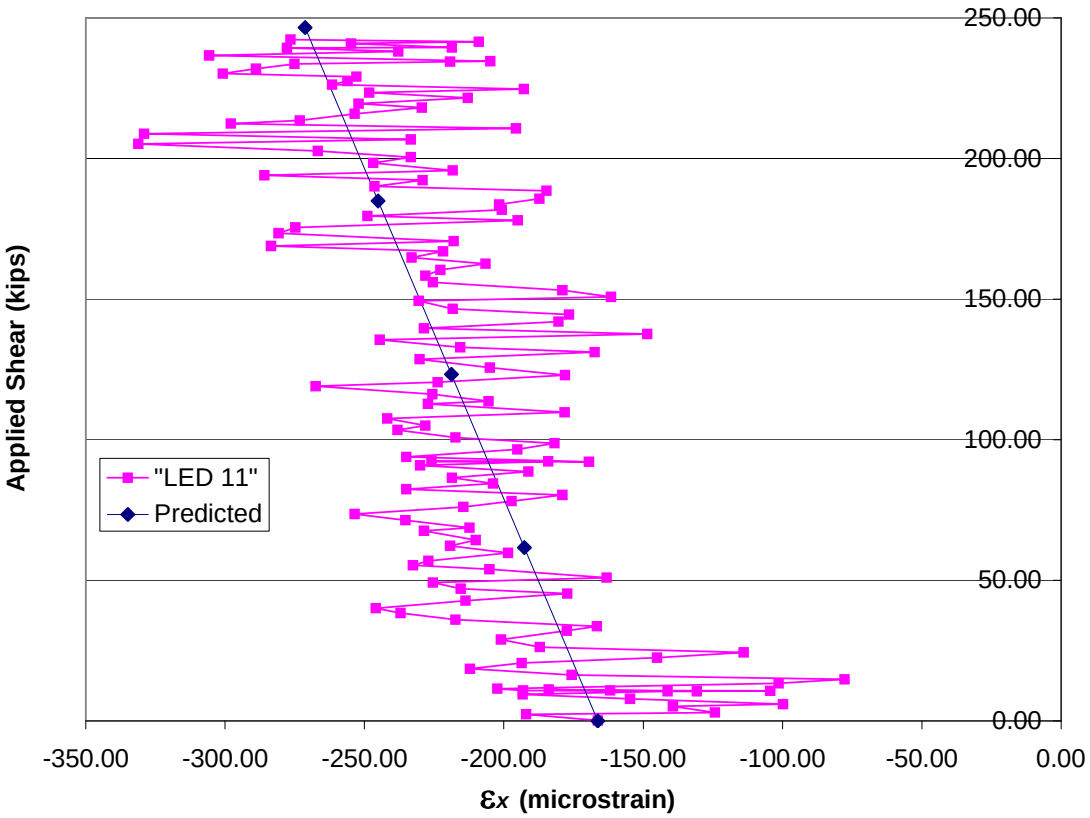

Figure B.4 Longitudinal Strain; LED 11, Specimen II

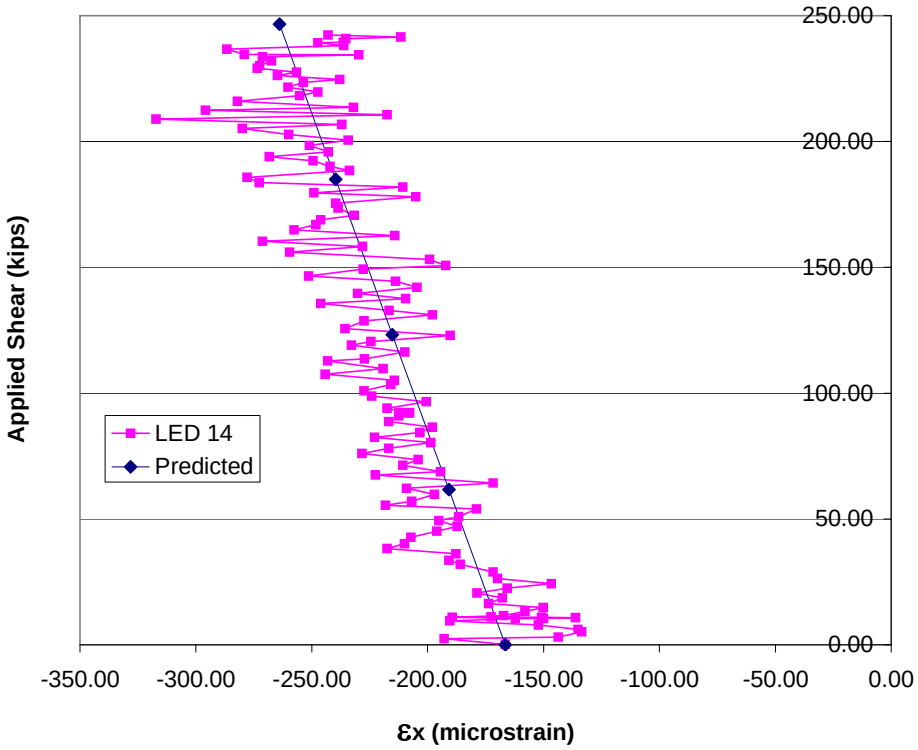

Figure B.5 Longitudinal Strain; LED 14, Specimen II

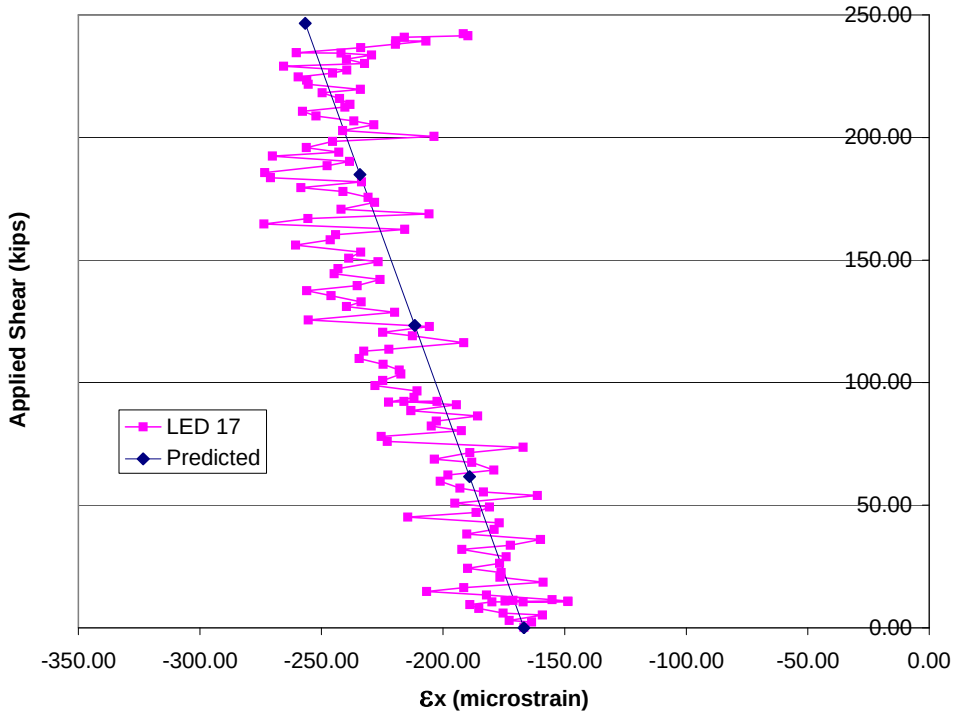

Figure B.6 Longitudinal Strain; LED 17, Specimen II

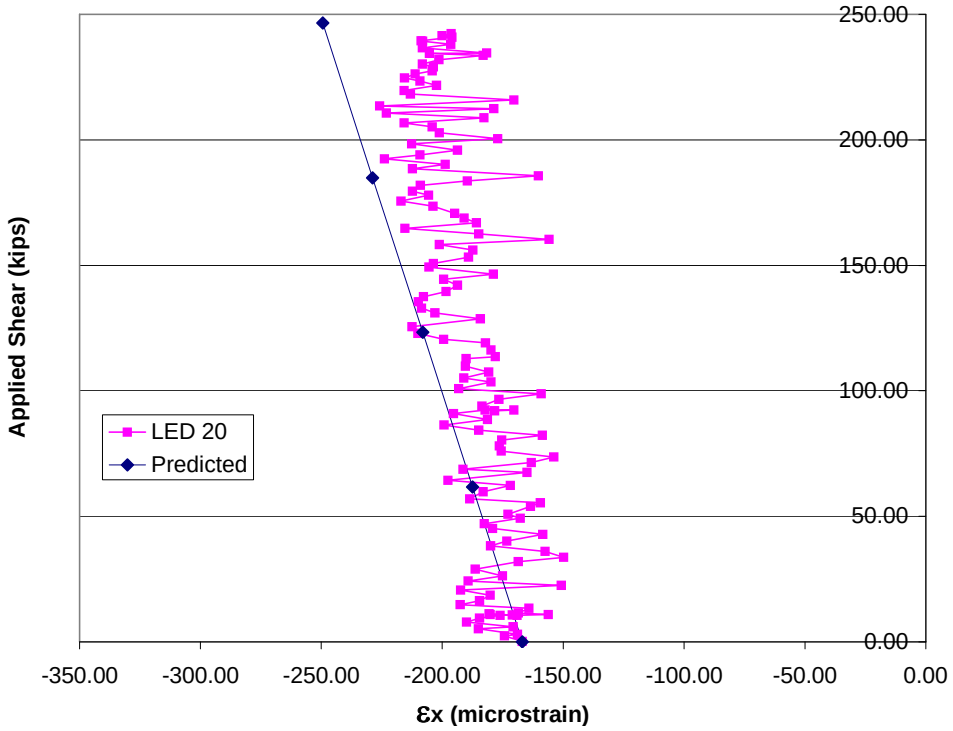

Figure B.7 Longitudinal Strain; LED 20, Specimen II

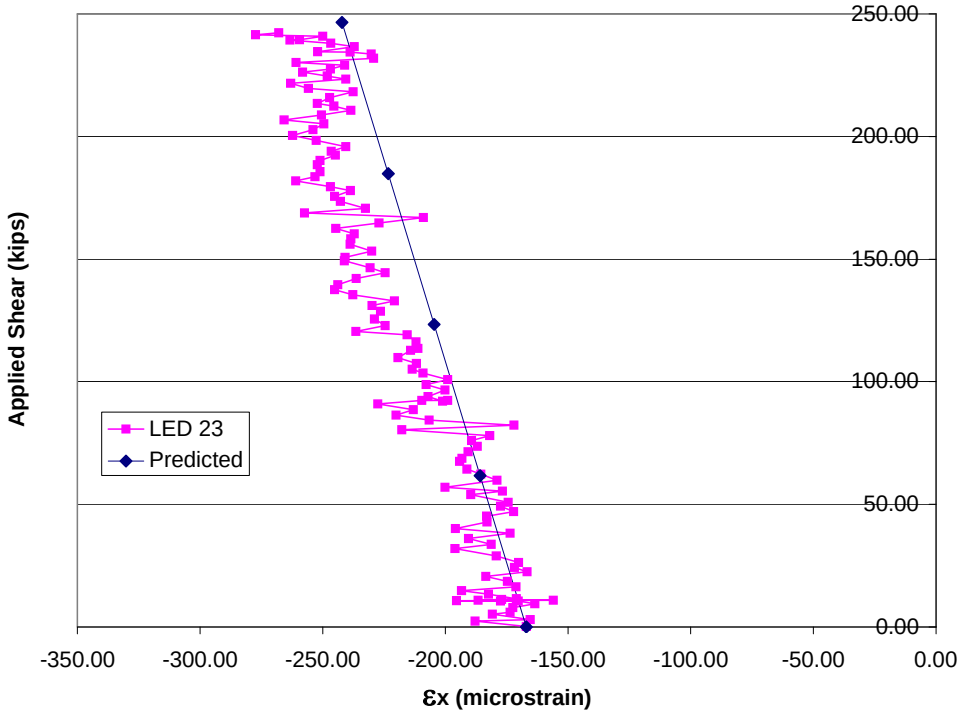

Figure B.8 Longitudinal Strain; LED 23, Specimen II

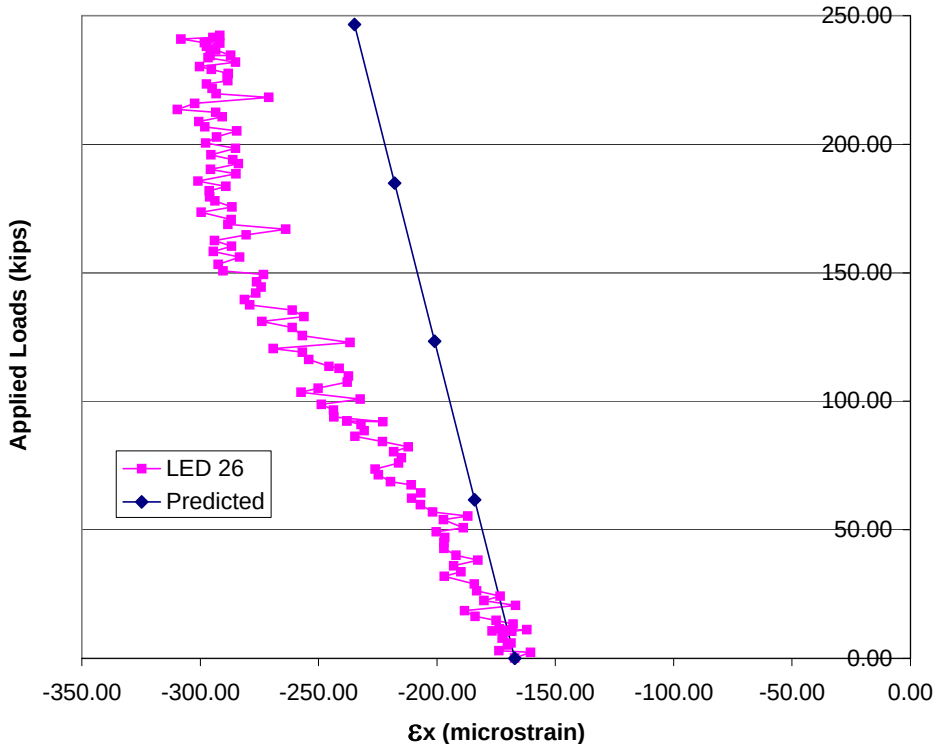

Figure B.9 Longitudinal Strain; LED 26, Specimen II

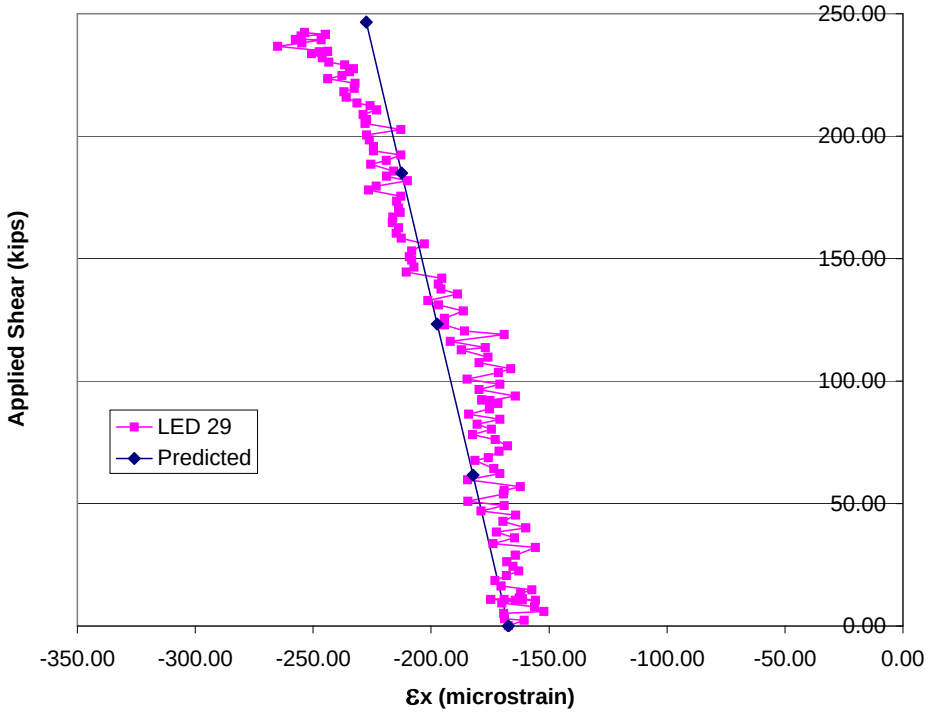

Figure B.10 Longitudinal Strain; LED 29, Specimen II

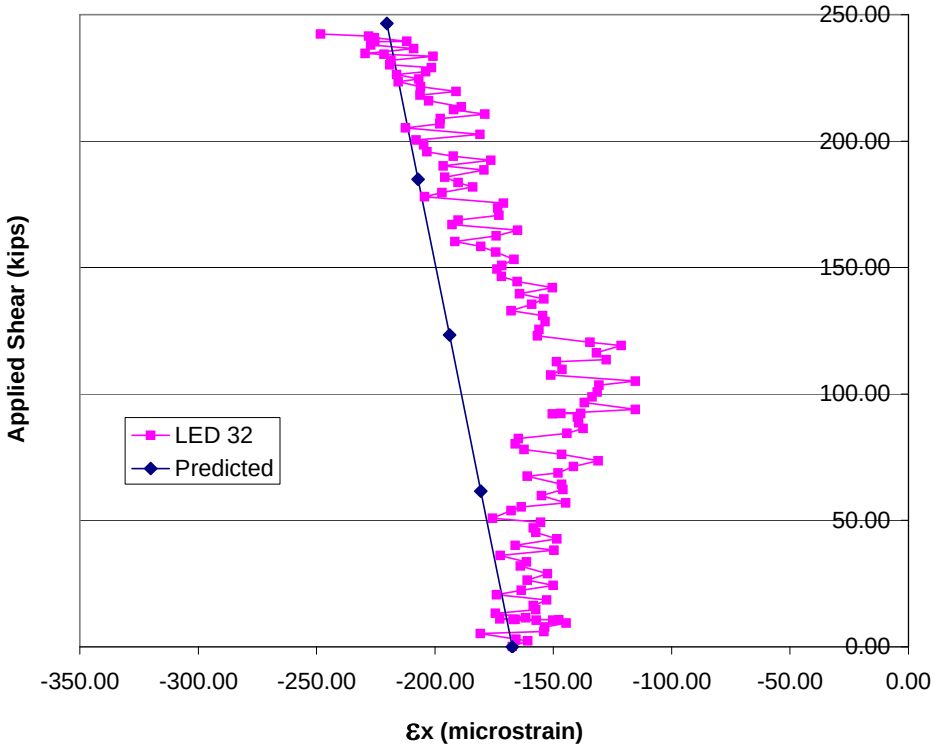

Figure B.11 Longitudinal Strain; LED 32, Specimen II

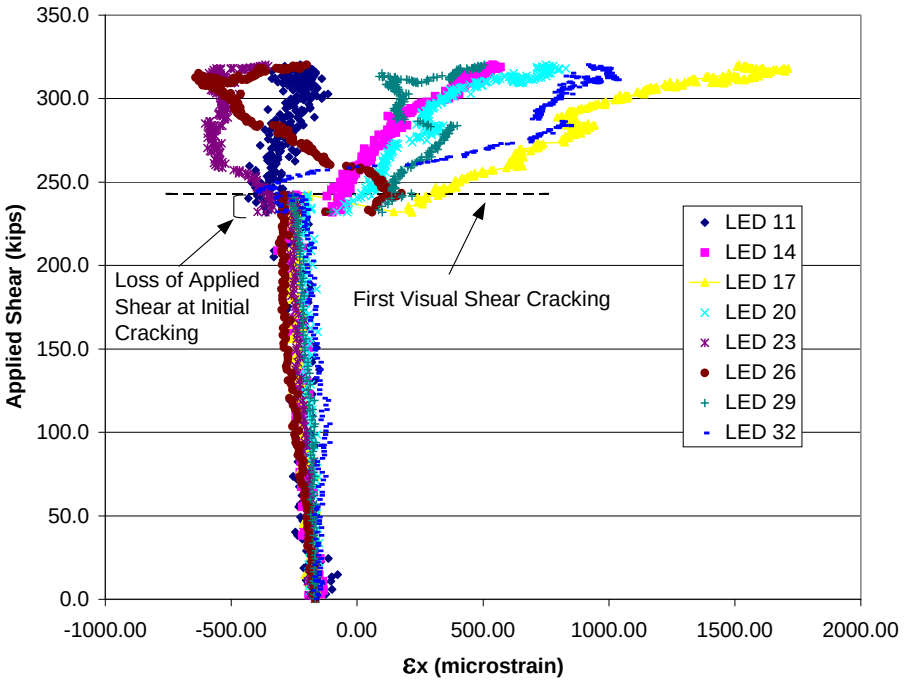

Figure B.12 Longitudinal Strain; All middle LEDs, Specimen II

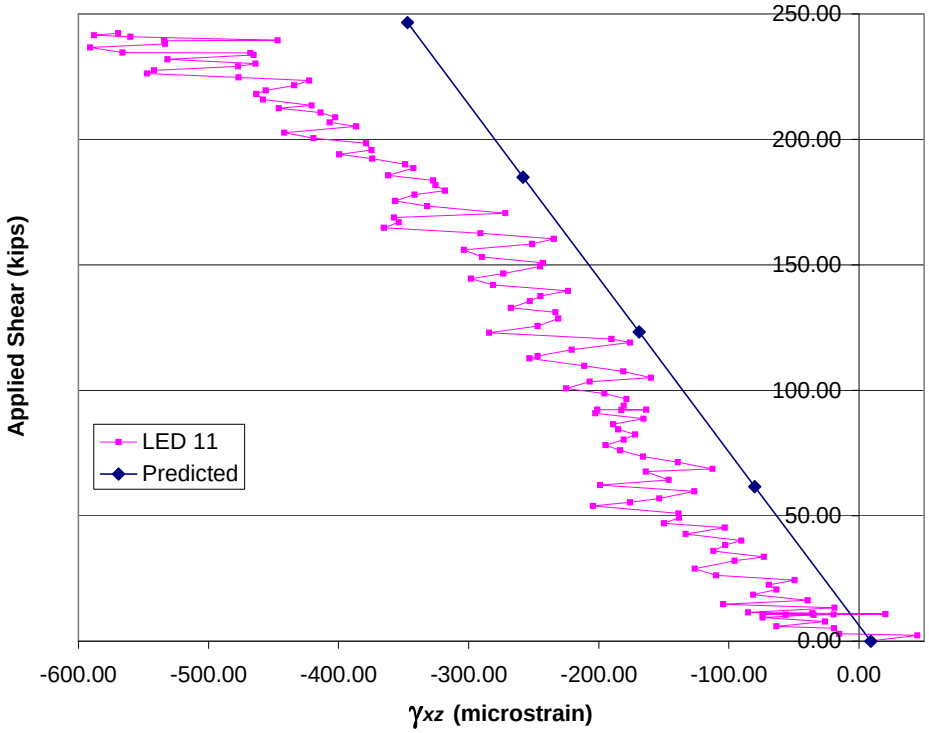

Figure B.13 Shear Strain; LED 11, Specimen II

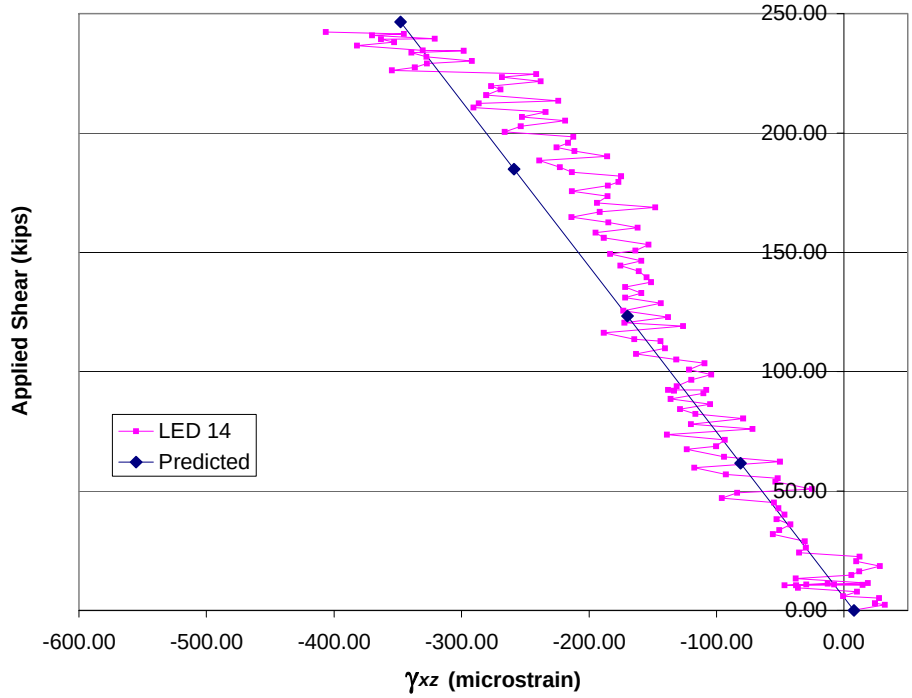

Figure B.14 Shear Strain; LED 14, Specimen II

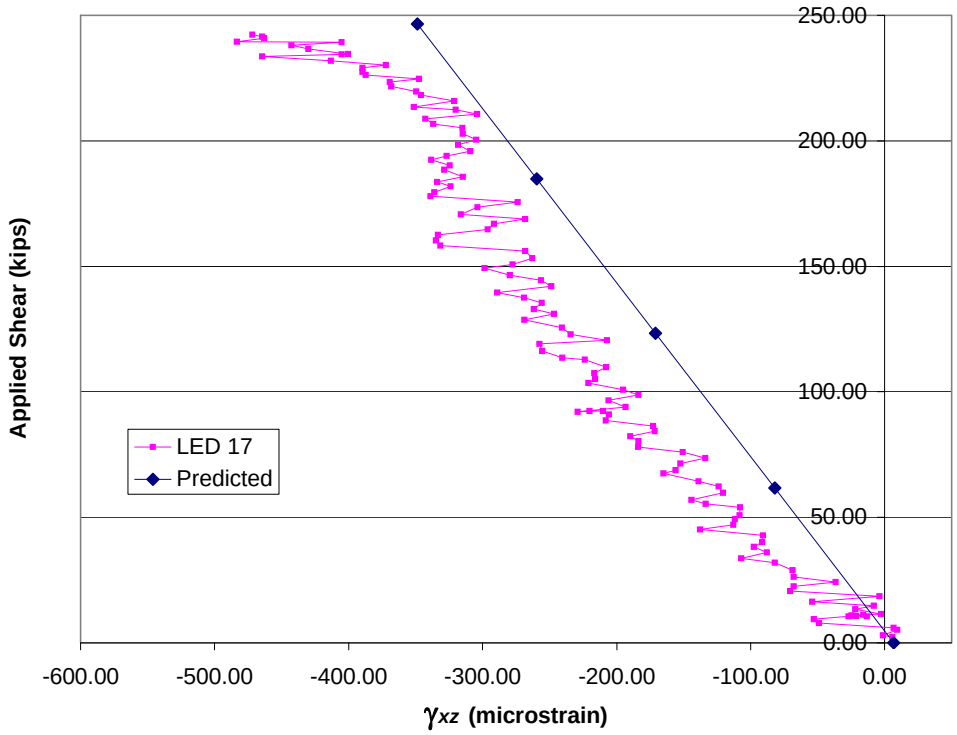

Figure B.15 Shear Strain; LED 17, Specimen II

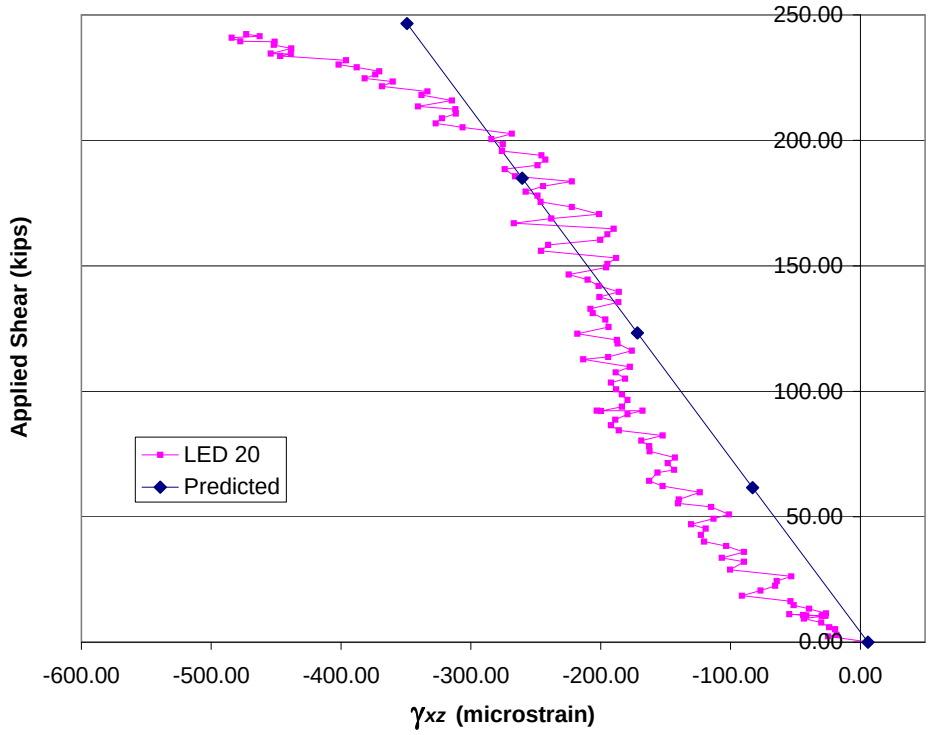

Figure B.16 Shear Strain; LED 20, Specimen II

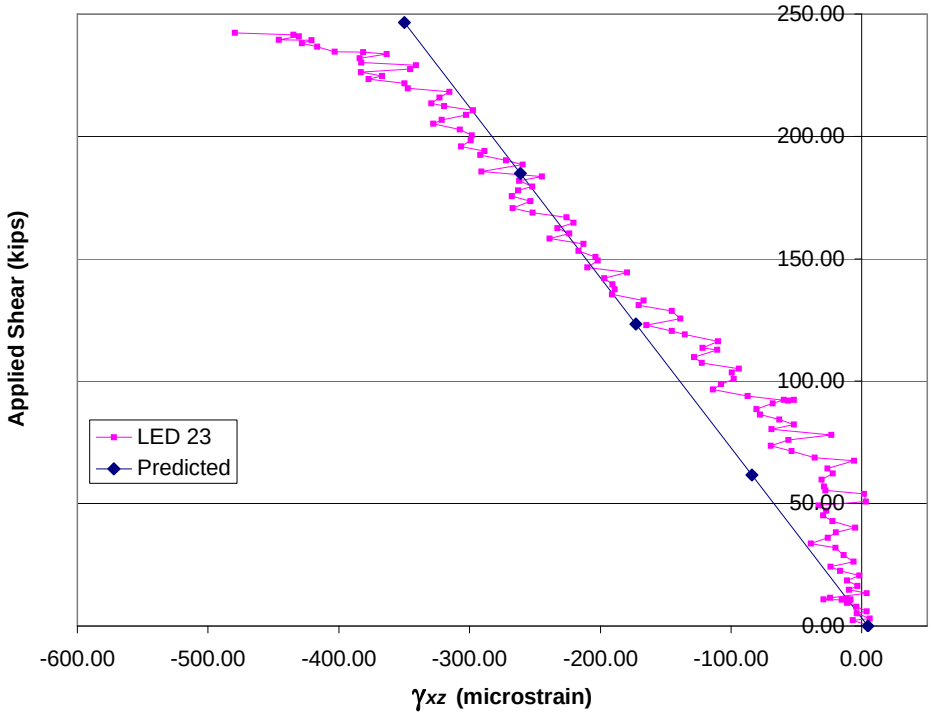

Figure B.17 Shear Strain; LED 23, Specimen II

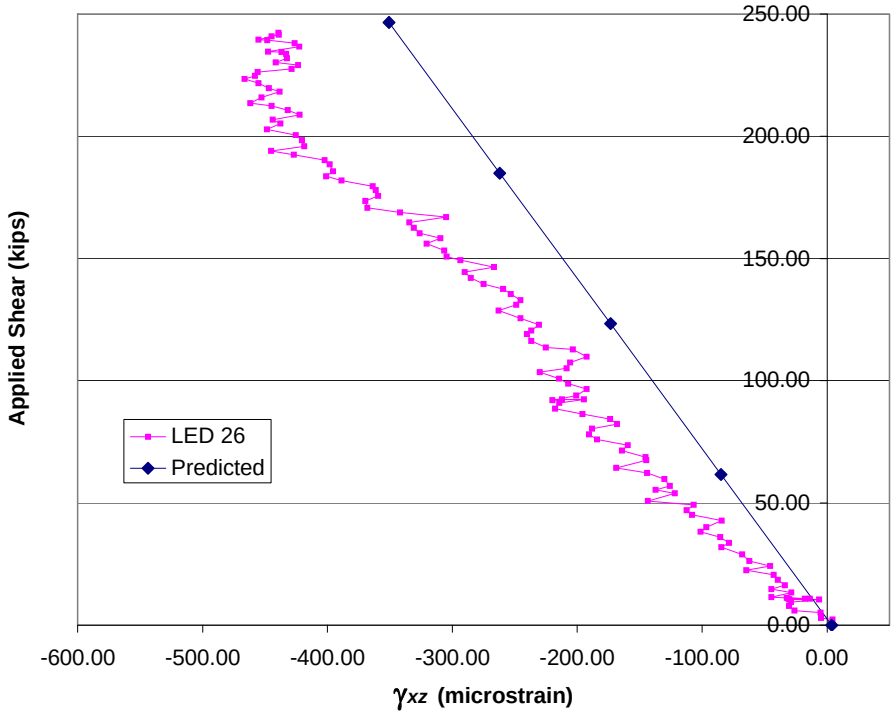

Figure B.18 Shear Strain; LED 26, Specimen II

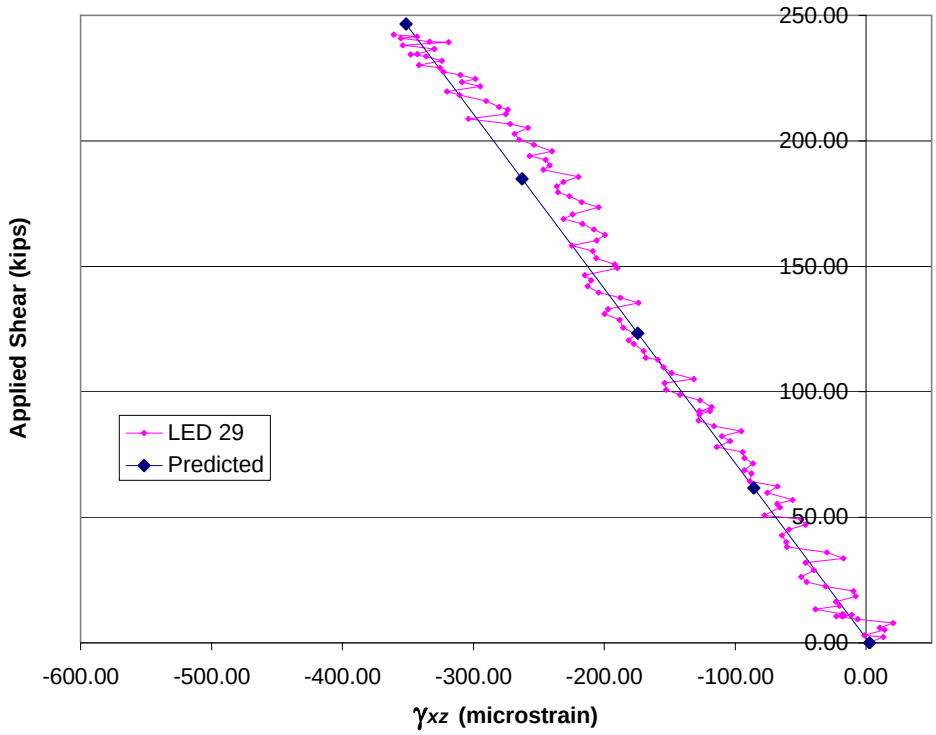

Figure B.19 Shear Strain; LED 29, Specimen II

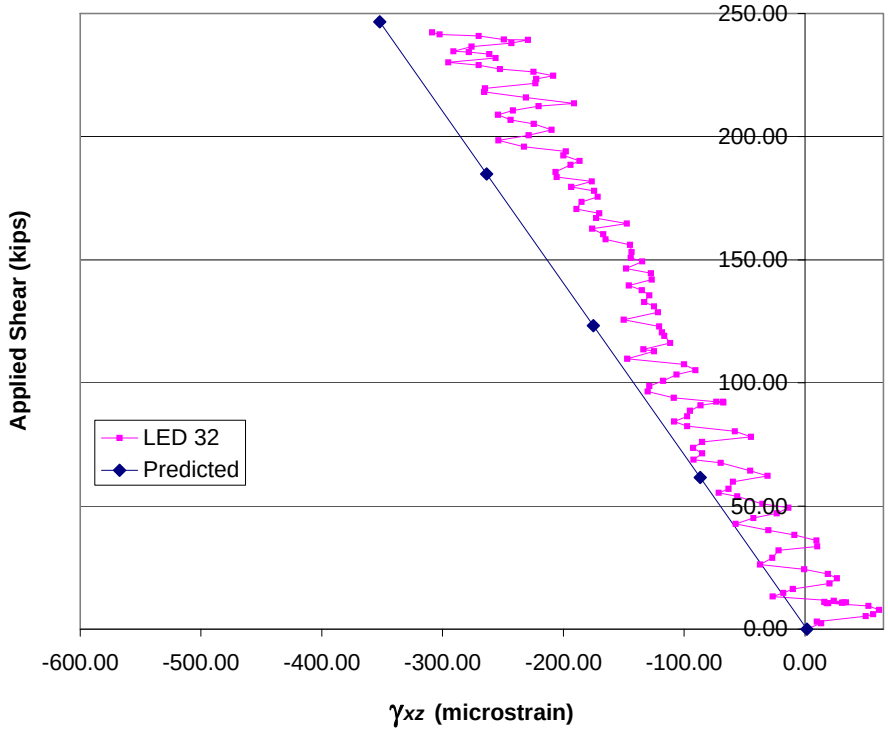

Figure B.20 Shear Strain; LED 32, Specimen II

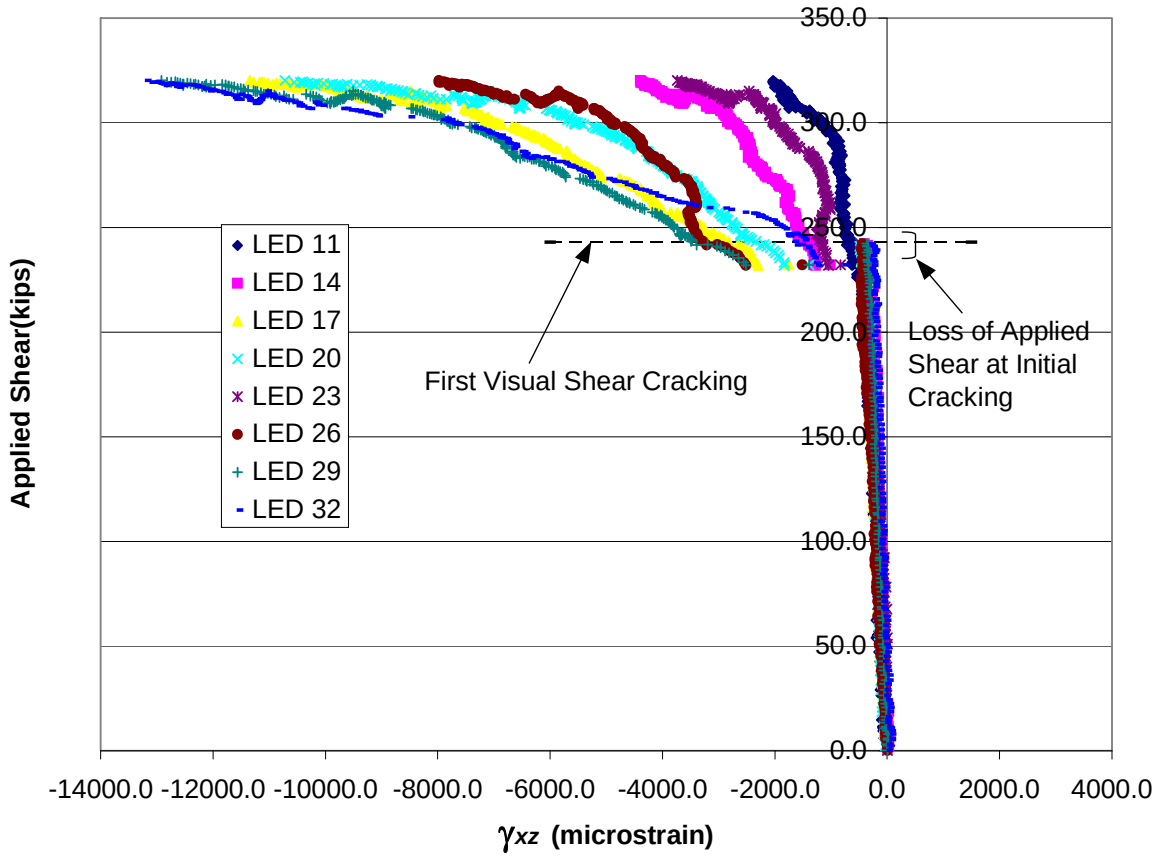

Figure B.21 Shear Strain; All Middle LEDs; Specimen II

Appendix C
Material Testing

C.1 Introduction

This appendix describes the procedures used to measure the material properties discussed in Chapter 5. The material properties measured in the laboratory were concrete compressive strength, concrete modulus of elasticity, stirrup yield strength, and effective prestress.

C.2 Concrete Compressive Strength (f_c')

The concrete cores taken for the compressive strength tests were obtained according to ASTM C42 (ASTM, 99). Upon completion of the capacity tests, a total of eight cores were taken from the non-test end of one of the specimens. Because both specimens were from same 88 ft. bridge girder, the results of the compression tests from these cores apply to both specimens. The cores were approximately 4 in. by 8 in., and were removed from uncracked regions of the web that contained no stirrups. As shown in Figure C.1, a concrete core drill was anchored to the web and leveled so that the cores were obtained with ends perpendicular to the longitudinal axis of the core. The specimen had what appeared to be a protective coating on one side of the beam, which had to be removed from each of the cores. The protective coating is shown in Figure C.2 and was removed by cutting off the end of each cylinder.

The compression tests were conducted according to ASTM C39, using a Forney testing machine (ASTM, 01). The concrete cores were capped with sulfur capping compound, and loaded at a rate of 450 lbs/s until they failed. The results of the tests are shown in Table C.1. This table shows that all of the cores had a length to diameter ratio greater than 2, therefore, none of the test results required the correction factors that apply when the ratio is below 1.75. The average concrete compressive strength of the eight cylinders was 10,130 psi, which was significantly greater than the design value of 6,000 psi.

In addition, two 4 in. by 8 in. cylinders cast from the bridge deck concrete were tested at 28 days, which resulted in compressive strengths of 5,500 psi and 5,860 psi. The average measured $f_{c'd}$ for the bridge deck was 5,680 psi.

C.3 Concrete Modulus of Elasticity (E_c)

Two concrete cores were obtained from the non-test end of one of the specimens using the same method described in Section C.2. The test to determine the concrete modulus of elasticity was conducted in a Forney testing machine according to ASTM C469 (ASTM, 94). The test was repeated four times for each cylinder to ensure accuracy. The concrete modulus of elasticity of the bridge deck was not measured. The average measured modulus of elasticity for the girders, reported in Table C.2, was 5,050 ksi. The concrete modulus used in the capacity calculations with nominal properties was 4,415 ksi. This value was calculated from the equation for modulus of elasticity given in the 2002 Standard code as $57{,}000\sqrt{f_c'}$. The modulus of elasticity based on the measured f_c' was 5,740 ksi.

C.4 Stirrup Yield Strength (f_{sy})

Four stirrup samples were removed from the non-test end of one of the specimens after it was tested to ultimate. The stirrups were removed from the web with a concrete saw by making a cut at the top and bottom of the web and on each side of the stirrup as shown in Figure C.3. Once cut from the specimen, the concrete still bonded to the sample was carefully chipped away to avoid damaging the stirrup sample. The stirrups in the beam were double legged, so the four samples were removed from two locations. The stirrup samples were each approximately 20 inches long, and had #4 bar markings.

The stirrups were tested to failure in a MTS 200 kip Universal Testing Machine, using the following procedure: The sample was loaded into the wedge grips of the testing machine, and an extensometer was attached at approximately mid-height of the specimen to obtain strain data through the test. The sample was then loaded by displacement of the grips at a rate of 0.001 in/s until the specimen had clearly begun to strain harden, which was beyond 10,000 με. The loading was paused after strain hardening had begun so the extensometer could be removed to prevent it from getting damaged when the stirrup reached ultimate. Displacement of the grips was then resumed at a rate of 0.01 in/s until the stirrup sample fractured.

The results of the stirrup sample tests are shown in Table C.3. The extensometer data are plotted in Figure C.4, and show that all of the stirrups samples behaved identically with a well-defined yield plateau at approximately 2,500με. The average yield strength was 67.3 ksi, which was 12.2% larger than the nominal f_{sy} of 60 ksi.

C.5 Effective Prestressing (f_{pe})

The plans for Mn/DOT Bridge No. 73023 indicated that during fabrication the prestressing strands were initially stressed to 189 ksi, which was 70% of their 270 ksi ultimate strength. At release, the immediate source of loss in the prestressing strands was due to elastic shortening of the concrete beam. The other sources of loss were long term and occurred over the life of the beams. These losses included creep and shrinkage of the concrete, and relaxation of the prestressing strand. To experimentally verify f_{pe}, two strands from each of the test specimens were exposed, instrumented with strain gages, and cut. The recorded change in strain was used to find the measured f_{pe} and verify the code predicted losses.

Prestressing strands on the non-test end, for shear, were cut prior to the ultimate shear test to ensure f_{pe} was measured from undamaged strands. The test location was approximately 50 in. from the end, which was well outside the 30 in. transfer region. A jackhammer was used to expose a 15 in. section of the bottom, outer strand on each side of the beam as shown in Figure C.5. The concrete was carefully removed to avoid damaging the strand with the jackhammer. At least three FLK-1-11-5LT strain gages were attached to the strand and oriented along the axis of the wire as shown in Figure C.6. A wet paper towel along with several rebar ties were then attached to the strand a short distance away from the strain gages, see Figure C.7, to protect them from heat during cutting and to prevent the strand from unwinding. The prestressing strand was then flame-cut with an oxy-acetylene torch while strain data were recorded.

Figure C.8 and Figure C.9 show the change in strain recorded during strand cutting for Specimens I and II, respectively. The strains were measured before the bridge deck was added to Specimen I. The values of the change in strain recorded by each gage are given in Table C.4.

The drop in strain during the test was due to relief of the tension in the strands after they were cut. Strain gage "North 2" from the specimen without the bridge deck is not reported in Table C.4 or Figure C.9 because it did not properly adhere to the strand and fell off during the test.

The average change in strain values from all of the gages was 3,964 με, neglecting the extreme high and low values. Because the change in strain was measured using strain gages oriented along the axis of the wires, it was necessary to measure the apparent modulus of elasticity of the strand along this axis so the change in strain could be converted to an effective prestressing.

To measure the apparent modulus of elasticity, several samples of prestressing strand were removed from the specimens after the ultimate shear tests. These samples were fitted with strain gages oriented along the axis of the strand and tested to ultimate. The apparent modulus of elasticity of the prestressing strand was 31,600 ksi, which was obtained from the stress vs. strain curves of the prestressing strands, shown in Figure C.10. These values are higher than the actual strand modulus of elasticity due to the gage orientation.

Using the average change in strain of 3,964 με and the apparent modulus of elasticity of 31,600 ksi that corresponded with the gage orientation, the effective prestressing for the two test beams was 125.3 ksi. The effective prestressing subtracted from the initial prestressing of 189 ksi gave losses of 63.7 ksi. The losses predicted using the 2004 LRFD and 2002 Standard codes were 51.5 ksi and 49.9 ksi respectively, putting the measured losses approximately 30% above the predictions for both codes. See Sections A.1.1 and A.1.2 for sample loss calculations.

Table C.1 Concrete Compressive Strength (f_c') Test Results

Cylinder Number	Diameter (in)	Length (in)	L/D	Failure load (lbs)	f_c' (psi)
1	3.85	8.12	2.11	121,450	10,430
2	3.85	8.09	2.1	123,230	10,590
3	3.85	8.15	2.12	117,360	10,080
4	3.85	8.22	2.14	124,020	10,650
5	3.85	8.13	2.11	115,060	9,880
6	3.85	8.13	2.11	104,750	9,000
7	3.85	8.05	2.09	135,350	11,630
8	3.85	8.27	2.15	102,230	8,780
				AVERAGE	10,130
				STD DEV	924

Table C.2 Concrete Modulus of Elasticity (E_c) Test Results

Cylinder Number	Diameter (in)	Length (in)	Modulus of Elasticity* (ksi)
1	3.85	8.45	5,000
2	3.85	8.33	5,100
		AVERAGE	5,050

*Average of the four tests on each cylinder

Table C.3 Stirrup Yield Strength (f_{sy}) Test Results

Stirrup number	Yield Strength (ksi)	Ultimate Strength (ksi)
1	67.0	106.8
2	67.0	106.6
3	67.6	106.8
4	67.6	107.1
AVERAGE	67.3	106.8

Table C.4 Effective Prestressing (f_{pe}) Test Results

Specimen I (with bridge deck)**			Specimen II (no bridge deck)	
Strain Gage	Final Strain (με)		Strain Gage	Final Strain (με)
South 1	-3410		South 1	-4136
South 2	-3869		South 2	-4055
South 3	-3855		South 3	-4120
South 4*	-3256		North 1	-3796
North 1	-4199		North 3	-3986
North 2*	-4347			
North 3	-4118			
North 4	-4055			
Average from all gages:		-3964 με		

* The high and low strain measurements were considered outliers and were not used to calculate the average value.

** Strands were cut prior to adding the bridge deck

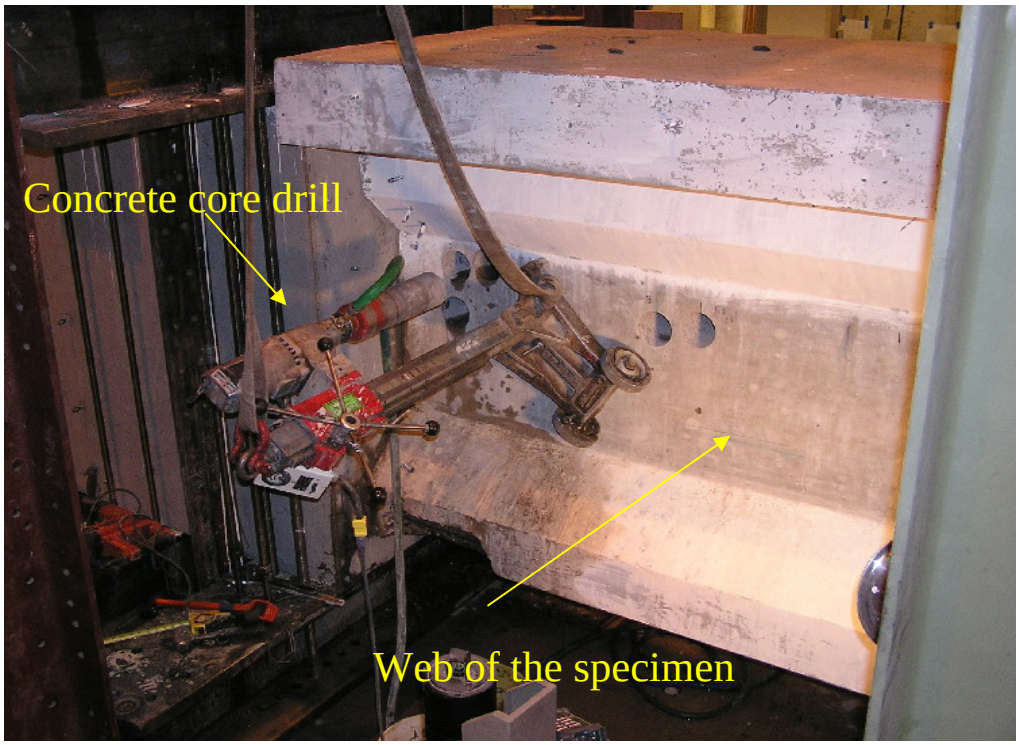

Figure C.1 Concrete Core Setup

Figure C.2 Protective Coating on Cores

Figure C.3 Stirrup Removal

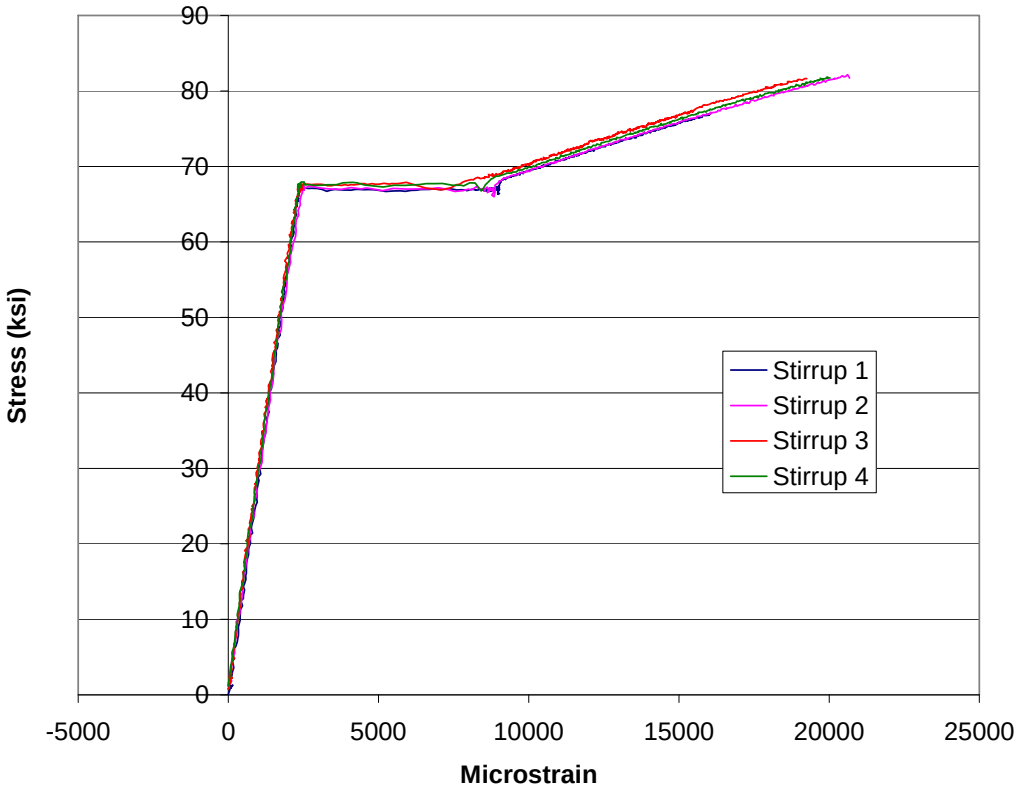

Figure C.4 Stirrup Stress vs. Strain

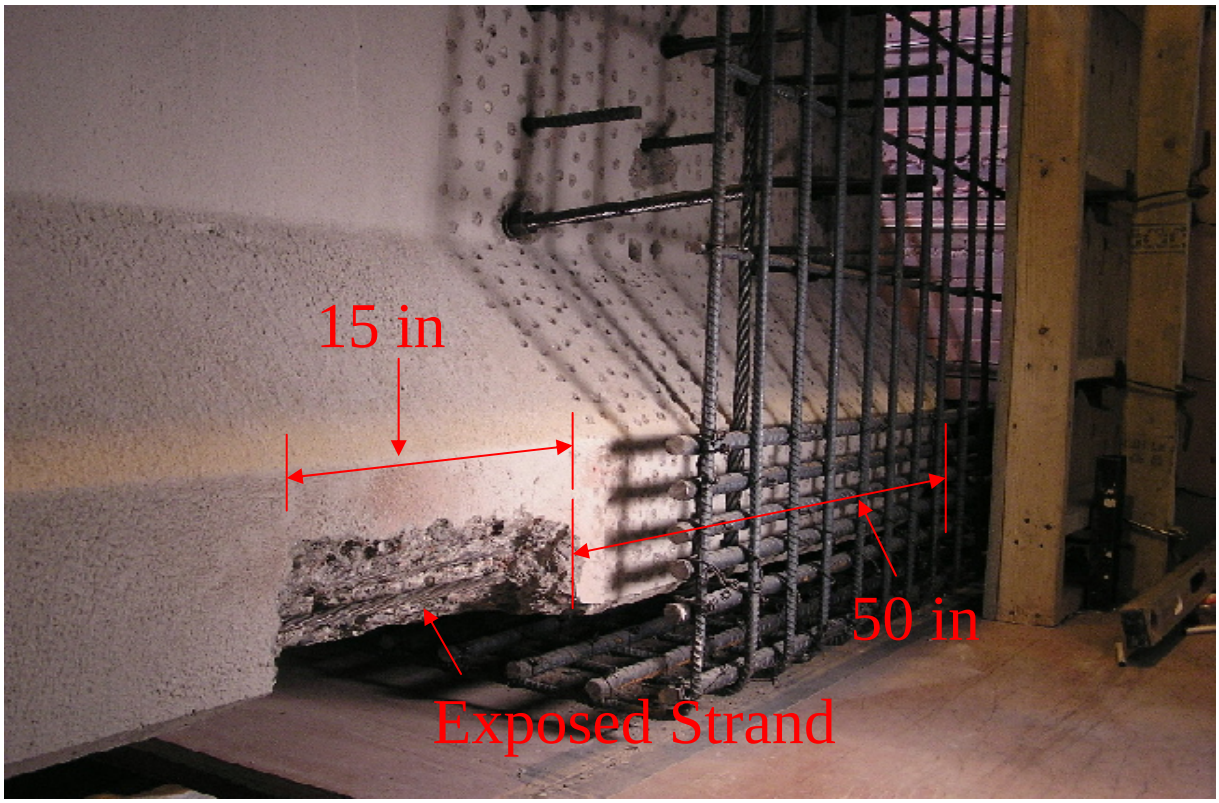

Figure C.5 Prestressing Strand Test Location

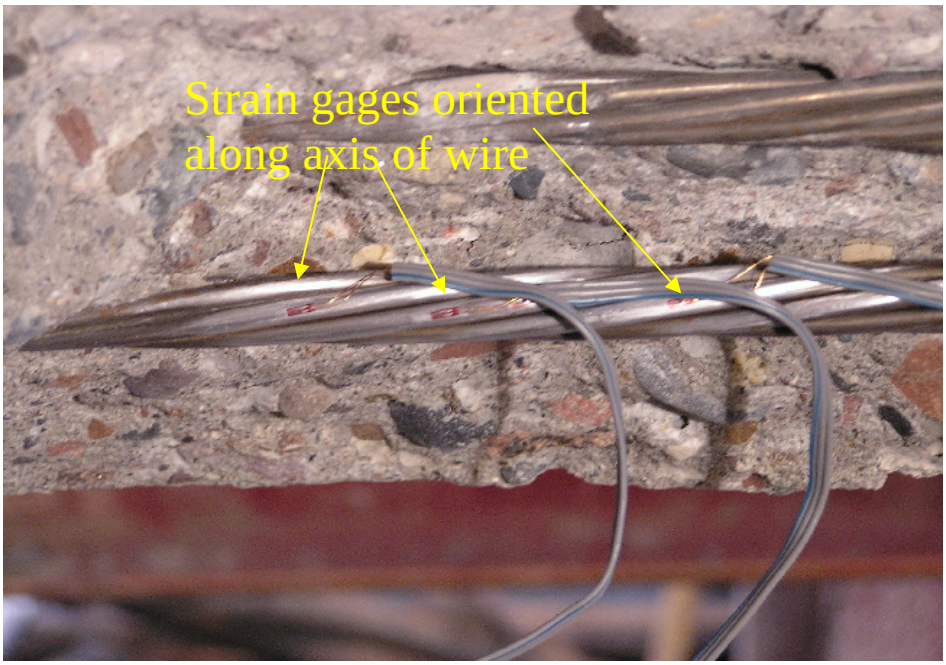

Figure C.6 Strain Gages on Prestressing Strand

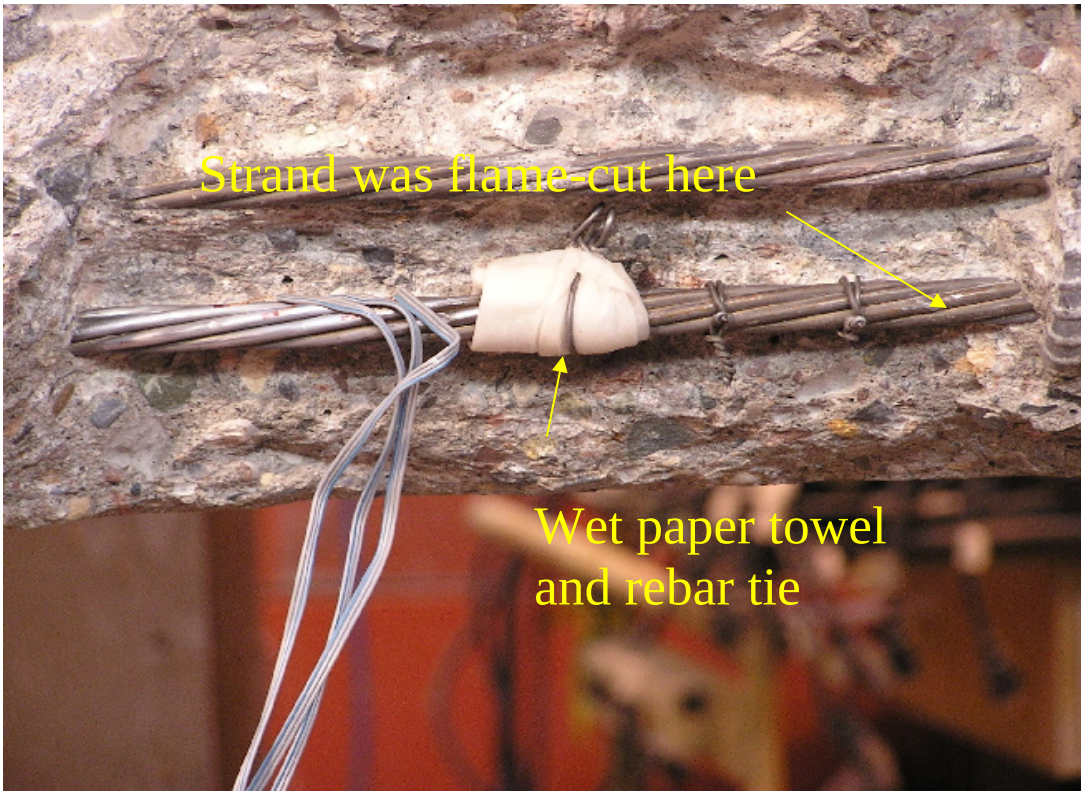

Figure C.7 Final Prestressing Strand Test Setup

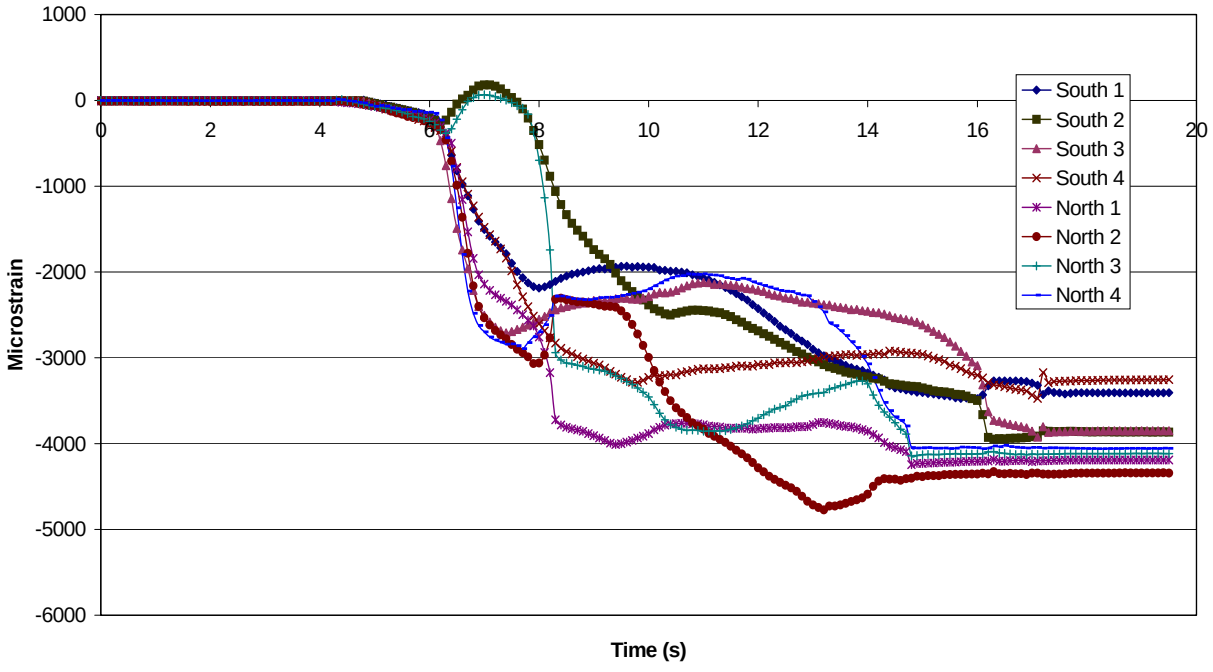

Figure C.8 Change in Strain from Strand Cutting (Specimen I prior to adding the bridge deck)

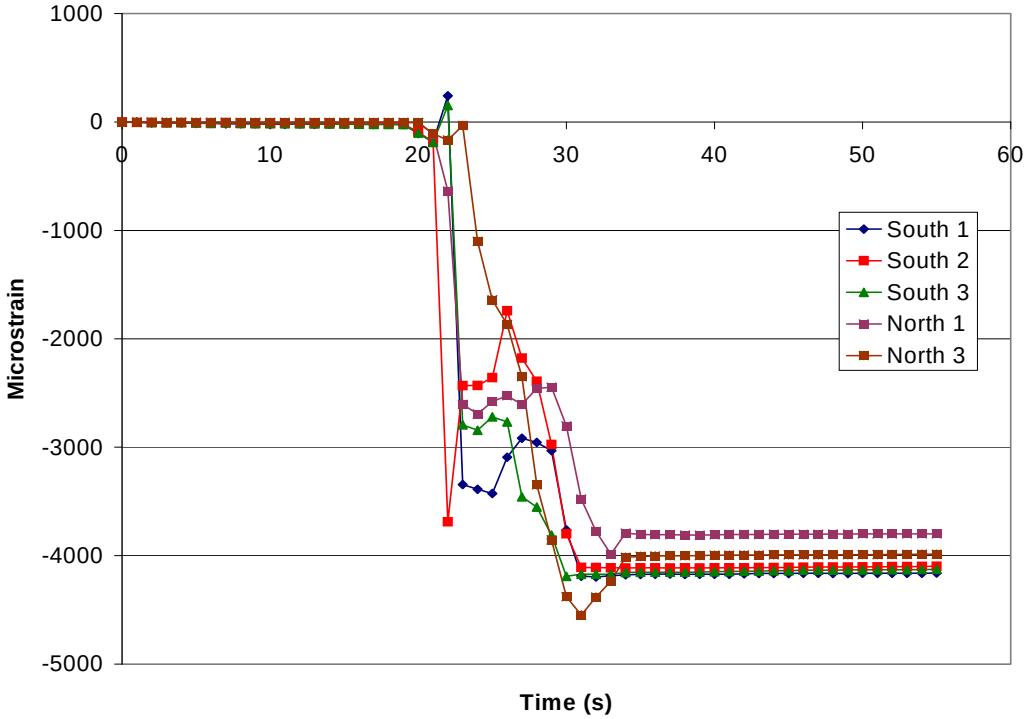

Figure C.9 Change in Strain from Strand Cutting (Specimen II no bridge deck)

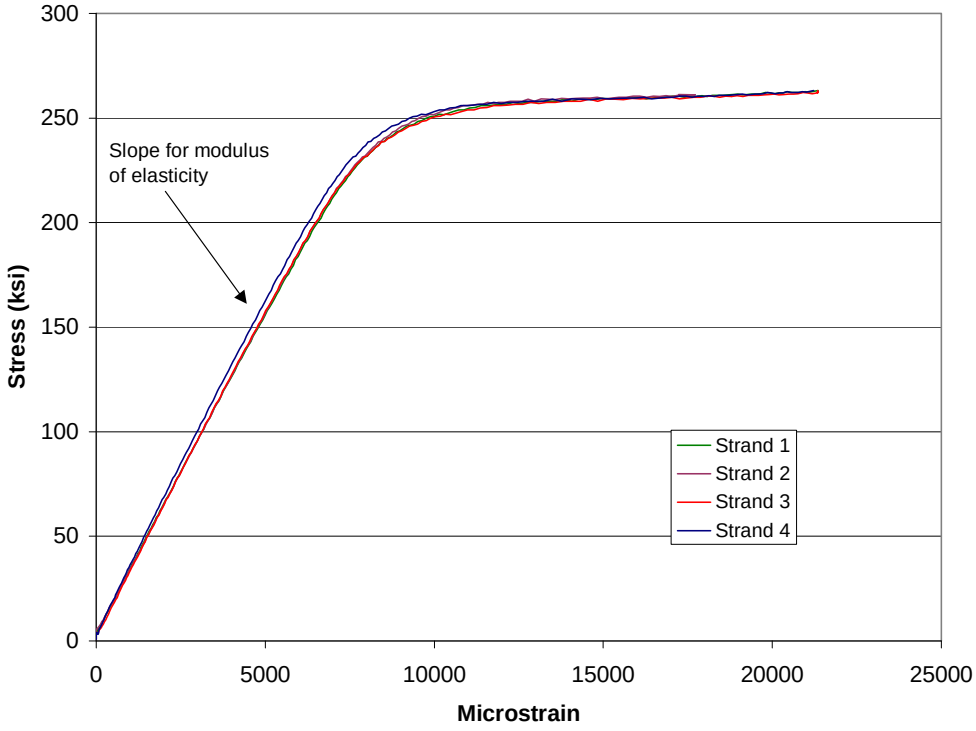

Figure C.10 Prestressing Strand Stress vs. Strain